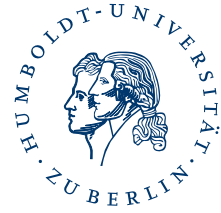


HUMBOLDT-UNIVERSITÄT ZU BERLIN



Search for a signal of quarks of a fourth generation in same-sign dilepton final states with ATLAS

Masterarbeit

zur Erlangung des akademischen Grades

Master of Science (M.Sc. Phys.)
im Fach Physik

eingereicht an der
Mathematisch-Naturwissenschaftlichen Fakultät I
Humboldt-Universität zu Berlin

von

B.Sc. Dennis Wendland
geboren am 13.09.1984 in Berlin

Präsident der Humboldt-Universität zu Berlin:
Prof. Dr. Dr. h.c. Christoph Marksches

Gutachter:

1. Prof. Dr. Heiko Lacker
2. Dr. Sven Moch

eingereicht am: 5. Oktober 2010



Abstract

Currently, a fourth generation of fermions can not be excluded, neither based on theoretical arguments nor by experimental constraints. In this thesis a method developed to extract a signal coming from quarks of such a fourth family with the ATLAS detector at the Large Hadron Collider is presented. The search is performed with the selection of final states containing two same-sign charged leptons, which is a rare Standard Model signature. The signal extraction method presented is a cut-based counting analysis and includes a data-driven background estimation. The analysis is tested on pseudo data which were created from simulated data sets. Furthermore, the uncertainties on the obtained results are estimated by a so-called "Toy Monte Carlo Study". An optimisation of the cuts is finally performed using a multivariate analysis in order to maximise the significance.

Zusammenfassung

Bis heute konnte eine vierte Familie von Fermionen nicht ausgeschlossen werden, weder auf Grund von theoretischen Argumenten noch durch experimentelle Ergebnisse. Das Ziel dieser Arbeit ist die Entwicklung einer Methode zur Extraktion eines Signals von Quarks dieser vierten Familie beim ATLAS Experiment am Large Hadron Collider. Die Suche erfolgt dabei mit der Selektion von Endzuständen mit zwei gleich geladenen Leptonen, welche eine seltene Signatur im Standardmodell darstellen. Die vorgestellte Signalextraktionsmethode ist eine auf Selektionsschnitte basierte Zählanalyse und bietet die Möglichkeit auftretende Untergründe mittels Daten zu kontrollieren. Die Analyse wird an Pseudodaten getestet, welche aus simulierten Datensätzen erstellt wurden. Außerdem werden die Unsicherheiten auf die Ergebnisse mit einer sogenannten "Toy Monte Carlo Studie" ermittelt. Schließlich wird eine Optimierung der Schnitte mittels einer multivariaten Analyse durchgeführt, um eine größtmögliche Signifikanz zu erhalten.

Contents

1. Introduction	1
1.1. The Standard Model of particle physics	1
1.1.1. Electromagnetic interaction	4
1.1.2. Strong Interaction	5
1.1.3. Weak interaction and electroweak unification	8
1.2. A fourth generation of fermions	13
1.2.1. Motivation for a fourth generation	16
1.2.2. Search limits	18
1.2.3. Constraints on CKM matrix elements	20
1.3. The Large Hadron Collider	22
2. The ATLAS detector	27
2.1. The inner detector	29
2.2. The calorimeters	31
2.3. The muon spectrometer	33
2.4. The trigger system	34
3. Reconstruction of physical objects at ATLAS	37
3.1. Electron reconstruction	37
3.2. Muon reconstruction	38
3.3. Jet reconstruction	38
3.3.1. Cone algorithm	39
3.4. Missing energy	39
4. Search for a fourth generation signal in same-sign dilepton final states	41
4.1. Search for fourth generation quarks at ATLAS	41
4.2. Simulated signal and background samples	45
4.3. Analysis framework	48
4.3.1. A^{++}	50
4.4. Selection cuts	50
4.4.1. Electrons	51
4.4.2. Muons	51
4.4.3. Jets	52
4.4.4. Trigger selection	53
4.4.5. Event selection	54
4.4.6. Cut efficiencies	60
4.4.7. Significance	64

Contents

4.5. Counting analysis	66
4.5.1. Basic idea	66
4.5.2. Controlling the main backgrounds	66
4.6. Results for pseudo data	70
4.6.1. Creation of pseudo data	71
4.6.2. Results with default cross sections	71
4.6.3. Results with modified cross sections	72
4.7. Toy studies	79
4.7.1. Results for single toy samples	79
4.7.2. Error estimation for counting analysis	80
4.8. Cut optimisation	83
4.8.1. Results for optimised cuts	90
5. Summary and outlook	93
A. MC samples	95
B. Cut efficiencies and event yields	99
B.1. Generator	99
B.1.1. Event numbers	99
B.1.2. Efficiencies	103
B.2. Event selection cuts	105
B.2.1. Event numbers	105
B.2.2. Efficiencies	109
B.3. Cut efficiency plots	114
B.4. Signal over background plots	117
C. Counting analysis	121
C.1. Single toy sample with modified cross sections	121
C.2. Yield and ratio distributions after toy studies	122
C.3. Mean and RMS values after toy studies	125
C.4. Yields and ratios as a function of the true signal contribution after toy studies	127
D. Cut optimisation	131
D.1. Optimisation with additional variable N_{Jets}	131

1. Introduction

The Standard Model of particle physics provides a full description of elementary particles and their interactions. It is highly successful in describing experimental results from high energy experiments. Observations from cosmology, indication of neutrino mixing and the missing connection between the Standard Model and general relativity imply, that there is room for an extension of the current Standard Model. Many such extensions were proposed, probed and dismissed in the last decades. One straight forward extension, that could potentially help explaining the dark matter content of the universe or the mechanism of Baryogenesis [1], would be the presence of a fourth family.

Three generations of fermions have been experimentally verified. However, a fourth family can not be excluded at this point, neither based on theoretical arguments nor by experimental constraints. Direct searches at previous and present particle physics experiments set limits on fourth generation particles masses. The non-discovery indicates, that new experiments at higher energies are needed for continuative searches. A new powerful particle accelerator is the Large Hadron Collider (LHC [2]) at Geneva. With its center of momentum energy of up to 14 TeV it has the capability of discovering (or excluding) a fourth generation of fermions.

The aim of this thesis is to introduce a strategy for the search for the fourth generation quarks. The decay channel examined is presented and possible background processes are discussed. Furthermore, a signal extraction method is explained, which aims at measuring a fourth generation signal on data taken with the ATLAS [3] detector.

The structure of this thesis is as follows: This chapter gives an introduction to the Standard Model and the facts concerning the fourth generation fermions relevant for this thesis. Besides, a short description of the LHC accelerator is given. Chapter 2 describes the ATLAS detector and its components. In chapter 3, different algorithms used for the reconstruction of physical objects at ATLAS are explained. The analysis is discussed in chapter 4, together with the particle and event selection criteria. The results and an outlook of further studies are presented in chapter 5.

1.1. The Standard Model of particle physics

The Standard Model describes the physics of the three fundamental interactions of the electromagnetic, strong and weak force. The elementary constituents of the Standard Model are twelve fermions with spin $1/2$ and $8 + 3 + 1$ gauge bosons with spin 1. Each fermion has a partner with opposite charge and quantum numbers, but same mass: its antiparticle.

The fermions are grouped into six quarks and six leptons, whereas the quarks carry each of the electromagnetic, strong and weak charge, the leptons only interact electro-

1. Introduction

magnetically and due to the weak force with each other. The fermions are illustrated in

	First family	Second family	Third family	Elm. charge [e]
up-type quarks	u (up)	c (charm)	t (top)	+2/3
down-type quarks	d (down)	s (strange)	b (bottom)	-1/3
neutrinos	ν_e	ν_μ	ν_τ	0
charged leptons	e	μ	τ	-1

Table 1.1.: Fermions of the Standard Model divided into three families. The electromagnetic (elm.) charges are given in units of the elementary charge e .

table 1.1.

The relative strength of an interaction is given by its coupling constant α_i and strength g_i with

$$\alpha_i = \frac{g_i^2}{4\pi} . \quad (1.1)$$

In perturbation theory, the amplitude of a particle transition via an interaction can be described in terms of a power series in the coupling constant. Figure 1.1 illustrates a typical Standard Model fermion pair production process in form of a Feynman diagram. The Feynman diagram is an illustration of perturbative contributions to the amplitude

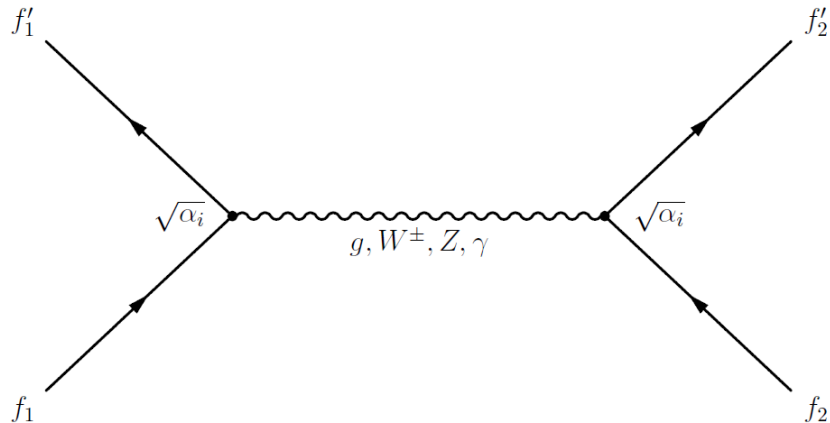


Figure 1.1.: Annihilation and production of a fermion pair by exchange of a gauge boson g , W^\pm , Z , or γ (see table 1.2).

of a process. The shown graph is a first order diagram (called tree-level diagram), where the coupling strength appears at the two vertices. Graphs with more vertices (e.g. due to additional loops) are higher order diagrams that describe contributions from higher order terms in the power series of the amplitude.

A summary of the range and coupling constants of all fundamental interactions is given

1.1. The Standard Model of particle physics

in table 1.2.

Force	Boson(s)	Elm. charge(s)	Mass	Range	Coupling constant
Strong	8 gluons g	0	0	$\sim 10^{-15}$ m	$\alpha_S(M_Z^2) \approx 0.119$
Weak	W^\pm	± 1	~ 80 GeV [4]	$\sim 10^{-18}$ m	$\alpha_W(M_Z^2) \approx 1/29$
	Z	0	~ 91 GeV [4]		
Electromagnetic	Photon γ	0	0	∞	$\alpha(M_Z^2) \approx 1/127$

Table 1.2.: The elementary forces described by the Standard Model. The corresponding gauge bosons, their electromagnetic (elm.) charges and masses, the typical range of the force and the coupling constants at a given mass scale (here the Z -boson mass $M_Z \approx 91$ GeV) are stated. The scale dependence of the coupling constants is further discussed in sections 1.1.1 and 1.1.2. The weak coupling constant α_W is calculated from $\alpha_W = g_W^2/4\pi = \alpha/\sin^2 \Theta_W$ (α is the coupling constant of the electromagnetic interaction and Θ_W the weak mixing angle. See section 1.1.3 for an explanation on the connection between electromagnetic and weak interaction).

The electromagnetic force is the best studied interaction in science: many experiments are devoted to study its Quantum Theory that explain the atomic structure, the build-up of larger molecules and in the classic limit many every day phenomena. In high energy physics its interactions are described by a Quantum Field Theory (QFT) called Quantum Electrodynamics (QED), which is further discussed in section 1.1.1.

Many experimental searches for free quarks lead to the conclusion that they only exist as bound states of either a quark and anti-quark (in the bracket notation of combined wave functions: $|q\bar{q}\rangle$), called mesons, or of three quarks or antiquarks ($|q_1q_2q_3\rangle$ or $|\bar{q}_1\bar{q}_2\bar{q}_3\rangle$), called baryons. These bound states are held together by the strong interaction. The lightest quarks, namely the u and d , are the constituents of the nucleons (proton $|p\rangle = |uud\rangle$ and neutron $|n\rangle = |udd\rangle$). Due to the "Heisenberg uncertainty principle", other quark-antiquark pairs (called sea-quarks) can be produced inside the nucleons for a very short time period $\Delta t < \frac{h}{\Delta E}$. This interval depends on the Planck constant h and the energy of this temporary state ΔE . Within these periods every quark flavor can appear.

Due to the non-perturbative nature of the strong interaction at low energies, the physics of bound states of quarks is very complicated. The theory describing such strongly interacting phenomena best is a Quantum Field Theory called Quantum Chromodynamics. Its main characteristics are discussed a bit further in section 1.1.2.

Another macroscopic phenomenon is radioactivity: radioactive decays of atoms are mediated by the weak interaction. The most simple decay is the β^- decay, transforming a neutron into a proton plus a neutrino and lepton pair: $|udd\rangle \rightarrow |uud\rangle + |\ell\rangle + |\nu\rangle$. At high energies Quantum Electrodynamics and the Quantum Field Theory describing the weak interactions can be unified, what is called the GSW model after Glashow, Salam and Weinberg. The parts relevant for this thesis are discussed in section 1.1.3.

1. Introduction

The striking similarity of the order of magnitude of the observed fermion masses (except the neutrinos), led to the grouping of quarks and leptons into three families, according to their masses. This is illustrated in figure 1.2. The main topic of this work

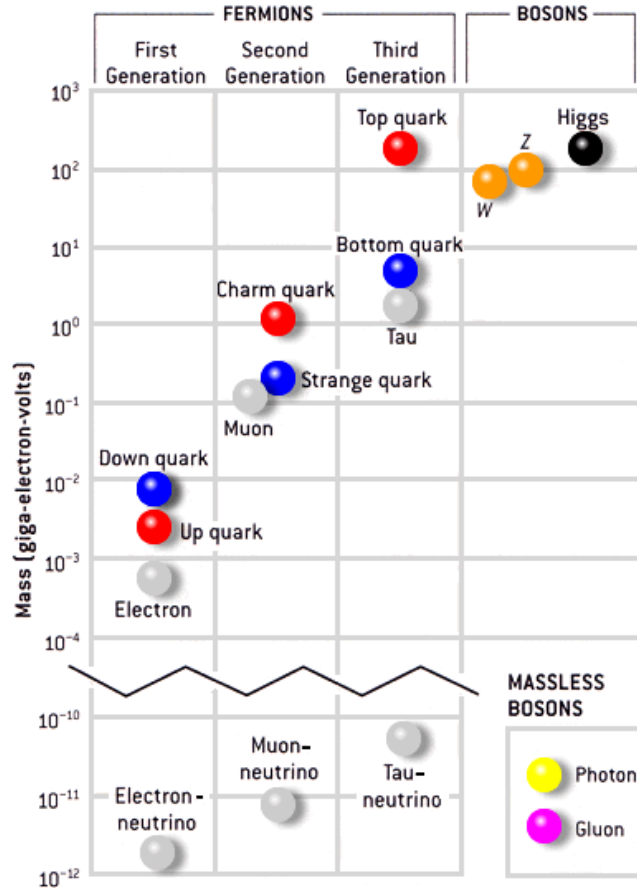


Figure 1.2.: Masses of the Standard Model particles in a logarithmic plot [5].

is to discuss an experimental method to detect fourth generation quarks at the Large Hadron Collider in Geneva. The theoretical implications of such a fourth family are discussed in section 1.2.

1.1.1. Electromagnetic interaction

The mediator of the electromagnetic interaction is the photon. It does not carry any electromagnetic charge and has zero mass. Due to this it travels with the speed of light and gives the electromagnetic interaction an infinite range. The electromagnetic interactions can be described by a Quantum Gauge Theory with a gauge group of $U(1)$.

1.1. The Standard Model of particle physics

This abelian gauge symmetry is apparent in the Lagrangian density of the theory

$$\sum \bar{\psi}_i (i\gamma^\mu D_\mu - m) \psi_i + \frac{1}{4} F^{\mu\nu} F_{\mu\nu} , \quad (1.2)$$

which is invariant under $U(1)$ transformations

$$\psi_i \rightarrow e^{ie\alpha(x)} \psi_i \quad (1.3)$$

$$A_\mu(x) \rightarrow A_\mu(x) + \partial_\mu \alpha(x) , \quad (1.4)$$

where $D_\mu = \partial_\mu + ieA_\mu$ is the covariant derivative, γ^μ are the Dirac-matrices appearing in the Dirac equation, e and m are the electromagnetic charge and the mass of the fermion field ψ_i and $F_{\mu\nu} = \partial_\mu A_\nu - \partial_\nu A_\mu$ the electromagnetic field tensor with the covariant four-potential of the electromagnetic field A_μ .

The connection between the electromagnetic charge e and the coupling constant α of the theory is given by

$$\alpha = \frac{e^2}{4\pi} \approx \frac{1}{137} . \quad (1.5)$$

Through perturbative corrections the coupling constant exhibits a running, as depicted in figure 1.3. At one loop in perturbation theory this running is given by (see section

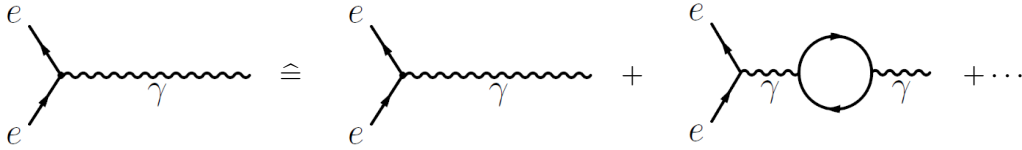


Figure 1.3.: The charge, as it appears in equation 1.5 and as it is measured, is not explained by the left graph. It is given by an infinite number of higher order loop graphs.

7.8 in ref. [6] for further reading)

$$\alpha(Q^2) = \frac{\alpha(\mu^2)}{1 - \frac{\alpha(\mu^2)}{3\pi} \log\left(\frac{Q^2}{\mu^2}\right)} \quad (1.6)$$

where $\alpha(\mu^2)$ is the coupling constant measured at a reference energy μ . The strength of the coupling increases with a higher exchanged momentum.

1.1.2. Strong Interaction

The strong interaction is responsible of binding quarks into hadrons. Its mediator is the gluon, which is massless and appears with eight different combinations of the color charges r , g and b . The theory, which is the currently best description of this interaction,

1. Introduction

is the Quantum Chromodynamics (QCD). QCD possesses a $SU(3)$ gauge symmetry and its Lagrangian density has the form

$$\sum_f \bar{Q}_f (i\gamma^\mu D_\mu - m_f) Q_f - \frac{1}{4} G_{\mu\nu}^a G^{\mu\nu,a}, \quad (1.7)$$

where $D_\mu = \partial_\mu + ig_S G_\mu^a T^a$ is the covariant derivative with the eight generators T^a ($a = 1, \dots, 8$) of $SU(3)$, the eight gauge fields G_μ^a and the strong coupling strength g_S ,

$$G_{\mu\nu}^a = \partial_\mu G_\nu^a - \partial_\nu G_\mu^a - g_S f^{abc} G_\mu^b G_\nu^c \quad (1.8)$$

is the field tensor with structure constants f^{abc} ($a, b, c = 1, \dots, 8$) and

$$Q_f = \begin{pmatrix} q_r \\ q_g \\ q_b \end{pmatrix} \quad (1.9)$$

is the $SU(3)$ -color-triplet of the quark fields with flavor f and mass m_f . Hence, each quark appears with one of these three color charges, which changes when the quark interacts with a gluon.

There have not been observed any color charged hadrons so far. Therefore the color wave function of a hadron has to describe a color neutral state.

The coupling constant of the strong interaction $\alpha_S = g_S^2/4\pi$ depends on the exchanged momentum in the interaction. In comparison to QED, where the photon can fluctuate into fermion loops, the gluons of the QCD can form quark loops and additionally couple to themselves. This results in a slightly different expression, which is then (at one-loop level) given by (see section 7.9 in ref. [6])

$$\alpha_S(Q^2) = \frac{12\pi}{(33 - 2n_f) \log\left(\frac{Q^2}{\Lambda^2}\right)}, \quad (1.10)$$

where n_f is the number of quark flavors, that can contribute to the quark loops at the energy scale Q . This constrains the possible maximum number of quark flavors to $n_f < 16$. Otherwise α_S would become negative. Λ is defined by

$$\alpha_S(\Lambda^2) = 1 \quad (1.11)$$

and constitutes the region, where perturbation theory is no longer an adequate description of the observed process. Λ is therefore called the "cut-off parameter" and it lies in the range of few hundred MeV. If Q^2 is much higher than Λ , then α_S gets sufficiently small so that quarks can be described as free particles ("asymptotic freedom"). Figure 1.4 shows the theoretical prediction and some experimental results for α_S as a function of Q^2 . The coupling increases considerably below values of the order of 1 GeV. The combined result from different experiments for α_S at the Z resonance ($Q = M_Z \approx 91$ GeV)

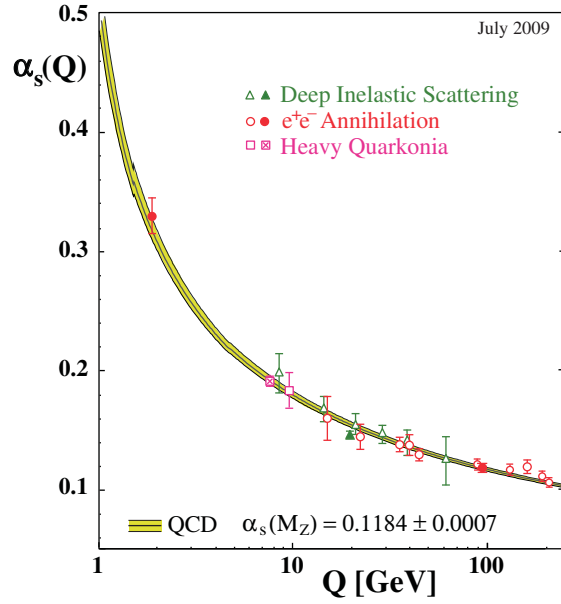


Figure 1.4.: Summary of measurements of α_S as a function of the respective energy scale Q [4]. The shown band illustrates the QCD prediction based on a given scale M_Z .

is [4]:

$$\alpha_S(M_Z^2) = 0.1184 \pm 0.0007 . \quad (1.12)$$

In contrast to the electromagnetic interaction, the attractive force between quarks increases with growing distance between them. An increasing distance corresponds to smaller Q^2 . Figure 1.5(b) displays the potential of the strong interaction between two quarks, calculated by lattice-QCD and perturbation theory [7]. The potential increases monotonically and gets almost linear with higher distances. But at a certain distance of around $r \approx \Lambda^{-1}$ (not visible in this plot), the potential energy is sufficient to create another quark-antiquark pair $q\bar{q}$. This process corresponds to the radiation of a gluon by one of the quarks, which then decays into the $q\bar{q}$ pair. An illustration of this process is given in figure 1.5(a). The blue and yellow ball at the beginning represent a quark-antiquark pair. The "glue" around the quarks illustrates the gluon cloud, which is formed of the permanently radiated gluons. After increasing the distance to a certain point, the quark pair splits and another $q\bar{q}$ pair is produced instantaneously. The phenomenon that quarks do not appear isolated in nature is called "confinement". Since the bound quarks have to form a color neutral state, the confinement also means the existence of only neutral color charged objects in nature.

1. Introduction

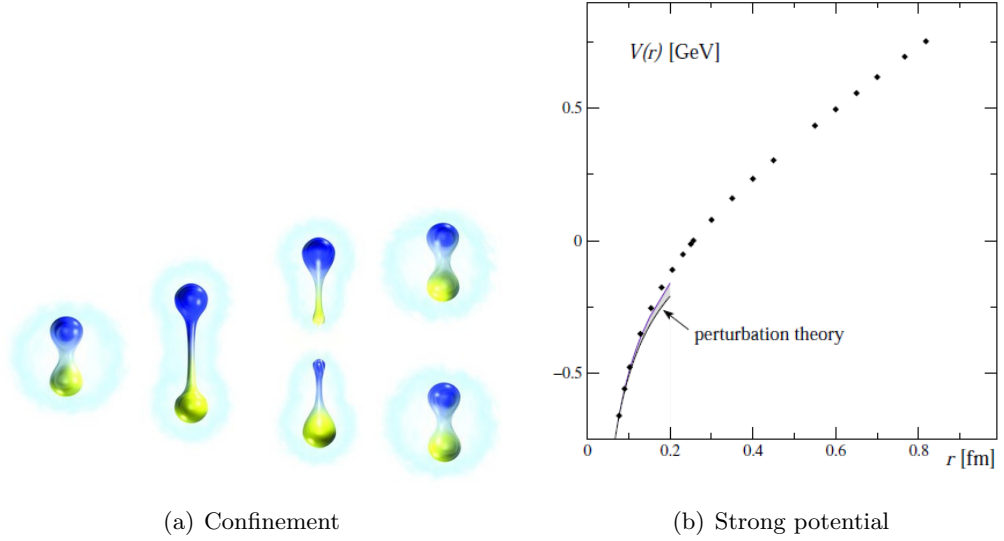


Figure 1.5.: The splitting of two quarks and the instantaneous production of an additional quark-antiquark-pair is illustrated in (a) [8]. Figure (b) shows the result of lattice-QCD (dots) and perturbation theory (curve) calculations for the strong potential as a function of the distance [7].

1.1.3. Weak interaction and electroweak unification

The weak interaction mainly appears in decays of particles in form of charged flavor changing j^{CC} or neutral currents j^{NC} . These currents couple to the electromagnetic charged W^+ - and W^- - and the neutral Z -Boson, respectively.

A typical weak flavor changing process is the μ -decay ($\mu \rightarrow \nu_\mu e^- \bar{\nu}_e$). In this process two currents $J_\mu^{\mu \rightarrow \nu}$ and $J_\mu^{\nu \rightarrow e}$ appear, which describe the particle transitions $\mu^- \rightarrow \nu_\mu$ and $\nu_e \rightarrow e^-$. Due to the flavor change in the process, both currents couple to a W -boson. The amplitude that describes this process is then of the form [6, Eq. 12.14] (with the exchanged four-momentum $q^2 = -Q^2$)

$$\mathcal{M} = \left(\frac{g}{\sqrt{2}} J_\mu^{\mu \rightarrow \nu} \right) \frac{1}{M_W^2 - q^2} \left(\frac{g}{\sqrt{2}} J_\mu^{\nu \rightarrow e} \right) \quad (1.13)$$

$$= \left(\frac{g}{\sqrt{2}} \bar{u}_{\nu_\mu} \gamma^\sigma \frac{1}{2} (1 - \gamma^5) u_\mu \right) \frac{1}{M_W^2 - q^2} \left(\frac{g}{\sqrt{2}} \bar{u}_e \gamma_\sigma \frac{1}{2} (1 - \gamma^5) u_{\nu_e} \right). \quad (1.14)$$

At small q^2 , the propagator, which describes the W -boson exchange, becomes

$$\frac{1}{M_W^2 - q^2} \approx \frac{1}{M_W^2}. \quad (1.15)$$

Note that the magnitude of the coupling strength g is not responsible for the relative

1.1. The Standard Model of particle physics

weakness of the weak interaction¹: at low energies the exchange of gauge bosons is effectively suppressed by the large W -boson mass.

The charged currents have the general form

$$J^\mu = \bar{u}_f \gamma^\mu \frac{1}{2} (1 - \gamma^5) u_i , \quad (1.16)$$

where $\gamma^5 = i\gamma^0\gamma^1\gamma^2\gamma^3$ is formed of the Dirac-matrices, and u_i and \bar{u}_f are the fermion fields of the initial and the final state fermion of the current. While $\bar{u}_f \gamma^\mu u_i$ describes a vector field changing sign of its spatial components under a parity transformation, $\bar{u}_f \gamma^\mu \gamma^5 u_i$ forms an axialvector field, which does not change its sign under the same transformation. The term $\frac{1}{2} (1 - \gamma^5)$ is also defined as the left-handed projector $P_L = \frac{1}{2} (1 - \gamma^5)$, that projects the left-handed component of a particle field u . This V-A (vector-axialvector) form results in the fact, that the gauge bosons W^+ and W^- couple only to left-handed particles. This means, that the particles spin \vec{S} , projected onto its momentum vector \vec{p} , and the momentum itself have to point to opposite directions. Thus in case of massless particles, the helicity

$$\vec{h} = \frac{\vec{S} \cdot \vec{p}}{|\vec{p}|} \quad (1.17)$$

of the particle is negative.

In contrast to the charged currents, neutral currents J^{NC} appear without flavor changes (at tree-level). These currents have the form

$$J_\mu^{NC} = \bar{u} \gamma_\mu \frac{1}{2} (c_V - c_A \gamma^5) u , \quad (1.18)$$

where c_V and c_A describe the vector- and axialvector contributions of the current and have to be determined by experiment. In the case of $c_V \neq c_A$, J_μ^{NC} is not a pure V-A current and has therefore right-handed components. Thus the gauge boson Z can couple to both, left- and right-handed particles.

From processes like the μ -decay, one knows that the flavors of the particles do not have to be conserved in weak interactions. The flavor can change within one family in the case of left-handed fermions. This suggests to introduce a quantum number, the weak isospin I , that changes in flavor changing processes. This isospin classifies the particles and can be seen as the charge of the weak interaction. An isospin of $I = 1/2$ is assigned to the left-handed fermions. Hence these fermions (including leptons and quarks) form

¹At any given scale the weak coupling strength is larger than the electromagnetic coupling. See also Eq. (1.30) for the relation between weak and electromagnetic coupling strength.

1. Introduction

isospin-doublets

$$\begin{pmatrix} u \\ d \end{pmatrix}_L, \begin{pmatrix} c \\ s \end{pmatrix}_L, \begin{pmatrix} t \\ b \end{pmatrix}_L, \quad (1.19)$$

$$\begin{pmatrix} \nu_e \\ e^- \end{pmatrix}_L, \begin{pmatrix} \nu_\mu \\ \mu^- \end{pmatrix}_L, \begin{pmatrix} \nu_\tau \\ \tau^- \end{pmatrix}_L. \quad (1.20)$$

and differ by the third component of its isospins

$$u, c, t, \nu_e, \nu_\mu, \nu_\tau : I_3 = +\frac{1}{2} \quad (1.21)$$

$$d, s, b, e, \mu, \tau : I_3 = -\frac{1}{2}. \quad (1.22)$$

Given the fact that right-handed particles do not appear in flavor changing currents, they are assigned a weak isospin of $I = 0$ and thus form isospin-singlets.

This mechanism can be described by a $SU(2)_L$ gauge symmetry group. The L denotes, that the weak isospin current couples only left-handed fermions.

The theories of electromagnetic and weak interactions can be unified to a theory of electroweak interaction. The corresponding model was developed by the physicists Glashow, Salam and Weinberg and is thus called the GSW-model. As mentioned before, QED and weak interaction can be described by a $U(1)_{em}$ and $SU(2)_L$ symmetry group, respectively. The simplest possible group capable of describing such unification is given by the product $SU(2)_L \otimes U(1)_Y$. The $U(1)_Y$ part does not have to be identical to the gauge group of QED. The conserved charge of this gauge group is called hypercharge and is denoted by Y . This hypercharge is connected to the weak isospin I_3 and the electromagnetic charge Q by

$$Y = 2(Q - I_3). \quad (1.23)$$

The change in the weak isospin in flavor changing charged currents (FCCC) is $\Delta I = 1$. Thus an isospin of $I = 1$ has to be assigned to the three gauge bosons W_μ^a ($a = 1, 2, 3$) of $SU(2)_L$, which form an isospin triplet. In addition, there is one gauge boson B_μ , forming an isospin singlet, which describes the flavor conserving currents. Note that these new gauge fields are not identical to the physical gauge bosons W^\pm , Z and γ .

In QED, the electromagnetic current j^{em} couples to the photon field A_μ and forms an interaction term (section 13.2 in ref. [6])

$$-ie j^{em} A_\mu. \quad (1.24)$$

Consequently, the assumption for the unification is that the basic electroweak interaction term is a combination of the weak isospin current J^i , coupled to the fields W_μ^i with

1.1. The Standard Model of particle physics

strength g , and the current J^Y coupled to a single vector field B_μ with strength g' :

$$-ig(J^i)^\mu W_\mu^i - i\frac{g'}{2}(J^Y)^\mu B_\mu . \quad (1.25)$$

Two symmetry groups still remain with independent coupling strengths g and g' . It is not possible to add mass terms for these gauge fields in the corresponding electroweak Lagrangian, because they would not leave the Lagrangian gauge invariant under $SU(2)_L$ transformations. These masses have to be generated by spontaneous symmetry breaking and the Higgs mechanism (for further reading see chapter 15 in ref. [6]). This results in two fields

$$W_\mu^\pm = \frac{1}{\sqrt{2}} \left(W_\mu^1 \mp W_\mu^2 \right) , \quad (1.26)$$

describing the massive charged W^\pm bosons. The mass terms for W_μ^3 and B_μ are more complicated and contain the non-diagonal mass matrix M . The corresponding term in the Lagrangian is proportional to:

$$\propto \left(W_\mu^3, B_\mu \right) M \begin{pmatrix} W_\mu^3 \\ B_\mu \end{pmatrix} . \quad (1.27)$$

After diagonalizing the matrix M , one obtains the physical fields for the massless photon A_μ and the massive Z -boson Z_μ

$$A_\mu = B_\mu \cos \Theta_W + W_\mu^3 \sin \Theta_W \quad (1.28)$$

$$Z_\mu = -B_\mu \sin \Theta_W + W_\mu^3 \cos \Theta_W , \quad (1.29)$$

which are mixed states of the $SU(2)_L$ field W_μ^3 and the $U(1)_Y$ field B_μ . These mixed states denote the unification of electromagnetic and weak interaction. The strength of the mixing is described by the Weinberg angle Θ_W ($\sin^2 \Theta_W \approx 0.23$), which is given by the two coupling constants $g'/g = \tan \Theta_W$. The Weinberg angle connects the weak to the electromagnetic coupling:

$$g \sin \Theta_W = g' \cos \Theta_W = e . \quad (1.30)$$

In order to introduce quark mass terms in a way that does not spoil gauge invariance, the terms have to be generated by symmetry breaking, following a procedure similar to the W_μ^3 and B_μ mass generation. The resulting mass terms for the down-type quarks have the form [9]

$$\mathcal{L}_{d,m} = -[Q_L^\dagger G Q_R + Q_R^\dagger G^\dagger Q_L] \quad (1.31)$$

1. Introduction

with the left- and right-handed quark triplets

$$Q_{L/R} = \begin{pmatrix} d' \\ s' \\ b' \end{pmatrix}_{L/R} \quad (1.32)$$

and the non-diagonal quark mass matrix G . The down-type quark fields are denoted as d' , s' and b' , since they are not necessarily identical to the physical quark fields (This notation should not be confused with the notation for the fourth generation quark b' , which will appear in the following sections. The description of the non-physical quark fields d' , s' and b' will only be used in this section.). The same applies for the up-type quarks with a mass matrix \tilde{G} .

Both mass matrices G and \tilde{G} cannot be diagonalized simultaneously. The common choice is to diagonalize the up-type quark mass matrix \tilde{G} . As a result, one obtains a mixing of the down-type quark fields. These fields d' , s' and b' , which couple to the W -bosons in charged weak currents, are then rotated states of the (physical) mass eigenstates d , s and b :

$$d' = V_{ud} \cdot d + V_{us} \cdot s + V_{ub} \cdot b \quad (1.33)$$

$$s' = V_{cd} \cdot d + V_{cs} \cdot s + V_{cb} \cdot b \quad (1.34)$$

$$b' = V_{td} \cdot d + V_{ts} \cdot s + V_{tb} \cdot b . \quad (1.35)$$

The parameters V_{ij} describe the mixings of these states. Using these parameters, the charged weak current can then be written as (Eq. 12.119 in [6])

$$J^\mu = \begin{pmatrix} \bar{u} & \bar{c} & \bar{t} \end{pmatrix} \frac{\gamma_\mu(1 - \gamma^5)}{2} V_{CKM} \begin{pmatrix} d \\ s \\ b \end{pmatrix}, \quad (1.36)$$

where V_{CKM} is the unitary 3x3 quark-mixing matrix, also called the CKM matrix (Cabibbo-Kobayashi-Maskawa matrix)

$$V_{CKM} = \begin{pmatrix} V_{ud} & V_{us} & V_{ub} \\ V_{cd} & V_{cs} & V_{cb} \\ V_{td} & V_{ts} & V_{tb} \end{pmatrix}. \quad (1.37)$$

In the case of N fermion families, V_{CKM} extends to a $N \times N$ matrix. In total, the matrix consists of $2N^2$ parameters, since each component has a real and complex part. From

1.2. A fourth generation of fermions

the unitarity of the matrix, one can construct N^2 unitary conditions

$$\sum_{k=1}^N |V_{ik}|^2 = 1 \quad (1.38)$$

$$\sum_{n=1}^N |V_{nj}|^2 = 1 \quad (1.39)$$

for all rows k and columns j . The $2N$ quark fields can each be changed by additional phases. These phases are not visible in physical observables and the phase changes are not altering the physics. Hence, one has the freedom to redefine these phases in a way, that $2N - 1$ phases vanish and one overall phase remains. The resulting number of parameters in the $N \times N$ quark mixing matrix is then:

$$2N^2 - \underbrace{N^2}_{\text{unitarity}} - \underbrace{(2N - 1)}_{\text{phase redefinition}} = N^2 - 2N + 1 \quad (1.40)$$

$$= (N - 1)^2 . \quad (1.41)$$

The values of the $(N - 1)^2$ parameters can not be predicted within the Standard Model and have to be measured by experiments. In the case of three families, one remains with 4 parameters. These consist of three real parameters and one overall phase factor.

A possible parametrization for the matrix with these parameters is to introduce three Euler angles $(\theta_{12}, \theta_{13}, \theta_{23})$, describing the mixing between the three families 1, 2 and 3, and a phase angle δ . The CKM-matrix is then of the form (see chapter 11 in ref. [4]):

$$V_{CKM} = \begin{pmatrix} c_{12}c_{13} & s_{12}c_{13} & s_{13}e^{-i\delta} \\ -s_{12}c_{23} - c_{12}s_{23}s_{13}e^{i\delta} & c_{12}c_{23} - s_{12}s_{23}s_{13}e^{i\delta} & s_{23}c_{13} \\ s_{12}s_{23} - c_{12}c_{23}s_{13}e^{i\delta} & -c_{12}s_{23} - s_{12}c_{23}s_{13}e^{i\delta} & c_{23}c_{13} \end{pmatrix} . \quad (1.42)$$

s_{ij} and c_{ij} describe the sinus and cosinus of the mixing angle θ_{ij} :

$$s_{ij} = \sin \theta_{ij} \quad (1.43)$$

$$c_{ij} = \cos \theta_{ij} . \quad (1.44)$$

The complexity of the CKM matrix ($\delta \neq 0$ or $\delta \neq \pi$) is a source of CP violation (see [10]), e.g. a non-invariance of physical states after parity and charge transformations.

1.2. A fourth generation of fermions

The Standard Model currently describes the presence of three fermion families (see section 1.1).

Measurements of the hadronic production cross section at the LEP experiment [11] predicted the number of light neutrino families. Figure 1.6 illustrates the measured cross sections as a function of the center of mass energy around the Z resonance. The

1. Introduction

curves indicate the theoretical Standard Model prediction for the cases of two, three and four light neutrino families. One notices a good consistence with the three family case. However, this does not exclude a neutrino of a fourth family. It only constrains its mass

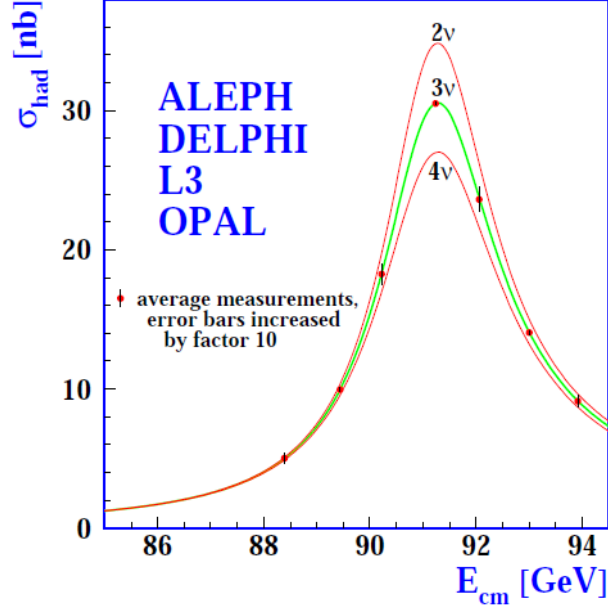


Figure 1.6.: Measurements of the hadronic production cross section around the Z resonance, done at the LEP experiment [11]. The curves indicate the theoretical Standard Model prediction for the cases of two, three and four neutrino families.

to be at least $m_{\nu_4} > \frac{M_Z}{2}$.

The existence of a fourth generation neutrino would also mean the presence of two additional quarks and a charged lepton in the same family, because the numbers of quark and lepton families have to be equal in the Standard Model. This is due to the requirement of a renormalizable gauge theory, which demands a cancellation of "anomalies" due to fermion loops, like the triangle diagram shown in figure 1.7. Each diagram with a specific fermion f itself gives an infinite contribution to the amplitude of this process, spoiling the renormalizability of the Standard Model. This arises from the momentum integral of the fermion loop. Moreover, each diagram is proportional to $\propto c_A^f Q_f^2$ with the electric charge Q_f and the axial coupling to the weak neutral current c_A^f of a fermion f . With the known charges of the fermions Q_f and considering the three color charges of the quarks ($N_C = 3$), the total anomaly only vanishes by the summation of a neutrino ($f = \nu$), a charged lepton ($f = \ell$), an up-type ($f = u$) and a down-type

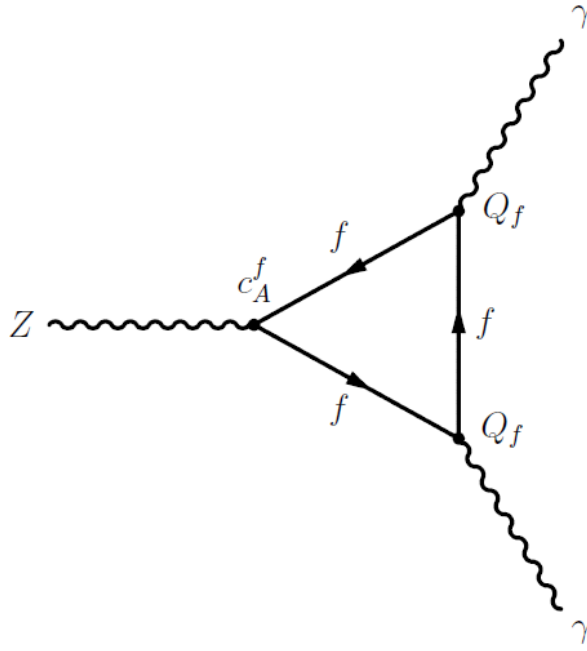


Figure 1.7.: Feynman graph showing the triangle anomaly. A Z-boson turns into a fermion loop, which radiates two photons.

($f = d$) quark contribution in each family i (see section 12.12 in ref. [6]):

$$\propto \sum_{i=1}^N [Q_{\nu_i} + Q_{\ell_i} + N_c \cdot (Q_{u_i} + Q_{d_i})] \quad (1.45)$$

$$\propto \sum_{i=1}^N [0 + (-1) + 3 \cdot (+2/3 + (-1/3))] = 0 . \quad (1.46)$$

N denotes the total number of fermion families.

By adding the 4th family to the Standard Model fermions, the table in section 1.1 has to be enlarged by a new column containing the new particles. In the following, these new particles will be referred to as t' (the up-type quark), b' (the down-type quark), ν_4 (the neutrino) and ℓ_4 (the charged lepton). Table 1.3 summarizes the particles.

The quark mixing matrix, mentioned in section 1.1.3, also has to be modified. It will turn into a 4x4-matrix:

$$V_{CKM}^{4 \times 4} = \begin{pmatrix} V_{ud} & V_{us} & V_{ub} & V_{ub'} \\ V_{cd} & V_{cs} & V_{cb} & V_{cb'} \\ V_{td} & V_{ts} & V_{tb} & V_{tb'} \\ V_{t'd} & V_{t's} & V_{t'b} & V_{t'b'} \end{pmatrix} . \quad (1.47)$$

1. Introduction

	1st family	2nd family	3rd family	4th family	charge [e]
up-type quarks	u (up)	c (charm)	t (top)	t'	+2/3
down-type quarks	d (down)	s (strange)	b (bottom)	b'	-1/3
neutrinos	ν_e	ν_μ	ν_τ	ν_4	0
charged leptons	e	μ	τ	ℓ_4	-1

Table 1.3.: Fermions of the Standard Model with an additional 4th family. The charges are the electromagnetic charges given in units of the elementary charge e .

In the case of $N = 4$ families, the matrix is now determined by $(4 - 1)^2 = 9$ parameters (see section 1.1.3), which split up into six real parameters and three phase angles. Like in the 3x3 case, these parameters also have to be determined from experiment. For the standard parametrization, introduced in equation (1.42), one has to multiply the matrix of the three family case $V_{CKM}^{3 \times 3}$ by three new matrices, describing the mixing of the fourth family with the other three known Standard Model families:

$$\begin{aligned}
 V_{CKM}^{4 \times 4} = & \begin{pmatrix} & & & 0 \\ & V_{CKM}^{3 \times 3} & & 0 \\ & & & 0 \\ 0 & 0 & 0 & 1 \end{pmatrix} \times \begin{pmatrix} 1 & 0 & 0 & 0 \\ 0 & 1 & 0 & 0 \\ 0 & 0 & c_{34} & s_{34} \\ 0 & 0 & -s_{34} & c_{34} \end{pmatrix} \times \\
 & \times \begin{pmatrix} 1 & 0 & 0 & 0 \\ 0 & c_{24} & 0 & s_{24}e^{-i\delta_2} \\ 0 & 0 & 1 & 0 \\ 0 & -s_{24}e^{i\delta_2} & 0 & c_{24} \end{pmatrix} \times \begin{pmatrix} c_{14} & 0 & 0 & s_{14}e^{-i\delta_3} \\ 0 & 1 & 0 & 0 \\ 0 & 0 & 1 & 0 \\ -s_{14}e^{i\delta_3} & 0 & 0 & c_{14} \end{pmatrix}. \quad (1.48)
 \end{aligned}$$

The new Euler angles $(\theta_{14}, \theta_{24}, \theta_{34})$ denote the mixings between the fourth family and the other three families. The phase angles are described by δ_1, δ_2 and δ_3 . s_{i4} and c_{i4} ($i = 1, 2, 3$) are the sinus and cosinus of the angles θ_{14}, θ_{24} and θ_{34} .

1.2.1. Motivation for a fourth generation

As long as a fourth generation is not ruled out, it is mandatory to search for such new particles in order to definitely decide whether the Standard Model has to be extended in this sense. Moreover, the existence of a fourth family could have significant impact on the Standard Model parameters or possibly provide ways to solve open problems of the Standard Model.

There are discussions about a possible role of the fourth generation in the explanation of the baryon asymmetry in the universe (BAU). One necessary condition to generate the BAU is the violation of the CP invariance (CPV) [12]. In the case of three families, the CPV introduced by the CKM matrix is too small in order to explain the BAU. But the large masses of the fourth generation quarks could provide an enhancement in the CP violation. See ref. [1] for further reading.

Due to the high masses of the new particles, a fourth family could play an important role in the electroweak symmetry breaking (EWSB). With quark masses as high as

1.2. A fourth generation of fermions

≈ 600 GeV, these fourth generation quarks could form a condensate via a new "strong" interaction. This condensate could then appear as a scalar field that would be responsible for the EWSB. Even if this "strong" interaction does not exist, a fourth generation would have an impact to the phenomenology of EWSB due to the strong coupling to the Higgs boson. See ref. [13] and [14] for further reading.

The introduction of a fourth family results in contributions to oblique electroweak (EW) corrections. EW precision variables (like the decay width and the mass of the Z -boson) can be parametrized by the three parameters S , T and U (also known as Peskin-Takeuchi parameters [15]). These are defined in a way that at a reference point in the Standard Model, with a particular value chosen for the Higgs boson mass, results $(S, T) = (0, 0)$. The parameter U can be set to zero, since it is in all calculations very small ($U < 0.02$). Thus, U will not be considered in the following.

The introduction of new physics (such as a fourth family) results in shifts (ΔS and ΔT) of these parameters. Fits of the electroweak data provide constraints on the oblique parameters and therefore constrain new physics. Figure 1.8(a) illustrates the 68% confidence level ellipse in the (S, T) -plane, obtained by the fit of the LEP electroweak working group (LEPEWWG) [16]. They find that the Standard Model (with defined Higgs boson and top masses of $m_H = 115$ GeV and $m_t = 170.9$ GeV) lies inside this ellipse. But higher Higgs masses would move the point outside of this ellipse by an increase in S and a reduction of T . This is denoted by the red solid curve in figure 1.8(b).

The effect of increasing the Higgs boson mass can be compensated by introducing a fourth generation. This would give an additional shift in S and T , depending on the masses of the new particles ([18] and [19]):

$$\Delta S = \frac{N_c}{6\pi} \left(1 - 2Y \left[\ln \frac{m_{t'}^2}{m_{b'}^2} - \ln \frac{m_{\nu_4}^2}{m_{\ell_4}^2} \right] \right) \quad (1.49)$$

$$\Delta T = \frac{N_c}{12\pi s_W^2 c_W^2} \left[\left(\frac{m_{t'}^2 - m_{b'}^2}{m_Z} \right)^2 + \left(\frac{m_{\nu_4}^2 - m_{\ell_4}^2}{m_Z} \right)^2 \right]. \quad (1.50)$$

This only applies if the fermion masses are nondegenerate. With higher Higgs boson masses, the shifts could move the point back into the ellipse in such a way, that the constraints extracted from the measurements are still fulfilled. Figure 1.8(b) illustrates the change of the S and T values for some combinations of masses for the new fermions and the Higgs boson. The corresponding values can be seen in table 1.4. The fit to EW precision data is in agreement with the existence of a fourth family in each mass scenario.

In the scenario with three families, the point lies clearly outside the 95% confidence ellipse for Higgs boson masses above 200 GeV. Due to the logarithmic dependence on the mass ratios in ΔS , higher mass differences would generally provide larger shifts in T than in S . By choosing suitable masses for the fourth generation particles, this would permit higher Higgs boson masses up to 750 GeV, when demanding an agreement with the data within the 95% confidence ellipse [18].

Due to the dependence of the shifts in S and T on the ratios and differences of the fourth

1. Introduction

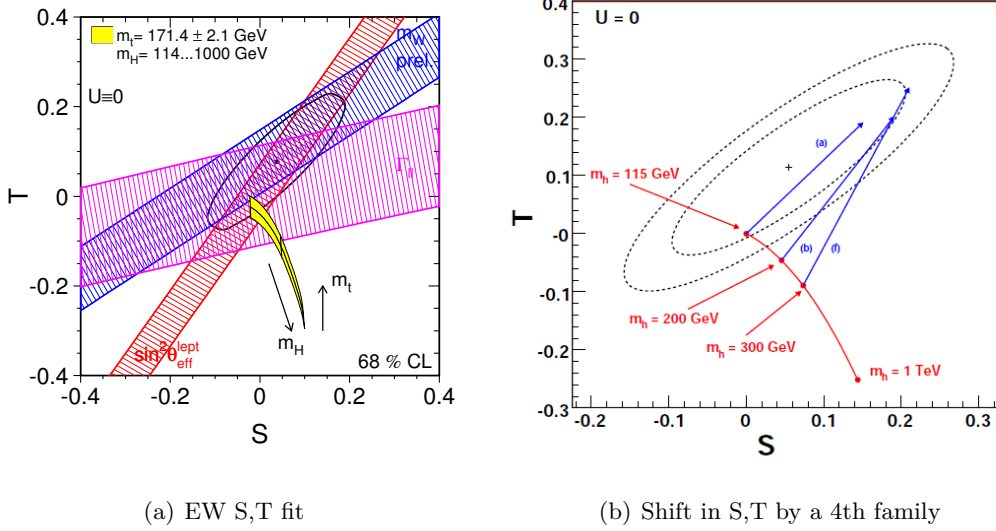


Figure 1.8.: Figure (a) shows the 68% confidence level constraint on the S and T parameter obtained from a fit to electroweak precision data performed by the LEPWWG [17].

Figure (b) illustrates the shift in S,T by adding additional 4th generation fermions with different mass combinations (blue arrow lines), listed in table 1.4, and increasing the Higgs boson mass (red solid line) [18]. Both, the 68% and the 95% confidence level ellipses are shown.

generation fermion masses, the constraints from the EW precision fits provide restrictions on the mass relations of the new quarks and leptons. It is obvious that the mass differences cannot be arbitrarily large in order to fulfill the experimental constraints.

Parameter set	$m_{t'}$ [GeV]	$m_{b'}$ [GeV]	m_H [GeV]	ΔS	ΔT
(a)	310	260	115	0.15	0.19
(b)	320	260	200	0.19	0.20
(f)	400	325	300	0.21	0.25

Table 1.4.: Parameter sets for the shifts in the (S, T) parameter space (figure 1.8(b)), due to a 4th family. The lepton masses are fixed to $m_{\ell_4} = 155$ GeV and $m_{\nu_4} = 100$ GeV [18].

1.2.2. Search limits

Searches for fourth generation quarks and leptons at Tevatron and LEP have led to mass limits, which are discussed in more detail in this section.

1.2. A fourth generation of fermions

Searches for the heavy quarks have been performed by the CDF [20] and DØ [21] experiments at the Tevatron. The current known mass limits were obtained from CDF. In the search for the t' [22] has been assumed a pair production $t'\bar{t}'$ of short-lived particles, which decay into a W -boson and a down-type quark ($q = d, s, b$) each. One of these W -bosons is assumed to decay leptonically. This results in the requirement of at least four jets, one single lepton (electron or muon) and missing transverse energy ($\cancel{E}_T > 20$ GeV). A binned Likelihood fit was used to extract the amount of signal and background events from a data set corresponding to an integrated luminosity of 2.8 fb^{-1} . These are used to set an upper limit on the production rate and the cross section times branching fraction ($\sigma \cdot B$) of this process. By comparing this limit with the theoretical cross sections of processes with different t' masses, this gives a lower limit on the t' mass of $m_{t'} > 335$ GeV at a 95% confidence level.

In the search for the b' [23] has been supposed a $b'\bar{b}'$ pair production. Each b' is assumed to have a short lifetime and to decay via $b' \rightarrow tW \rightarrow bWW$ into two oppositely charged W -bosons and one b quark. The resulting final state is: $W^+W^+W^-W^-b\bar{b}$. In the analysis, events with two same-sign charged leptons (electrons or muons), one b -jet, one light quark jet and missing transverse energy ($\cancel{E}_T > 20$ GeV) were selected. As for the t' search, a Likelihood fit was done and limits to the cross section were calculated. By comparing with the theoretical predictions, a lower limit of $m_{b'} > 338$ GeV was set at a 95% confidence level.

Searches for the heavy leptons have been performed by the L3 experiment [24]. In the search for the charged lepton ℓ_4 [25] has been assumed a pair production via the decay of a directly produced Z -boson or photon γ . They distinguish between different scenarios:

- The charged heavy lepton has a short lifetime and decays into a W -boson and either one light neutrino or one neutrino of the fourth generation ν_4 . The W -bosons have to decay either leptonically or hadronically.
- The ℓ_4 is assumed to be long-lived so that it traverses the detector without a decay. In this case, events with two back-to-back high momentum tracks were selected.

For each scenario, the observed events are extracted from a data set corresponding to an integrated luminosity of 450 pb^{-1} . Lower mass limits are calculated for each scenario by comparing the determined cross sections with the theoretical cross sections. The lowest limit excludes heavy charged leptons of a fourth generation with masses below 100.8 GeV at a 95% confidence level.

In the search for the heavy neutrino ν_4 [25], a pair production $\nu_4\bar{\nu}_4$ was assumed, but only via the decay of a Z -boson. Neutrinos only participate in weak interactions. The analysis was split into two scenarios: The fourth generation neutrinos are either Dirac or Majorana (neutrino and anti-neutrino are the same particle) particles. The search was restricted to neutrinos with a decay length smaller than 1 cm. This is done in order to avoid decays far away from the interaction point and to ensure high detection and reconstruction efficiencies. They considered decays of the neutrino into electrons, muons or taus and an additional W -boson. In the same way as in the ℓ_4 search, they

1. Introduction

calculated lower mass limits for each decay and neutrino (Dirac or Majorana) scenario. The lowest limit for the Dirac neutrino is $m_{\nu_4}^{Dirac} > 90.3 \text{ GeV}$ and for the Majorana neutrino $m_{\nu_4}^{Majorana} > 80.5 \text{ GeV}$.

All previously discussed mass limits are summarized in table 1.5.

Particle	m_{min} [GeV]	Experiment
t'	335	CDF [22]
b'	338	CDF [23]
ν_4^{Dirac}	90.3	L3 [25]
$\nu_4^{Majorana}$	80.5	L3 [25]
ℓ_4	100.8	L3 [25]

Table 1.5.: The current mass limits on fourth generation fermions at a 95% confidence limit.

1.2.3. Constraints on CKM matrix elements

The absolute values of several elements of the 3x3 CKM matrix are already precisely measured. The ones most precisely determined, including their uncertainties, are sum-

CKM matrix element	Value [4]
V_{ud}	0.97425 ± 0.00022
V_{us}	0.2252 ± 0.0009
V_{cd}	0.230 ± 0.011
V_{cs}	1.023 ± 0.036
V_{cb}	$(40.6 \pm 1.3) \times 10^{-3}$
V_{ub}	$(3.89 \pm 0.44) \times 10^{-3}$

Table 1.6.: The most precisely measured CKM matrix elements with their uncertainties. Further details on how these elements have been measured are described in chapter 11 of ref. [4].

marized in table 1.6.

In the four family case, the CKM matrix turns into a 4x4 matrix, as mentioned in section 1.2. Furthermore, the introduction of the fourth generation has influences on the extraction methods of the already determined 3x3 CKM matrix elements. For instance, the branching fractions of tree-level W -boson decays yield further constraints on the element $|V_{cs}|$ (this applies also for the three family case, but a fourth family gives further constraints). The same applies for the constraints from top quark decay branching fractions on the element $|V_{tb}|$. The extraction of the most precisely measured CKM element, $|V_{ud}|$, considerably depends on the accurate measurement of the Fermi constant G_F . Due to the fact that the extraction of G_F has to be reconsidered in the four family scenario, this also influences the determination of $|V_{ud}|$. See [26], [27] and

1.2. A fourth generation of fermions

[28] for further information on the influences on the CKM matrix by the introduction of a fourth generation.

The above mentioned changes of the constraints on the 3x3 CKM matrix elements and the unitarity of the 4x4 CKM matrix can now be used to obtain values and allowed ranges for the fourth generation CKM matrix elements. For instance, the unitarity relations for the first three rows can be used to determine the absolute values of the following elements:

$$|V_{ub'}|^2 = 1 - |V_{ud}|^2 - |V_{us}|^2 - |V_{ub}|^2 \quad (1.51)$$

$$|V_{cb'}|^2 = 1 - |V_{cd}|^2 - |V_{cs}|^2 - |V_{cb}|^2 \quad (1.52)$$

$$|V_{tb'}|^2 = 1 - |V_{td}|^2 - |V_{ts}|^2 - |V_{tb}|^2 \quad (1.53)$$

$$(1.54)$$

Similar relations can be used for the other elements. The estimation of the values was done using a global fit to several quantities with the *CKMfitter* [29] package in ref. [28]. The obtained central absolute values and the corresponding 1σ standard deviations are as follows:

$$|V_{CKM}^{4x4}| = \begin{pmatrix} 0.97414_{-0.00023}^{+0.00032} & 0.2245_{-0.0012}^{+0.0012} & (4.200_{-0.910}^{+0.090}) \cdot 10^{-3} & 0.025_{-0.025}^{+0.011} \\ 0.2256_{-0.0059}^{+0.0011} & 0.9717_{-0.0105}^{+0.0024} & (41.09_{-1.45}^{+0.45}) \cdot 10^{-3} & 0.057_{-0.057}^{+0.097} \\ 0.001_{-0.001}^{+0.035} & 0.062_{-0.062}^{+0.044} & 0.910_{-0.080}^{+0.079} & 0.41_{-0.27}^{+0.15} \\ 0.013_{-0.013}^{+0.039} & 0.04_{-0.04}^{+0.12} & 0.41_{-0.27}^{+0.14} & 0.910_{-0.083}^{+0.078} \end{pmatrix}. \quad (1.55)$$

In quark transitions with flavor changes, e.g. $b' \rightarrow t$, the considered amplitude \mathcal{M} is proportional to the corresponding absolute CKM element squared: $\mathcal{M} \propto |V_{tb'}|^2$. Hence, the elements $|V_{ib'}|$ and $|V_{t'j}|$ describe the strength of the mixing between the fourth family and the family to which the quarks i and j belong. In the matrix above, the constraints on the elements $|V_{tb'}|$ and $|V_{t'b}|$ allow a sufficient large mixing between the fourth and the third family with respect to the mixings between fourth and second or rather fourth and first family:

$$0.41 \gg 0.057, 0.025 \quad (1.56)$$

$$0.41 \gg 0.04, 0.013. \quad (1.57)$$

A CKM matrix is now selected by assuming exact unitarity and calculating the elements starting from the unitarity relation for a row or column. The absolute values of the elements of the chosen CKM matrix, which is used in this analysis, are as follows:

1. Introduction

$$|V_{CKM}^{4x4}| = \begin{pmatrix} 0.97417 & 0.22530 & 0.00341 & 0.01460 \\ 0.22443 & 0.97271 & 0.04117 & 0.04200 \\ 0.00642 & 0.03769 & 0.99413 & 0.10125 \\ 0.02393 & 0.04062 & 0.10003 & 0.99387 \end{pmatrix} \quad (1.58)$$

It fulfills all given constraints in Eq. (1.55) at least within 2σ standard deviations. Due to its elements $|V_{tb'}|$ and $|V_{t'b}|$, the quark decays $b' \rightarrow tW$ would be preferred with respect to decays $b' \rightarrow cW$ and $b' \rightarrow uW$.

1.3. The Large Hadron Collider

The Large Hadron Collider (LHC) is a particle accelerator designed to collide protons and also heavy ions. It is located near Geneva (Switzerland) at the European Organization for Nuclear Research (CERN). The LHC is installed in the already existing tunnel, built for the previous accelerator Large Electron Positron Collider (LEP), and has a circumference of 26.7 km [2].

Before being injected into the main LHC ring, the protons are accelerated by several pre-accelerators, which were used by previous experiments at CERN. The protons accelerating stages are the following: after ionizing hydrogen gas, the protons are speeded up by a linear accelerator (LINAC) in form of bunches with up to 10^{11} protons each. These bunches get successively injected into different synchrotrons, namely the proton synchrotron booster (PSB), the proton synchrotron (PS) and the super proton synchrotron (SPS), each accelerating the bunches to higher energies. Finally, these bunches are transferred into the main LHC ring, where they are accelerated to the energy of 7 TeV. Injecting the bunches into two counter-rotating beams and colliding them at specific points results in a total center of mass energy of 14 TeV ($\sqrt{s} = 14$ TeV). An overview of the accelerator complex at CERN is illustrated in figure 1.9. Although the design energy of the LHC is 14 TeV, it is currently running only at $\sqrt{s} = 7$ TeV. This is due to an incident, that occurred after the start-up in September 2008 [31].

When running at design parameters, the LHC can reach a luminosity of $\mathcal{L} = 10^{34} \text{ cm}^{-2}\text{s}^{-1}$. This means, that 10^{34} protons are traversing in the beam pipe per cm^2 and second. The luminosity is defined as

$$\mathcal{L} = f \cdot \frac{n_1 n_2}{4\pi\sigma_x\sigma_y}, \quad (1.59)$$

where f describes the collision frequency, n_1 and n_2 the number of protons in the two colliding bunches and $\sigma_{x/y}$ the beam width in x/y direction. With a bunch spacing of 25 ns this results in a bunch crossing rate at the interaction points of 40 MHz.

By multiplying the luminosity with the cross section of a physical process σ , one obtains

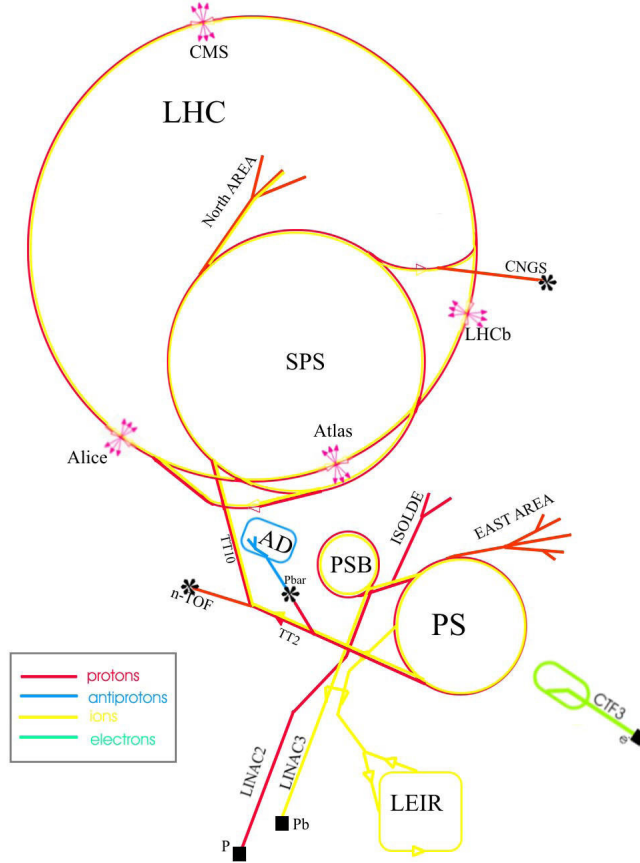


Figure 1.9.: The CERN accelerator complex used for the different acceleration stages [30]. Also some other experiments are shown, which use the same infrastructure. The particle beams start either at LINAC2 with protons or at LINAC3 with heavy lead ions, depending on the current running mode of the LHC.

the event rate R for this process:

$$R = \mathcal{L} \cdot \sigma . \quad (1.60)$$

Although the protons collide at a center of momentum energy of $\sqrt{s} = 14 \text{ TeV}$, this is not the energy available for the particle processes. The exchanged momentum Q in the process depends on the four-momenta p , carried by the interacting partons. Each parton contributes with a fraction x to the total four-momentum P of the proton:

$$p = x \cdot P . \quad (1.61)$$

The probability density of a parton of type i carrying a specific momentum fraction x is given by the parton distribution function (PDF) $f_i(x, Q^2)$. It also depends on the

1. Introduction

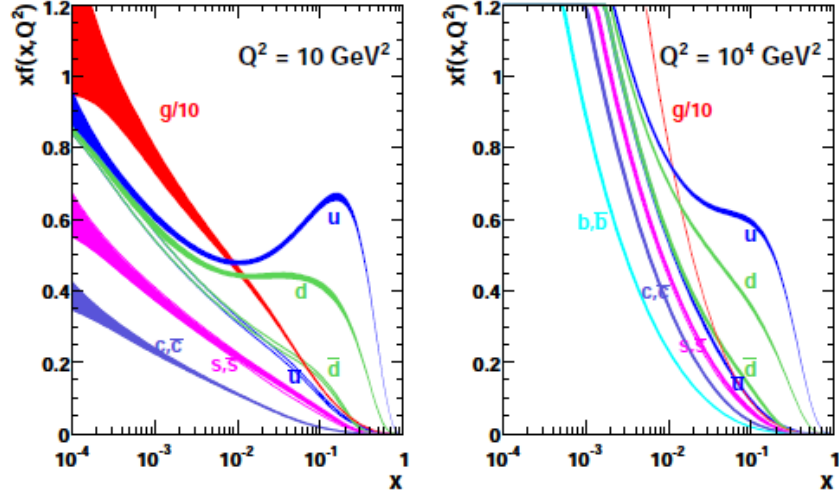


Figure 1.10.: Parton distribution functions f_i and their 1σ confidence level uncertainty bands, multiplied by the momentum fraction x , for several partons in the proton at two different scales of Q^2 . The distribution for the gluons is downscaled by a factor of 0.1. This plot shows the PDFs from the MSTW group [32].

considered transferred momentum Q , which is achievable at a specific proton energy. The product $x \cdot f_i$ is the probability of finding a parton with such a momentum fraction. These functions cannot be calculated by theory and have to be determined by experiment. Figure 1.10 shows some PDFs at momentum scales of $Q^2 = 10 \text{ GeV}^2$ and $Q^2 = 10^4 \text{ GeV}^2$. Due to the large contribution in the PDFs, gluons mostly carry the highest fraction of the protons momentum. Thus processes with the production of heavy particles, which need large Q^2 , start with the interaction of gluons. The second highest contribution comes from the quarks u and d , in which the distribution for the u quark is higher than for the d quark. Both appear as sea quarks, but the u appears in the form of a valence quark twice as often as the d . For the other sea quarks (\bar{u} , \bar{d} , $c\bar{c}$ and $s\bar{s}$), the distributions are all smaller than for the u and d quarks.

For measuring the processes happening at the collision points, huge particle detectors have been built around these interaction points. The four main experiments at LHC are namely ATLAS [3], CMS [33], LHCb [34] and ALICE [35]. Figure 1.11 displays their locations at the LHC. While ATLAS and CMS are multi-purpose detectors, covering different aspects of particle physics, ALICE and LHCb are detectors built for special aims. The LHCb detector focuses on the measurement of b -hadrons and their decays, which gives the possibility to investigate CP violation and several other parameters of the standard model. The aim of the ALICE detector is the measurement of properties of the quark-gluon-plasma, presumably produced by the collision of lead ions. By investigating this plasma, one obtains information about the state of the universe just micro seconds

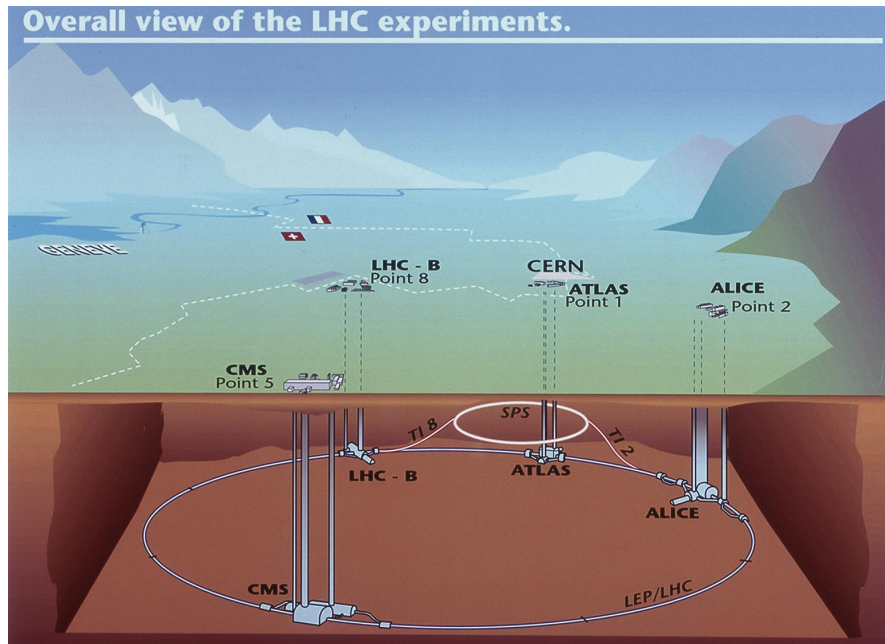


Figure 1.11.: The experiments at the Large Hadron Collider (LHC). They are located at the collision points of the two proton beams, which circulate in the particle accelerator installed in a 26.7 km tunnel under the surface of Switzerland and France [36].

after the big bang.

This thesis deals with the search for fourth generation quarks with the ATLAS detector, which is described in chapter 2.

2. The ATLAS detector

The ATLAS detector (A Toroidal Lhc ApparatuS) is a multi-purpose particle detector, capable of measuring particles and their kinematics in a 4π symmetry. This means a coverage of almost the entire solid angle around the collision point. An overview of the detector can be seen in figure 2.1. With a length of 45 m and a height of 22 m, ATLAS

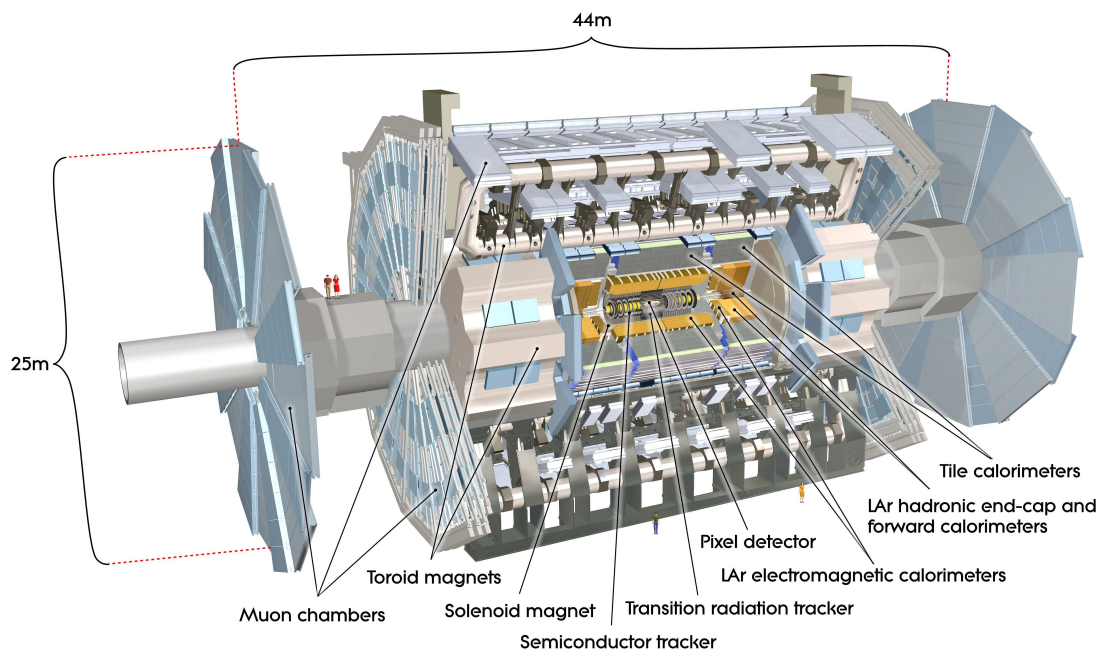


Figure 2.1.: Overview of the ATLAS detector [3].

is the biggest detector not only at the LHC, but also ever built. With a mass of around 7000 t it is lighter than CMS, the heaviest detector, which weighs up to 12 000 t.

The ATLAS detector has a cylindrical symmetry comprised of a central barrel part and end-caps on each end along the beam pipe. Due to this symmetry, one uses a cylindrical coordinate system to describe positions and directions of particles, traversing the detector. The z coordinate then describes the position along the beam pipe in the clockwise direction of the LHC. ϕ is the azimuthal angle in the x-y plane and Θ the polar angle between the beam pipe and the particles direction. But instead of Θ one

2. The ATLAS detector

uses commonly the pseudorapidity

$$\eta = -\ln\left(\tan\frac{\Theta}{2}\right). \quad (2.1)$$

In the massless limit, η is equal to the rapidity

$$y = \frac{1}{2} \ln\left(\frac{E + p_z}{E - p_z}\right), \quad (2.2)$$

which contains the particles energy E and the z component of its momentum. The advantage of the rapidity is its invariance under Lorentz boosts. This can be seen by first rearranging the rapidity formula to

$$y = \ln\left(\frac{\sqrt{E + p_z}}{\sqrt{E - p_z}}\right) = \ln\left(\frac{E + p_z}{E^2 - p_z^2}\right) = \ln\left(\frac{E + p_z}{\sqrt{p_T^2 + m^2}}\right). \quad (2.3)$$

The last equality derives from splitting the momentum p in $E^2 = p^2 + m^2$ into its longitudinal (p_z) and transversal (p_T) part. By introduction of a Lorentz boost with velocity $v = \beta c$ along the z axis, E and p_z transform to (with $\gamma = \sqrt{1 - \beta^2}^{-1}$):

$$E \rightarrow \gamma(E + \beta p_z) \quad (2.4)$$

$$p_z \rightarrow \gamma(p_z + \beta E). \quad (2.5)$$

The insertion of these expressions yields in the boosted rapidity

$$y' = \ln\left(\frac{\gamma(E + p_z)(\beta + 1)}{\sqrt{p_T^2 + m^2}}\right) = y + \ln[\gamma(\beta + 1)], \quad (2.6)$$

which is just the sum of the original rapidity y and an additional constant. The difference in the rapidity of two particles is therefore independent of Lorentz boosts along the z axis.

Figure 2.2 shows some values of the pseudorapidity η for the corresponding value of the polar angle Θ . Another quantity used often is ΔR , that describes the difference of two particles tracks in the η - ϕ space and is defined as

$$\Delta R = \sqrt{(\Delta\phi)^2 + (\Delta\eta)^2}. \quad (2.7)$$

To identify different types of particles and to measure their kinematics, the ATLAS detector consists of several subsystems. The closest one to the interaction point is the inner detector (section 2.1), which measures coordinates and tracks of charged particles and their momenta. Energies of electrons, photons and jets are determined in the calorimeters (section 2.2). Muons are identified by means of the outer-most subsystem, the muon spectrometer (section 2.3), since muons can traverse through all previous detector components.

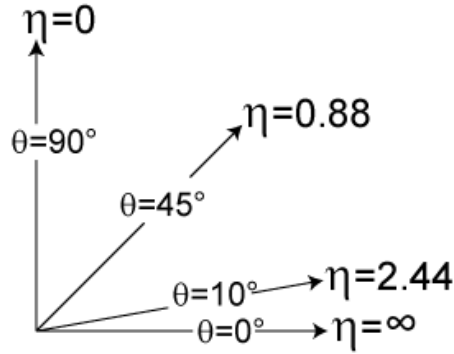


Figure 2.2.: Pseudorapidity for several polar angles Θ [37].

2.1. The inner detector

The inner detector (ID) is the inner-most detector component and located directly around the beam pipe including the collision point. It consists of three subsystems: The pixel system, the semi conducting tracker (SCT) and the transition radiation tracker (TRT). An overview of the ID is illustrated in figure 2.3. To measure the tracks and momenta of charged particles, the ID is put into a solenoidal magnetic field with a strength of 2 T .

The pixel detector system is the innermost part of the Inner Detector and is the most important detector used in the identification and reconstruction of secondary vertices. In addition, it provides excellent spatial resolution for reconstructing primary vertices of the proton-proton interactions. The pixel tracker covers a pseudorapidity range of $|\eta| < 2.5$ and is designed to provide at least three points on a charged track emanating from the collision region. The pixel detector consists of three barrel layers, namely Layer 0 (so-called b-layer, as it provides the critical information to reconstruct vertices from b -quark decays), Layer 1 and Layer 2 and two identical endcap regions, each with three disk layers (see figure 2.4).

The basic functional element of the pixel detector is a module, which is composed of silicon sensors, front-end electronics and flex-hybrids with control circuits. All modules are functionally identical at the sensor/integrated circuit level, but differ somewhat in the interconnection schemes for barrel modules and disk modules. The nominal pixel size is 50 microns in the ϕ direction and 400 microns in z (barrel region, along the beam axis) or r (disk region, transverse to the beam axis). A few special pixels in the region between integrated circuits on a module have somewhat larger dimensions.

There are 16 front-end chips (FE) in each pixel module, which are arranged in two rows of eight chips. The FEs are read out by a Module Control Chip (MCC). Each FE has 2880 readout channels, resulting in $2800 \times 16 = 46.080$ readout channels per module. The total number of readout channels in the pixel system is approximately 67 million in the barrel part and 13 million in the endcaps, covering a total active area of about 1.7 m^2 .

2. The ATLAS detector

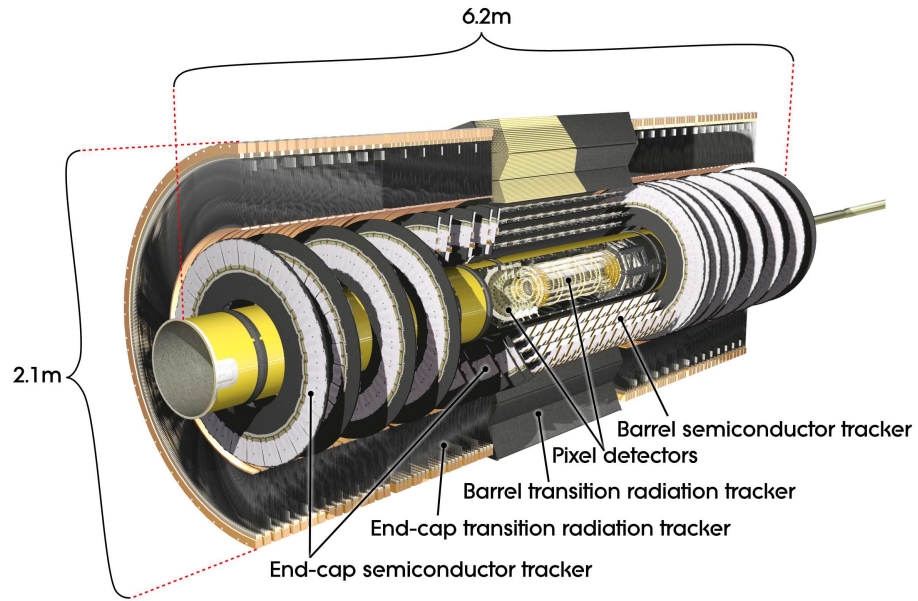


Figure 2.3.: Inner detector (ID) component of the ATLAS detector. The ID consists of the pixel detector, the semiconducting tracker (SCT) and the transition radiation tracker (TRT) [3].

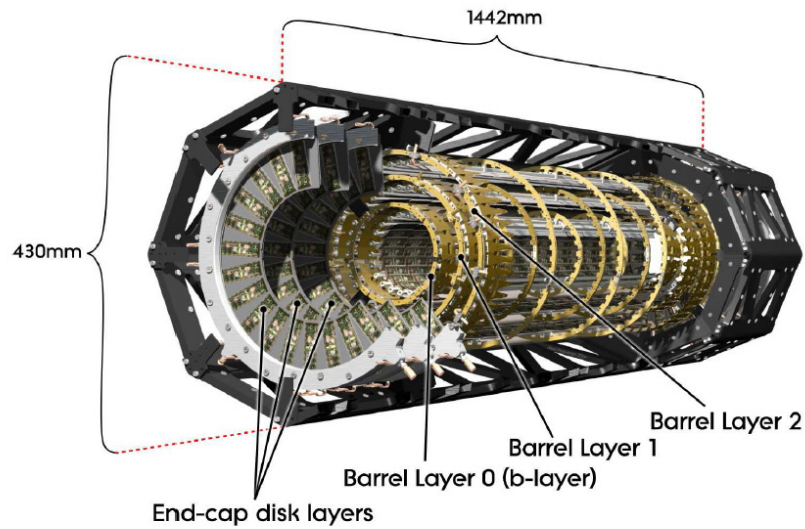


Figure 2.4.: Pixel detector component of the ATLAS inner detector [38]. The pixel detector consists of three barrel layers and two identical endcap regions, each with three disk layers.

The pixel detector is surrounded by the SCT, consisting also of silicon sensors, but segmented in strips. This gives a position determination in the azimuthal $R - \phi$ frame. The information coming from the SCT are used for the measurement of the impact parameter and the momenta of charged particles. Both, pixel detector and SCT, cover a η region of $|\eta| < 2.5$. This defines the maximum η -range for reconstructing tracks corresponding to charged particles.

For the momentum measurement, the SCT is supported by the outer-most part of the ID, the TRT. It consists of gas filled straws interleaved with transition radiation material. The straws are placed parallel to the z -axis in the barrel part and radially in the end-caps. A traversing particle produces transition radiation, which is then measured by the ionization of the gas inside the straws. The TRT covers a region up to $|\eta| < 2.0$. By combining all components, the ID reaches a momentum resolution of [39]:

$$\sigma\left(\frac{1}{p_T}\right) [\text{TeV}^{-1}] = 0.36 \oplus \frac{13}{p_T \sqrt{\sin \Theta}} . \quad (2.8)$$

2.2. The calorimeters

The energy measurements of the traversing particles are done in the calorimeters. The ATLAS calorimeter system is divided into an electromagnetic calorimeter, measuring the energy of electrons and photons, and a hadronic calorimeter, determining the energy and direction of charged and neutral hadrons, formed inside particle jets (see section 1.1.2). Both subsystems are built in the form of a sampling calorimeter: they consist of layers of dense material (absorbers), producing particle showers when traversed by a particle, and active materials which detect the particles created in the showers. These layers are placed alternated in series. An overview of the calorimeter system can be seen in figure 2.5.

The electromagnetic calorimeter (ECAL) uses liquid argon as the active material and lead plates as absorber. These plates are folded into an accordion-like shape, resulting in a complete coverage in the ϕ space. It is divided into a barrel part ($|\eta| < 1.475$) and two end-caps ($1.375 < |\eta| < 3.2$). The barrel part is split into two identical half-barrels with a small gap (4 mm) between them. Although the ECAL provides full η coverage up to $|\eta| = 3.2$, the region between the barrel and the end-cap part ($1.37 < |\eta| < 1.52$), also called "crack region", is not used in most analyses: this space is used as a service area containing cables and particles interacting with this material can produce secondary particles (e.g. photons).

The ECAL is surrounded by the hadronic calorimeter (HCAL). For the barrel part, iron plates are used as absorber material and plastic scintillator tiles as the active medium. The HCAL consists of a central barrel ($|\eta| < 1.0$) and two extended barrels ($0.8 < |\eta| < 1.7$). In the end-cap components liquid argon is used as the active material like in the ECAL, along with copper plates as absorber. The hadronic end-cap segment covers a region of $1.5 < |\eta| < 3.2$.

In addition to the barrel and end-cap parts, the calorimeter system has also a forward calorimeter (FCAL), covering the region of $3.1 < |\eta| < 4.9$. The FCAL uses liquid argon

2. The ATLAS detector

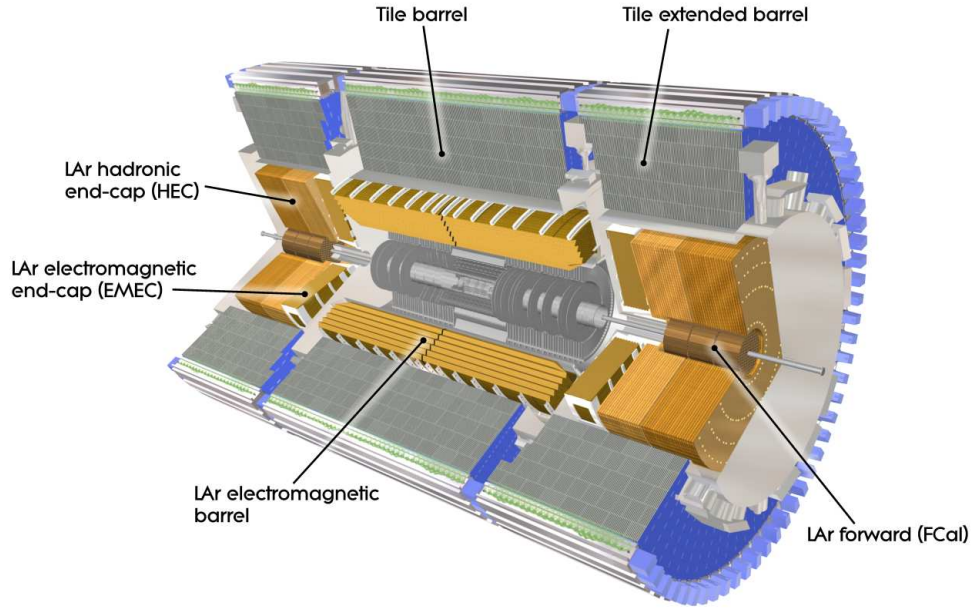


Figure 2.5.: The ATLAS calorimeters used for the energy measurement. One sees on the one hand the electromagnetic calorimeter, consisting of the barrel and the end-cap (EMEC) part and on the other hand the hadronic calorimeter, consisting of barrel, extended barrel and the end-cap (HEC) part. In addition there is on both sides the forward calorimeter (FCAL), also consisting of an electromagnetic and a hadronic part [3].

as detector medium and copper and tungsten as absorber.

Energy resolutions of calorimeters are often parametrized by:

$$\frac{\sigma_E}{E} = \frac{a}{\sqrt{E}} \oplus \frac{b}{E} \oplus c . \quad (2.9)$$

a is the sampling term, which describes the statistical fluctuations in the development of the shower. The second term (b) includes uncertainties due to electronic noise and the last contribution (c) describes the constant systematics (e.g. inhomogeneities in the calorimeter response).

The measured parameters for the energy resolutions of ECAL and HCAL are ([40] and [41]):

$$\frac{\sigma_E^{ECAL}}{E} = \frac{11.2\%}{\sqrt{E[\text{GeV}]}} \oplus \frac{0.283}{E[\text{GeV}]} \oplus 0.26\% \quad (2.10)$$

$$\frac{\sigma_E^{HCAL}}{E} = \frac{38.3\%}{\sqrt{E[\text{GeV}]}} \oplus \frac{3.06}{E[\text{GeV}]} \oplus 1.62\% . \quad (2.11)$$

2.3. The muon spectrometer

The muon spectrometer is used for the muon tracking, its momentum measurement and for the triggering of muons. It is split into several detector chambers. Figure 2.6 shows an overview of the muon detector system. The muon spectrometer forms the outer-most part of the ATLAS detector, since muons pass all other detector components nearly without interaction. As well as the inner detector, the muon spectrometer also needs a magnetic field in order to perform a momentum measurement. This magnet system consists of several superconducting toroid coils in the barrel and the two end-caps, which are independent on the inner detector magnetic system.

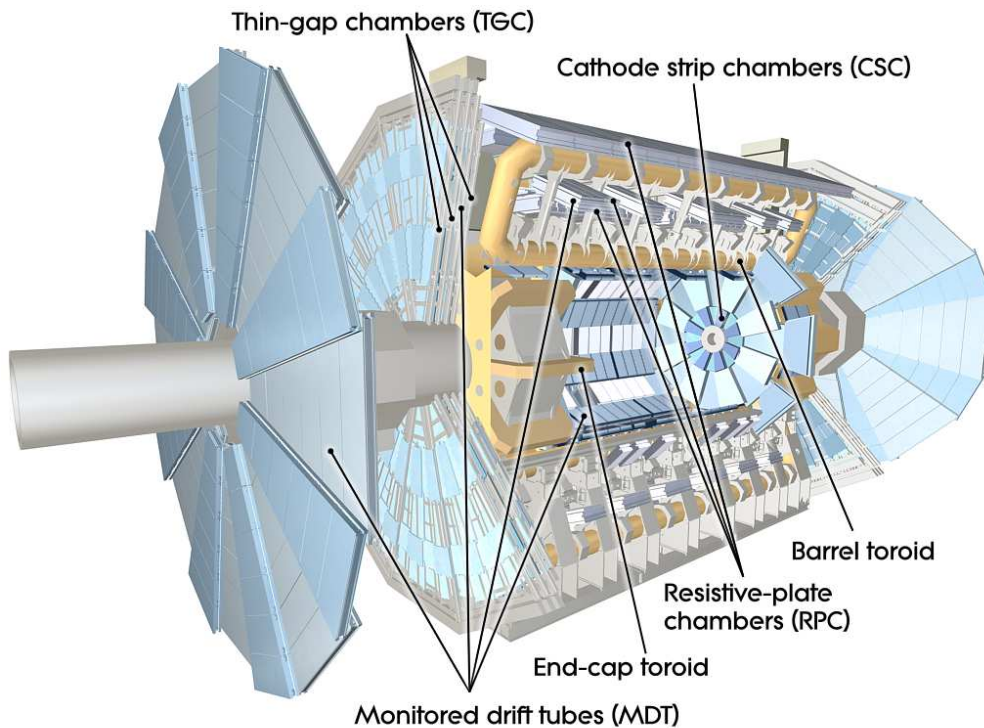


Figure 2.6.: The ATLAS muon spectrometer, consisting of the monitored drift tube chambers and the cathode strip chambers, both used for the muon tracking, and the resistive plate chambers and the thin gap chambers providing the muon triggering [3].

There are four types of muon detection chambers: the monitored drift tubes (MDT) and the cathode strip chambers (CSC) are used for the precision tracking of the muons. They consist of gas filled aluminium drift tubes (in case of MDT) and multiwire proportional chambers (in case of CSC) that provide a finer granularity than the MDTs. The muon triggering is done by the resistive plate chambers (RPC) and the thin gap chambers (TGC). Like the CSC, the TGC consists of multiwire proportional chambers.

2. The ATLAS detector

The RPC is composed of bakelite plates, covered with readout strips, and has narrow gas gaps between them.

The spectrometer is designed for a muon momentum resolution of [42]:

$$\frac{\sigma_{p_T}}{p_T} = \frac{10^{-4}}{p_T[\text{GeV}]} . \quad (2.12)$$

Table 2.1 summarizes the η coverage of the different muon detection chambers.

Detection chamber	Coverage
MDT	$ \eta < 2.7$ ($ \eta < 2.0$ for innermost layer)
CSC	$2.0 < \eta < 2.7$
RPC	$ \eta < 1.05$
TGC	$1.05 < \eta < 2.7$

Table 2.1.: The η coverage of the different muon detection chambers.

2.4. The trigger system

At the design luminosity, the LHC delivers a bunch crossing rate of 40 MHz. Since the data recorded for one bunch crossing is about 1 MB, it is obvious that it is not possible to store all these data on disk or tape. Therefore ATLAS features a three level trigger system to reduce the event storage rate down to about 100 MB/s. Figure 2.7 shows the event rates of several physical processes and the processing times of the different trigger stages. The high rates of the standard model processes (e.g. QCD processes or W/Z -production) have to be reduced by the different trigger levels to lower rates, that include mainly the interesting physics processes (e.g. top or Higgs production). By reducing these rates, there is more time available for analysing the events in later steps. Thus, the trigger system is split into several trigger levels, each with a different amount of processing time.

A schematic overview of the ATLAS trigger system is given in figure 2.8. It is composed of a hardware based Level-1 Trigger (LVL1) and a software based High Level Trigger (HLT), consisting of the Level-2 Trigger (LVL2) and the Event Filter (EF).

The first Trigger Level (LVL1) has access to all events. It uses only data from the calorimeters (ECAL and HCAL) and the muon sub-detectors. The inner detector components are not used for a first selection. Otherwise this step would take too long in time. Hence, the muon triggering and its momentum measurement as well as the total measured energy and missing transverse energy are used by the LVL1 trigger. Interesting events are stored into the Read-Out Buffers (ROBs). The event rate is reduced to about 75 kHz.

Small amounts of information are passed to the software based LVL2 trigger in form of so called "regions of interest" (ROIs), which flag the regions that need to be analysed further. Hence, the LVL2 cannot access the full event information. The event rate is

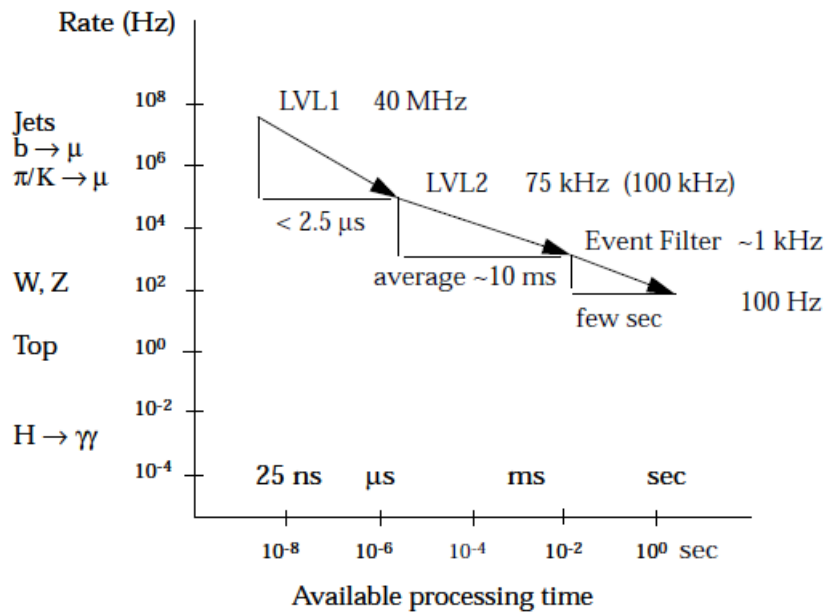


Figure 2.7.: Event rates versus available event processing time for the three levels of the ATLAS trigger system [39]. Indicated are the event rates of various physical processes.

reduced to about 1 kHz by the LVL2.

The last trigger stage is the Event Filter. It gets the event data of the ROBs for those events accepted by the LVL2. In comparison to the LVL2 it has access to the complete event information and can already run complex reconstruction algorithms. The event rate after the EF is about 100 Hz, what can be stored easily onto the storage tape.

2. The ATLAS detector

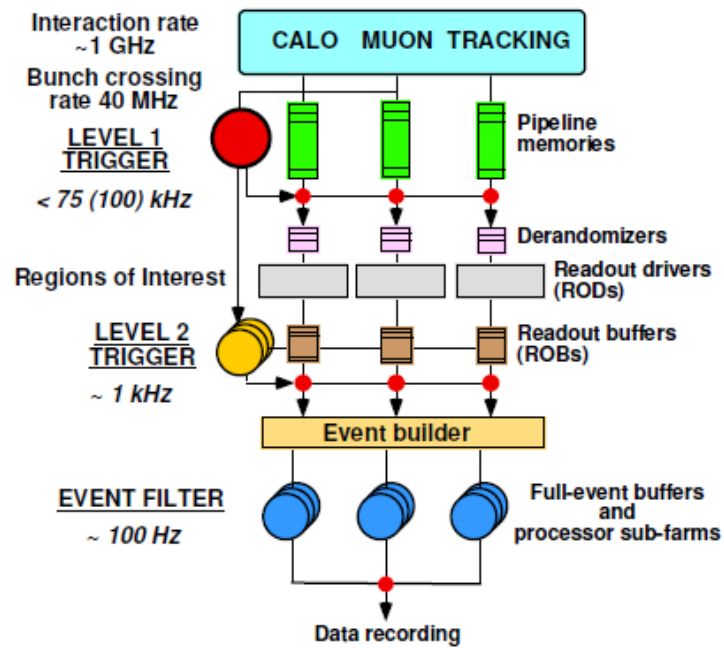


Figure 2.8.: Overview of the three level trigger system of ATLAS [43].

3. Reconstruction of physical objects at ATLAS

The analysis presented in this thesis selects events in a final state with two same-sign leptons (namely electrons and muons) (see section 4.1). Moreover, a large jet multiplicity is expected. Hence, reliable electron, muon and jet reconstruction algorithms are needed. These algorithms use and combine the information provided by several sub-detectors. This chapter gives an overview of the different reconstruction algorithms developed in ATLAS, relevant for this analysis.

3.1. Electron reconstruction

Three algorithms have been developed in ATLAS to reconstruct electrons: the standard, soft and forward algorithm. Further information can be found in [44].

The standard (or high p_T) algorithm is designed for most analyses covering high energetic electrons and is also called a cluster based algorithm. A cluster is the sum of energy deposits in a specific region in the η - ϕ space. The reconstruction starts with the search of a detected cluster with $E_T > 2.5$ GeV in the full acceptance region of the electromagnetic calorimeter. This cluster is then matched to a track in the ID to avoid the misidentification of photons as electrons. High p_T electron candidates are then subdivided into three different classes, based on several criteria on the calorimeter and ID measurements. These classes are indicated by the *isEM* flags **loose**, **medium** and **tight**:

- **Loose:** This class mainly consists of an requirement on the ratio of the energies measured in the ECAL and the HCAL. Furthermore, the track matching and the analysis of the shower are based on loose cuts.
- **Medium:** The loose criteria are inherited by this set, but with stronger requirements. Moreover, additional cuts on calorimeter variables are applied in order to suppress the misidentification rate of pions as electrons.
- **Tight:** In this set, the medium criteria are preserved. In addition, a hit in the pixel B-layer is required in order to reject secondary electrons from photon conversions. Further cuts are applied on the energy deposits in the different calorimeter parts. In addition, the tight criteria consist of cuts on the hits in the TRT sub-detector of the ID in order to reject charged hadrons. Hadrons should radiate less transition radiation due to their higher masses with respect to electrons.

3. Reconstruction of physical objects at ATLAS

The energy measurement for the electrons is mainly performed by the ECAL.

The soft electron algorithm is designed to reconstruct electrons with low momenta in the region $|\eta| < 2.5$. It is track based and focuses on the reconstruction of low p_T electrons and electrons in jets. This algorithm starts with a track selection (with a $p_T > 2$ GeV) and tries to match it to a cluster in the ECAL.

The third algorithm focuses on the reconstruction of forward electrons in the region $2.5 < |\eta| < 4.9$ where no track information is available. In this algorithm, only the calorimeter information can be used.

3.2. Muon reconstruction

Three reconstruction algorithms are currently used in ATLAS. One of them uses only the muon spectrometer information (*Muonboy*). Two other algorithms combine the ID and spectrometer information (*STACO* and *MuTag*). Further details are in ref. [45].

The strategy of the *Muonboy* algorithm is to look first for regions of activity in the muon system. In these regions of activity, local segments are reconstructed for each system and then combined, from which first preliminary muon track candidates are built. For each of the candidates, a global track fit is done using the individual hit information.

Muon tracks, reconstructed by *Muonboy*, can then be used for the *STACO* algorithm, which is a combined reconstruction algorithm. The *STACO* algorithm performs a statistical combination of the two independent measurements in the muon spectrometer and the ID using the parameters of the reconstructed tracks and their covariance matrices. This allows to reject muons coming from secondary interactions or π/K decays in flight.

Another combined muon reconstruction algorithm is *MuTag*. It was developed to identify low P_T muons and uses first the ID track information. The ID tracks are then extrapolated to the muon spectrometer and tried to match with reconstructed muon segments that are not associated to a STACO track. In this algorithm, the ID track is used to measure the muon kinematics.

The energy calculation of the muon candidates uses the muon momentum measured in the muon spectrometer. The momentum measurement for low momentum muons ($P_T \lesssim 30$ GeV) can be improved by the additional use of the ID track.

3.3. Jet reconstruction

Quarks and gluons can arise in the "hard" short distance (high energetic) interaction process of the collision. Due to the confinement, these partons produce several other gluons and quark-antiquark pairs (see section 1.1.2), which will then form a large amount of hadrons. This process is called hadronisation. In addition, hadrons can be composed from partons appearing in the so-called "underlying event". This contains partons from initial and final state radiation (ISR and FSR; gluons radiated from the initial and final state quarks) and from the beam-beam remnants (quarks remaining after the protons break up).

The produced hadrons form so called jets. Jets are features of the final state of the process after the hadronisation and have integer electric charge and zero color charge. Two different kinds of jet reconstruction algorithms are used in ATLAS, namely cone and cluster algorithms. The analysis in this thesis will use jets reconstructed by the ATLAS cone algorithm that will be described in the following section. The information are taken from ref. [46], which also provides further details.

A typical resolution for the measured jet energy is

$$\frac{60\%}{\sqrt{E[\text{GeV}]}} , \quad (3.1)$$

which is obtained by detector simulations in [47].

3.3.1. Cone algorithm

The basic idea of the cone algorithm [48] is to maximize the energy, measured in the calorimeter cells in a given cone. Key parameter is the quantity ΔR (see equation 2.7), that specifies the solid angle of the cone in the $\eta - \phi$ space.

The standard ATLAS cone algorithm starts with a seed, in order to initiate the first candidate cones. The seed is usually an energy deposit in a calorimeter tower or cluster (these are in general areas in the $\eta - \phi$ space) above a specific threshold. By summing up all the momenta and energy deposits of the clusters/towers inside a cone with radius ΔR , one obtains the four momentum vector of the candidate cone

$$p^k = \sum_i p^i . \quad (3.2)$$

The three-momentum is obtained by using the cluster position in the $\eta - \phi$ space as the direction and $|\vec{p}| = E$ (assuming zero mass) as the magnitude. The final direction of the three-momentum contained in p^k will be in the following referred to as the central track of the jet.

After forming the candidate cone, the p^i of the objects within the same ΔR around the direction of the calculated four-momentum in Eq. (3.2) are then again summarized, in order to form a new four-momentum of the cone. This will be repeated until the cone is stable.

After identifying all stable cones, those that share energy are either split into two jets or merged into a single jet.

Typical values for ΔR in ATLAS are 0.4 and 0.7. A cone algorithm with $\Delta R = 0.4$ will be used in the analysis presented in this thesis (see also section 4.4.3).

3.4. Missing energy

Assuming no transverse component in the momenta of the colliding partons, the transverse vectorial energy components of all detected particles have to sum up to zero, due

3. Reconstruction of physical objects at ATLAS

to momentum and energy conservation:

$$\sqrt{\left(\sum E_T \cos \phi\right)^2 + \left(\sum E_T \sin \phi\right)^2} = 0 . \quad (3.3)$$

But particles traversing the detector undetected (such as neutrinos or particles outside the detector acceptance region) result in an energy summation unequal to 0 in Eq. (3.3), which is also called "missing transverse energy" (E_T^{Miss} or \cancel{E}_T). This quantity is calculated by using the energy deposited in all calorimeters (from electrons, γ and jets) as well as the measured energies of all muons. The energy loss of the jets in the cryostat is also taken into account as well as the electronic noise of the detector components. A typical resolution for the \cancel{E}_T given in units of GeV is

$$\sigma[\text{GeV}] = a \cdot \sqrt{\cancel{E}_T[\text{GeV}]} , \quad (3.4)$$

where a is between 0.53 and 0.57 [47].

4. Search for a fourth generation signal in same-sign dilepton final states

In the following, a method for the search for fourth generation quarks at ATLAS will be discussed. At first, the considered decay channel will be introduced (section 4.1), followed by a discussion of the possible background processes and a listing of the simulated samples used in this analysis (section 4.2). Furthermore, the particle and event selection criteria are introduced (section 4.4), which are used in the signal extraction method described in the following (section 4.5). This method is based on a simple counting analysis with a data-driven background estimation and will be tested using pseudo-data, which is created from the simulated data sets (section 4.6). In addition, a dedicated toy Monte Carlo study is performed (section 4.7). At the end, an optimisation of the previously used event selection criteria using a multivariate analysis will be discussed (section 4.8).

4.1. Search for fourth generation quarks at ATLAS

The aim of this thesis is the search for heavy fourth generation quarks Q produced as quark pairs $Q\bar{Q}$. These can appear in the decays of neutrally charged gauge bosons, namely gluons g , Z -bosons and photons γ . At a hadron collider like the LHC, gluons are produced either via gluon-gluon fusion or quark-antiquark $q\bar{q}$ annihilation in strong interactions. The photons/ Z -bosons are formed in electromagnetic/weak interactions after $q\bar{q}$ annihilation. This yields in the following possible production channels:

1. $gg \rightarrow g \rightarrow Q\bar{Q}$
2. $q\bar{q} \rightarrow g \rightarrow Q\bar{Q}$
3. $q\bar{q} \rightarrow \gamma/Z \rightarrow Q\bar{Q}$

At the LHC, gluons carry a large fraction of the protons momentum (see the discussion about the PDFs in section 1.3). Hence, the production process 1 will dominate. Only in the case of very large heavy quark masses m_Q , a large momentum fraction is needed for the two interacting constituents of the protons. At momentum fractions $x \gtrsim 0.1$, gluons no longer dominate and the production channels 2 and 3 will prevail for large m_Q .

The possible and preferred decay channels of the produced heavy quark pair $Q\bar{Q}$ depend on the masses of the fourth generation quarks and the magnitudes of the CKM matrix elements. This thesis will concentrate on the studies of the decays of $b'\bar{b}'$ quark pairs. The following discussion about the decay channels will focus on these fourth

4. Search for a fourth generation signal in same-sign dilepton final states

generation quarks.

From the allowed ranges of the absolute values of the CKM matrix elements in Eq. (1.55), one knows that a sufficient large mixing between the fourth and the third family is possible (with respect to the mixings between the fourth and second or rather the fourth and the first family). As a result, the relations

$$|V_{34}| \gg |V_{14}| \text{ and } |V_{34}| \gg |V_{24}| \quad (4.1)$$

will be assumed in the following¹, where the CKM matrix element $|V_{ij}|$ describes the mixing between fermion family i and j (e.g. the elements $|V_{tb'}|$ and $|V_{t'b}|$ in the case of $|V_{34}|$). This will prefer decays $b' \rightarrow tW$ and $b' \rightarrow t'W$ (if it is kinematically possible).

Decays $b' \rightarrow t$ are accompanied with the production of a W -boson. Hence a sufficient mass difference is needed, if these decays are allowed:

$$m_{b'} - m_t > m_W \quad (4.2)$$

The mass difference between b' and t' is currently not well constrained. With the assumptions in Eq. (4.1) and (4.2), one can distinguish between several mass scenarios. These are summarized in table 4.1.

$m(t') > m(b')$	$m(t') - m(b') > m(W)$	$b'\bar{b}' \rightarrow tW^- \bar{t}W^+ \rightarrow \bar{b}\bar{b}2W^+2W^-$
	$m(t') - m(b') < m(W)$	$b'\bar{b}' \rightarrow tW^- \bar{t}W^+ \rightarrow \bar{b}\bar{b}2W^+2W^-$
$m(b') > m(t')$	$m(b') - m(t') > m(W)$	$b'\bar{b}' \rightarrow t'W^- \bar{t}'W^+ \rightarrow \bar{b}\bar{b}2W^+2W^-$ $b'\bar{b}' \rightarrow tW^- \bar{t}W^+ \rightarrow \bar{b}\bar{b}2W^+2W^-$
	$m(b') - m(t') < m(W)$	$b'\bar{b}' \rightarrow tW^- \bar{t}W^+ \rightarrow \bar{b}\bar{b}2W^+2W^-$

Table 4.1.: Possible final states of b' decays, depending on the masses of b' and t' . A sufficiently large CKM element $V_{tb'}$ (with relation to $V_{ub'}$ and $V_{cb'}$) is assumed. At the same time, the difference between the b' mass and the t quark mass has to be larger than the W -boson mass.

If the t' is heavier than the b' , then the b' is not capable of decaying into a t' and W . Hence in the scenario $m_{t'} > m_{b'}$, the decay channel $b'\bar{b}' \rightarrow t\bar{t} + W^+W^-$ is independent of the mass difference between b' and t' .

In the case of $m_{b'} > m_{t'}$, one can distinguish between two scenarios for the mass difference of b' and t' : On the one hand, one can have $m_{b'} - m_{t'} < m_W$, which means that the b' can not decay into $t' + W$. The $b'\bar{b}'$ pair would then preferably decay into $t\bar{t} + W^+W^-$, too. On the other hand, the mass difference between b' and t' can be larger than the W -boson mass. This can result either in the preferred decay $b'\bar{b}' \rightarrow t'\bar{t}' + W^+W^-$ or in the decay $b'\bar{b}' \rightarrow t\bar{t} + W^+W^-$, which would also have a sufficient branching fraction.

All discussed mass scenarios appear with a $t\bar{t}$ or $t'\bar{t}'$ and two W in the final state. Considering only the decays of t and t' into b quarks, this will always result in final states

¹This is also reflected in the chosen CKM matrix in Eq. (1.58).

$\bar{b}b + 2W^+ + 2W^-$ with a sufficient branching fraction. The four W -bosons can decay either leptonically or hadronically. By selecting those events, in which two same-charged W^+W^+ or W^-W^- decay into leptons and the other two W into quarks, this results in a final state with same-sign charged dileptons $\ell^+\ell^+/\ell^-\ell^-$. These final states can be either two same-sign charged electrons, muons or a combination of both. The final state $\ell^+\ell^+/\ell^-\ell^-$ is a rare standard model signature and as a result should contain only few background events.² Moreover, it has been shown that this final state is independent of the mass difference between b' and t' .

The presence of the two b quarks and the quarks from the two W decaying hadronically results in a high jet multiplicity in the signal events. This could be additionally used for background suppression and will be discussed at the end in section 4.8.

The Feynman graph, illustrating the considered $b'\bar{b}'$ production and decay process with two same-sign leptons in the final state (here: positively charged), is shown in figure 4.1.

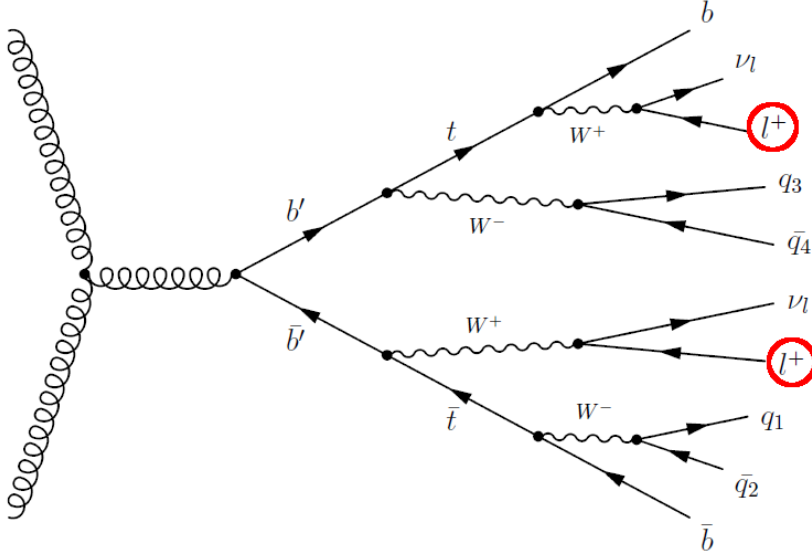


Figure 4.1.: The production of a $b'\bar{b}'$ pair and the decay channel with two same-sign leptons in the final state.

In the following, the "signal candidate events" are events lying in the "signal region" defined by exactly two same-sign charged leptons in the event and several event selection criteria, which will be described in section 4.4.5. Additional leptons to the two same-sign charged leptons are not allowed. Heavy quark masses of at least $m > 300$ GeV will be assumed in the following analysis, due to the known mass limits obtained by other experiments (see section 1.2.2).

²See section 4.2 for a discussion of possible background channels. A discussion of further event selection criteria, in order to additionally suppress the background contributions, is given in section 4.4.5.

4. Search for a fourth generation signal in same-sign dilepton final states

The number of fourth generation quark pairs produced depends on the production cross section. These cross sections were calculated using a tool called *HATHOR* [49], which allows the calculation of the heavy quark pair production cross sections up to next-to-next-to leading order (NNLO). Figure 4.2 shows the calculated cross sections for different quark masses and center-of-momentum energies. The difference between

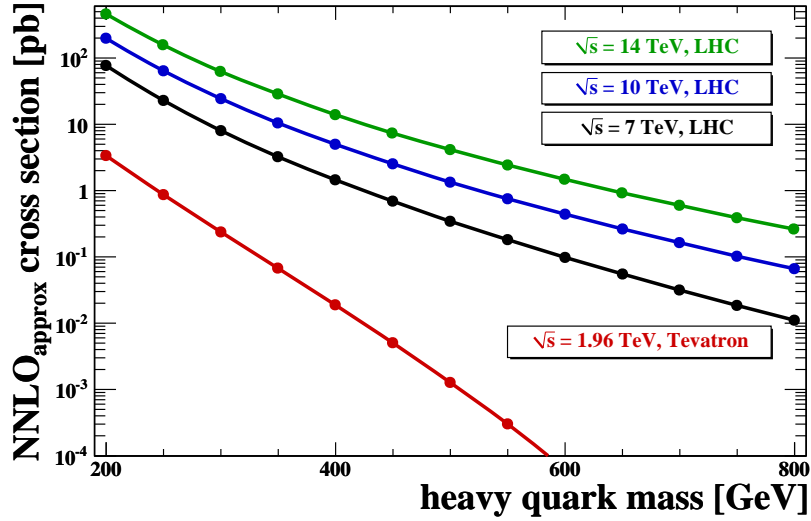


Figure 4.2.: Approximate next-to-next-to-leading order (in the sense some terms of NNLO contribution are calculated in an approximate way) cross sections for heavy quark pair production as a function of the heavy quark mass and for different center-of-mass energies [49]. The cross sections are calculated for pp (LHC: green, blue and black) and $p\bar{p}$ (Tevatron: red) collisions.

the cross sections for the current colliding energy ($\sqrt{s} = 7$ TeV) and the design energy ($\sqrt{s} = 14$ TeV) of the LHC is about one order of magnitude. The cross sections for pp collisions decrease with increasing quark masses, but not as strongly as for $p\bar{p}$ collisions. Assuming a quark mass of 300 GeV, one obtains a cross section of about $\sigma \approx 9$ pb at the current center-of-mass energy of the LHC ($\sqrt{s} = 7$ TeV). Assuming the expected integrated luminosity of about $\mathcal{L} \approx 1 \text{ fb}^{-1}$ at the end of the year 2011, one would expect the production of approximately

$$N = \sigma \cdot \mathcal{L} = 9 \text{ pb} \cdot 1 \text{ fb}^{-1} \quad (4.3)$$

$$= 9000 \quad (4.4)$$

$b'\bar{b}'$ or $t'\bar{t}'$ quark-antiquark pairs with a mass of 300 GeV.

4.2. Simulated signal and background samples

A set of simulated event samples is needed for the extraction method in order to estimate the background contributions. In addition, the simulated signal and background data sets are used to create pseudo data for tests of the extraction method. The simulated samples have to contain all physics processes that can contribute to the signal region. A detailed description of the sample production process at ATLAS can be found in refs. [50] and [51].

The production of the simulated samples is explained using the example of the fourth generation samples. In the first step of the simulation, the Monte-Carlo (MC) generator *Pythia* [52] is used to simulate the parton-parton interaction, in order to produce signal events with fourth generation quark pairs (for the background samples production other generators are also used, e.g. *Alpgen* [53] or *MC@NLO* [54]). Then, starting with the produced final state, a simulation of the parton shower and the underlying event is done. At the end of the shower simulation, the quarks and gluons are combined in the hadronisation process (all done with *Pythia*). In order to produce only events with desired final states, a generator filter can be applied, which rejects all events that does not fulfill specific constraints (e.g. at least one high energetic lepton). This enhances the fraction of signal events in the samples. Moreover, to simulate the interaction of the particles with the detector material and the responding of the detector parts itself, a detector simulation is done afterwards (*Geant4* [55]). The electronics response is simulated by the digitization algorithm. Finally, the reconstruction algorithms detailed in chapter 3 are run.

There are currently four signal samples available, generated with different scenarios for the initial quarks, their decays and masses. The number of produced events N , the

Process	Mass m_Q [GeV]	Number of events	Cross section σ [pb]	\mathcal{L} [pb ⁻¹]
$b'(350 \text{ GeV}) \rightarrow t$	350	149726	0.843	177610.92
$t'(350 \text{ GeV}) \rightarrow q$	350	149803	0.03634	412262.25
$t'(350 \text{ GeV}) \rightarrow b$	350	148823	1.08272	137452.89
$t'(440 \text{ GeV}) \rightarrow b'$	440	9980	0.11475	86971.68

Table 4.2.: MC samples containing the production of fourth generation quark pairs used in this analysis. For each process, the number of produced events, the cross section σ (obtained from the MC generator) and the integrated luminosity \mathcal{L} is given. m_Q is the mass of the produced heavy quarks, which is also contained in the brackets of the process name (e.g. $b'(350 \text{ GeV}) \rightarrow t$). q defines the light quarks d and s .

cross section σ obtained from the generator and the corresponding integrated luminosity \mathcal{L} are summarized in table 4.2. The luminosities are calculated by the formula:

$$\mathcal{L} = \frac{N}{\sigma} . \quad (4.5)$$

4. Search for a fourth generation signal in same-sign dilepton final states

Besides the signal process other background (BG) processes can contribute to the signal region of two same-sign charged leptons. This final state has been chosen, because it is a rare standard model signature. Nevertheless, BG processes can contribute to the signal region for several reasons:

- The final states of background processes can already contain same-sign dileptons, together with additional leptons (e.g. $WZ \rightarrow \ell^\pm \ell^+ \ell^-$ or $ZZ \rightarrow \ell^+ \ell^- \ell^+ \ell^-$). It is possible that not all leptons are reconstructed and only those two same-sign charged ones remain. For instance, this can occur if leptons are low energetic, outside the acceptance region of the detector or inside a jet.
- There can be sources of leptons, which provide additional leptons to processes that only contain single or opposite-sign charged leptons.

One of these sources is bremsstrahlung: Accelerated charged particles (with mass m) radiate photons with a probability that is proportional to $\propto 1/m^4$. This mainly occurs for light particles like electrons. Considering an electron pair production process, like in fig. 4.3, one of the electrons (e_4^-) could radiate a photon when traversing the detector. This photon then can convert into another lepton-antilepton pair (by interacting with the detector material). Again, it is possible

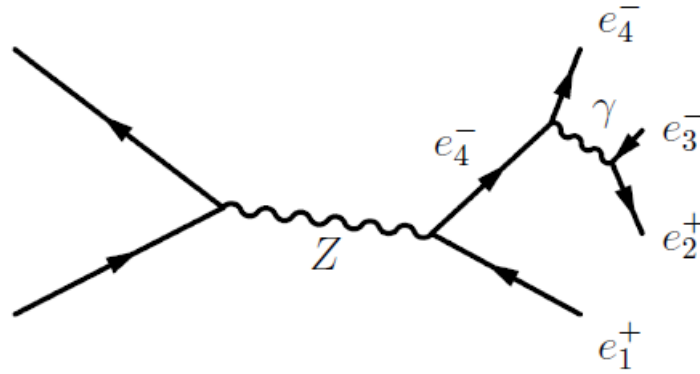


Figure 4.3.: Feynman graph showing the production of a Z-boson and the decay into two oppositely charged leptons (here electrons). One of the electrons radiates a photon, which converts into another lepton-antilepton pair.

that only two same-sign charged leptons are reconstructed, while the other leptons do not pass the reconstruction process. This conversion process will mainly occur in processes with electrons in the final state (e.g. $Z \rightarrow e^+ e^-$ or $W \rightarrow e \nu$).

Another source of leptons are unstable hadrons inside jets, especially inside B-jets. B-jets are formed by B-mesons that originate in b -quarks after the hadronisation. The B-mesons are unstable and can decay into leptons. Hence, this is a significant source of leptons in processes containing b -quarks in the final state (such as $t\bar{t} \rightarrow b\bar{b}W^+W^-$).

4.2. Simulated signal and background samples

- Beside the sources of real leptons, additional leptons can occur due to misidentification in the detector. These wrongly reconstructed leptons are called "fakes". For instance, this effect can arise if charged hadrons inside jets generate showers in the ECAL and then are reconstructed as electrons. Nearly all background processes are affected by fakes.

In the following, the different background processes are discussed, which can contribute to the signal region due to the above reasons. The available simulated samples that contain these BG processes are combined to several BG categories:

- **$t\bar{t}$:** The decay chain of the $t\bar{t}$ process is very similar to the decay of the fourth generation quark pair, but only with two oppositely charged W-bosons and two b-quarks $b\bar{b}$ in the final state: $t\bar{t} \rightarrow b\bar{b}W^+W^-$. The two W can either decay leptonically or hadronically.
- **Z+jets:** In this process, a Z-boson is directly produced and decays into e^+e^- , $\mu^+\mu^-$ or $\tau^+\tau^-$ pairs. The Z-bosons are produced together with several numbers of additional partons (npX) forming jets in the final state. The additional partons can have several sources: one source is the radiation of gluons by the initial partons. Another source are splittings of the initial state gluons before the scattering process

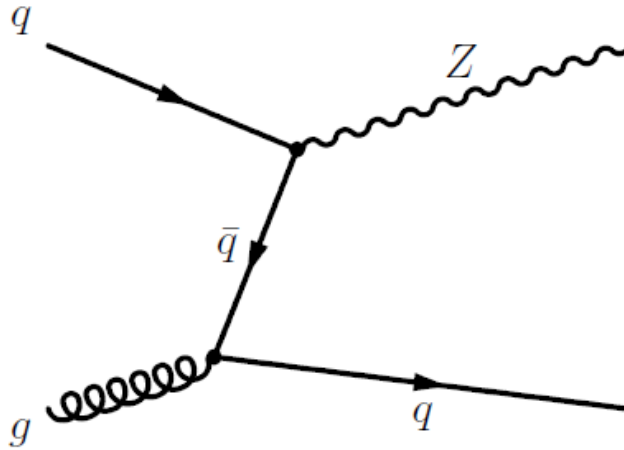


Figure 4.4.: Feynman graph showing the production of a Z-boson together with an additional parton. This occurs, if the initial gluon splits into a quark-antiquark pair before the scattering process.

(fig. 4.4). One of the produced quarks participates in the interaction with the other initial quark. The other quark does not take part in the interaction and can form a jet.

In each decay channel there are simulated samples available with up to 5 additional partons.

4. Search for a fourth generation signal in same-sign dilepton final states

- **W+jets:** Like for Z +jets, the W -boson is directly produced with several additional partons. The W decays into $e\nu$, $\mu\nu$ or $\tau\nu$. The available MC samples contain up to 5 additional partons.
- **Dibosons+jets:** These samples contain pairs of bosons (WW , WZ and ZZ) with additional partons, where the bosons decay leptonically into electrons, muons and taus. The available MC samples contain up to 3 additional partons for each diboson production process.
- **Drell Yan:** Drell Yan processes are lepton-antilepton $\ell^+\ell^-$ pairs produced by a virtual photon or Z -boson. The available MC samples contain $\ell^+\ell^-$ final states with electrons or muons. The invariant mass

$$m_{inv}^2 = \left(\sum_i E_i \right)^2 - \left(\sum_i \vec{P}_i \right)^2 \quad (4.6)$$

of the two leptons does not have to be within the Z resonance (E_i and \vec{P}_i are the energy and the three momentum of the lepton i).

- **Single top:** In single top (sgtop) events, only one top quark is appearing (in contrast to $t\bar{t}$). This can happen in either a t-channel, s-channel or Wt -channel process (see fig. 4.5).
- **QCD $b\bar{b}$ jets:** b -quark pairs with additional partons are produced by QCD processes $q\bar{q}/gg \rightarrow g \rightarrow b\bar{b}$. Like in the case of Z +jets, the available samples consist of several numbers of additional partons produced. Moreover, the simulated samples are split into several processes with different energy ranges for the jets (marked by j1-j5).
- **W+ $b\bar{b}$ +jets, Z+ $b\bar{b}$ +jets:** These processes are similar to Z +jets and W +jets, but with an additional $b\bar{b}$ -quark pair. The pair occurs, if the initial gluons split into quark-antiquark pairs before the scattering process (fig. 4.6). The available samples consist of up to 3 additional partons produced.

A detailed overview of the MC samples used, their file names and the available numbers of events with the corresponding integrated luminosities can be found in appendix A.

The mainly used signal sample in the following analysis is the fourth generation sample containing the production of $b'\bar{b}'$ -quark pairs ($m_{b'} = 350$ GeV) with decays into t -quarks and W -bosons ($b'(350 \text{ GeV}) \rightarrow t$). This sample will be in the following referred to as "signal sample".

4.3. Analysis framework

The event information in ATLAS is stored in different output formats. These are directly produced from the raw data. The mostly used formats for common analyses are ESD and AOD [51]:

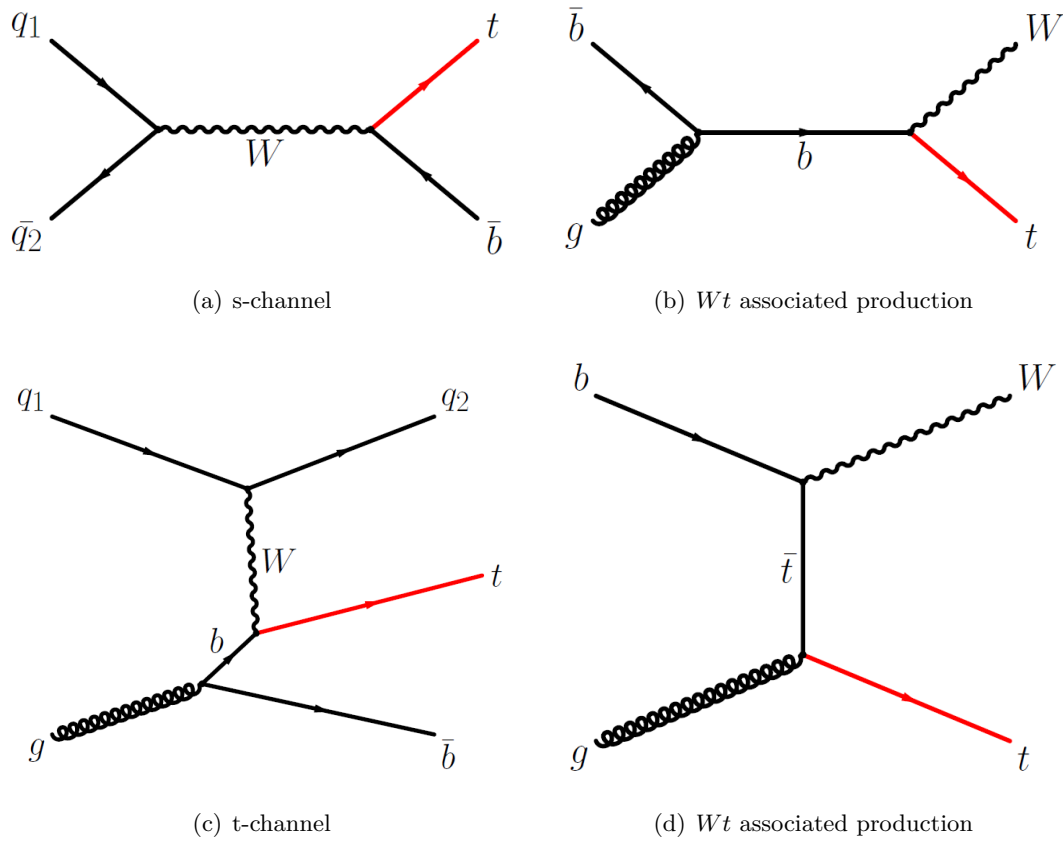


Figure 4.5.: Production processes for single tops in the s-channel (a), t-channel (c) and in Wt associated production ((b) and (d)).

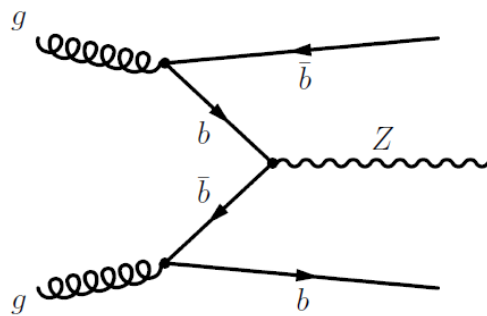


Figure 4.6.: Feynman graph showing the production of a Z -boson together with an additional parton. This occurs, if the initial gluon splits into a quark-antiquark pair before the scattering process.

4. Search for a fourth generation signal in same-sign dilepton final states

- **ESD (Event Summary Data):** This format contains detailed output of the reconstruction algorithms and is directly produced from the raw data. Beside of particle identification the content of ESDs allows to e.g. perform a track-refitting or change the jet calibration. The stored event size from the raw data (~ 1.6 MB/event) is reduced to ~ 1 MB/event.
- **AOD (Analysis Object Data):** AODs contain a summary of the reconstructed events. The information are sufficient for common analyses. AODs can be produced from the ESD and the event size is ~ 100 kB/event.

This analysis will use the samples in the *AOD* format, which contains all necessary event information.

The analysis codes used in this thesis are written in *C++* using the classes and objects of the *A++* framework (described in the following section 4.3.1) and *ROOT* [56]. *ROOT* is an object-oriented software framework, which contains several packages and classes for the analysis of data, statistical analyses and the production of plots and histograms. The *ROOT* version used is *v5.22/00*.

4.3.1. A++

A++ [57] is an object oriented analysis framework to be used for the analysis of ATLAS data sets. It is written in *C++* and is heavily based on the *ROOT* libraries.

The framework is split into two parts: one, the converter, is an interface, that converts the ATLAS data sets (here: AODs) into object based *A++* *ROOT* event files. The other part is a set of event classes and analysis libraries, written for several analyses (e.g. fourth generation analysis). Within this framework, the analysis will use these *A++* event files. Particles and events can be selected according to specific selection criteria (see section 4.4). Histogram files can then be produced for each MC or data sample.

These final histograms are later on used to perform further studies, like the counting analysis (described in section 4.5).

4.4. Selection cuts

In the analysis, specific reconstruction algorithms and cuts on kinematic variables have to be chosen, in order to select well reconstructed particles and jets. After selecting the desired particles and jets, one needs to apply additional cuts in order to suppress BG processes.

All cuts and variables used are described in the sections 4.4.1-4.4.5. The chosen cuts are mainly adopted from the CMS analysis in [58], which is based on the same search strategy. Section 4.4.6 then presents the effect of the event selection cuts on the signal and background events.

4.4.1. Electrons

In this analysis, electrons reconstructed with the *standard algorithm* will be used (see section 3.1). For a good suppression of fakes and electrons from secondary processes, the *isEM* flag *tight* is selected.

Leptons from W -decays that have been produced in the decay chain of fourth generation quarks are high energetic due to the large heavy quark mass in the initial state. Hence,

Variable	Selection
Author	<i>Standard/HighPt</i>
<i>IsEM</i>	<i>Tight</i>
P_T	$> 20 \text{ GeV}$
$ \eta $	< 2.5
E_T^{Cone20}	$< 8 \text{ GeV}$

Table 4.3.: Electron selection criteria including the cuts on the transverse momentum P_T , pseudorapidity η and an isolation cut E_T^{Cone20} . The "author" defines the electron reconstruction algorithm used.

BG can be suppressed by rejecting events with low P_T electrons.

Electrons inside jets can be removed by the isolation criterion E_T^{Cone20} . This requires an energy deposition in a cone (radius $\Delta R = 0.2$) around the electron candidate in the calorimeter of less than 8 GeV.

A η cut of $|\eta| < 2.5$ is needed, because the ID only covers a region up to $|\eta| = 2.5$. Outside this region no electron candidates with reconstructed ID track are available. Table 4.3 summarizes the electron selection criteria.

4.4.2. Muons

For the muon selection the *STACO* reconstruction algorithm is used, which combines information from the muon spectrometer and the ID (see section 3.2). For the same

Variable	Selection
Author	<i>STACO</i>
P_T	$> 20 \text{ GeV}$
$ \eta $	< 2.5
E_T^{Cone20}	$< 10 \text{ GeV}$
χ^2/ndf	< 5

Table 4.4.: Muon selection criteria including the cuts on the transverse momentum P_T , pseudorapidity η and an isolation cut E_T^{Cone20} . Additionally, there is a cut on the χ^2/ndf , describing the fit between the muon spectrometer- and the ID-track. The "author" defines the muon reconstruction algorithm used.

reasons as in the electron selection, cuts on the muons momentum, η and the isolation

4. Search for a fourth generation signal in same-sign dilepton final states

variable E_T^{Cone20} are applied.

Furthermore, a cut on the χ^2 of the global track fit is done, which combines the measured muon spectrometer- and ID-tracks. The obtained χ^2 describes the goodness of this fit. The variable is divided by the number of degrees of freedom (ndf), that depends on the number of track parameters. Wrongly combined tracks or misidentified muons in the ID should result in high χ^2/ndf . All muon selection criteria are given in table 4.4.

4.4.3. Jets

The jets, used in this analysis, are reconstructed by the *Cone4H1Tower* algorithm. This is a cone algorithm, maximizing the energy in a cone of radius $\Delta R = 0.4$ (see section 3.3.1). The inputs to the jet finder are calorimeter towers. These are formed by summarizing the energy deposits inside a $\Delta\eta \times \Delta\phi = 0.1 \times 0.1$ bin. After the jet finding, a *H1* jet calibration is done. This approach has been developed for the Liquid-Argon-Calorimeter of the H1 experiment [59]. Further information to jet finding and calibration can be found in sections 10.5.2 and 10.5.3 of ref. [3].

Such as for electrons and muons, jets produced in the decay chain of the fourth generation quarks should be high energetic due to the large heavy quark masses. Therefore jets with $E_T > 25$ GeV are required.

The problem of the jet reconstruction algorithm is, that leptons and photons can also be reconstructed as jets. This is due to the cone algorithm, which searches for energy deposits in the whole calorimeter (both ECAL and HCAL). The jet search is not restricted to the HCAL, because low energetic hadrons inside the jets may deposit all their energy in the ECAL and do not reach the HCAL. To reject such leptons and photons that are misidentified as jets, an overlap removal is done described in the following.

Figure 4.7(a) shows the transverse energy distribution of jets in the $W e \nu$ Np0 sample (0 additional partons produced). This samples contains directly produced W -bosons

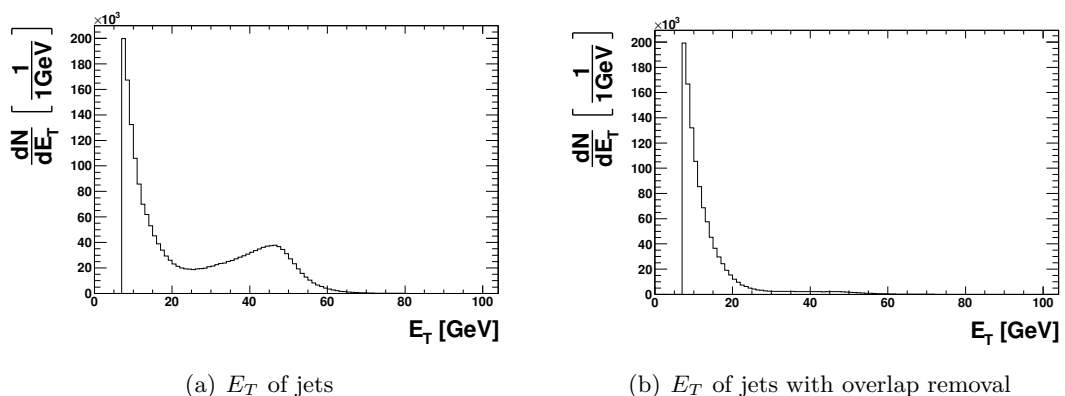


Figure 4.7.: E_T of jets distribution in the $W e \nu$ Np0 sample. In (a) one notices a peak at the half W -boson mass, coming from electrons falsely reconstructed as jets. This peak vanishes after performing an overlap removal (b).

decaying into an electron and an electron neutrino. In this process should not be any jet with high transverse energy, besides of low energetic jets coming from initial and final state radiation of gluon from the partons. One notices a peak at about half of the W -boson mass ($m_W \approx 80 \text{ GeV}$). In the rest frame of the W , the two decay products have both a transverse energy of $E_T = m_W/2$. Hence, the peak has to originate from the electrons of the W -decay, falsely reconstructed as jets. The peak is not exactly at the half W -boson mass, because the W is generally not produced at rest. The overlap removal aims at rejecting jets that have a reconstructed lepton or photon inside a cone of $\Delta R^{OR} = 0.2$ around the jets central track. Only leptons with the criteria listed in tables 4.3 and 4.4 are used for the overlap removal. Figure 4.7(b) shows the jet distribution after the overlap removal and one notices that the peak is significantly reduced. There are still some events remaining, which indicates that the overlap removal procedure can be improved.

A requirement of $|\eta| < 2.5$ is chosen for the jets, since only leptons selected within the same range are used for the overlap removal.

Table 4.5 summarizes the jet selection criteria.

Variable	Selection
Type	<i>Cone4H1Tower</i>
E_T	$> 25 \text{ GeV}$
$ \eta $	< 2.5
ΔR^{OR}	< 0.2

Table 4.5.: Jet selection criteria including the cuts on the transverse energy E_T , pseudorapidity η and the cone radius ΔR^{OR} for the overlap removal.

4.4.4. Trigger selection

As discussed in section 2.4, the high event rate at ATLAS needs to be reduced by the trigger system. Each trigger level (LVL1, LVL2 and EF) consists of several trigger items, which combine specific requirements for the events. The trigger items are assigned to an event, if it fulfills these requirements. When asking for a specific trigger item on EF level, this corresponds to a trigger chain. That implies that also specific LVL1 and LVL2 items have been assigned to the considered event. All trigger items and trigger chains are listed in the ATLAS trigger menu.

In the search for fourth generation quarks with two same-sign charged leptons in the final state, one needs to select events with high P_T leptons. Therefore the trigger items selected for this analysis require at least on high P_T electron or muon. The chosen trigger items on event filter level are:

- **EF_e10_medium:** This trigger item requires an electron above a threshold momentum of 10 GeV (with $\approx 60\%$ efficiency) and medium selection criteria. The corresponding trigger chain is $L1_EM5 \rightarrow L2_e10_medium \rightarrow EF_e10_medium$.

4. Search for a fourth generation signal in same-sign dilepton final states

- **EF_mu10i_loose:** For the muons, there is also a momentum requirement of 10 GeV and loose selection criteria. In addition, only isolated muons are chosen. This criterion rejects muons that are surrounded by other particles. The rejection performed is based on an analysis of the energy patterns in ECAL and HCAL released by the muons. The corresponding trigger chain consists in the items $L1_MU10 \rightarrow L2_mu10i_loose \rightarrow EF_mu10i_loose$.

4.4.5. Event selection

As previously discussed, the final state same-sign charged dileptons ($\ell^+\ell^+/\ell^-\ell^-$) is a rare standard model signature. Figure 4.8(a) shows the number of jets distribution in the $\ell^+\ell^+/\ell^-\ell^-$ region (events with $\ell^+\ell^+/\ell^-\ell^-$ final state), which is largely dominated by several backgrounds. These backgrounds are mainly the production processes of Z +jets, W +jets, $t\bar{t}$ and $b\bar{b}$ jets. Hence, additional kinematical cuts are necessary in order to suppress the background processes. A zoom into the area of small number of entries

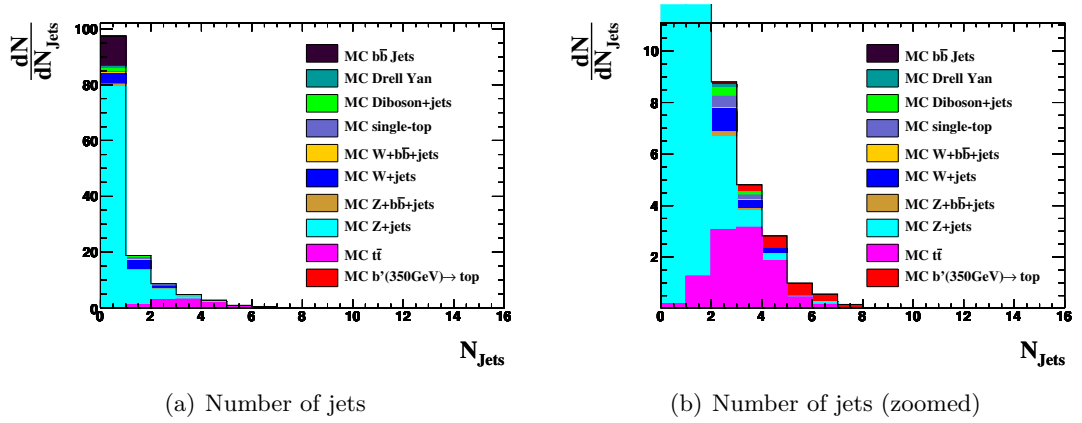


Figure 4.8.: Distributions of N_{Jets} for same-sign charged dileptons. No additional cuts are applied. The signal entries are not visible in (a), but when zooming into the area of small entry numbers, the signal entries appear (b). The histograms are rescaled to an integrated luminosity of $\mathcal{L} = 50 \text{ pb}^{-1}$.

(figure 4.8(b)) reveals the presence of the signal entries. The idea of the event selection cuts is to lower the background contributions while maintaining the signal contribution.

As mentioned in the beginning of section 4.4, the selection criteria used in this analysis are mainly adopted from the CMS analysis [58]. These cuts have been chosen to start with the analysis. Nevertheless, a method for optimising the event selection criteria has been performed at the end. This will be presented at the end of this thesis (section 4.8).

The chosen cuts, based on the CMS analysis, are listed in the following. The discussion is based on the analysis of the BG samples listed in section 4.2 and the $(b'(350 \text{ GeV}) \rightarrow t)$ signal sample. In all shown distributions the trigger items, presented in section 4.4.4, and two same-sign charged leptons are required. All histograms are rescaled to an integrated

luminosity of $\mathcal{L} = 50 \text{ pb}^{-1}$. The chosen event selection cuts are:

- **Missing transverse energy \cancel{E}_T :** Missing energy mainly appears in events with neutrinos or if particles pass the detector outside the acceptance region. By requiring a minimum on \cancel{E}_T , one can suppress processes without neutrinos. These are mainly processes containing Z -bosons or photons decaying into charged leptons. Processes with leptonically decaying W -bosons (e.g. signal $b' \rightarrow tW$ or top $t \rightarrow bW$ processes) are in general not affected due to the neutrinos appearing. The distribution of the \cancel{E}_T for same-sign charged dilepton events can be seen in figure 4.9. A cut of $\cancel{E}_T > 20 \text{ GeV}$ is chosen, because this rejects mainly BG and barely

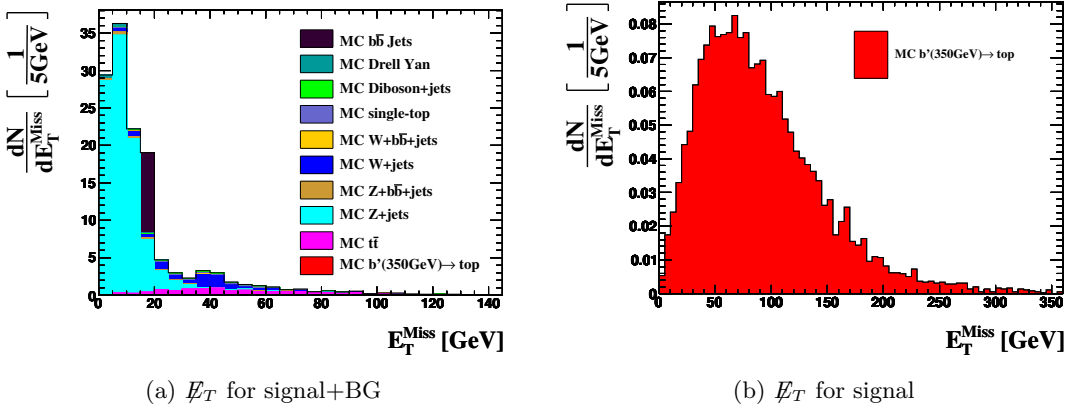


Figure 4.9.: Distributions of \cancel{E}_T for either signal+BG (a) or only signal (b) in same-sign charged dilepton events. The entries are rescaled to an integrated luminosity of $\mathcal{L} = 50 \text{ pb}^{-1}$.

affects the signal. A higher value could completely remove the Z +jets BG, but would also reject many signal events at the same time.

- **Transverse energy of leading jet E_T^{LeadJet} and transverse momentum of leading lepton P_T^{LeadLep} :** The decaying W -bosons in the signal process will result in high energetic jets and leptons. The final state b -quarks are another source of high- E_T jets. Therefore cuts on the energy or momentum of the leading jet and lepton allow to suppress SM background processes as well. Leading jets/leptons are those with the highest energy/momentum in the event. The distributions for the leading jets energy and leading leptons momentum are illustrated in figure 4.10. The chosen cuts, adopted of the CMS analysis, are $E_T^{\text{LeadJet}} > 85 \text{ GeV}$ and $P_T^{\text{LeadLep}} > 35 \text{ GeV}$. Despite of that, stronger cuts could result in a higher BG suppression and a still low signal rejection.
- **Pseudorapidity of leading lepton $|\eta^{\text{LeadLep}}|$:** Depending on the event topology, the lepton η distributions have different shapes. Considering a directly produced vector boson (W , Z) at rest, this will decay isotropically. A W -boson arising

4. Search for a fourth generation signal in same-sign dilepton final states

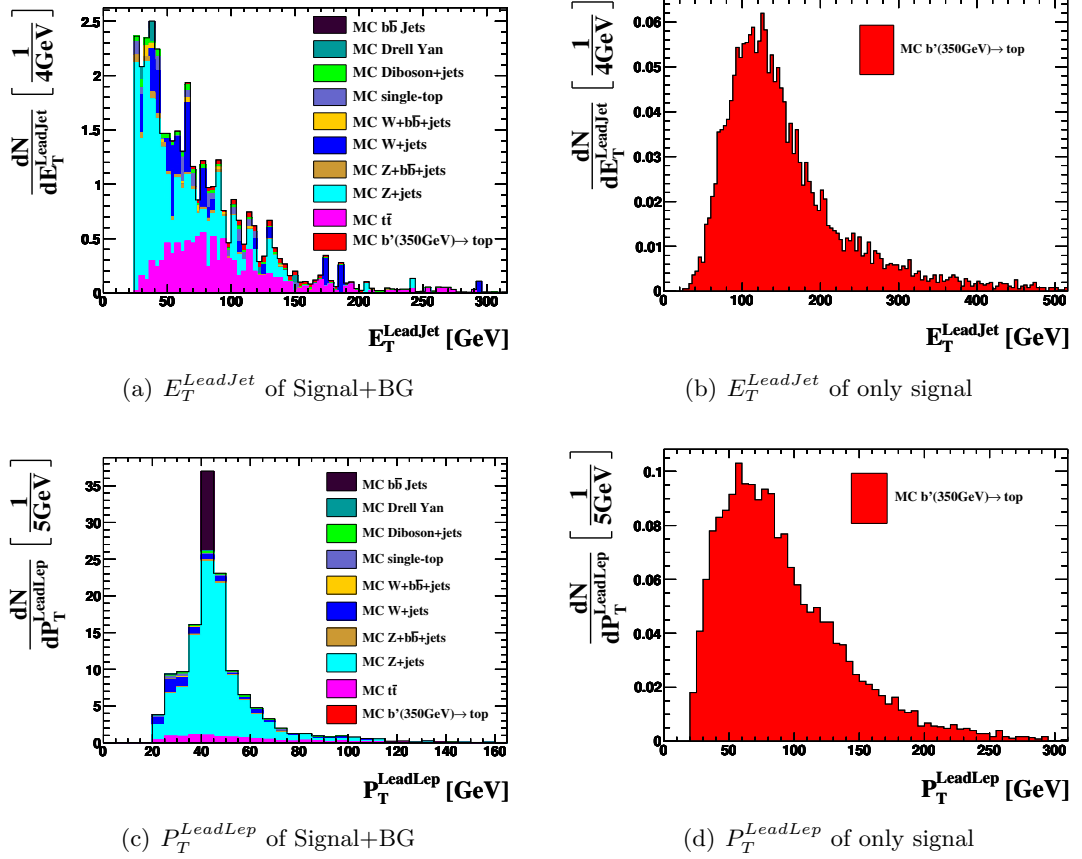


Figure 4.10.: Distributions of $E_T^{LeadJet}$ and $P_T^{LeadLep}$ for Signal+BG ((a) and (c)) and for only the signal ((b) and (d)) in same-sign charged dilepton events. The entries are rescaled to an integrated luminosity of $\mathcal{L} = 50 \text{ pb}^{-1}$.

from a heavy quark decay (e.g. $b' \rightarrow tW$ or $t \rightarrow bW$) will have a large boost transverse to the beam direction. The decay products of the W will then mainly move along the central direction. This behavior is visible in fig. 4.11. The left plot shows

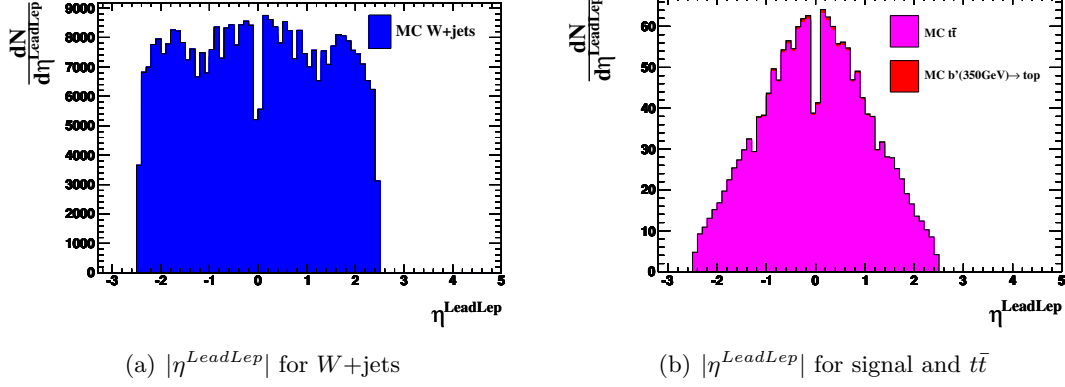


Figure 4.11.: Distributions of $|\eta^{LeadLep}|$ for either W +jets (a) or signal+ $t\bar{t}$ (b). The entries are rescaled to an integrated luminosity of $\mathcal{L} = 50 \text{ pb}^{-1}$.

the η distribution of the leading lepton of W +jets events. The same distribution is illustrated in the right plot for the $b'\bar{b}'$ and $t\bar{t}$ events. While the distribution is flat for the W +jets samples, it peaks in the central region for the heavy quark decays $b' \rightarrow tW$ and $t \rightarrow bW$. For $|\eta| \approx 0$, there exists a dip due to the small gap between the half-barrels of the calorimeters (see section 2.2).

The η distribution of all backgrounds and the signal is plotted in figure 4.12. At

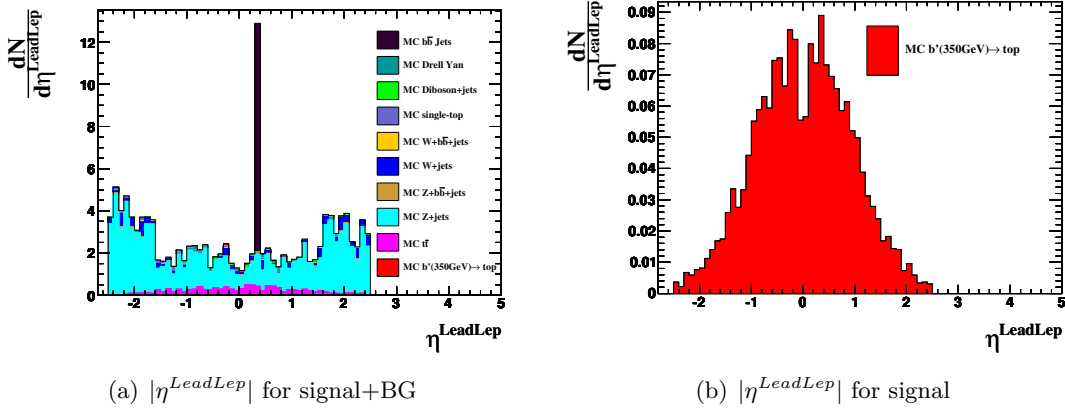
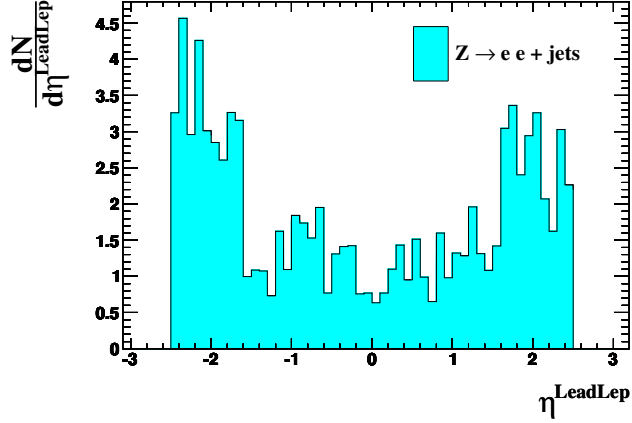


Figure 4.12.: Distributions of $|\eta^{LeadLep}|$ for either signal+BG (a) or only signal (b) in same-sign charged dilepton events. The entries are rescaled to an integrated luminosity of $\mathcal{L} = 50 \text{ pb}^{-1}$.

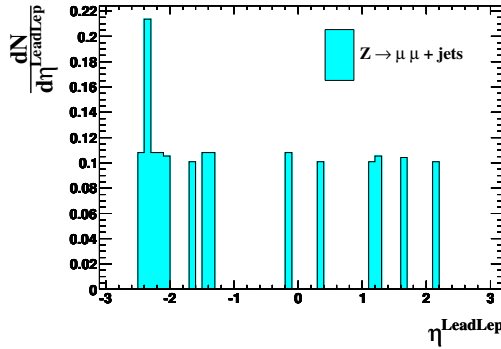
$\eta \approx 0.3$ is a large bin entry from the $b\bar{b}$ jets BG. It has been upscaled due to low

4. Search for a fourth generation signal in same-sign dilepton final states

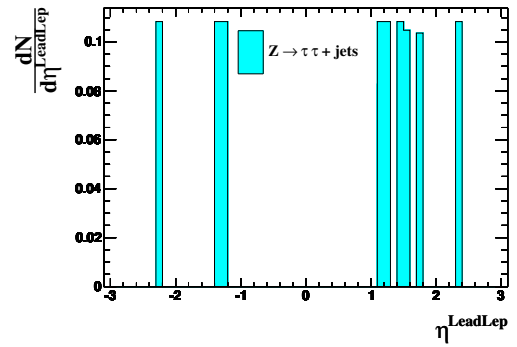
statistics in the sample. One notices also a non-flat distribution for the Z +jets background. This is affected by the $Z \rightarrow e^+e^-$ +jets samples, as can be seen in figure 4.13. This reflects the contribution from photon conversions (see section 4.2),



(a) $Z \rightarrow ee$



(b) $Z \rightarrow \mu\mu$



(c) $Z \rightarrow \tau\tau$

Figure 4.13.: Distributions of $|\eta^{LeadLep}|$ for different Z decay channels in same-sign charged dilepton events. One notices an increase in the forward region for the $Z \rightarrow e^+e^-$ channel. The entries are rescaled to an integrated luminosity of $\mathcal{L} = 50 \text{ pb}^{-1}$.

which obviously dominate with decays into the forward region in $Z \rightarrow e^+e^-$ events due to the presence of more detector material. There is only a low contribution from the $\mu^+\mu^-$ and $\tau^+\tau^-$ decay channels in the Z +jets events.

A cut of $|\eta^{LeadLep}| < 1.0$ will reject $\approx 25\%$ signal events, but largely removes the background processes containing directly produced vector bosons.

All event selection criteria, including the chosen trigger items, are summarized in table 4.6. The distributions of the number of jets for different same-sign dilepton fi-

Variable	Selection
Trigger	EF_e10_medium OR EF_mu10i_loose
\cancel{E}_T	> 20 GeV
P_T^{LeadLep}	> 35 GeV
E_T^{LeadJet}	> 85 GeV
$ \eta^{\text{LeadLep}} $	< 1.0

Table 4.6.: Event selection criteria including the trigger items and cuts on the the energy/momentum of the leading jet/lepton, on the missing transverse energy and the pseudorapidity of the leading lepton.

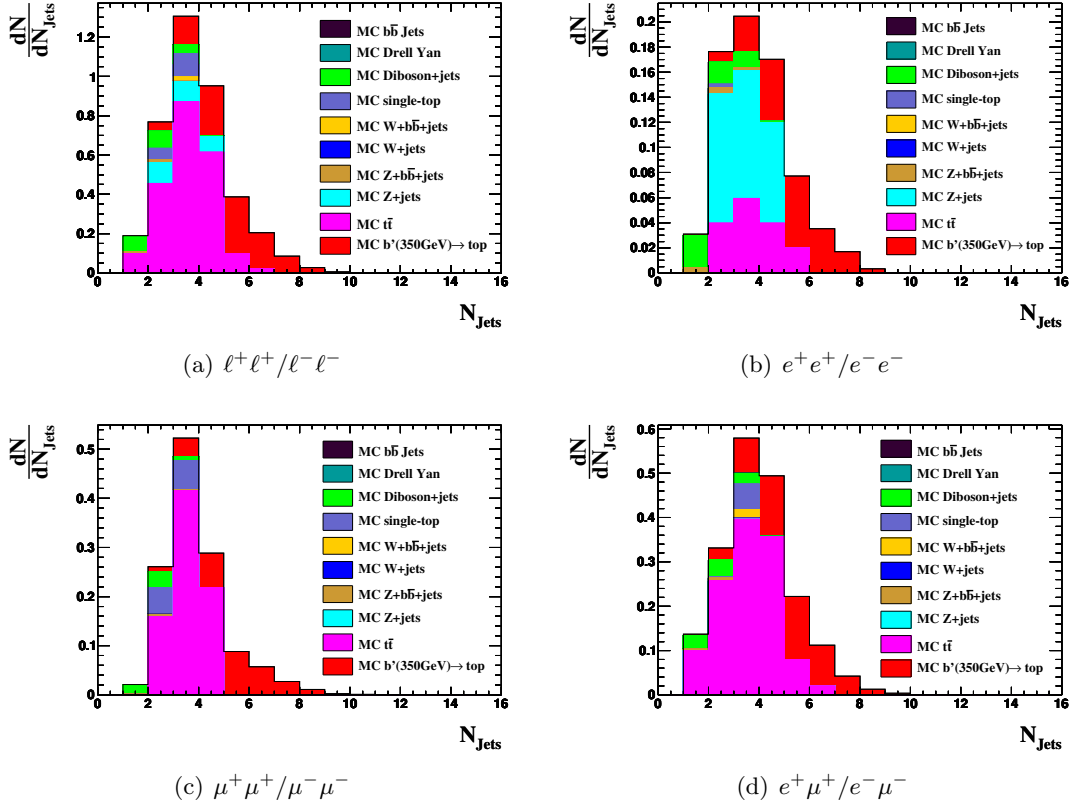


Figure 4.14.: The number of jets distribution after applying all event selection cuts for different same-sign dilepton categories. $\ell^+\ell^+/\ell^-\ell^-$ shows the sum of all plots. The entries are rescaled according to an integrated luminosity of $\mathcal{L} = 50 \text{ pb}^{-1}$.

4. Search for a fourth generation signal in same-sign dilepton final states

nal states after applying all the event selection criteria are shown in figure 4.14. The figures illustrate the distributions for events in the lepton categories e^+e^+/e^-e^- (b), $\mu^+\mu^+/\mu^-\mu^-$ (c), $e^+\mu^+/e^-\mu^-$ (d) and the combination of all three categories $\ell^+\ell^+/\ell^-\ell^-$ (a). The background contributions are all lowered in comparison to the distribution without event selection (figure 4.8). Moreover, the signal entries are much more significant now.

The remaining main backgrounds are $t\bar{t}$ and Z +jets. The contribution from Z +jets appears in the e^+e^+/e^-e^- category, due to the photon conversion processes (see section 4.2). A stronger requirement on the \cancel{E}_T could further reject this BG. The $t\bar{t}$ background mainly influences the $\mu^+\mu^+/\mu^-\mu^-$ and $e^+\mu^+/e^-\mu^-$ categories. This is possibly due to fake muons that enter the final selection and provide a same-sign charged dilepton signature for the $t\bar{t}$ background. Thus, a further investigation of the muon selection will be needed.

Although there are no W +jets and $b\bar{b}$ jets events visible anymore, this backgrounds cannot be neglected. The complete lack of these events after the final selection cuts is an effect of low statistics in the MC samples.

A detailed discussion on the effects of the cuts on the different samples is given in the following section.

4.4.6. Cut efficiencies

In the following, the cut efficiencies for signal and background events selection determined from the MC simulation are presented, which highlights the capability for each cut to reject background events. The efficiency ϵ_i of event selection cut i is defined as

$$\epsilon_i = \frac{n_i}{n_{i-1}}, \quad (4.7)$$

where n_i is the number of events passing cut i and all previous cuts and n_{i-1} is the number of events fulfilling all previous cuts.

The error estimation of these efficiencies is based on a frequentist approach for binomial distributed values. This results in asymmetric errors, in particular for efficiencies close to 0, which can occur due to the "hard" event selection cuts. For further details see section 32.3.2.5 in ref. [4]. The lower (ϵ_{lo}) and upper (ϵ_{up}) limits on the efficiencies are then defined as:

$$\epsilon_{lo} = \frac{n_i F_F^{-1}[\alpha_{lo}; 2n_i, 2(n_{i-1} - n_i + 1)]}{n_{i-1} - n_i + 1 + n_i F_F^{-1}[\alpha_{lo}; 2n_i, 2(n_{i-1} - n_i + 1)]} \quad (4.8)$$

$$\epsilon_{up} = \frac{(n_i + 1) F_F^{-1}[1 - \alpha_{up}; 2(n_i + 1), 2(n_{i-1} - n_i)]}{(n_{i-1} - n_i) + (n_i + 1) F_F^{-1}[1 - \alpha_{up}; 2(n_i + 1), 2(n_{i-1} - n_i)]}, \quad (4.9)$$

where F_F^{-1} is the quantile of the Fisher-Snedecor distribution and $(1 - \alpha_{lo})$ and $(1 - \alpha_{up})$ are the confidence levels for the lower and upper limit on the efficiencies. In this case $\alpha_{lo} = \alpha_{up} = 0.16$ is used, which corresponds to a 68% confidence interval.

Tables 4.7 and 4.8 show the number of events and efficiencies for all generated events, after the generator filter (see the discussion of the MC sample production process in

section 4.2) and events after the trigger selection. The column $\epsilon_{Trigger}$ is defined as the number of events after the generator filter and trigger divided by the number of generated events. This is the total trigger efficiency.

The background samples are combined to the background categories introduced in section 4.2. This is denoted by the symbol " Σ ". For instance, the BG category ΣZ +jets contains the processes $Z \rightarrow e^+e^-$, $Z \rightarrow \mu^+\mu^-$ and $Z \rightarrow \tau^+\tau^-$, each with different numbers of additional partons produced (np0-np5). A single sample of a process with a specific decay channel and a specific number of additional partons will be referred to as "sub-sample".

The efficiencies for each cut are calculated for each sub-sample. The combined efficiency ϵ for a whole category is then calculated by summing up the weighted efficiencies $w_i \cdot \epsilon_i$ of the sub-samples:

$$\epsilon = \sum_i w_i \cdot \epsilon_i \quad (4.10)$$

$$w_i = \frac{n_i}{\sum_j n_j}, \quad (4.11)$$

where $n_{i/j}$ denotes the number of events passing the cuts for sub-sample i/j and the sum \sum_j runs over all sub-samples of the considered background category. The upper σ^+ and lower σ^- limits on these combined efficiencies are obtained by

$$\sigma^\pm = \sqrt{\sum_i w_i^2 (\sigma_i^\pm)^2}, \quad (4.12)$$

where σ_i^\pm are the upper/lower limits on the efficiencies of sub-sample i . Tables with the detailed information of every sub-sample are in appendix B.1 (tables B.1 and B.2). If no generator filter exists, the corresponding efficiency is 1, as for all samples beside the signal and $t\bar{t}$ samples. In the case of the signal samples there is a requirement of at least one lepton with $P_T > 10$ GeV and $\eta < 2.7$ at generator level. The $t\bar{t}$ category consists of two MC samples: In one sample the generator filter requires a leptonic or semi-leptonic decay chain (this means at least one lepton in the final state). A full hadronic decay is required in the other sample.

The lepton triggers suppress very well (efficiency $\approx 2\%$) the QCD- $b\bar{b}$ -jets background, since it should not contain any isolated leptons. The remaining events of the QCD- $b\bar{b}$ -jets sample must be fakes or leptons coming from the b-jets passing the isolation criteria.

Figure 4.15 shows the cut flow for the efficiencies after the different event selection cuts, described in section 4.4.5. They are plotted for the ($b'(350 \text{ GeV}) \rightarrow t$) signal sample and all BG categories. Tables with the numbers for the events passing the cuts and for the plotted efficiencies are in appendix B.2. The plots for the other signal samples are shown in appendix B.3.

The requirement of two same-sign charged leptons has a large effect on all samples. All efficiencies are below 10%.

The following cut on the missing transverse energy \cancel{E}_T affects mainly the backgrounds

4. Search for a fourth generation signal in same-sign dilepton final states

Sample	Generated events	After filter	EF_e10_medium OR EF_mu10i_loose
$b'(350 \text{ GeV}) \rightarrow t$	$1.96 \cdot 10^5 \pm 443$	$1.5 \cdot 10^5 \pm 387$	$1.04 \cdot 10^5 \pm 323$
$t'(350 \text{ GeV}) \rightarrow q$	$3.26 \cdot 10^5 \pm 571$	$1.5 \cdot 10^5 \pm 387$	$1.08 \cdot 10^5 \pm 329$
$t'(350 \text{ GeV}) \rightarrow b$	$2.22 \cdot 10^5 \pm 472$	$1.49 \cdot 10^5 \pm 386$	$7.72 \cdot 10^4 \pm 278$
$t'(440 \text{ GeV}) \rightarrow b'$	$1.16 \cdot 10^4 \pm 108$	$9.98 \cdot 10^3 \pm 99.9$	$7.46 \cdot 10^3 \pm 86.4$
$\sum t\bar{t}$	$6.93 \cdot 10^5 \pm 832$	$3.5 \cdot 10^5 \pm 591$	$1.24 \cdot 10^5 \pm 352$
$\sum Z+\text{jets}$	$1.18 \cdot 10^6 \pm 1.08 \cdot 10^3$	$1.18 \cdot 10^6 \pm 1.08 \cdot 10^3$	$7.01 \cdot 10^5 \pm 837$
$\sum Z + b\bar{b}+\text{jets}$	$8.99 \cdot 10^5 \pm 948$	$8.99 \cdot 10^5 \pm 948$	$6.01 \cdot 10^5 \pm 775$
$\sum W+\text{jets}$	$5.67 \cdot 10^6 \pm 2.38 \cdot 10^3$	$5.67 \cdot 10^6 \pm 2.38 \cdot 10^3$	$2.43 \cdot 10^6 \pm 1.56 \cdot 10^3$
$\sum W + b\bar{b}+\text{jets}$	$1.65 \cdot 10^4 \pm 128$	$1.65 \cdot 10^4 \pm 128$	$8.24 \cdot 10^3 \pm 90.8$
$\sum \text{sgtop}$	$5.65 \cdot 10^4 \pm 238$	$5.65 \cdot 10^4 \pm 238$	$2.75 \cdot 10^4 \pm 166$
$\sum \text{Diboson}$	$1.57 \cdot 10^5 \pm 396$	$1.57 \cdot 10^5 \pm 396$	$1.17 \cdot 10^5 \pm 342$
$\sum \text{DrellYan}$	$2 \cdot 10^6 \pm 1.41 \cdot 10^3$	$2 \cdot 10^6 \pm 1.41 \cdot 10^3$	$4.89 \cdot 10^5 \pm 700$
$\sum b\bar{b} \text{ jets}$	$2.09 \cdot 10^5 \pm 457$	$2.09 \cdot 10^5 \pm 457$	$4.73 \cdot 10^3 \pm 68.8$

Table 4.7.: Number of generated events, events after the filter and events after the trigger used in the simulation.

$Z+\text{jets}$, $Z+b\bar{b}+\text{jets}$ and Drell Yan (as expected; see section 4.4.5). The efficiencies for these BG samples are below 40%. A stronger cut on E_T would further reduce the efficiencies.

As previously discussed, the decay products in the signal process will appear with high energies due to the large heavy quark masses. This is reflected by the efficiencies for the cut on E_T^{LeadJet} . While the efficiencies for all background channels is between 30% and 60%, the signal stays above 80%.

The following cuts on the momentum and η of the leading lepton have not such big effects. Only the samples containing W or Z bosons get a bit more suppressed by the η^{LeadLep} cut than the signal/top samples, due to the different η distributions (as discussed in section 4.4.5). While the efficiency after the η^{LeadLep} cut for $W+\text{jets}$ is close to 0, the $W+b\bar{b}+\text{jets}$ background has an efficiency close to 1. This is caused by the low statistics in these samples, which can be seen by the error on this efficiency (table B.4 in appendix B.2). The efficiency for the $W+b\bar{b}+\text{jets}$ category after the η^{LeadLep} cut has a value of $1.00^{+0.00}_{-0.84}$.

After all cuts, the signal efficiency ($\approx 2.5\%$) is much higher than for the background channels ($\epsilon < 0.5\%$ for the diboson BG and $\epsilon < 0.1\%$ for the other backgrounds).

In addition to the efficiencies, figure 4.16 shows the signal over background ratio as a function of the event selection cuts. This is defined as follows

$$SBR = \frac{S}{B}, \quad (4.13)$$

Sample	Generated events	After filter	EF_e10_medium OR EF_mu10i_loose	$\epsilon_{\text{Trigger}}$
$b'(350 \text{ GeV}) \rightarrow t$	$1.96 \cdot 10^5 \pm 443$	$0.76200^{+0.00096}_{-0.00096}$	$0.69683^{+0.00118}_{-0.00119}$	$0.53098^{+0.00112}_{-0.00112}$
$t'(350 \text{ GeV}) \rightarrow q$	$3.26 \cdot 10^5 \pm 571$	$0.46000^{+0.00087}_{-0.00087}$	$0.72268^{+0.00115}_{-0.00116}$	$0.33243^{+0.00082}_{-0.00082}$
$t'(350 \text{ GeV}) \rightarrow b$	$2.22 \cdot 10^5 \pm 472$	$0.66900^{+0.00099}_{-0.00100}$	$0.51895^{+0.00129}_{-0.00129}$	$0.34718^{+0.00101}_{-0.00101}$
$b'(440 \text{ GeV}) \rightarrow b'$	$1.16 \cdot 10^4 \pm 108$	$0.85900^{+0.00322}_{-0.00328}$	$0.74729^{+0.00435}_{-0.00440}$	$0.64193^{+0.00445}_{-0.00448}$
$\sum t\bar{t}$	$6.93 \cdot 10^5 \pm 832$	$0.50901^{+0.00060}_{-0.00060}$	$0.55577^{+0.00104}_{-0.00104}$	$0.30432^{+0.00073}_{-0.00073}$
$\sum Z+\text{jets}$	$1.18 \cdot 10^6 \pm 1.08 \cdot 10^3$	$1.00000^{+0.00000}_{-0.00001}$	$0.72795^{+0.00041}_{-0.00041}$	$0.72795^{+0.00041}_{-0.00041}$
$\sum Z + b\bar{b}+\text{jets}$	$8.99 \cdot 10^5 \pm 948$	$1.00000^{+0.00000}_{-0.00001}$	$0.79704^{+0.00038}_{-0.00038}$	$0.79704^{+0.00038}_{-0.00038}$
$\sum W+\text{jets}$	$5.67 \cdot 10^6 \pm 2.38 \cdot 10^3$	$1.00000^{+0.00000}_{-0.00000}$	$0.55230^{+0.00023}_{-0.00023}$	$0.55230^{+0.00023}_{-0.00023}$
$\sum W + b\bar{b}+\text{jets}$	$1.65 \cdot 10^4 \pm 128$	$1.00000^{+0.00000}_{-0.00022}$	$0.49985^{+0.00393}_{-0.00393}$	$0.49985^{+0.00393}_{-0.00393}$
$\sum \text{sgtop}$	$5.65 \cdot 10^4 \pm 238$	$1.00000^{+0.00000}_{-0.00009}$	$0.61053^{+0.00210}_{-0.00212}$	$0.61053^{+0.00210}_{-0.00212}$
$\sum \text{Diboson}+\text{jets}$	$1.57 \cdot 10^5 \pm 396$	$1.00000^{+0.00000}_{-0.00004}$	$0.74605^{+0.00110}_{-0.00111}$	$0.74605^{+0.00110}_{-0.00111}$
$\sum \text{DrellYan}$	$2 \cdot 10^6 \pm 1.41 \cdot 10^3$	$1.00000^{+0.00000}_{-0.00000}$	$0.24531^{+0.00030}_{-0.00030}$	$0.24531^{+0.00030}_{-0.00030}$
$\sum b\bar{b} \text{ jets}$	$2.09 \cdot 10^5 \pm 457$	$1.00000^{+0.00000}_{-0.00004}$	$0.02546^{+0.00040}_{-0.00038}$	$0.02546^{+0.00040}_{-0.00038}$

Table 4.8.: Efficiency after the filter, efficiency after the trigger and total trigger efficiency $\epsilon_{\text{Trigger}}$.

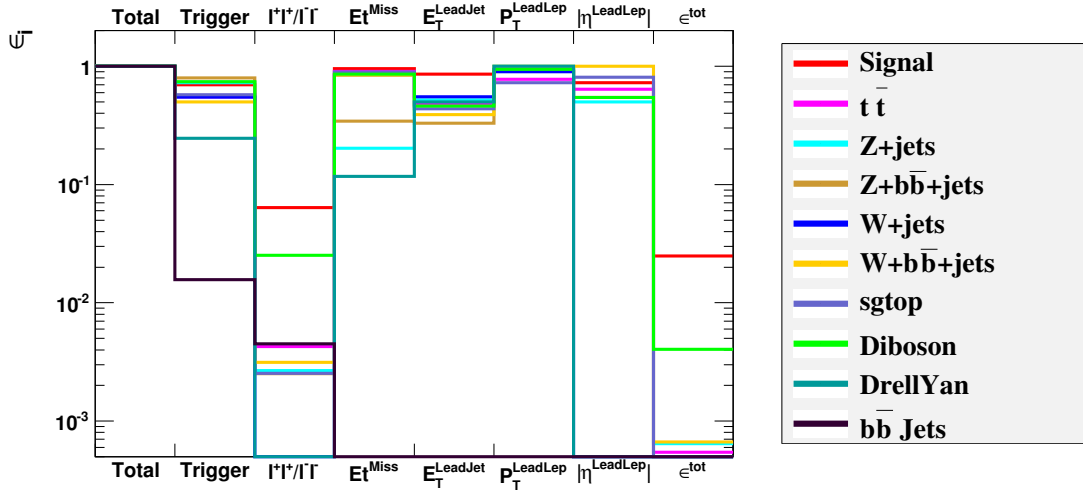


Figure 4.15.: Cut efficiencies (as defined in Eq. (4.7)) for the $b'(350) \rightarrow t$ sample (Signal) and all BG categories.

4. Search for a fourth generation signal in same-sign dilepton final states

where S is the number of signal events and B the sum of all background events. In

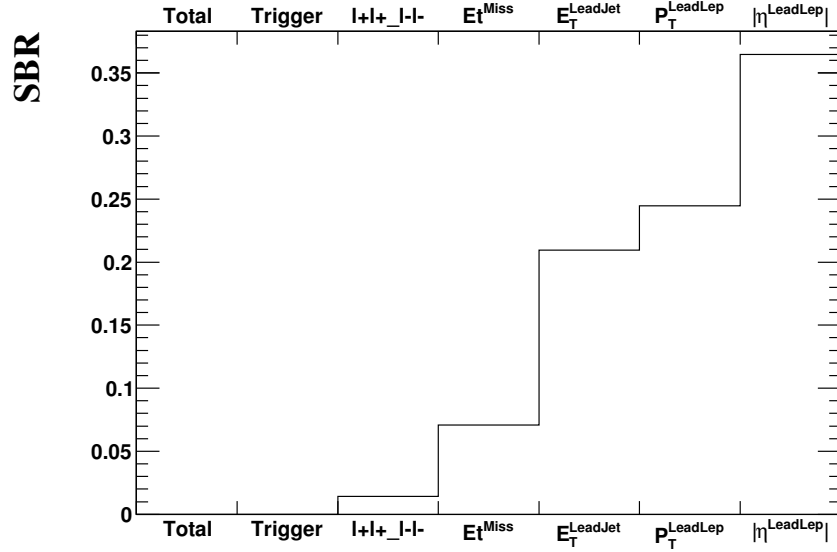


Figure 4.16.: Signal over background ratios as a function of the different event selection cuts. The ratios are calculated for the $b'(350) \rightarrow t$ sample.

the plot, there is an increase in SBR from cut to cut, which is a good hint, that all the chosen cuts make sense. There is a large improvement in the SBR by the cut on $E_T^{LeadJet}$. This is due to the large difference in the efficiencies between the signal and BG. Moreover, one notices a large raise in SBR by the $\eta^{LeadLep}$ cut. This is due to the vanishing background contribution from W +jets.

The numbers and plots for the other signal samples are in appendix B.2 and B.4.

The discussed results in this section can be further improved by introducing an additional cut on the jet multiplicity N_{Jets} and by applying optimised event selection cuts. This will be presented in section 4.8.

4.4.7. Significance

The significance is defined by

$$Sign. = \frac{S}{\sqrt{B}}, \quad (4.14)$$

where S and B are the signal and background yields after applying all event selection criteria. The significance is connected to the probability for a specific deviation of signal and background. A value of $Sign. = 1$ would mean a 1σ deviation between signal and the expected background, which corresponds to a probability for this deviation to be a statistical fluctuation of the background of $\approx 1 - 68\% = 32\%$ in a Gaussian approach. As a convention, a deviation of 5σ is needed to speak of a discovery of new particles. This means that between the signal and the expected background has to be a deviation

of at least 5σ . A 5σ deviation corresponds to a probability of $\approx 5.7 \cdot 10^{-5}\%$ for the occurrence of this deviation. This low probability is necessary in order to be confident that the measured signal is not a statistical fluctuation of the background.

The significance can be used to determine the integrated luminosity \mathcal{L} needed for a 5σ discovery. If S and B are the signal and background yields after all event selection cuts normalised to 1 pb^{-1} , the needed luminosity in pb^{-1} can then be derived by

$$\mathcal{L}[\text{pb}^{-1}] = \frac{5^2 \cdot B}{S^2} . \quad (4.15)$$

This has been done for samples containing $b'\bar{b}'$ production with different masses in the range $m_{b'} \in [300 \text{ GeV}, 600 \text{ GeV}]$ with steps of 50 GeV . These have been produced in addition to the already available samples (see table 4.2). Figure 4.17 illustrates the calculated needed luminosities as a function of the heavy quark mass $m_{b'}$. The required

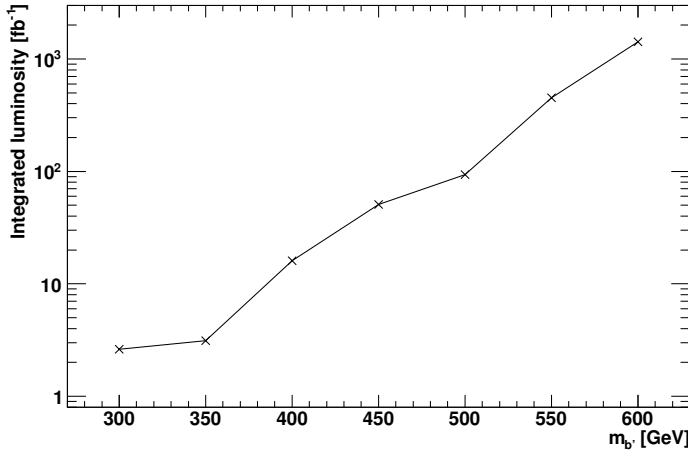


Figure 4.17.: Logarithmic plot of the needed integrated luminosity for a 5σ discovery with significance S/\sqrt{B} . The luminosity is given as a function of the b' mass.

luminosity for the signal discovery increases with higher heavy quark masses. With masses of 400 GeV and higher, there is a large increase in the luminosity over several orders of magnitude. This is due to the higher needed momentum fraction x of the colliding partons. The PDFs decrease heavily for fractions above $\approx 20\%$ (see figure 1.10). Hence, there is only a low probability for partons colliding with sufficient momenta in order to produce the heavy quark pairs.

At the lowest mass of $m_{b'} = 300 \text{ GeV}$ the needed luminosity is above 2 fb^{-1} . With the expected luminosity of $\mathcal{L} = 1 \text{ fb}^{-1}$ at the end of the year 2011, a b' quark could be not discovered at this confidence level ($5\sigma \cong 99.999943\%$) in the considered scenario.

It will be shown at the end of this thesis (section 4.8) that this result can be improved by applying optimised cuts.

4. Search for a fourth generation signal in same-sign dilepton final states

4.5. Counting analysis

In this section, the idea of the counting analysis is described. It extracts the number of measured signal entries from a data sample with usage of the simulated background samples. The background is controlled by a data-driven background estimation. The following sections show results obtained with pseudo data sets and the conclusions from a dedicated toy MC study.

4.5.1. Basic idea

The idea of this analysis is based on a simple counting method. One chooses a signal region, where the signal contribution is preferably high, and counts all observed events N_{Data}^{Obs} in this region. From this number is subtracted the sum of all possible background events N_{MC}^{BG} in the same region, estimated from the simulated MC samples. The remaining events N_{Sig} then should be the number of measured signal events:

$$N_{Sig} = N_{Data}^{Obs} - N_{MC}^{BG} . \quad (4.16)$$

4.5.2. Controlling the main backgrounds

The calculation in equation (4.16) gives only the correct result, if the MC estimations for the backgrounds are well known. This is not the case for every sample and especially not for the given cross sections σ used in the generator.

First, the counted number of events for a MC sample i with integrated luminosity L_i gets rescaled according to a desired luminosity L^* by the weight

$$w_i = \frac{L^*}{L_i} = \frac{\sigma_i}{N_i} \cdot L^* , \quad (4.17)$$

where N_i denotes the total number of events in the sample. If the cross section value σ_i used does not equal the correct value realized in nature, then this results in a weight over- or underestimating the background contribution. In the case of, for instance, underestimating a specific background by a factor c , the applied weight changes to $w_i \rightarrow \frac{w_i}{c}$. Therefore one has to correct the estimation by another factor $R_i \approx c$:

$$\frac{w_i}{c} \rightarrow \frac{w_i}{c} \cdot R_i . \quad (4.18)$$

This correction factor R_i needs to be determined from the measured data.

A possible way would be to calculate the ratio between measured data events and simulated MC events

$$R_i = \frac{N_{Data}}{N_{MC,i}} \quad (4.19)$$

to correct the contribution from a background i . This ratio needs to be determined in a region with a specific event selection so that the corresponding BG i is dominating.

These regions are in the following referred to as control regions (CR). In this analysis, the control regions can be found in complementary lepton categories (final states with different lepton multiplicities and lepton charges), but still using the same kinematical event selection criteria (as presented in section 4.4.5).

This procedure needs to be performed for the main backgrounds contributing to the signal region $\ell^+\ell^+/\ell^-\ell^-$. The main backgrounds that dominate in a lepton category are $t\bar{t}$, W +jets in the decay channels $W \rightarrow e\nu$ and $W \rightarrow \mu\nu$ and Z +jets with the decays $Z \rightarrow e^+e^-$ and $Z \rightarrow \mu^+\mu^-$. All other background processes (introduced in section 4.2) that are not corrected, including the processes $W \rightarrow \tau\nu$ and $Z \rightarrow \tau^+\tau^-$, are in the following combined to the BG category "other". The controlled background processes $t\bar{t}$, $W \rightarrow e\nu$, $W \rightarrow \mu\nu$, $Z \rightarrow e^+e^-$ and $Z \rightarrow \mu^+\mu^-$ are in the following referred to as unique background categories. The control regions and the corresponding dominating BG are listed below:

- **e^+/e^- and μ^+/μ^- :** Single lepton final states are mainly dominated by $W \rightarrow e\nu$ and $W \rightarrow \mu\nu$ events, due to the leptonic W -decays (figures 4.19(a) and 4.19(b)). When comparing the number of events N^{e^+/e^-} in the electron channel (fig. 4.19(a)) with the number of events N^{μ^+/μ^-} in the muon channel (fig. 4.19(b)), one notices a large difference. The ratio is about $R_{\ell^+/\ell^-} = \frac{N^{\mu^+/\mu^-}}{N^{e^+/e^-}} \approx 1.6$. Due to the lepton universality (the weak coupling constant is the same for all lepton flavors), the W -decays into electrons and muons should appear with the same probability (when neglecting the different masses of electron and muon). The observed difference indicates different selection efficiencies for electrons and muons.

- **e^+e^- and $\mu^+\mu^-$:** These opposite-sign charged dilepton final states are dominated by $Z \rightarrow e^+e^-$ and $Z \rightarrow \mu^+\mu^-$ events (figures 4.19(c) and 4.19(d)). It was assumed from figures 4.19(a) and 4.19(b) that there are different selection efficiencies for electrons and muons. The same difference is not visible between the e^+e^- and $\mu^+\mu^-$ categories. Here, the ratio has a value of $R_{\ell^+\ell^-} = \frac{N^{\mu^+\mu^-}}{N^{e^+e^-}} \approx 0.7$.

It has been worked out that the cut on the transverse missing energy ($\cancel{E}_T \geq 20$ GeV) compensates the difference in e^+e^- and $\mu^+\mu^-$ events. Figure 4.18 shows the \cancel{E}_T distribution for e^+e^- and $\mu^+\mu^-$ final states. The ratio of the total number of events between $\mu^+\mu^-$ and e^+e^- final states is about 1.6 and so equal to the observed ratio in the single lepton categories. The Z +jets control regions are obviously also affected by the different selection efficiencies for electrons and muons. But the shapes of the two \cancel{E}_T distributions are not similar. The ratios between the number of events passing the \cancel{E}_T cut $N(\cancel{E}_T \geq 20 \text{ GeV})$ and the total number of events $N(\text{total})$ differ for the two final states:

$$R(e^+e^-) = \frac{N^{e^+e^-}(\cancel{E}_T \geq 20 \text{ GeV})}{N^{e^+e^-}(\text{total})} \approx 4.11\% \quad (4.20)$$

$$R(\mu^+\mu^-) = \frac{N^{\mu^+\mu^-}(\cancel{E}_T \geq 20 \text{ GeV})}{N^{\mu^+\mu^-}(\text{total})} \approx 2.23\% . \quad (4.21)$$

4. Search for a fourth generation signal in same-sign dilepton final states

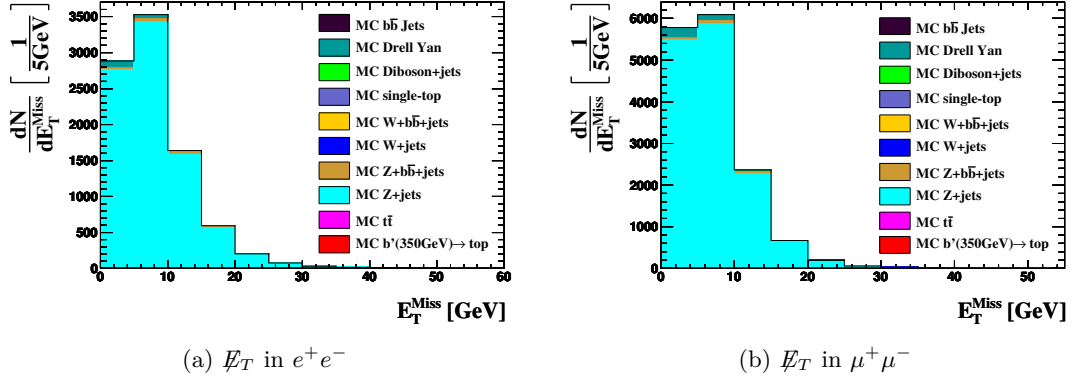


Figure 4.18.: Missing transverse energy \cancel{E}_T in e^+e^- and $\mu^+\mu^-$ final states. One notices a difference in the shapes of these distributions.

The two ratios differ by a factor of about

$$\frac{R(e^+e^-)}{R(\mu^+\mu^-)} \approx 1.8. \quad (4.22)$$

The reconstruction of \cancel{E}_T is obviously different between events containing electrons and events with muons. This effect occurs only at low \cancel{E}_T values around ~ 20 GeV. The single lepton category for the W +jets background is not affected by this difference, because W +jets events appear generally with a larger \cancel{E}_T due to the neutrino from the W -decay. Hence, the difference in the reconstruction efficiencies for \cancel{E}_T in the Z +jets control regions seems to compensate the different selection efficiencies for electrons and muons observed in the single lepton categories.

- $e^+\mu^-/e^-\mu^+$: This final state is dominated by the $t\bar{t}$ background (figure 4.19(e)). Although the two leptons are opposite-sign charged, the Z +jets BG does not contribute due to the different flavors. The signal appears as well in this lepton category, but with small entries.

All control regions are summarized in table 4.9.

Lepton category	Dominant contribution from
e^+/e^-	$W \rightarrow e\nu$
μ^+/μ^-	$W \rightarrow \mu\nu$
e^+e^-	$Z \rightarrow ee$
$\mu^+\mu^-$	$Z \rightarrow \mu\mu$
$e^+\mu^-/e^-\mu^+$	$t\bar{t}$

Table 4.9.: Lepton categories with the corresponding dominant contribution of background processes for which the correction factors R_i are determined.

4.5. Counting analysis

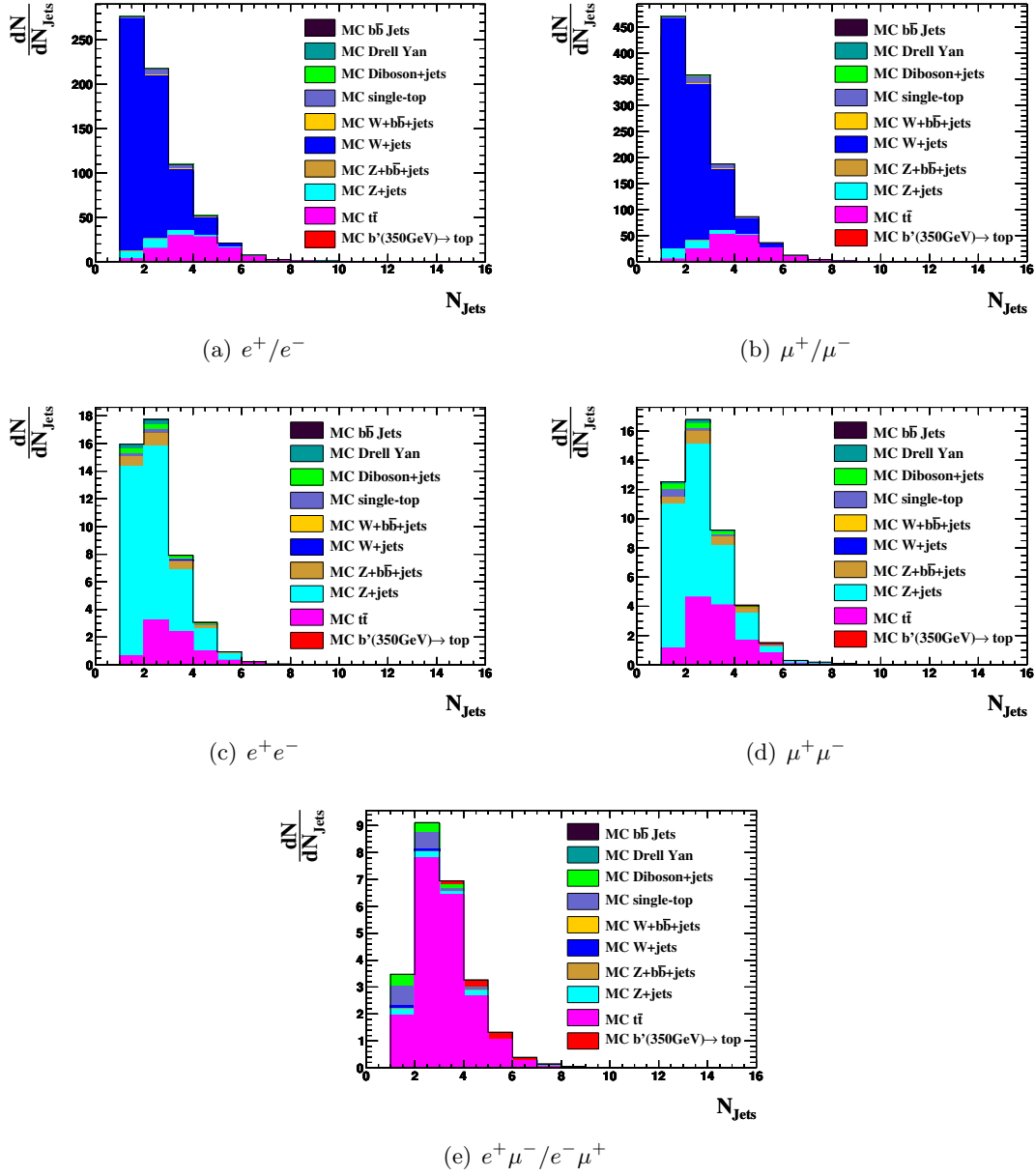


Figure 4.19.: Control regions for the main backgrounds in the counting analysis. These consist of different lepton categories (with a dominant BG contribution): e^+/e^- ($W \rightarrow e\nu$), μ^+/μ^- ($W \rightarrow \mu\nu$), e^+e^- ($Z \rightarrow ee$), $\mu^+\mu^-$ ($Z \rightarrow \mu\mu$) and $e^+\mu^-/e^-\mu^+$ ($t\bar{t}$). The event selection cuts in section 4.4.5 are applied and the histograms are rescaled to an integrated luminosity of $\mathcal{L} = 50 \text{ pb}^{-1}$.

4. Search for a fourth generation signal in same-sign dilepton final states

As previously discussed, the correction factor for a background, introduced in equation (4.19), can be simply obtained by comparing the measured data with the MC predictions in the corresponding control region. Equation (4.16) then has to be modified to

$$N_{Sig} = N_{data}^{SR} - \sum_i \left(N_{MC,i}^{SR} \cdot R_i \right) - \sum_{i_{other}} N_{MC,i_{other}}^{SR}, \quad (4.23)$$

with the correction factor

$$R_i = \frac{N_{data}^{CR,i}}{N_{MC,i}^{CR,i}}, \quad (4.24)$$

where R_i is calculated in the specific control region for background i as listed in table 4.9. The summation over the backgrounds is split into the sum over backgrounds i that obtain the correction factor R_i and all the other backgrounds i_{other} (like single top, dibosons, Drell Yan, etc.).

As seen in the control region histograms (figure 4.19), each lepton category consists not purely only of one background sample. There are contributions from other backgrounds and from the signal. These have to be taken into account when calculating the control ratios R_i . Therefore, one has to subtract the other background and the signal estimates from the number of data events in the control region. These MC estimates should be also corrected by the control ratios, which turns the calculation into an iterative procedure. At iteration step 0, the number of signal events are evaluated from equation (4.23) and the control ratios R_i^0 are obtained. In the next steps k , the correction factors are calculated by

$$R_i^k = \frac{N_{data}^{CR,i} - \sum_{m \neq i} R_m^{k-1} \cdot N_{MC,m}^{CR}}{N_{MC,i}^{CR,i}}, \quad (4.25)$$

where the ratios R_i^{k-1} of the previous iteration step $k-1$ are used. The summation over $m \neq i$ means to sum over all samples except the corrected one. The signal contribution to the control regions has to be subtracted as well. Hence, a correction ratio R_i^k will be also calculated in the signal region.

The complete formula for the number of signal events after iteration step k is then:

$$N_{Sig}^k = N_{data}^{SR} - \sum_i \left(N_{MC,i}^{SR} \cdot \frac{N_{data}^{CR,i} - \sum_{m \neq i} R_m^{k-1} \cdot N_{MC,m}^{CR}}{N_{MC,i}^{CR,i}} \right) - \sum_{i_{other}} N_{MC,i_{other}}^{SR} \quad (4.26)$$

4.6. Results for pseudo data

In the following, the signal extraction method described in section 4.5 will be tested with pseudo data. The pseudo data is created from the MC signal and BG samples. The creation procedure gives the possibility to vary the contributions of the signal and BG processes. This is done by modifying the cross section of the processes. The creation

procedure will be described in the following section. Then the results of the counting analysis performed on pseudo data are presented.

4.6.1. Creation of pseudo data

The pseudo data is created in terms of a "mixing sample". Basically this is done by merging a specific amount of signal and background events, taken from the simulated MC samples. The amount of events N^* taken from each sample depends on the cross sections σ of the samples and the integrated luminosity \mathcal{L}^* under consideration. The amount N^* is selected from a sample with a total of N events with a probability w calculated as:

$$N^* = w \cdot N = \sigma \cdot L^* \quad (4.27)$$

$$\Rightarrow w = \frac{\sigma \cdot L^*}{N} . \quad (4.28)$$

For each event of the sample a random number x between 0 and 1 is taken from uniform probability. If $x < w$, the event is accepted for the mixing sample, otherwise the event is rejected and used to build the MC sample.

This procedure only works, if there is a sufficient amount of events available in each sample. This requires that the available luminosity \mathcal{L} of each sample has to be larger than the luminosity under consideration $\mathcal{L} > \mathcal{L}^*$, which was not the case for the $b\bar{b}$ jets background sample. Hence, this sample is left out in the tests of the counting analysis with pseudo data.

4.6.2. Results with default cross sections

As a first test a pseudo data sample has been generated according to the default MC cross sections and the counting analysis method has been performed on this pseudo data set. Therefore one expects that the MC describes the pseudo data distributions very well and that the calculated control ratios are all close to 1.

The first check is if the iterative method converges. In this run, the number of iteration steps is set to 10. Figure 4.20 shows the different calculated control ratios as a function of the iteration step. One notices, that in all cases the ratio is too high at iteration step 0, since there is no subtraction done on the pseudo data in the nominator of the control ratio (see Eq. 4.24). In the second step, the ratio goes down and fluctuates around the final value. The method converges already after a few steps (iteration ≈ 4).

The final computed control ratios after the 10 iteration steps, together with the final MC background predictions, are shown in table 4.10. The errors on these values are obtained from a dedicated toy study that will be described in section 4.7.2. Moreover, the table lists the expected yields for background and signal. The values are taken directly from the MC distributions scaled to $\mathcal{L} = 50 \text{ pb}^{-1}$.

As already mentioned, the control ratios are all expected to be 1, because there was no change in the cross sections performed in the creation of the pseudo data. The obtained control ratios, listed in the table, do all match the expected value of 1 within 1σ to 3σ

4. Search for a fourth generation signal in same-sign dilepton final states

Sample	Measured events in signal region	Measured ratio in control regions	Expected events in signal region	Expected ratio in control regions
pseudo data	5			
$W e \nu$ +jets	0.0 ± 0.0	1.02 ± 0.05	0.00 ± 0.46	1
$W \mu \nu$ +jets	0.0 ± 0.0	1.13 ± 0.05	0.00 ± 0.46	1
$Z e e$ +jets	0.20 ± 0.06	0.6 ± 0.2	0.3 ± 0.3	1
$Z \mu \mu$ +jets	0.0 ± 0.0	1.6 ± 0.3	0.00 ± 0.28	1
$t \bar{t}$	1.1 ± 0.7	0.5 ± 0.3	2.2 ± 0.2	1
other	0.45		0.4 ± 0.6	
Result	3.25 ± 2.34		1.05 ± 0.02	

Table 4.10.: Results for the measured events and control ratios after the counting analysis. The analysis is run on a mixing pseudo data sample, which is created with default cross sections and with an integrated luminosity of $\mathcal{L} = 50 \text{ pb}^{-1}$. In the measured event yields for the background contributions, the calculated control ratios are already applied. The errors on the measured quantities are obtained from a dedicated toy study, described in section 4.7.2 (table 4.13). The expected events are taken directly from the MC distributions and the expected ratio is always 1, since there has been no change in the cross sections of the MC contributions. The last line presents the measured number of signal events after subtracting the backgrounds.

standard deviations. Indeed, the measured ratios for the W +jets control regions are closer to 1 than the ratios for Z +jets and $t \bar{t}$. The reason can be seen from the control region histograms, containing the MC distributions and the pseudo data points (figure 4.21). The Z +jets and $t \bar{t}$ control regions suffer from low statistics in comparison to the W +jets distributions. This is also noticeable in the much larger relative errors δ on the ratios of the $Z e e$ +jets ($\delta = 33\%$), $Z \mu \mu$ +jets ($\delta = 19\%$) and $t \bar{t}$ ($\delta = 60\%$) control regions in comparison to the errors on the $W e \nu$ +jets ($\delta = 4.9\%$) and $W \mu \nu$ +jets ($\delta = 4.4\%$) regions.

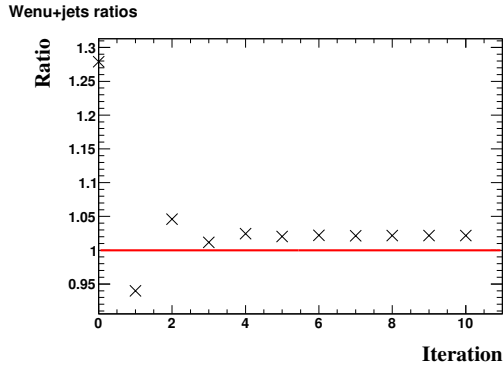
Moreover, one notices a bias in the obtained signal yield after the subtraction of the corrected backgrounds. The measured and expected signal yield differ by more than 2 events, but still match within the 1σ standard deviation.

With higher statistics, the pseudo data could fit better to the MC predictions in the control regions regions. The same applies on the signal region. A study of the counting analysis with a pseudo data sample produced with a much higher integrated luminosity and hence more statistics is discussed in section 4.7.1.

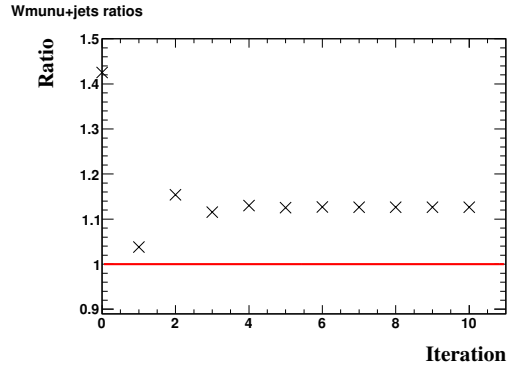
4.6.3. Results with modified cross sections

In the following, the analysis from the previous section is repeated with another pseudo data sample. The creation method (section 4.6.1) gives the possibility to change the contributions from samples inside the pseudo data. When modifying the cross section

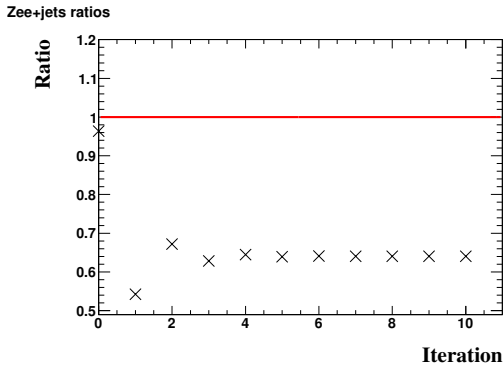
4.6. Results for pseudo data



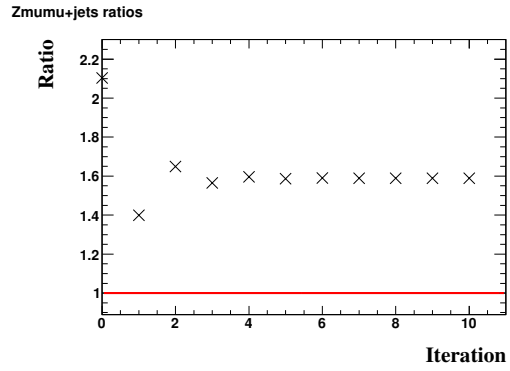
(a) $W \rightarrow e\nu$ ratios



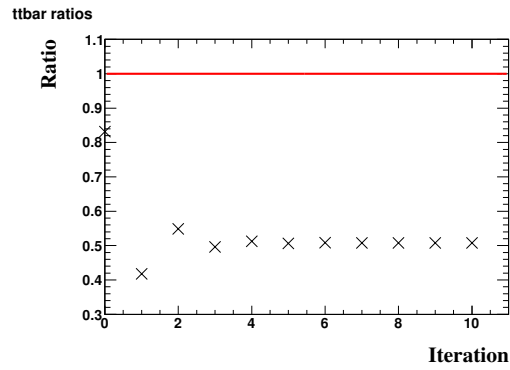
(b) $W \rightarrow \mu\nu$ ratios



(c) $Z \rightarrow ee$ ratios



(d) $Z \rightarrow \mu\mu$ ratios



(e) $t\bar{t}$ ratios

Figure 4.20.: Control ratios as a function of the iteration step. The method already converges after a few steps.

4. Search for a fourth generation signal in same-sign dilepton final states

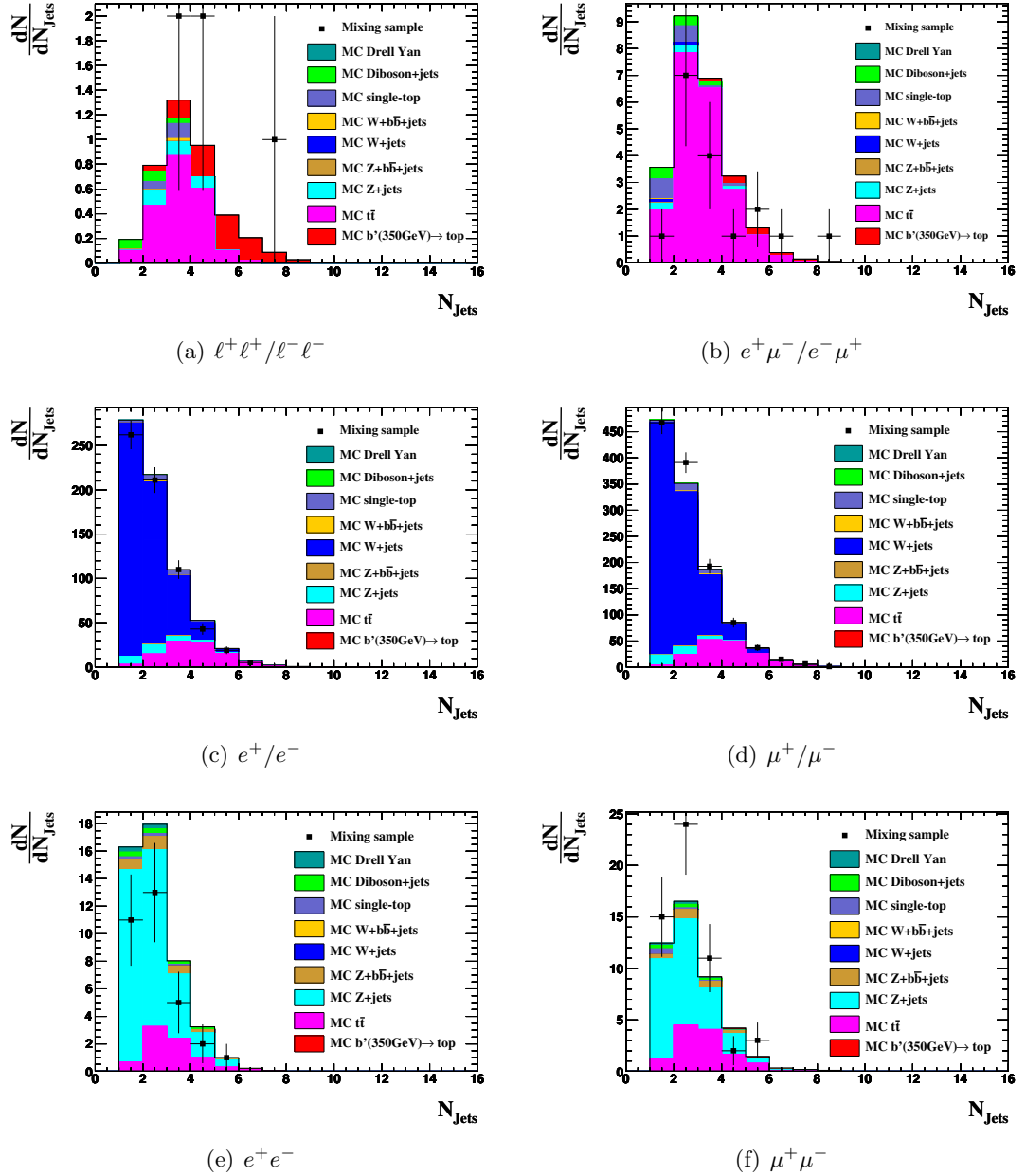


Figure 4.21.: Signal and control regions for the counting analysis with a mixing sample created of the MC with default cross sections. The histograms are rescaled to an integrated luminosity of $\mathcal{L} = 50 \text{ pb}^{-1}$.

of a specific sample by a factor c , the calculated weight changes to:

$$w = \frac{c \cdot \sigma}{N} \cdot L^* . \quad (4.29)$$

The modifications in the cross sections for the pseudo data sample used in this analysis are:

- For signal, $t\bar{t}$ and single top: **+60%** $\Rightarrow c = 1.6$
- For W +jets, Z +jets, $W/Z+bb$ +jets and dibosons+jets: **-40%** $\Rightarrow c = 0.6$

The changes of the cross sections should be reflected by the calculated control ratios. Ideally, the measured ratio in a control region equals the modification factor c that has been applied to the corresponding BG contribution.

The analysis was performed on this pseudo data set with 10 iteration steps. Figure 4.22 illustrates the calculated ratios as a function of the iteration step, which show a similar behavior to the plots in figure 4.20. Here, too, one notices a convergence of the ratios after 4 – 5 iteration steps.

The results, together with the expected values, are shown in table 4.11. The errors

Sample	Measured events in signal region	Measured ratio in control regions	Expected events in signal region	Expected ratio in control regions
pseudo data	6			
$W\nu$ +jets	0.00 ± 0.00	0.57 ± 0.06	0.00 ± 0.28	0.6
$W\mu\nu$ +jets	0.00 ± 0.00	0.64 ± 0.06	0.00 ± 0.28	0.6
Zee +jets	0.31 ± 0.06	1.0 ± 0.2	0.17 ± 0.16	0.6
$Z\mu\mu$ +jets	0.0 ± 0.0	0.2 ± 0.3	0.00 ± 0.17	0.6
$t\bar{t}$	3.3 ± 0.8	1.5 ± 0.4	3.45 ± 0.33	1.6
other	0.45		0.44 ± 0.42	
Result	1.95 ± 2.89		1.68 ± 0.03	

Table 4.11.: Results for the measured events and control ratios after the counting analysis. The analysis is run on a mixing pseudo data sample with modified cross sections and with an integrated luminosity of $\mathcal{L} = 50 \text{ pb}^{-1}$. The errors on the measured quantities are obtained from a dedicated toy study, described in section 4.7.2 (table C.2).

are obtained again from a toy study (section 4.7.2).

Such as for the analysis with default cross sections (table 4.10), one notices a good agreement between the measured and expected ratios in the W +jets control regions. The ratios for the Z +jets control regions and the measured signal yield again show a bias. This is due to low statistics, as described in the previous section. In contrast, the ratio for the $t\bar{t}$ CR appears with a better agreement than in the analysis with the default cross sections. However, all calculated quantities agree within 1σ and 3σ standard deviations with the expected values.

In figure 4.23, the distributions for the signal and the W +jets control regions are illustrated. The histograms on the left show the distributions before running the counting

4. Search for a fourth generation signal in same-sign dilepton final states

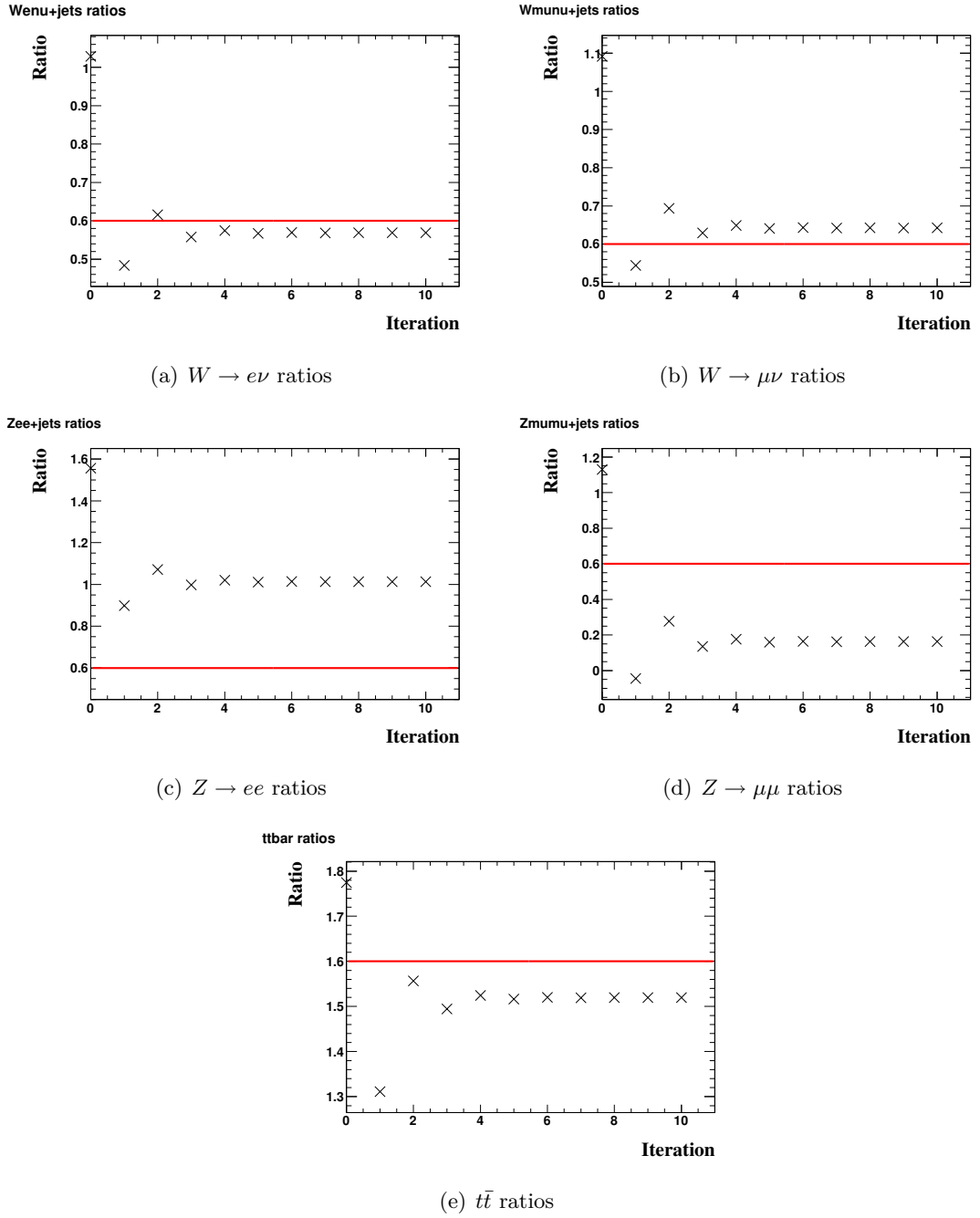
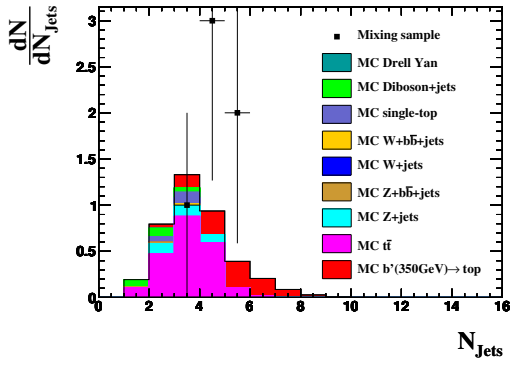
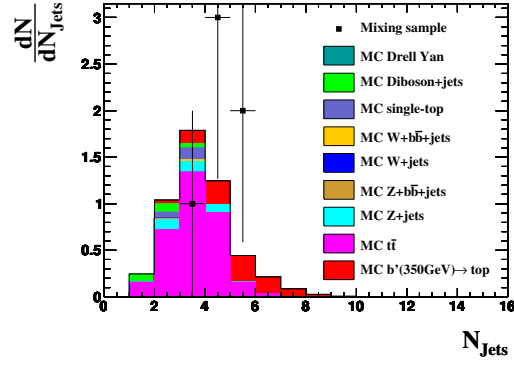


Figure 4.22.: Control ratios as a function of the iteration step.

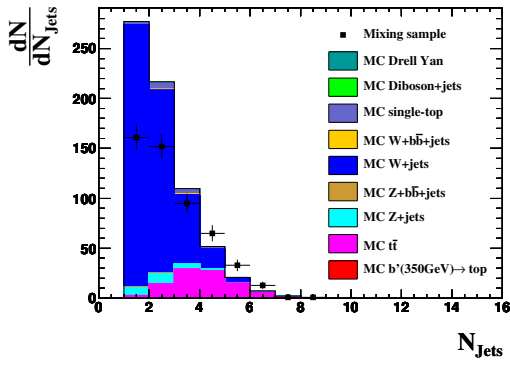
4.6. Results for pseudo data



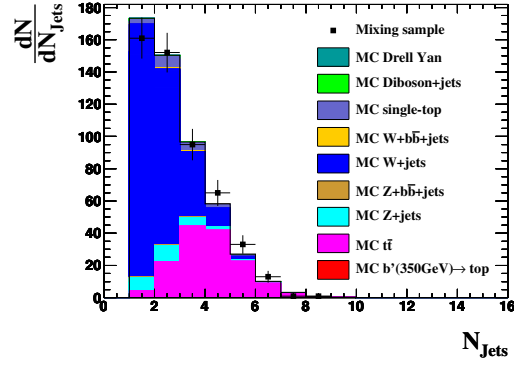
(a) $\ell^+\ell^+/\ell^-\ell^-$



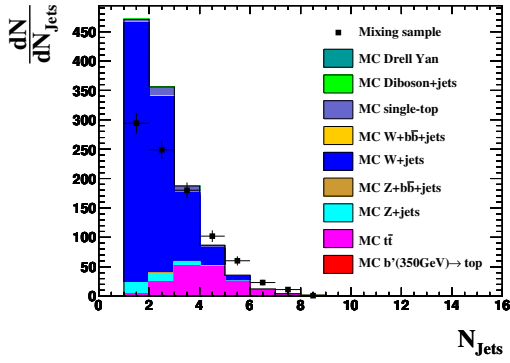
(b) $\ell^+\ell^+/\ell^-\ell^-$ with applied ratio



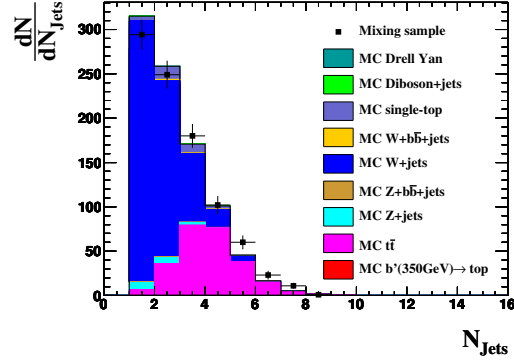
(c) e^+/e^-



(d) e^+/e^- with applied ratio



(e) μ^+/μ^-



(f) μ^+/μ^- with applied ratio

Figure 4.23.: Signal and W +jets control regions for the counting analysis with a mixing sample created of the MC with varied cross sections. The distributions at the beginning of the analysis are shown on the left ((a), (c) and (e)). On the right ((b), (d) and (f)), the histograms after applying the computed control ratios to the MC predictions are illustrated. The histograms are rescaled to an integrated luminosity of $\mathcal{L} = 50 \text{ pb}^{-1}$.

4. Search for a fourth generation signal in same-sign dilepton final states

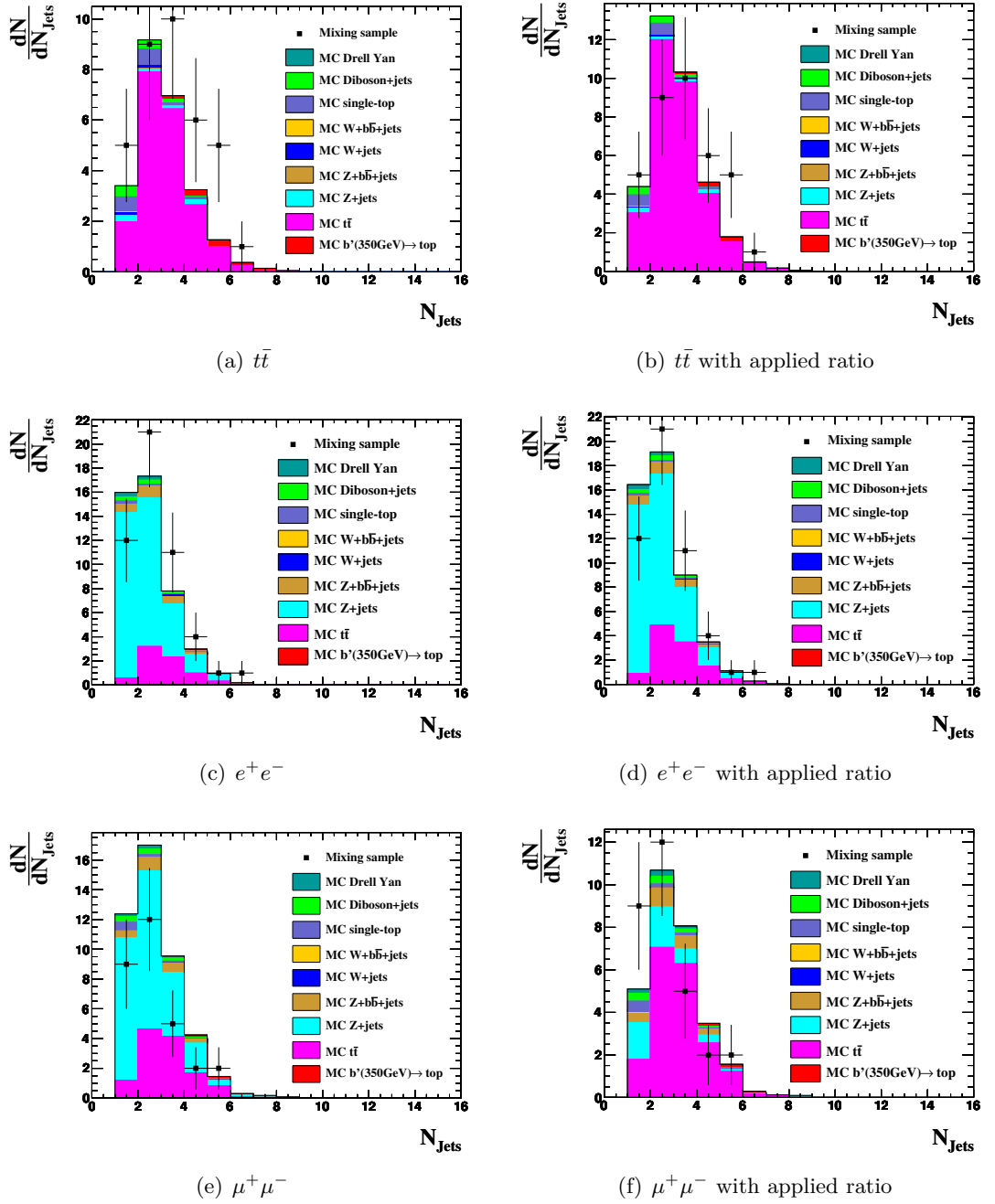


Figure 4.24.: $t\bar{t}$ and Z +jets control regions for the counting analysis with a mixing sample created of the MC with varied cross sections. The distributions at the beginning of the analysis are shown on the left ((a), (c) and (e)). On the right ((b), (d) and (f)), the histograms after applying the computed control ratios to the MC predictions are shown. The histograms are rescaled to an integrated luminosity of $\mathcal{L} = 50 \text{ pb}^{-1}$.

analysis. On the right are the same plots after applying the computed ratios on the MC. In the W +jets control regions, the MC estimations describe the pseudo data distributions very well after correcting them by the control ratio.

The same distributions are illustrated in figure 4.24 for the Z +jets and $t\bar{t}$ control regions.

4.7. Toy studies

In the following, toy studies are performed on the counting analysis.

In this way, it is possible to obtain errors on the calculated control ratios and event yields. This will be presented in section 4.7.2. The obtained errors were already listed in the results of the counting analysis with the two different mixing samples (tables 4.10 and 4.11).

Moreover, one noticed a bias for some calculated quantities due to the lack of statistics at an integrated luminosity of $\mathcal{L} = 50 \text{ pb}^{-1}$. Mixing samples with higher luminosities are not possible with the current available MC samples. Another way is to use a toy sample as pseudo data. Thus one can produce a pseudo data sample with an arbitrary luminosity. The results of the counting analysis performed on such a toy sample are presented in section 4.7.1.

A toy sample is produced from the final MC distributions of signal and background after applying all required event selection cuts. First, these MC distributions are rescaled to any desired integrated luminosity. Then, based on the rescaled MC distributions for the signal (fig. 4.14) and control regions (fig. 4.19), new histograms are produced using statistical methods. This is done by calculating for each bin entry b a new pseudo random number x_b using the *ROOT* random number generator. The obtained x_b is then used as the new value for the bin entry. The numbers x_b are calculated according to a Poisson distribution with mean value b . The probability $P(x_b)$ for getting the random number x_b is then

$$P(x_b) = \frac{e^{-b} \cdot b^{x_b}}{x_b!} . \quad (4.30)$$

4.7.1. Results for single toy samples

At first, a single toy sample is created with an integrated luminosity of $\mathcal{L} = 1 \text{ fb}^{-1}$. Then, the counting analysis is performed on this toy sample as a test with higher statistics in comparison to the analyses with the mixing samples (sections 4.6.2 and 4.6.3). This is done in order to see if the biases vanish, which appeared due to low statistics.

Table 4.12 lists the results for the counting analysis. The errors on the measured quantities are again obtained from a toy study described in the next section. The calculated ratios show a good agreement with the expected value of 1 within a 1σ standard deviation in the W +jets and Z +jets control regions. A match of the calculated ratio with the expected ratio 1 within 2σ standard deviations is noticeable in the $t\bar{t}$ CR. All ratios have an error below 7% now.

A similar analysis was performed on a toy sample with varied cross sections and a lumi-

4. Search for a fourth generation signal in same-sign dilepton final states

Sample	Measured events in signal region	Measured ratio in control regions	Expected events in signal region	Expected ratio in control regions
pseudo data	71			
$W e \nu$ +jets	0.0 ± 0.0	1.00 ± 0.01	0.0 ± 9.2	1
$W \mu \nu$ +jets	0.0 ± 0.0	1.01 ± 0.01	0.0 ± 9.3	1
$Z e e$ +jets	6.0 ± 0.3	1.04 ± 0.05	5.7 ± 5.2	1
$Z \mu \mu$ +jets	0.0 ± 0.0	1.06 ± 0.06	0.0 ± 5.5	1
$t \bar{t}$	39.8 ± 2.8	0.92 ± 0.06	43.1 ± 4.2	1
other	8.80		8.8 ± 11.3	
Result	16.5 ± 10.6		21.0 ± 0.3	

Table 4.12.: Results for the measured events and control ratios after the counting analysis. The analysis is run on a toy pseudo data sample with an integrated luminosity of $\mathcal{L} = 1 \text{ fb}^{-1}$. The errors on the measured quantities are obtained from a dedicated toy study, described in section 4.7.2 (table C.3).

nosity of $\mathcal{L} = 1 \text{ fb}^{-1}$. The same cross section modification factors as in section 4.6.3 have been applied. The results are listed in appendix C.1 and show the same good agreement between measured and expected values as in table 4.12.

In comparison to the results obtained with pseudo data at $\mathcal{L} = 50 \text{ pb}^{-1}$, there is a better agreement noticeable for the results obtained from pseudo data with higher statistics.

However, the BG contribution of W +jets and $Z \rightarrow \mu\mu$ events to the signal region still cannot be described well. This is due to the lack of statistics in these samples. Therefore, MC samples with more statistics would be needed for a better description of these backgrounds.

4.7.2. Error estimation for counting analysis

For a better understanding of the precision of the calculated control ratios and event yields obtained by the counting analysis, an estimation of the uncertainties is needed. A direct calculation of the statistical errors is a quite complicated task. The iterative derivation of the control ratios of a specific control region includes the ratios of the other control regions from the previous iteration steps (see section 4.5.2). As a result, all ratios are strongly correlated at the end of the iterative calculation. This would have to be considered in the derivation of the statistical uncertainties.

Therefore, another strategy has been followed: A large set (here: 1000) of different toy samples is created and the counting analysis is performed on each of them. For each toy sample one obtains the calculated control ratios and event yields.

In the toy sample creation, the bins of each histogram are recalculated according to a Poisson distribution, starting from the original MC histograms. Thus, the total number of events contained in a histogram should also follow a Poisson distribution, when repeating the creation procedure 1000 times. As a result, the final calculated yields and ratios of the counting analysis performed on each sample should fluctuate within the statistical errors. Each quantity is plotted into a histogram and the standard deviation (or RMS) of these distributions are then taken as an error estimate.

In the following, such an analysis is presented for an integrated luminosity of $\mathcal{L} = 50 \text{ pb}^{-1}$ and with the default cross sections.

As an example, the computed signal yield after the counting analysis for the 1000 different toy samples is plotted in figure 4.25. The distribution has an asymmetric shape, but

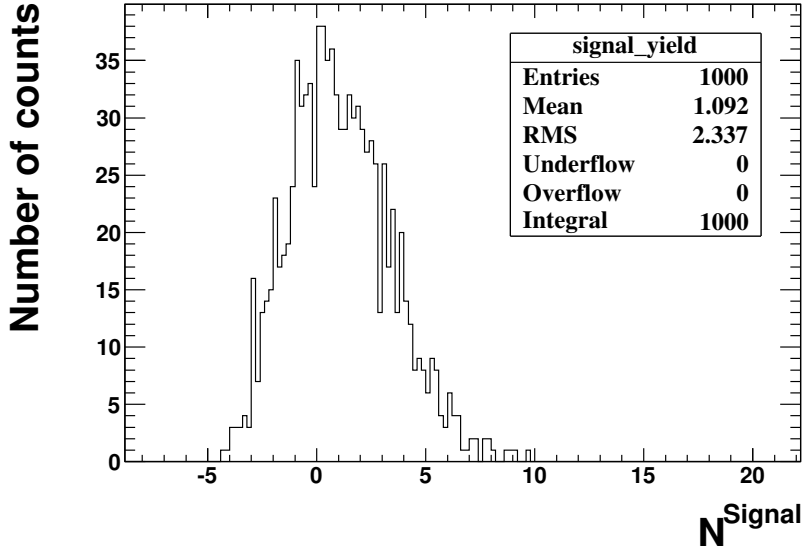


Figure 4.25.: The computed signal yield after the counting analysis for 1000 different toy samples.

the RMS will be taken from the histogram as an error estimate under the assumption of a symmetric Gaussian shape. This was repeated for the BG yields and control ratios and the corresponding histograms are given in appendix C.2. Table 4.13 summarizes the mean (μ) and RMS (σ) values of all quantities. The obtained σ were assigned to

Sample	Yield μ	Yield σ	Yield $\frac{\sigma}{\sqrt{1000}}$	Ratio μ	Ratio σ	Ratio $\frac{\sigma}{\sqrt{1000}}$
$W e \nu + \text{jets}$	0	0	0	1.000	0.050	0.002
$W \mu \nu + \text{jets}$	0	0	0	1.000	0.053	0.002
$Z e e + \text{jets}$	0.287	0.060	0.002	1.008	0.212	0.007
$Z \mu \mu + \text{jets}$	0	0	0	0.998	0.273	0.009
$t \bar{t}$	2.166	0.649	0.021	0.995	0.298	0.009
Signal yield	1.09	2.34	0.07			

Table 4.13.: Mean values μ and standard deviations σ of yields and ratios after the counting analysis with 1000 different toy samples. The analysis was performed with $\mathcal{L} = 50 \text{ pb}^{-1}$ and default cross sections.

the yields and ratios calculated in the counting analysis performed on a mixing sample in section 4.6.2 (table 4.10).

Similar toy studies have been performed on toy samples with different luminosities

4. Search for a fourth generation signal in same-sign dilepton final states

and/or a cross section modification, in order to quantify the uncertainties on the obtained values in tables 4.11 and 4.12. All obtained mean and RMS values for each toy study are listed in appendix C.3.

However, it is not possible to quantify errors for the W +jets and $Z \rightarrow \mu\mu$ yields, since they do not have entries in the signal region histogram due to the lack of statistics in the MC generation for these samples.

The true contribution from the signal is unknown, since it depends on unquantified parameters like the particles mass or the branching fraction of the decay scenario. Hence, one needs to study the error dependence on the true signal contribution. This is done by repeating the previous analysis with several toy samples, that have different contributions from the signal. For each true signal value $N_{\text{True signal}}$, the analysis is performed again on 1000 different toy histograms.

At $\mathcal{L} = 50 \text{ pb}^{-1}$, one expects ≈ 1 signal event with the current search strategy. From the heavy quarks mass dependence of the cross section (figure 4.2), one can estimate the change in the signal yield with different masses. For masses between

$$m \in [300 \text{ GeV}, 500 \text{ GeV}] , \quad (4.31)$$

this results in a signal yield range of:

$$N_{\text{True}} \in [0.1, 2.5] . \quad (4.32)$$

To study the method also at large N_{True} , the signal contribution was varied in a wider range. In order to obtain the different true signal contributions, the signal cross section was varied by factors between 0 and 40, which results in a N_{True} range of $N_{\text{True}} \in [0, 42]$. In plotting the mean values and standard deviations (as error bars) from the calculated signal yield as a function of $N_{\text{True signal}}$, one is able to construct a 1σ -confidence belt for the measured signal yield N_{Measured} (figure 4.26). Depending on the determined N_{Measured} value after the analysis, one can read off the corresponding 1σ uncertainty for $N_{\text{True signal}}$. The obtained N_{Measured} values do not show a bias, since they equal the values for $N_{\text{True signal}}$ within the errors.

The constructed confidence belt is now used to obtain an error on the previously measured signal yield of 3.25 ± 2.34 in the counting analysis performed on a mixing sample (table 4.10). This is done by a linear approximation of the confidence belt in the considered region of $N_{\text{Measured}} = 3.25$. The result now changes to:

$$N_{\text{Signal}} = 3.295^{+3.647}_{-2.239} . \quad (4.33)$$

The BG yields and control ratios were also plotted as a function of $N_{\text{True signal}}$. These plots are given in appendix C.4. However, in order to obtain an error estimate depending on the measured BG yield or ratio, one needs to repeat this toy study with different true contributions N_{True} for the backgrounds.

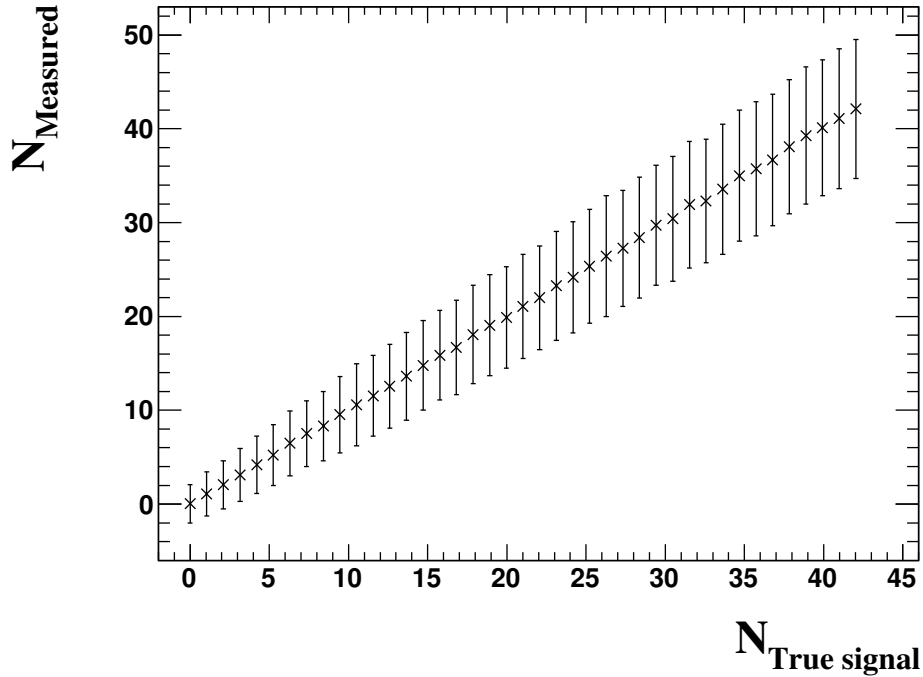


Figure 4.26.: The computed signal yield as a function of the true signal contribution. Each point consists of 1000 different toy samples. Plotted are the mean values and the standard deviations are denoted by the error bars.

4.8. Cut optimisation

The event selection cuts used for the analysis (section 4.4.5) were mainly adopted from the CMS analysis in [58]. It was discussed in section 4.4.7 that a discovery of a b' quark in the considered scenario will be not possible with the data set expected until the end of 2011. Therefore, an optimisation of the event selection cuts has been performed in order to get an optimal significance. The cuts are improved using the *Toolkit for Multivariate Data Analysis with ROOT (TMVA)* [60].

The input variables for the optimisation are those discussed in section 4.4.5, namely the missing transverse energy \cancel{E}_T , the transverse energy of the leading jet E_T^{LeadJet} , the transverse momentum P_T^{LeadLep} , and absolute value of the pseudo-rapidity $|\eta^{\text{LeadLep}}|$ of the leading lepton. Only events with two same-sign charged leptons after the particle selection described in section 4.4 are used as input for *TMVA*.

Figure 4.27 illustrates the input variables distributions of signal (blue) and background (red). The background includes all processes discussed in section 4.2.

The *TMVA* package contains several algorithms for performing multivariate analyses. Here, the "Cuts" method with the "Genetic algorithm" (GA) as minimisation algorithm is chosen for the optimisation. It is a rectangular cut optimisation, which sets the signal

4. Search for a fourth generation signal in same-sign dilepton final states

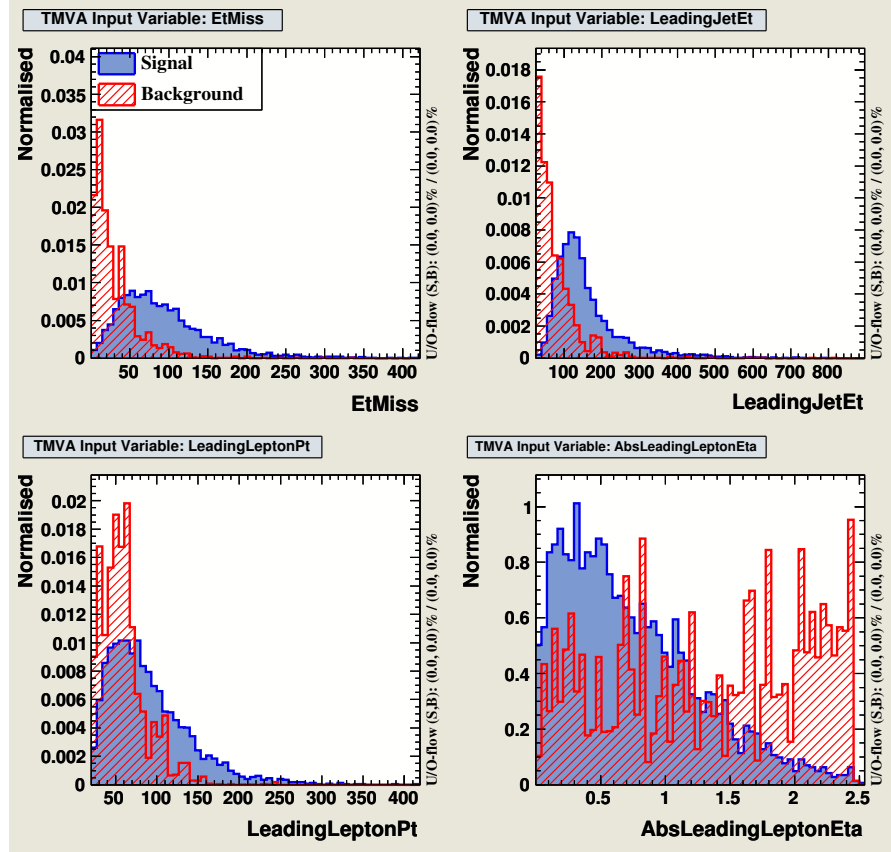


Figure 4.27.: Input variables distributions of signal and background used for the TMV analysis. The shown variables are $\text{EtMiss} = \cancel{E}_T$, $\text{LeadingJetEt} = E_T^{\text{LeadJet}}$, $\text{LeadingLeptonPt} = P_T^{\text{LeadLep}}$ and $\text{AbsLeadingLeptonEta} = |\eta^{\text{LeadLep}}|$.

efficiency ϵ_S to a specific value and maximises the background rejection $r = 1 - \epsilon_B$, where ϵ_B is the background efficiency. This is done by varying the input variables, until the rejection reaches its maximum value. The algorithm iterates over signal efficiencies ϵ_S between 0% and 100% in steps of 1%. The result is then a set of optimal minimum and maximum values for the event selection variables to each signal efficiency ϵ_S .

The final background rejection r after the optimisation with *TMVA* is plotted as a function of the signal efficiency ϵ_S in figure 4.28. It illustrates the correlation between

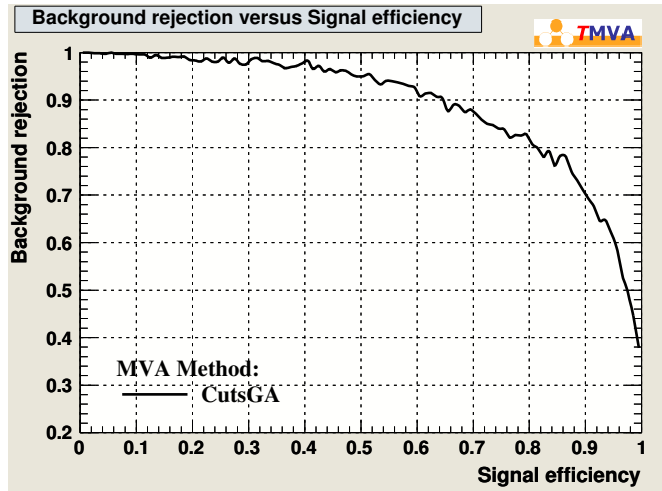


Figure 4.28.: Signal efficiency ϵ_S as a function of the background rejection $r_B = 1 - \epsilon_B$ after the cut optimisation.

an increasing signal efficiency and a decreasing background rejection. The curve shows small fluctuations, which arise from the lack of statistics in some background samples (mainly W +jets and $b\bar{b}$ jets).

Each obtained signal efficiency ϵ_S corresponds to a set of cut values for the event selection variables and to a background efficiency ϵ_B , which was minimal with these cuts (since $r = 1 - \epsilon_B$ was maximised). The signal and background efficiencies are plotted as a function of the obtained optimised cut values in figure 4.29. The minimum cut values for \cancel{E}_T and $P_T^{LeadLep}$ are decreasing, while the maximum value for $|\eta^{LeadLep}|$ is increasing with higher signal efficiencies. The value for $E_T^{LeadJet}$ is almost constant at around ≈ 70 GeV for all efficiencies.

The output of *TMVA* are sets of cuts corresponding to specific signal efficiencies ϵ_S . In order to obtain the optimal cuts, it is necessary to select those cut values which maximise the significance described in section 4.4.7 (Eq. 4.14):

$$Sign. = \frac{S}{\sqrt{B}}, \quad (4.34)$$

where S and B are the final signal and background yields after applying the optimised

4. Search for a fourth generation signal in same-sign dilepton final states

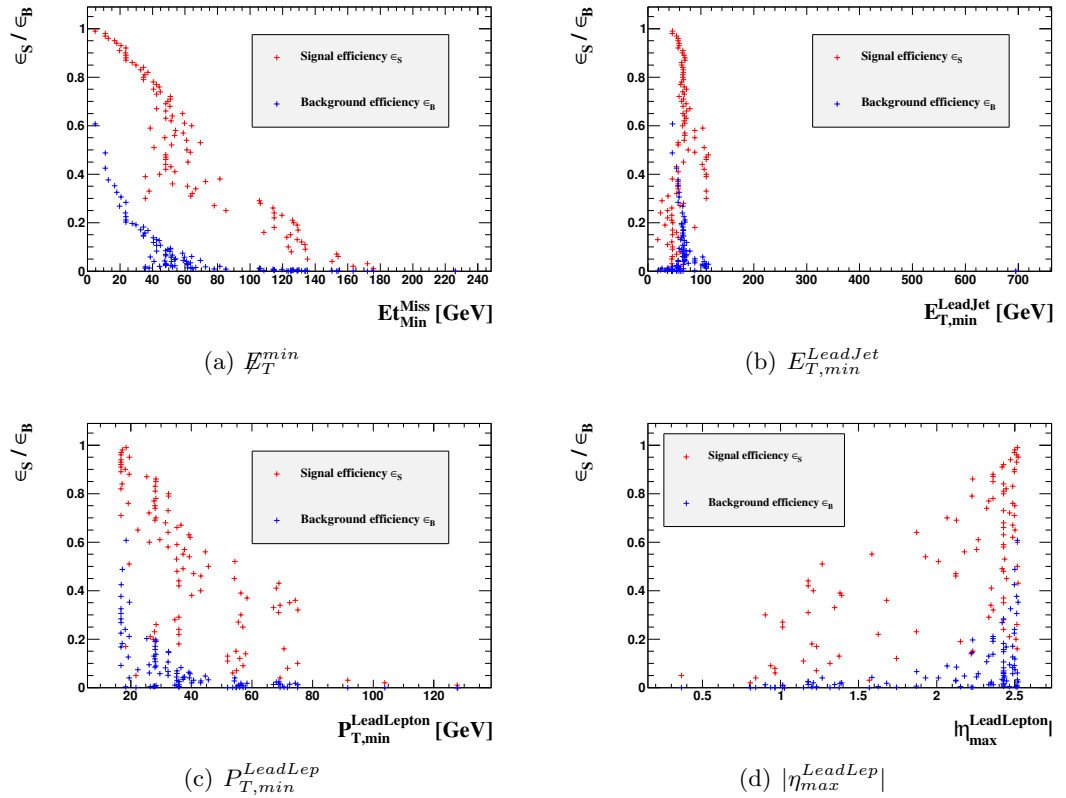


Figure 4.29.: Signal ϵ_S and background ϵ_B efficiency as a function of the cut values after optimisation with *TMVA*.

cuts (and rescaling to $\mathcal{L} = 50 \text{ pb}^{-1}$). Since each set of optimised cuts corresponds to a specific signal and background efficiency, the significances can be plotted as a function of the signal efficiency ϵ_S and of the optimised cut values (figure 4.30). The significance in fig. 4.30(a) is almost flat at signal efficiencies between 30% and 70% with a value of $Sign. \approx 0.8$. There is a large rise at $\epsilon_S \lesssim 0.3$, which arises from low statistics in some background samples that are completely vanishing due to the hard cuts leading to these low efficiency values. Figures 4.30(b) and 4.30(d) also show such effects of low statistics, especially at high cut values that result in a large rise of the significance. In figure 4.30(e) the significance is nearly independent on the cut value $|\eta_{max}^{LeadLep}|$.

Another definition for the significance is

$$Sign.' = \frac{S}{\sqrt{S+B}}. \quad (4.35)$$

It describes the relative precision of a measurement after performing the analysis in comparison to the significance in Eq. 4.14, which described the probability of measuring a specific deviation.

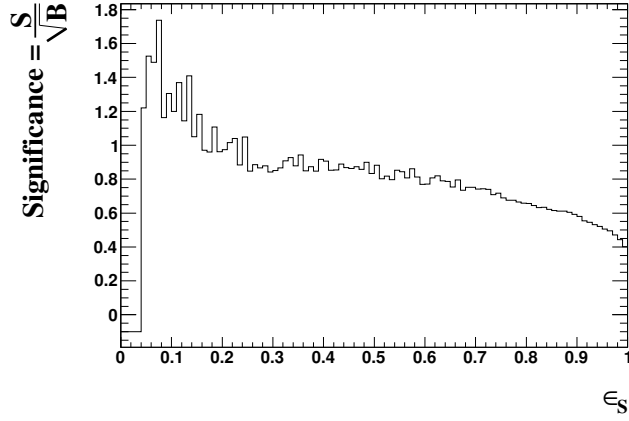
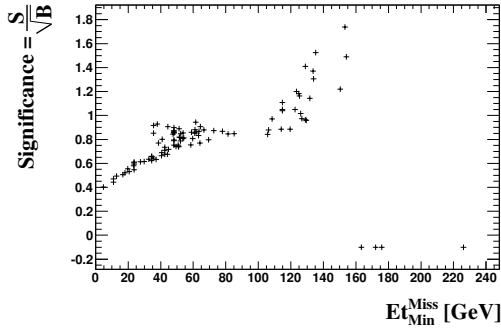
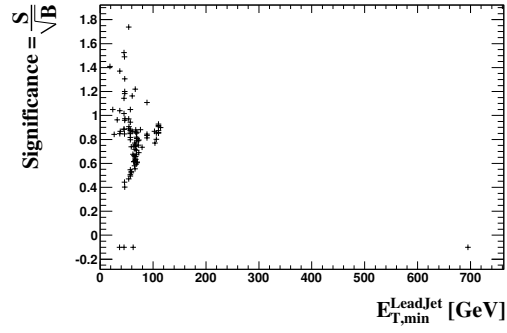
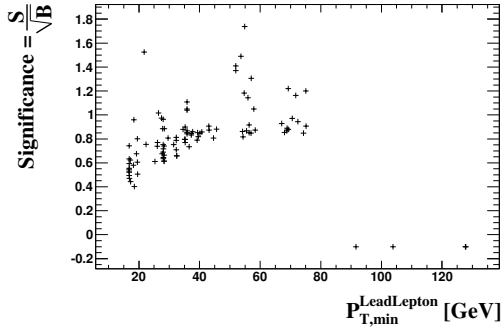
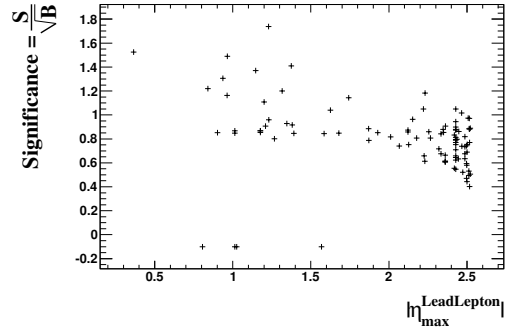
(a) ϵ_S (b) E_T^{min} (c) $E_{T,min}^{LeadJet}$ (d) $P_{T,min}^{LeadLep}$ (e) $|\eta_{max}^{LeadLep}|$

Figure 4.30.: Significance S/\sqrt{B} as a function of the signal efficiency ϵ_S (a) and of the cut values ((b)-(e)) after optimisation with *TMVA*.

4. Search for a fourth generation signal in same-sign dilepton final states

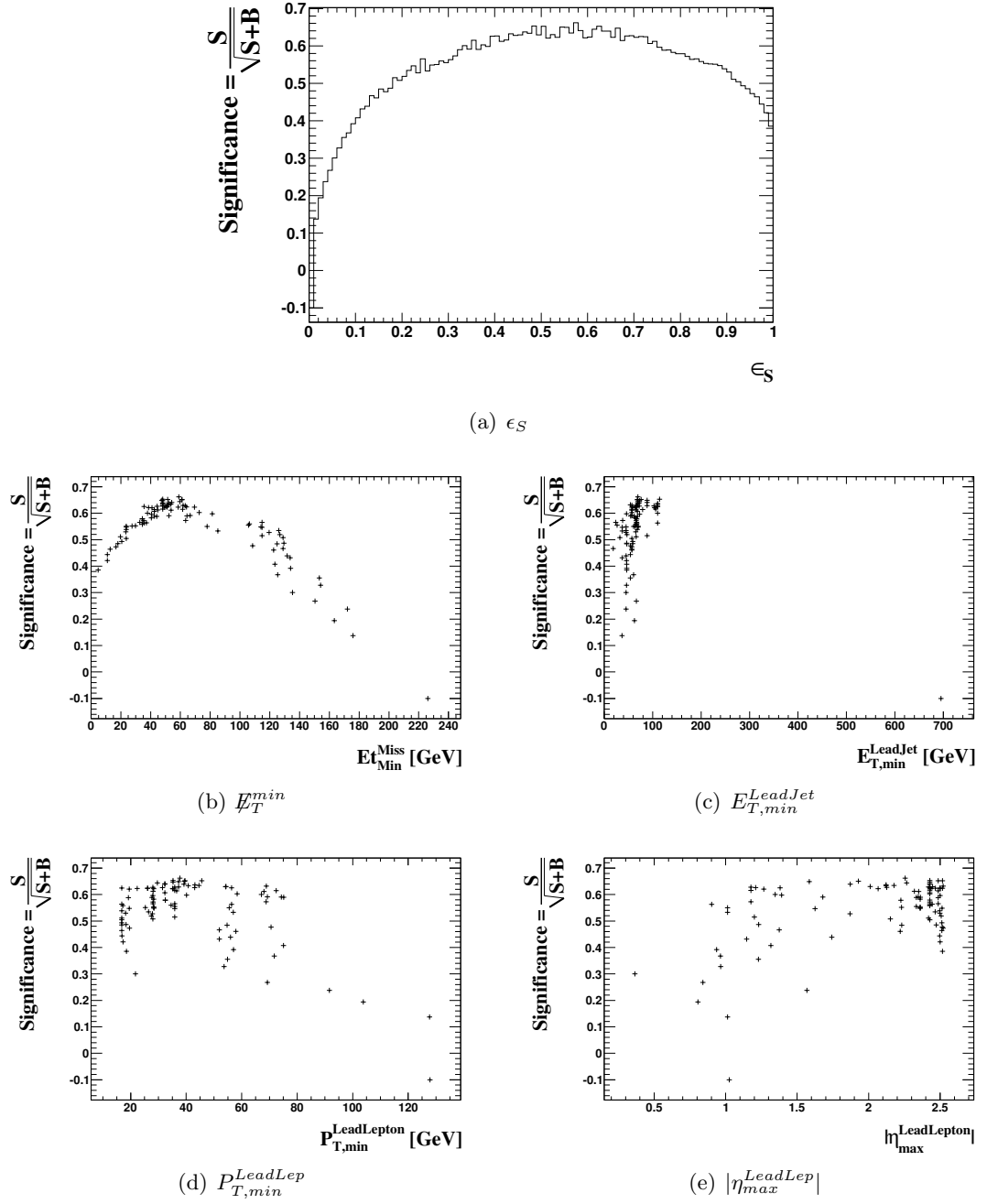


Figure 4.31.: Significance $S/\sqrt{S+B}$ as a function of the signal efficiencies ϵ_S (a) and of the cut values ((b)-(e)) after optimisation with *TMVA*.

4.8. Cut optimisation

Figure 4.31 illustrates the significance (Eq. (4.35)) as a function of the signal efficiency ϵ_S and of the optimised cut values. Since the signal yield S also appears in the denominator, the significance is not affected by the low statistic effects discussed before. Thus, the plots in figure 4.31 are more suitable to read off the optimal cut values leading to a maximum significance.

The significance in figure 4.31(a) reaches its maximum at $\epsilon_S \approx 50\% - 70\%$ with $Sign.' \approx 0.6$.

In the case of \cancel{E}_T^{min} (fig. 4.31(b)) the distribution is almost flat between 40 GeV and 80 GeV. We choose $\cancel{E}_T^{min} \approx 50$ GeV as an optimal value.

The entries in the distribution for $E_{T,min}^{LeadJet}$ (fig. 4.31(c)) concentrate in the range between 20 GeV and 120 GeV. We choose a cut of $E_{T,min}^{LeadJet} \approx 70$ GeV that provides the highest significance.

The distribution for $P_{T,min}^{LeadLep}$ (fig. 4.31(d)) fluctuates at values above 50 GeV and is almost flat between 20 GeV and 50 GeV. Hence, the previous cut on $P_{T,min}^{LeadLep}$ of 35 GeV can be maintained.

As already noted, the significance is nearly independent on the cut value of $|\eta_{max}^{LeadLep}|$ (fig. 4.31(e)). We choose to cut at the crack region (see section 2.2), since this should be excluded anyway to avoid unwanted physical processes in this region.

All chosen optimised cut values are summarized in table 4.14, together with the previously chosen values for comparison.

Variable	Old value	New value
\cancel{E}_T	> 20 GeV	> 50 GeV
$E_T^{LeadJet}$	> 85 GeV	> 70 GeV
$P_T^{LeadLep}$	> 35 GeV	> 35 GeV
$ \eta^{LeadLep} $	< 1	< 1.37 (Crack region)

Table 4.14.: The final optimised cut values (New value) after the analysis with *TMVA*. The values are taken at a signal efficiency of about $\epsilon_S \approx 60\%$. For comparison, the previously chosen cut values are shown (Old value).

As denoted in section 4.1, the high jet multiplicity in the signal can be also used for background suppression. A search for the fourth generation quarks with cuts on the number of jets N_{Jets} has been already discussed in [61]. In order to see the effect of cutting on this variable, the *TMVA* analysis is performed also with N_{Jets} as an additional input variable. The results for the significances as a function of the signal efficiency ϵ_S and the optimised minimum value for the jet multiplicity N_{Jets}^{Min} are plotted in figure 4.32.

When adding N_{Jets} in the optimisation the significances increase to $Sign. \approx 1$ and $Sign.' \approx 0.75$ in the ϵ_S region between 50% and 70% (figures 4.32(a) and 4.32(b)). The distributions are more fluctuating, because there are in general less events remaining

4. Search for a fourth generation signal in same-sign dilepton final states

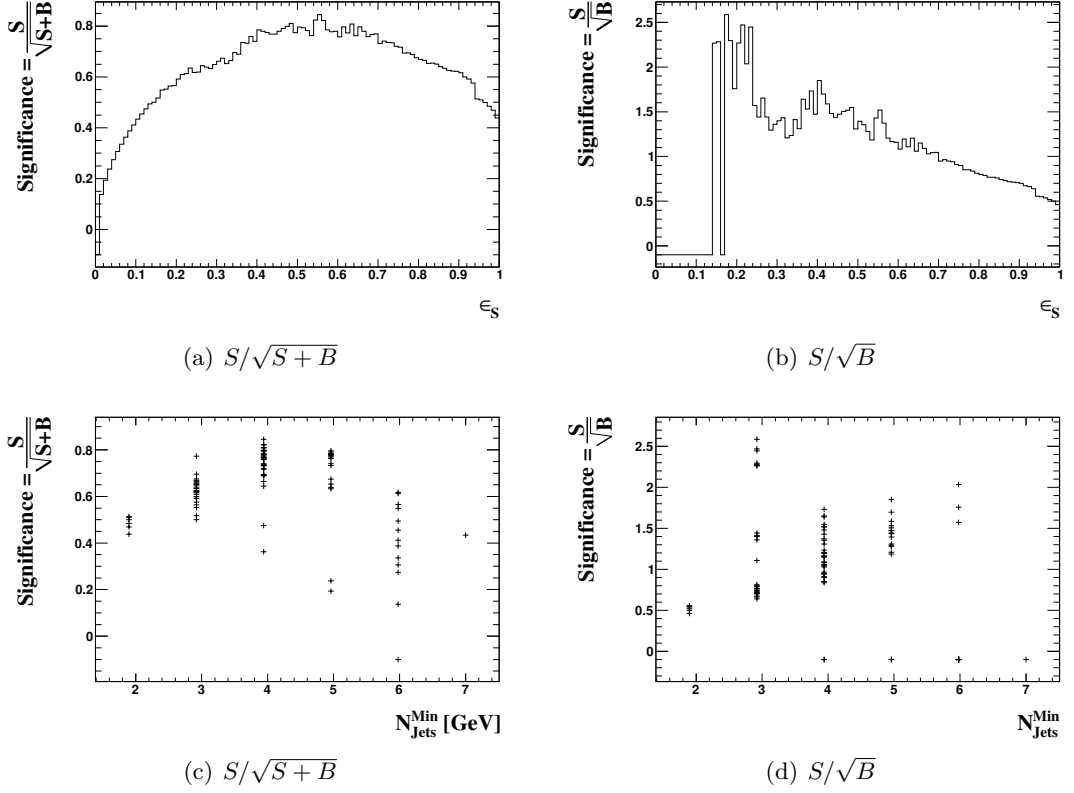


Figure 4.32.: Significances S/\sqrt{B} and $S/\sqrt{S+B}$ after optimisation with *TMVA* and with additional optimised variable N_{Jets} . The significances are plotted as a function of the signal efficiency and N_{Jets}^{Min} .

due to the additional event selection cut N_{Jets} .

The significance in figure 4.32(c) reaches its maximum by requiring at least four jets. Hence, we choose a cut value of $N_{Jets}^{min} = 4$.

The histograms for the other cut variables E_T^{min} , $E_{T,min}^{LeadJet}$, $P_{T,min}^{LeadLep}$ and $|\eta_{max}^{LeadLep}|$ are shown in appendix D.1. The previously denoted cuts on these variables can be maintained, since the resulting significance plots are similar to those previously obtained in the optimisation without the variable N_{Jets} (compare figures D.1 and D.2 with figures 4.30 and 4.31).

4.8.1. Results for optimised cuts

The obtained optimised event selection cuts (table 4.14) are now applied to the signal and background events from the samples discussed in section 4.2. The resulting N_{Jets} distribution for same-sign charged dilepton events $\ell^+\ell^+/\ell^-\ell^-$ is presented in figure 4.33. In comparison to figure 4.14, one notices a reduction of the BG contributions, while the signal is nearly maintained.

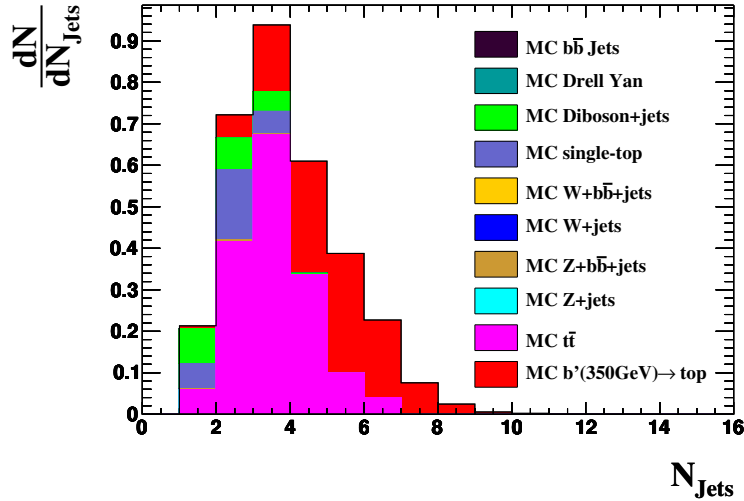


Figure 4.33.: Number of jets distribution in the $\ell^+\ell^+/\ell^-\ell^-$ signal region. The optimised event selection cuts from table 4.14 have been applied.

This is also noticeable in table 4.15, which lists the signal and BG yields and the significances after applying the old event selection cuts and the new optimised cuts. Furthermore, by additionally applying the cut on the jet multiplicity ($N_{Jets} \geq 4$), the

	Old cuts	New cuts	New cuts and $N_{Jets} \geq 4$
Signal yield S	1.05	1.08	0.85
Background yield B	2.96	2.13	0.48
$S/\sqrt{S+B}$	0.52	0.60	0.74
S/\sqrt{B}	0.61	0.74	1.24

Table 4.15.: Signal/background yields and the corresponding significances. The values are given after using the old event selection cuts (section 4.4.5), the optimised cuts (table 4.14) and with additional cut on the jet multiplicity. The numbers are given for an integrated luminosity of $\mathcal{L} = 50 \text{ pb}^{-1}$.

BG yield is largely reduced.

It was discussed in section 4.4.7 that a b' can be not discovered at $\mathcal{L} = 1 \text{ fb}^{-1}$ in the considered scenario with the event selection criteria from section 4.4.5. As shown in figure 4.17, the integrated luminosity needed for the discovery of a b' with a mass of 300 GeV was above 2 fb^{-1} and increased with higher masses.

The same plot was now produced with the new optimised event selection cuts (table 4.14) including the requirement of at least four jets. The integrated luminosity needed for a 5σ -discovery is derived from Eq. 4.15, where S and B are now the yields after the new cuts. Again, the luminosities are plotted as a function of the b' mass. The resulting

4. Search for a fourth generation signal in same-sign dilepton final states

plot is presented in figure 4.34. The required luminosity is reduced by nearly one order of

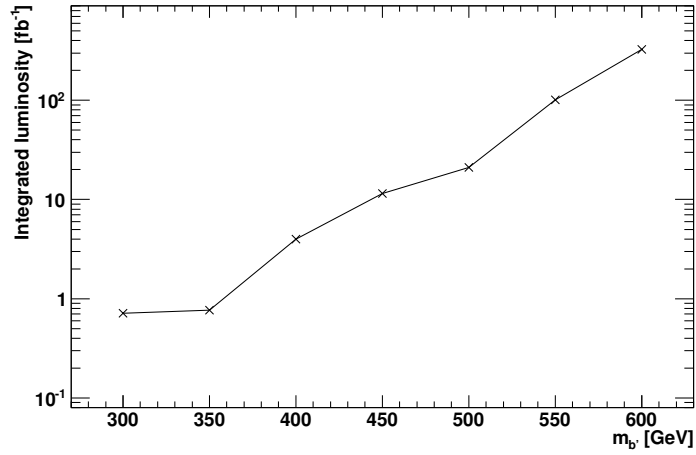


Figure 4.34.: Logarithmic plot of the needed integrated luminosity for a 5σ discovery with significance S/\sqrt{B} . The luminosity is given as a function of the b' mass and is calculated from the yields after applying the optimised cuts (table 4.14) including the requirement of $N_{Jets} \geq 4$.

magnitude in comparison to the plot obtained with the old cuts (fig. 4.17). For a b' with a mass of $m_{b'} \leq 350$ GeV, a luminosity of less than 1 fb^{-1} is needed for a 5σ significance. Thus, a discovery of a b' in this mass range could be possible in the considered scenario. This requires that the LHC reaches the expected integrated luminosity of 1 fb^{-1} by the end of the year 2011.

5. Summary and outlook

In this thesis a strategy for the search for fourth generation quarks has been discussed.

The possible decay scenarios of a heavy fourth generation down-type quark b' depend on the mass difference between the b' and the fourth generation up-type quark t' . This mass difference is currently not well constrained. The decay scenarios of a b' have been discussed under the assumption of a sufficient large mixing in the CKM sector between the fourth and third family with respect to the mixings between the fourth and second and between the fourth and first family. Then final states with four W -bosons ($2W^+2W^-$) and two b -quarks appear with sufficient branching fraction and independently of the mass difference between b' and t' . It was required that two same-sign charged W -bosons decay leptonically. This resulted in the selected rare Standard Model signature of same-sign charged dileptons $\ell^+\ell^+/\ell^-\ell^-$.

The particle and event selection criteria have been discussed next. The selected criteria yield in a further suppression of the Standard Model backgrounds and were chosen quantitatively based on an analysis from CDF.

Furthermore, the efficiencies of the cuts on the event selection variables have been studied. The variables are the transverse missing energy \cancel{E}_T , the transverse energy of the highest energetic jet $E_T^{LeadJet}$ and the transverse momentum $P_T^{LeadLep}$ and pseudorapidity $\eta^{LeadLep}$ of the highest energetic lepton. The studies showed that the chosen cut on \cancel{E}_T results in a good suppression of the Z +jets, $Z + b\bar{b}$ +jets and Drell Yan production backgrounds with signal efficiencies below 40%. Moreover, the selected cut on $E_T^{LeadJet}$ affects all backgrounds resulting in signal efficiencies below 60%.

In the presented analysis, the signal is extracted by means of a counting analysis with a data-driven background estimation from specific control regions. The results of the counting analysis performed on pseudo data (with $\mathcal{L} = 50 \text{ pb}^{-1}$) have been presented. The pseudo data were created from the simulated MC data set, assuming either default or modified cross sections for the signal and particular background contributions. All obtained results showed consistence with the expected values within the errors. It has been presented that the results were improved by using pseudo data with higher statistics ($\mathcal{L} = 1 \text{ fb}^{-1}$).

The statistical uncertainties were obtained by a dedicated toy Monte Carlo study. A confidence belt has been constructed, which can be used to determine confidence intervals on the true signal yield. The calculated signal and background yields as a function of the true signal contribution did not show a bias.

Finally, an optimisation of the event selection criteria has been performed using the *TMVA* tool. The study showed that the cut value on \cancel{E}_T has to be increased from 20 GeV to 50 GeV in order to obtain an optimal significance. The cuts on the other variables can be nearly kept. An additional requirement of at least four jets further improved the

5. Summary and outlook

background suppression.

The significances have been also studied including an estimation of the required integrated luminosity \mathcal{L} for a 5σ -discovery as a function of the b' mass $m_{b'}$. The studies with the old event selection criteria that were used before the cut optimisation revealed that for $m_{b'} > 300$ GeV the required luminosity is above 2 fb^{-1} . With the expected data set at the end of the year 2011 ($\mathcal{L} = 1 \text{ fb}^{-1}$) at the LHC, a discovery of a b' would be not possible in the considered scenario. Lower masses of the b' are already excluded from CDF.

This study has been repeated with the new optimised event selection cuts. It was obtained that the required luminosity is less than 1 fb^{-1} for $m_{b'} \leq 350$ GeV. In this case, a discovery could be possible with the data set taken until the end of 2011 at the LHC.

Some results of the analysis showed a lack of statistics in some of the simulated samples (especially W +jets and $b\bar{b}$ jets). Thus, larger simulated MC data sets or another estimation method for these backgrounds are needed.

A large contribution to the final states of same-sign charged dileptons is caused by the $t\bar{t}$ background due to misidentified muons. Therefore, a more detailed study of the muon selection cuts is needed which could lead to a reduction of the $t\bar{t}$ background resulting in an improved significance.

Several systematic uncertainties have to be studied, which can have an impact on the analysis. For instance, the selected PDF set in the creation of the MC samples influences the simulated collision events. Choosing other PDF sets could result in different kinematics of the produced final state particles and therefore result in different event yields after applying the particle and event selection criteria.

The studies should be continued by performing the counting analysis on data taken at the LHC. The signal and the search limits can then be studied as a function of the CKM parameters. Moreover, the obtained results can be compared to the results of a Likelihood fit performed on the data set, in order to achieve an identification of the measured signal.

In the counting analysis the backgrounds are controlled by calculating ratios between the measured events on data and the expected events obtained from the MC samples. If the measured distributions for the jet multiplicity N_{Jets} are inconsistent to the expected MC distributions, this could be either considered in an enhancement of the uncertainties for the yields or in a bin-wise calculation of the control ratios.

A. MC samples

A. MC samples

Process	MC sample	\mathcal{L} [pb^{-1}]	Number of events
$b' \text{ (350)} \rightarrow t$	mc09_7TeV.105319.Pythia_d4PairToWtWbbar_350_1LepIncl.merge.AOD.e526_s765_s767_r1302_r1306	177610.92	149726
$t' \text{ (350)} \rightarrow q$	mc09_7TeV.105304.Pythia_u4PairToWqWbbar_350_1LepIncl.merge.AOD.e526_s765_s767_r1302_r1306	4122262.25	149803
$t' \text{ (350)} \rightarrow b$	mc09_7TeV.105305.Pythia_u4PairToWbWbbar_350_1LepIncl.merge.AOD.e526_s765_s767_r1302_r1306	137452.89	148823
$t' \text{ (440)} \rightarrow b'$	mc09_7TeV.105318.Pythia_u4PairToWd4Wd4bar_440_1LepIncl.merge.AOD.e526_s765_s767_r1302_r1306	86971.68	9980
$t\bar{t}$	mc09_7TeV.105860.TTbar_PowHeg_JimmyPythia.merge.AOD.e540_s765_s767_r1302_r1306	2526.38	199882
$t\bar{t}$ FullHad	mc09_7TeV.107941.TTbar_FullHad_JimmyPythia.merge.AOD.e540_s765_s767_r1302_r1306	2248.08	149841
Zee np0	mc09_7TeV.107650.AlpgenJimmyZeeNp0_pt20.merge.AOD.e529_s765_s767_r1302_r1306	452.06	299217
Zee np1	mc09_7TeV.107651.AlpgenJimmyZeeNp1_pt20.merge.AOD.e529_s765_s767_r1302_r1306	475.92	63440
Zee np2	mc09_7TeV.107652.AlpgenJimmyZeeNp2_pt20.merge.AOD.e529_s765_s767_r1302_r1306	483.80	19497
Zee np3	mc09_7TeV.107653.AlpgenJimmyZeeNp3_pt20.merge.AOD.e529_s765_s767_r1302_r1306	490.98	5499
Zee np4	mc09_7TeV.107654.AlpgenJimmyZeeNp4_pt20.merge.AOD.e529_s765_s767_r1302_r1306	555.19	1499
Zee np5	mc09_7TeV.107655.AlpgenJimmyZeeNp5_pt20.merge.AOD.e529_s765_s767_r1302_r1306	625.00	500
Zμμ np0	mc09_7TeV.107660.AlpgenJimmyZmuNp0_pt20.merge.AOD.e529_s765_s767_r1302_r1306	462.14	303947
Zμμ np1	mc09_7TeV.107661.AlpgenJimmyZmuNp1_pt20.merge.AOD.e529_s765_s767_r1302_r1306	474.37	62996
Zμμ np2	mc09_7TeV.107662.AlpgenJimmyZmuNp2_pt20.merge.AOD.e529_s765_s767_r1302_r1306	479.62	18993
Zμμ np3	mc09_7TeV.107663.AlpgenJimmyZmuNp3_pt20.merge.AOD.e529_s765_s767_r1302_r1306	495.23	5497
Zμμ np4	mc09_7TeV.107664.AlpgenJimmyZmuNp4_pt20.merge.AOD.e529_s765_s767_r1302_r1306	535.36	1499
Zμμ np5	mc09_7TeV.107665.AlpgenJimmyZmuNp5_pt20.merge.AOD.e529_s765_s767_r1302_r1306	623.75	499
Zττ np0	mc09_7TeV.107670.AlpgenJimmyZtautauNp0_pt20.merge.AOD.e529_s765_s767_r1302_r1306	461.45	303359
Zττ np1	mc09_7TeV.107671.AlpgenJimmyZtautauNp1_pt20.merge.AOD.e529_s765_s767_r1302_r1306	477.30	63481
Zττ np2	mc09_7TeV.107672.AlpgenJimmyZtautauNp2_pt20.merge.AOD.e529_s765_s767_r1302_r1306	482.48	19492
Zττ np3	mc09_7TeV.107673.AlpgenJimmyZtautauNp3_pt20.merge.AOD.e529_s765_s767_r1302_r1306	499.73	5497
Zττ np4	mc09_7TeV.107674.AlpgenJimmyZtautauNp4_pt20.merge.AOD.e529_s765_s767_r1302_r1306	516.90	1499
Zττ np5	mc09_7TeV.107675.AlpgenJimmyZtautauNp5_pt20.merge.AOD.e529_s765_s767_r1302_r1306	712.86	499
Zee bb np0	mc09_7TeV.109300.AlpgenJimmyZeebbNp0_nofilter.merge.AOD.e539_s765_s767_r1302_r1306	23770.08	149925
Zee bb np1	mc09_7TeV.109301.AlpgenJimmyZeebbNp1_nofilter.merge.AOD.e539_s765_s767_r1302_r1306	41044.88	99973
Zee bb np2	mc09_7TeV.109302.AlpgenJimmyZeebbNp2_nofilter.merge.AOD.e539_s765_s767_r1302_r1306	47301.87	39989
Zee bb np3	mc09_7TeV.109303.AlpgenJimmyZeebbNp3_nofilter.merge.AOD.e539_s765_s767_r1302_r1306	26085.47	9949
Zμμ bb np0	mc09_7TeV.109305.AlpgenJimmyZmubbNp0_nofilter.merge.AOD.e539_s765_s767_r1302_r1306	23639.78	149968
Zμμ bb np1	mc09_7TeV.109306.AlpgenJimmyZmubbNp1_nofilter.merge.AOD.e539_s765_s767_r1302_r1306	40806.12	99975
Zμμ bb np2	mc09_7TeV.109307.AlpgenJimmyZmubbNp2_nofilter.merge.AOD.e539_s765_s767_r1302_r1306	47300.69	39988
Zμμ bb np3	mc09_7TeV.109308.AlpgenJimmyZmubbNp3_nofilter.merge.AOD.e539_s765_s767_r1302_r1306	26468.10	9997
Zττ bb np0	mc09_7TeV.109310.AlpgenJimmyZtautauNp0_nofilter.merge.AOD.e539_s765_s767_r1302_r1306	23516.09	149821
Zττ bb np1	mc09_7TeV.109311.AlpgenJimmyZtautauNp1_nofilter.merge.AOD.e539_s765_s767_r1302_r1306	41213.04	99921
Zττ bb np2	mc09_7TeV.109312.AlpgenJimmyZtautauNp2_nofilter.merge.AOD.e539_s765_s767_r1302_r1306	46216.62	39982
Zττ bb np3	mc09_7TeV.109313.AlpgenJimmyZtautauNp3_nofilter.merge.AOD.e539_s765_s767_r1302_r1306	26229.34	9996
W eν np0	mc09_7TeV.107680.AlpgenJimmyWenuNp0_pt20.merge.AOD.e511_s765_s767_r1302_r1306	199.89	1381931
W eν np1	mc09_7TeV.107681.AlpgenJimmyWenuNp1_pt20.merge.AOD.e511_s765_s767_r1302_r1306	199.85	258408
W eν np2	mc09_7TeV.107682.AlpgenJimmyWenuNp2_pt20.merge.AOD.e511_s765_s767_r1302_r1306	500.92	188896
W eν np3	mc09_7TeV.107683.AlpgenJimmyWenuNp3_pt20.merge.AOD.e511_s765_s767_r1302_r1306	500.27	50477
W eν np4	mc09_7TeV.107684.AlpgenJimmyWenuNp4_pt20.merge.AOD.e511_s765_s767_r1302_r1306	513.48	12991
W eν np5	mc09_7TeV.107685.AlpgenJimmyWenuNp5_pt20.merge.AOD.e511_s765_s767_r1302_r1306	499.86	3449
W μν np0	mc09_7TeV.107690.AlpgenJimmyWmunuNp0_pt20.merge.AOD.e511_s765_s767_r1302_r1306	199.85	1386038
W μν np1	mc09_7TeV.107691.AlpgenJimmyWmunuNp1_pt20.merge.AOD.e511_s765_s767_r1302_r1306	199.74	255909
W μν np2	mc09_7TeV.107692.AlpgenJimmyWmunuNp2_pt20.merge.AOD.e511_s765_s767_r1302_r1306	500.56	187860
W μν np3	mc09_7TeV.107693.AlpgenJimmyWmunuNp3_pt20.merge.AOD.e511_s765_s767_r1302_r1306	503.33	50887
W μν np4	mc09_7TeV.107694.AlpgenJimmyWmunuNp4_pt20.merge.AOD.e511_s765_s767_r1302_r1306	505.49	12991
W μν np5	mc09_7TeV.107695.AlpgenJimmyWmunuNp5_pt20.merge.AOD.e511_s765_s767_r1302_r1306	499.71	3498
W τν np0	mc09_7TeV.107700.AlpgenJimmyWtaunuNp0_pt20.merge.AOD.e511_s765_s767_r1302_r1306	199.76	1365491
W τν np1	mc09_7TeV.107701.AlpgenJimmyWtaunuNp1_pt20.merge.AOD.e511_s765_s767_r1302_r1306	199.52	254753
W τν np2	mc09_7TeV.107702.AlpgenJimmyWtaunuNp2_pt20.merge.AOD.e511_s765_s767_r1302_r1306	500.39	188446
W τν np3	mc09_7TeV.107703.AlpgenJimmyWtaunuNp3_pt20.merge.AOD.e511_s765_s767_r1302_r1306	500.71	50472
W τν np4	mc09_7TeV.107704.AlpgenJimmyWtaunuNp4_pt20.merge.AOD.e511_s765_s767_r1302_r1306	505.68	12996
W τν np5	mc09_7TeV.107705.AlpgenJimmyWtaunuNp5_pt20.merge.AOD.e511_s765_s767_r1302_r1306	571.14	3998
W bb np0	mc09_7TeV.106280.AlpgenJimmyWbbNp0_pt20.merge.AOD.e524_s765_s767_r1302_r1306	2030.94	6499

Wbb np1	mc09_7TeV.106281.AlpgenJimmyWbBnp1_pt20.merge.AOD.e524_s765_s767_r1302_r1306	2115.38	5500
Wbb np2	mc09_7TeV.106282.AlpgenJimmyWbBnp2_pt20.merge.AOD.e524_s765_s767_r1302_r1306	2140.71	2997
Wbb np3	mc09_7TeV.106283.AlpgenJimmyWbBnp3_pt20.merge.AOD.e524_s765_s767_r1302_r1306	2500.00	1500
tchannel ev	mc09_7TeV.108340.st_tchan_enu_McAtNlo_Jimmy.merge.AOD.e508_s765_s767_r1302_r1306	831.24	5945
tchannel mu	mc09_7TeV.108341.st_tchan_mumu_McAtNlo_Jimmy.merge.AOD.e508_s765_s767_r1302_r1306	833.75	5983
tchannel tau	mc09_7TeV.108342.st_tchan_tauunu_McAtNlo_Jimmy.merge.AOD.e508_s765_s767_r1302_r1306	831.65	5928
schannel ev	mc09_7TeV.108343.st_schan_enu_McAtNlo_Jimmy.merge.AOD.e534_s765_s767_r1302_r1306	17980.79	8424
schannel mu	mc09_7TeV.108344.st_schan_mumu_McAtNlo_Jimmy.merge.AOD.e534_s765_s767_r1302_r1306	18001.71	8432
schannel tau	mc09_7TeV.108345.st_schan_tauunu_McAtNlo_Jimmy.merge.AOD.e534_s765_s767_r1302_r1306	18042.55	8480
Wtchannel	mc09_7TeV.108346.st_Wt_McAtNlo_Jimmy.merge.AOD.e508_s765_s767_r1302_r1306	910.57	13277
WWlnh np0	mc09_7TeV.107100.AlpgenJimmyWWlnhnuNp0.merge.AOD.e536_s765_s767_r1302_r1306	24325.04	49842
WWlnh np1	mc09_7TeV.107101.AlpgenJimmyWWlnhnuNp1.merge.AOD.e536_s765_s767_r1302_r1306	25324.21	24995
WWlnh np2	mc09_7TeV.107102.AlpgenJimmyWWlnhnuNp2.merge.AOD.e536_s765_s767_r1302_r1306	34004.54	14996
WWlnh np3	mc09_7TeV.107103.AlpgenJimmyWWlnhnuNp3.merge.AOD.e536_s765_s767_r1302_r1306	56162.92	9997
WZincl np0	mc09_7TeV.107104.AlpgenJimmyWZinclNp0.merge.AOD.e536_s765_s767_r1302_r1306	22588.86	14999
WZincl np1	mc09_7TeV.107105.AlpgenJimmyWZinclNp1.merge.AOD.e536_s765_s767_r1302_r1306	25052.63	9996
WZincl np2	mc09_7TeV.107106.AlpgenJimmyWZinclNp2.merge.AOD.e536_s765_s767_r1302_r1306	22601.81	4995
WZincl np3	mc09_7TeV.107107.AlpgenJimmyWZinclNp3.merge.AOD.e536_s765_s767_r1302_r1306	53731.18	4997
ZZincl np0	mc09_7TeV.107108.AlpgenJimmyZZinclNp0.merge.AOD.e536_s765_s767_r1302_r1306	20236.84	9997
ZZincl np1	mc09_7TeV.107109.AlpgenJimmyZZinclNp1.merge.AOD.e536_s765_s767_r1302_r1306	20000.00	4500
ZZincl np2	mc09_7TeV.107110.AlpgenJimmyZZinclNp2.merge.AOD.e536_s765_s767_r1302_r1306	56738.64	4993
ZZincl np3	mc09_7TeV.107111.AlpgenJimmyZZinclNp3.merge.AOD.e536_s765_s767_r1302_r1306	89214.28	2498
DrellYan ee	mc09_7TeV.108320.PythiaDrellYan_ee.merge.AOD.e518_s765_s767_r1302_r1306	814.48	999969
DrellYan mu	mc09_7TeV.108319.PythiaDrellYan_mumu.merge.AOD.e518_s765_s767_r1302_r1306	784.77	999503
bbjets np0 j1x	mc09_7TeV.113159.AlpgenJimmyBBjetsNp0_J1x.merge.AOD.e530_s765_s767_r1302_r1306	0.01	10000
bbjets np0 j2	mc09_7TeV.113160.AlpgenJimmyBBjetsNp0_J2.merge.AOD.e530_s765_s767_r1302_r1306	0.17	9998
bbjets np0 j3	mc09_7TeV.113161.AlpgenJimmyBBjetsNp0_J3.merge.AOD.e530_s765_s767_r1302_r1306	4.65	9944
bbjets np0 j4	mc09_7TeV.113162.AlpgenJimmyBBjetsNp0_J4.merge.AOD.e530_s765_s767_r1302_r1306	206.68	9993
bbjets np0 j5p	mc09_7TeV.113163.AlpgenJimmyBBjetsNp0_J5p.merge.AOD.e530_s765_s767_r1302_r1306	2046.13	1996
bbjets np1 j1x	mc09_7TeV.113164.AlpgenJimmyBBjetsNp1_J1x.merge.AOD.e530_s765_s767_r1302_r1306	0.03	9899
bbjets np1 j2	mc09_7TeV.113165.AlpgenJimmyBBjetsNp1_J2.merge.AOD.e530_s765_s767_r1302_r1306	0.05	9898
bbjets np1 j3	mc09_7TeV.113166.AlpgenJimmyBBjetsNp1_J3.merge.AOD.e530_s765_s767_r1302_r1306	0.75	9997
bbjets np1 j4	mc09_7TeV.113167.AlpgenJimmyBBjetsNp1_J4.merge.AOD.e530_s765_s767_r1302_r1306	25.16	9992
bbjets np1 j5p	mc09_7TeV.113168.AlpgenJimmyBBjetsNp1_J5p.merge.AOD.e530_s765_s767_r1302_r1306	288.92	1999
bbjets np2 j1x	mc09_7TeV.113169.AlpgenJimmyBBjetsNp2_J1x.merge.AOD.e530_s765_s767_r1302_r1306	0.15	9995
bbjets np2 j2	mc09_7TeV.113170.AlpgenJimmyBBjetsNp2_J2.merge.AOD.e530_s765_s767_r1302_r1306	0.13	9995
bbjets np2 j3	mc09_7TeV.113171.AlpgenJimmyBBjetsNp2_J3.merge.AOD.e530_s765_s767_r1302_r1306	0.74	9999
bbjets np2 j4	mc09_7TeV.113172.AlpgenJimmyBBjetsNp2_J4.merge.AOD.e530_s765_s767_r1302_r1306	13.97	9992
bbjets np2 j5p	mc09_7TeV.113173.AlpgenJimmyBBjetsNp2_J5p.merge.AOD.e530_s765_s767_r1302_r1306	118.16	1998
bbjets np3 j1x	mc09_7TeV.113174.AlpgenJimmyBBjetsNp3_J1x.merge.AOD.e530_s765_s767_r1302_r1306	1.01	9997
bbjets np3 j2	mc09_7TeV.113175.AlpgenJimmyBBjetsNp3_J2.merge.AOD.e530_s765_s767_r1302_r1306	0.43	9996
bbjets np3 j3	mc09_7TeV.113176.AlpgenJimmyBBjetsNp3_J3.merge.AOD.e530_s765_s767_r1302_r1306	1.33	9994
bbjets np3 j4	mc09_7TeV.113177.AlpgenJimmyBBjetsNp3_J4.merge.AOD.e530_s765_s767_r1302_r1306	17.70	9996
bbjets np3 j5p	mc09_7TeV.113178.AlpgenJimmyBBjetsNp3_J5p.merge.AOD.e530_s765_s767_r1302_r1306	103.90	1999
bbjets np4 j1x	mc09_7TeV.113179.AlpgenJimmyBBjetsNp4_J1x.merge.AOD.e530_s765_s767_r1302_r1306	7.19	10000
bbjets np4 j2	mc09_7TeV.113180.AlpgenJimmyBBjetsNp4_J2.merge.AOD.e530_s765_s767_r1302_r1306	1.47	9996
bbjets np4 j3	mc09_7TeV.113181.AlpgenJimmyBBjetsNp4_J3.merge.AOD.e530_s765_s767_r1302_r1306	2.49	9996
bbjets np4 j4	mc09_7TeV.113182.AlpgenJimmyBBjetsNp4_J4.merge.AOD.e530_s765_s767_r1302_r1306	17.37	9993
bbjets np4 j5p	mc09_7TeV.113183.AlpgenJimmyBBjetsNp4_J5p.merge.AOD.e530_s765_s767_r1302_r1306	37.43	1000

Table A.1.: Monte-Carlo samples used in the analysis. For each process/sample, the number of produced events and the corresponding integrated luminosity \mathcal{L} are given.

B. Cut efficiencies and event yields

B.1. Generator

B.1.1. Event numbers

Sample	Generated events	After filter	EF_e10_medium OR EF_mu10i_loose
$b'(350\text{GeV}) \rightarrow t$	$1.96 \cdot 10^5 \pm 443$	$1.5 \cdot 10^5 \pm 387$	$1.04 \cdot 10^5 \pm 323$
$t'(350\text{GeV}) \rightarrow q$	$3.26 \cdot 10^5 \pm 571$	$1.5 \cdot 10^5 \pm 387$	$1.08 \cdot 10^5 \pm 329$
$t'(350\text{GeV}) \rightarrow b$	$2.22 \cdot 10^5 \pm 472$	$1.49 \cdot 10^5 \pm 386$	$7.72 \cdot 10^4 \pm 278$
$t'(440\text{GeV}) \rightarrow b'$	$1.16 \cdot 10^4 \pm 108$	$9.98 \cdot 10^3 \pm 99.9$	$7.46 \cdot 10^3 \pm 86.4$
$t\bar{t}$	$3.65 \cdot 10^5 \pm 604$	$2 \cdot 10^5 \pm 447$	$1.17 \cdot 10^5 \pm 342$
$t\bar{t}$ FullHad	$3.28 \cdot 10^5 \pm 573$	$1.5 \cdot 10^5 \pm 387$	$7.01 \cdot 10^3 \pm 83.7$
$\sum t\bar{t}$	$6.93 \cdot 10^5 \pm 832$	$3.5 \cdot 10^5 \pm 591$	$1.24 \cdot 10^5 \pm 352$
Zee np0	$2.99 \cdot 10^5 \pm 547$	$2.99 \cdot 10^5 \pm 547$	$2.39 \cdot 10^5 \pm 489$
Zee np1	$6.34 \cdot 10^4 \pm 252$	$6.34 \cdot 10^4 \pm 252$	$5.46 \cdot 10^4 \pm 234$
Zee np2	$1.95 \cdot 10^4 \pm 140$	$1.95 \cdot 10^4 \pm 140$	$1.7 \cdot 10^4 \pm 131$
Zee np3	$5.5 \cdot 10^3 \pm 74.2$	$5.5 \cdot 10^3 \pm 74.2$	$4.88 \cdot 10^3 \pm 69.9$
Zee np4	$1.5 \cdot 10^3 \pm 38.7$	$1.5 \cdot 10^3 \pm 38.7$	$1.34 \cdot 10^3 \pm 36.6$
Zee np5	500 ± 22.4	500 ± 22.4	441 ± 21
$Z\mu\mu$ np0	$3.04 \cdot 10^5 \pm 551$	$3.04 \cdot 10^5 \pm 551$	$2.31 \cdot 10^5 \pm 481$
$Z\mu\mu$ np1	$6.3 \cdot 10^4 \pm 251$	$6.3 \cdot 10^4 \pm 251$	$5.1 \cdot 10^4 \pm 226$
$Z\mu\mu$ np2	$1.9 \cdot 10^4 \pm 138$	$1.9 \cdot 10^4 \pm 138$	$1.54 \cdot 10^4 \pm 124$
$Z\mu\mu$ np3	$5.5 \cdot 10^3 \pm 74.1$	$5.5 \cdot 10^3 \pm 74.1$	$4.56 \cdot 10^3 \pm 67.5$
$Z\mu\mu$ np4	$1.5 \cdot 10^3 \pm 38.7$	$1.5 \cdot 10^3 \pm 38.7$	$1.22 \cdot 10^3 \pm 34.9$
$Z\mu\mu$ np5	499 ± 22.3	499 ± 22.3	383 ± 19.6
$Z\tau\tau$ np0	$3.03 \cdot 10^5 \pm 551$	$3.03 \cdot 10^5 \pm 551$	$5.73 \cdot 10^4 \pm 239$
$Z\tau\tau$ np1	$6.35 \cdot 10^4 \pm 252$	$6.35 \cdot 10^4 \pm 252$	$1.49 \cdot 10^4 \pm 122$
$Z\tau\tau$ np2	$1.95 \cdot 10^4 \pm 140$	$1.95 \cdot 10^4 \pm 140$	$5 \cdot 10^3 \pm 70.7$
$Z\tau\tau$ np3	$5.5 \cdot 10^3 \pm 74.1$	$5.5 \cdot 10^3 \pm 74.1$	$1.49 \cdot 10^3 \pm 38.6$
$Z\tau\tau$ np4	$1.5 \cdot 10^3 \pm 38.7$	$1.5 \cdot 10^3 \pm 38.7$	432 ± 20.8
$Z\tau\tau$ np5	499 ± 22.3	499 ± 22.3	154 ± 12.4
$\sum Z+\text{jets}$	$1.18 \cdot 10^6 \pm 1.08 \cdot 10^3$	$1.18 \cdot 10^6 \pm 1.08 \cdot 10^3$	$7.01 \cdot 10^5 \pm 837$
$Zee+b\bar{b}$ np0	$1.5 \cdot 10^5 \pm 387$	$1.5 \cdot 10^5 \pm 387$	$1.36 \cdot 10^5 \pm 368$
$Zee+b\bar{b}$ np1	$1 \cdot 10^5 \pm 316$	$1 \cdot 10^5 \pm 316$	$9.06 \cdot 10^4 \pm 301$
$Zee+b\bar{b}$ np2	$4 \cdot 10^4 \pm 200$	$4 \cdot 10^4 \pm 200$	$3.62 \cdot 10^4 \pm 190$

B. Cut efficiencies and event yields

$Zee+b\bar{b}$ np3	$9.95 \cdot 10^3 \pm 99.7$	$9.95 \cdot 10^3 \pm 99.7$	$9.01 \cdot 10^3 \pm 94.9$
$Z\mu\mu+b\bar{b}$ np0	$1.5 \cdot 10^5 \pm 387$	$1.5 \cdot 10^5 \pm 387$	$1.28 \cdot 10^5 \pm 358$
$Z\mu\mu+b\bar{b}$ np1	$1 \cdot 10^5 \pm 316$	$1 \cdot 10^5 \pm 316$	$8.39 \cdot 10^4 \pm 290$
$Z\mu\mu+b\bar{b}$ np2	$4 \cdot 10^4 \pm 200$	$4 \cdot 10^4 \pm 200$	$3.32 \cdot 10^4 \pm 182$
$Z\mu\mu+b\bar{b}$ np3	$1 \cdot 10^4 \pm 100$	$1 \cdot 10^4 \pm 100$	$8.24 \cdot 10^3 \pm 90.8$
$Z\tau\tau+b\bar{b}$ np0	$1.5 \cdot 10^5 \pm 387$	$1.5 \cdot 10^5 \pm 387$	$3.59 \cdot 10^4 \pm 189$
$Z\tau\tau+b\bar{b}$ np1	$9.99 \cdot 10^4 \pm 316$	$9.99 \cdot 10^4 \pm 316$	$2.64 \cdot 10^4 \pm 163$
$Z\tau\tau+b\bar{b}$ np2	$4 \cdot 10^4 \pm 200$	$4 \cdot 10^4 \pm 200$	$1.12 \cdot 10^4 \pm 106$
$Z\tau\tau+b\bar{b}$ np3	$1 \cdot 10^4 \pm 100$	$1 \cdot 10^4 \pm 100$	$2.93 \cdot 10^3 \pm 54.1$
$\sum Z + b\bar{b}+\text{jets}$	$8.99 \cdot 10^5 \pm 948$	$8.99 \cdot 10^5 \pm 948$	$6.01 \cdot 10^5 \pm 775$
$W e\nu$ np0	$1.38 \cdot 10^6 \pm 1.18 \cdot 10^3$	$1.38 \cdot 10^6 \pm 1.18 \cdot 10^3$	$8.35 \cdot 10^5 \pm 914$
$W e\nu$ np1	$2.58 \cdot 10^5 \pm 508$	$2.58 \cdot 10^5 \pm 508$	$1.72 \cdot 10^5 \pm 415$
$W e\nu$ np2	$1.89 \cdot 10^5 \pm 435$	$1.89 \cdot 10^5 \pm 435$	$1.28 \cdot 10^5 \pm 358$
$W e\nu$ np3	$5.05 \cdot 10^4 \pm 225$	$5.05 \cdot 10^4 \pm 225$	$3.49 \cdot 10^4 \pm 187$
$W e\nu$ np4	$1.3 \cdot 10^4 \pm 114$	$1.3 \cdot 10^4 \pm 114$	$9.08 \cdot 10^3 \pm 95.3$
$W e\nu$ np5	$3.45 \cdot 10^3 \pm 58.7$	$3.45 \cdot 10^3 \pm 58.7$	$2.43 \cdot 10^3 \pm 49.3$
$W \mu\nu$ np0	$1.39 \cdot 10^6 \pm 1.18 \cdot 10^3$	$1.39 \cdot 10^6 \pm 1.18 \cdot 10^3$	$7.52 \cdot 10^5 \pm 867$
$W \mu\nu$ np1	$2.56 \cdot 10^5 \pm 506$	$2.56 \cdot 10^5 \pm 506$	$1.48 \cdot 10^5 \pm 385$
$W \mu\nu$ np2	$1.88 \cdot 10^5 \pm 433$	$1.88 \cdot 10^5 \pm 433$	$1.09 \cdot 10^5 \pm 331$
$W \mu\nu$ np3	$5.09 \cdot 10^4 \pm 226$	$5.09 \cdot 10^4 \pm 226$	$2.97 \cdot 10^4 \pm 172$
$W \mu\nu$ np4	$1.3 \cdot 10^4 \pm 114$	$1.3 \cdot 10^4 \pm 114$	$7.51 \cdot 10^3 \pm 86.7$
$W \mu\nu$ np5	$3.5 \cdot 10^3 \pm 59.1$	$3.5 \cdot 10^3 \pm 59.1$	$1.94 \cdot 10^3 \pm 44.1$
$W \tau\nu$ np0	$1.37 \cdot 10^6 \pm 1.17 \cdot 10^3$	$1.37 \cdot 10^6 \pm 1.17 \cdot 10^3$	$1.29 \cdot 10^5 \pm 360$
$W \tau\nu$ np1	$2.55 \cdot 10^5 \pm 505$	$2.55 \cdot 10^5 \pm 505$	$3.09 \cdot 10^4 \pm 176$
$W \tau\nu$ np2	$1.88 \cdot 10^5 \pm 434$	$1.88 \cdot 10^5 \pm 434$	$2.47 \cdot 10^4 \pm 157$
$W \tau\nu$ np3	$5.05 \cdot 10^4 \pm 225$	$5.05 \cdot 10^4 \pm 225$	$7.21 \cdot 10^3 \pm 84.9$
$W \tau\nu$ np4	$1.3 \cdot 10^4 \pm 114$	$1.3 \cdot 10^4 \pm 114$	$1.94 \cdot 10^3 \pm 44.1$
$W \tau\nu$ np5	$4 \cdot 10^3 \pm 63.2$	$4 \cdot 10^3 \pm 63.2$	588 ± 24.2
$\sum W + \text{jets}$	$5.67 \cdot 10^6 \pm 2.38 \cdot 10^3$	$5.67 \cdot 10^6 \pm 2.38 \cdot 10^3$	$2.43 \cdot 10^6 \pm 1.56 \cdot 10^3$
$W + b\bar{b}$ np0	$6.5 \cdot 10^3 \pm 80.6$	$6.5 \cdot 10^3 \pm 80.6$	$3.32 \cdot 10^3 \pm 57.6$
$W + b\bar{b}$ np1	$5.5 \cdot 10^3 \pm 74.2$	$5.5 \cdot 10^3 \pm 74.2$	$2.7 \cdot 10^3 \pm 52$
$W + b\bar{b}$ np2	$3 \cdot 10^3 \pm 54.7$	$3 \cdot 10^3 \pm 54.7$	$1.46 \cdot 10^3 \pm 38.2$
$W + b\bar{b}$ np3	$1.5 \cdot 10^3 \pm 38.7$	$1.5 \cdot 10^3 \pm 38.7$	755 ± 27.5
$\sum W + b\bar{b}+\text{jets}$	$1.65 \cdot 10^4 \pm 128$	$1.65 \cdot 10^4 \pm 128$	$8.24 \cdot 10^3 \pm 90.8$
tchannel $e\nu$	$5.94 \cdot 10^3 \pm 77.1$	$5.94 \cdot 10^3 \pm 77.1$	$4.66 \cdot 10^3 \pm 68.3$
tchannel $\mu\nu$	$5.98 \cdot 10^3 \pm 77.3$	$5.98 \cdot 10^3 \pm 77.3$	$3.92 \cdot 10^3 \pm 62.6$
tchannel $\tau\nu$	$5.93 \cdot 10^3 \pm 77$	$5.93 \cdot 10^3 \pm 77$	907 ± 30.1
schannel $e\nu$	$8.42 \cdot 10^3 \pm 91.8$	$8.42 \cdot 10^3 \pm 91.8$	$6.52 \cdot 10^3 \pm 80.8$
schannel $\mu\nu$	$8.43 \cdot 10^3 \pm 91.8$	$8.43 \cdot 10^3 \pm 91.8$	$5.44 \cdot 10^3 \pm 73.7$
schannel $\tau\nu$	$8.48 \cdot 10^3 \pm 92.1$	$8.48 \cdot 10^3 \pm 92.1$	$1.38 \cdot 10^3 \pm 37.2$

Wtchannel	$1.33 \cdot 10^4 \pm 115$	$1.33 \cdot 10^4 \pm 115$	$4.69 \cdot 10^3 \pm 68.5$
\sum sg top	$5.65 \cdot 10^4 \pm 238$	$5.65 \cdot 10^4 \pm 238$	$2.75 \cdot 10^4 \pm 166$
WWlnln np0	$4.98 \cdot 10^4 \pm 223$	$4.98 \cdot 10^4 \pm 223$	$3.69 \cdot 10^4 \pm 192$
WWlnln np1	$2.5 \cdot 10^4 \pm 158$	$2.5 \cdot 10^4 \pm 158$	$1.89 \cdot 10^4 \pm 137$
WWlnln np2	$1.5 \cdot 10^4 \pm 122$	$1.5 \cdot 10^4 \pm 122$	$1.16 \cdot 10^4 \pm 108$
WWlnln np3	$1 \cdot 10^4 \pm 100$	$1 \cdot 10^4 \pm 100$	$7.74 \cdot 10^3 \pm 87.9$
WZincll np0	$1.5 \cdot 10^4 \pm 122$	$1.5 \cdot 10^4 \pm 122$	$1.1 \cdot 10^4 \pm 105$
WZincll np1	$1 \cdot 10^4 \pm 100$	$1 \cdot 10^4 \pm 100$	$7.44 \cdot 10^3 \pm 86.2$
WZincll np2	$5 \cdot 10^3 \pm 70.7$	$5 \cdot 10^3 \pm 70.7$	$3.74 \cdot 10^3 \pm 61.2$
WZincll np3	$5 \cdot 10^3 \pm 70.7$	$5 \cdot 10^3 \pm 70.7$	$3.86 \cdot 10^3 \pm 62.1$
ZZincll np0	$1 \cdot 10^4 \pm 100$	$1 \cdot 10^4 \pm 100$	$7.07 \cdot 10^3 \pm 84.1$
ZZincll np1	$4.5 \cdot 10^3 \pm 67.1$	$4.5 \cdot 10^3 \pm 67.1$	$3.22 \cdot 10^3 \pm 56.7$
ZZincll np2	$4.99 \cdot 10^3 \pm 70.7$	$4.99 \cdot 10^3 \pm 70.7$	$3.66 \cdot 10^3 \pm 60.5$
ZZincll np3	$2.5 \cdot 10^3 \pm 50$	$2.5 \cdot 10^3 \pm 50$	$1.8 \cdot 10^3 \pm 42.4$
\sum diboson	$1.57 \cdot 10^5 \pm 396$	$1.57 \cdot 10^5 \pm 396$	$1.17 \cdot 10^5 \pm 342$
DrellYan ee	$1 \cdot 10^6 \pm 1 \cdot 10^3$	$1 \cdot 10^6 \pm 1 \cdot 10^3$	$2.33 \cdot 10^5 \pm 483$
DrellYan $\mu\mu$	$1 \cdot 10^6 \pm 1 \cdot 10^3$	$1 \cdot 10^6 \pm 1 \cdot 10^3$	$2.56 \cdot 10^5 \pm 506$
\sum DrellYan	$2 \cdot 10^6 \pm 1.41 \cdot 10^3$	$2 \cdot 10^6 \pm 1.41 \cdot 10^3$	$4.89 \cdot 10^5 \pm 700$
$b\bar{b}$ jets np0 j1x	$1 \cdot 10^4 \pm 100$	$1 \cdot 10^4 \pm 100$	90 ± 9.49
$b\bar{b}$ jets np0 j2	$1 \cdot 10^4 \pm 100$	$1 \cdot 10^4 \pm 100$	357 ± 18.9
$b\bar{b}$ jets np0 j3	$9.94 \cdot 10^3 \pm 99.7$	$9.94 \cdot 10^3 \pm 99.7$	222 ± 14.9
$b\bar{b}$ jets np0 j4	$9.99 \cdot 10^3 \pm 100$	$9.99 \cdot 10^3 \pm 100$	112 ± 10.6
$b\bar{b}$ jets np0 j5p	$2 \cdot 10^3 \pm 44.7$	$2 \cdot 10^3 \pm 44.7$	12 ± 3.46
$b\bar{b}$ jets np1 j1x	$9.9 \cdot 10^3 \pm 99.5$	$9.9 \cdot 10^3 \pm 99.5$	129 ± 11.4
$b\bar{b}$ jets np1 j2	$9.9 \cdot 10^3 \pm 99.5$	$9.9 \cdot 10^3 \pm 99.5$	232 ± 15.2
$b\bar{b}$ jets np1 j3	$1 \cdot 10^4 \pm 100$	$1 \cdot 10^4 \pm 100$	282 ± 16.8
$b\bar{b}$ jets np1 j4	$9.99 \cdot 10^3 \pm 100$	$9.99 \cdot 10^3 \pm 100$	231 ± 15.2
$b\bar{b}$ jets np1 j5p	$2 \cdot 10^3 \pm 44.7$	$2 \cdot 10^3 \pm 44.7$	27 ± 5.2
$b\bar{b}$ jets np2 j1x	$1 \cdot 10^4 \pm 100$	$1 \cdot 10^4 \pm 100$	111 ± 10.5
$b\bar{b}$ jets np2 j2	$1 \cdot 10^4 \pm 100$	$1 \cdot 10^4 \pm 100$	231 ± 15.2
$b\bar{b}$ jets np2 j3	$1 \cdot 10^4 \pm 100$	$1 \cdot 10^4 \pm 100$	296 ± 17.2
$b\bar{b}$ jets np2 j4	$9.99 \cdot 10^3 \pm 100$	$9.99 \cdot 10^3 \pm 100$	222 ± 14.9
$b\bar{b}$ jets np2 j5p	$2 \cdot 10^3 \pm 44.7$	$2 \cdot 10^3 \pm 44.7$	60 ± 7.75
$b\bar{b}$ jets np3 j1x	$1 \cdot 10^4 \pm 100$	$1 \cdot 10^4 \pm 100$	134 ± 11.6
$b\bar{b}$ jets np3 j2	$1 \cdot 10^4 \pm 100$	$1 \cdot 10^4 \pm 100$	235 ± 15.3
$b\bar{b}$ jets np3 j3	$9.99 \cdot 10^3 \pm 100$	$9.99 \cdot 10^3 \pm 100$	307 ± 17.5
$b\bar{b}$ jets np3 j4	$1 \cdot 10^4 \pm 100$	$1 \cdot 10^4 \pm 100$	285 ± 16.9
$b\bar{b}$ jets np3 j5p	$2 \cdot 10^3 \pm 44.7$	$2 \cdot 10^3 \pm 44.7$	65 ± 8.06
$b\bar{b}$ jets np4 j1x	$1 \cdot 10^4 \pm 100$	$1 \cdot 10^4 \pm 100$	159 ± 12.6
$b\bar{b}$ jets np4 j2	$1 \cdot 10^4 \pm 100$	$1 \cdot 10^4 \pm 100$	269 ± 16.4

B. Cut efficiencies and event yields

$b\bar{b}$ jets np4 j3	$1 \cdot 10^4 \pm 100$	$1 \cdot 10^4 \pm 100$	330 ± 18.2
$b\bar{b}$ jets np4 j4	$9.99 \cdot 10^3 \pm 100$	$9.99 \cdot 10^3 \pm 100$	304 ± 17.4
$b\bar{b}$ jets np4 j5p	$1 \cdot 10^3 \pm 31.6$	$1 \cdot 10^3 \pm 31.6$	29 ± 5.39
$\sum b\bar{b}$ jets	$2.09 \cdot 10^5 \pm 457$	$2.09 \cdot 10^5 \pm 457$	$4.73 \cdot 10^3 \pm 68.8$

Table B.1.: Number of generated events, events after the filter and events after the trigger used in the simulation.

B.1.2. Efficiencies

Sample	Generated events	After filter	EF_e10_medium OR EF_mu10i_loose	$\epsilon_{\text{Trigger}}$
$b'(350\text{GeV}) \rightarrow t$	$1.96 \cdot 10^5 \pm 443$	$0.76200^{+0.00096}_{-0.00096}$	$0.69683^{+0.00118}_{-0.00119}$	$0.53098^{+0.00112}_{-0.00112}$
$t'(350\text{GeV}) \rightarrow q$	$3.26 \cdot 10^5 \pm 571$	$0.46000^{+0.00087}_{-0.00087}$	$0.72268^{+0.00115}_{-0.00116}$	$0.33243^{+0.00082}_{-0.00082}$
$t'(350\text{GeV}) \rightarrow b$	$2.22 \cdot 10^5 \pm 472$	$0.66900^{+0.00099}_{-0.00100}$	$0.51895^{+0.00129}_{-0.00129}$	$0.34718^{+0.00101}_{-0.00101}$
$t'(440\text{GeV}) \rightarrow b'$	$1.16 \cdot 10^4 \pm 108$	$0.85900^{+0.00322}_{-0.00328}$	$0.74729^{+0.00435}_{-0.00440}$	$0.64193^{+0.00445}_{-0.00448}$
$t\bar{t}$	$3.65 \cdot 10^5 \pm 604$	$0.54800^{+0.00082}_{-0.00082}$	$0.58621^{+0.00110}_{-0.00110}$	$0.32124^{+0.00077}_{-0.00077}$
$t\bar{t}$ FullHad	$3.28 \cdot 10^5 \pm 573$	$0.45700^{+0.00087}_{-0.00087}$	$0.04676^{+0.00055}_{-0.00054}$	$0.02137^{+0.00025}_{-0.00025}$
$\sum t\bar{t}$	$6.93 \cdot 10^5 \pm 832$	$0.50901^{+0.00060}_{-0.00060}$	$0.55577^{+0.00104}_{-0.00104}$	$0.30432^{+0.00073}_{-0.00073}$
Zee np0	$2.99 \cdot 10^5 \pm 547$	$1.00000^{+0.00000}_{-0.00001}$	$0.79916^{+0.00073}_{-0.00073}$	$0.79916^{+0.00073}_{-0.00073}$
Zee np1	$6.34 \cdot 10^4 \pm 252$	$1.00000^{+0.00000}_{-0.00003}$	$0.86003^{+0.00137}_{-0.00138}$	$0.86003^{+0.00137}_{-0.00138}$
Zee np2	$1.95 \cdot 10^4 \pm 140$	$1.00000^{+0.00000}_{-0.00009}$	$0.87372^{+0.00237}_{-0.00241}$	$0.87372^{+0.00237}_{-0.00241}$
Zee np3	$5.5 \cdot 10^3 \pm 74.2$	$1.00000^{+0.00000}_{-0.00033}$	$0.88780^{+0.00425}_{-0.00439}$	$0.88780^{+0.00425}_{-0.00439}$
Zee np4	$1.5 \cdot 10^3 \pm 38.7$	$1.00000^{+0.00000}_{-0.00122}$	$0.89326^{+0.00799}_{-0.00854}$	$0.89326^{+0.00799}_{-0.00854}$
Zee np5	500 ± 22.4	$1.00000^{+0.00000}_{-0.00366}$	$0.88200^{+0.01453}_{-0.01615}$	$0.88200^{+0.01453}_{-0.01615}$
$Z\mu\mu$ np0	$3.04 \cdot 10^5 \pm 551$	$1.00000^{+0.00000}_{-0.00001}$	$0.76132^{+0.00077}_{-0.00077}$	$0.76132^{+0.00077}_{-0.00077}$
$Z\mu\mu$ np1	$6.3 \cdot 10^4 \pm 251$	$1.00000^{+0.00000}_{-0.00003}$	$0.80924^{+0.00156}_{-0.00157}$	$0.80924^{+0.00156}_{-0.00157}$
$Z\mu\mu$ np2	$1.9 \cdot 10^4 \pm 138$	$1.00000^{+0.00000}_{-0.00010}$	$0.81146^{+0.00283}_{-0.00287}$	$0.81146^{+0.00283}_{-0.00287}$
$Z\mu\mu$ np3	$5.5 \cdot 10^3 \pm 74.1$	$1.00000^{+0.00000}_{-0.00033}$	$0.82863^{+0.00508}_{-0.00521}$	$0.82863^{+0.00508}_{-0.00521}$
$Z\mu\mu$ np4	$1.5 \cdot 10^3 \pm 38.7$	$1.00000^{+0.00000}_{-0.00122}$	$0.81388^{+0.01011}_{-0.01054}$	$0.81388^{+0.01011}_{-0.01054}$
$Z\mu\mu$ np5	499 ± 22.3	$1.00000^{+0.00000}_{-0.00367}$	$0.76754^{+0.01923}_{-0.02035}$	$0.76754^{+0.01923}_{-0.02035}$
$Z\tau\tau$ np0	$3.03 \cdot 10^5 \pm 551$	$1.00000^{+0.00000}_{-0.00001}$	$0.18882^{+0.00071}_{-0.00071}$	$0.18882^{+0.00071}_{-0.00071}$
$Z\tau\tau$ np1	$6.35 \cdot 10^4 \pm 252$	$1.00000^{+0.00000}_{-0.00003}$	$0.23448^{+0.00168}_{-0.00168}$	$0.23448^{+0.00168}_{-0.00168}$
$Z\tau\tau$ np2	$1.95 \cdot 10^4 \pm 140$	$1.00000^{+0.00000}_{-0.00009}$	$0.25657^{+0.00315}_{-0.00312}$	$0.25657^{+0.00315}_{-0.00312}$
$Z\tau\tau$ np3	$5.5 \cdot 10^3 \pm 74.1$	$1.00000^{+0.00000}_{-0.00033}$	$0.27124^{+0.00610}_{-0.00601}$	$0.27124^{+0.00610}_{-0.00601}$
$Z\tau\tau$ np4	$1.5 \cdot 10^3 \pm 38.7$	$1.00000^{+0.00000}_{-0.00122}$	$0.28819^{+0.01211}_{-0.01182}$	$0.28819^{+0.01211}_{-0.01182}$
$Z\tau\tau$ np5	499 ± 22.3	$1.00000^{+0.00000}_{-0.00367}$	$0.30862^{+0.02194}_{-0.02115}$	$0.30862^{+0.02194}_{-0.02115}$
$\sum Z + jets$	$1.18 \cdot 10^6 \pm 1.08 \cdot 10^3$	$1.00000^{+0.00000}_{-0.00001}$	$0.72795^{+0.00041}_{-0.00041}$	$0.72795^{+0.00041}_{-0.00041}$
$Zee+b\bar{b}$ np0	$1.5 \cdot 10^5 \pm 387$	$1.00000^{+0.00000}_{-0.00001}$	$0.90394^{+0.00076}_{-0.00076}$	$0.90394^{+0.00076}_{-0.00076}$
$Zee+b\bar{b}$ np1	$1 \cdot 10^5 \pm 316$	$1.00000^{+0.00000}_{-0.00002}$	$0.90660^{+0.00092}_{-0.00092}$	$0.90660^{+0.00092}_{-0.00092}$
$Zee+b\bar{b}$ np2	$4 \cdot 10^4 \pm 200$	$1.00000^{+0.00000}_{-0.00005}$	$0.90560^{+0.00146}_{-0.00148}$	$0.90560^{+0.00146}_{-0.00148}$
$Zee+b\bar{b}$ np3	$9.95 \cdot 10^3 \pm 99.7$	$1.00000^{+0.00000}_{-0.00018}$	$0.90592^{+0.00292}_{-0.00300}$	$0.90592^{+0.00292}_{-0.00300}$
$Z\mu\mu+b\bar{b}$ np0	$1.5 \cdot 10^5 \pm 387$	$1.00000^{+0.00000}_{-0.00001}$	$0.85266^{+0.00091}_{-0.00092}$	$0.85266^{+0.00091}_{-0.00092}$
$Z\mu\mu+b\bar{b}$ np1	$1 \cdot 10^5 \pm 316$	$1.00000^{+0.00000}_{-0.00002}$	$0.83943^{+0.00116}_{-0.00116}$	$0.83943^{+0.00116}_{-0.00116}$
$Z\mu\mu+b\bar{b}$ np2	$4 \cdot 10^4 \pm 200$	$1.00000^{+0.00000}_{-0.00005}$	$0.83072^{+0.00187}_{-0.00189}$	$0.83072^{+0.00187}_{-0.00189}$
$Z\mu\mu+b\bar{b}$ np3	$1 \cdot 10^4 \pm 100$	$1.00000^{+0.00000}_{-0.00018}$	$0.82435^{+0.00380}_{-0.00387}$	$0.82435^{+0.00380}_{-0.00387}$
$Z\tau\tau+b\bar{b}$ np0	$1.5 \cdot 10^5 \pm 387$	$1.00000^{+0.00000}_{-0.00001}$	$0.23951^{+0.00110}_{-0.00110}$	$0.23951^{+0.00110}_{-0.00110}$
$Z\tau\tau+b\bar{b}$ np1	$9.99 \cdot 10^4 \pm 316$	$1.00000^{+0.00000}_{-0.00002}$	$0.26454^{+0.00140}_{-0.00139}$	$0.26454^{+0.00140}_{-0.00139}$
$Z\tau\tau+b\bar{b}$ np2	$4 \cdot 10^4 \pm 200$	$1.00000^{+0.00000}_{-0.00005}$	$0.27985^{+0.00225}_{-0.00224}$	$0.27985^{+0.00225}_{-0.00224}$
$Z\tau\tau+b\bar{b}$ np3	$1 \cdot 10^4 \pm 100$	$1.00000^{+0.00000}_{-0.00018}$	$0.29282^{+0.00460}_{-0.00456}$	$0.29282^{+0.00460}_{-0.00456}$

B. Cut efficiencies and event yields

$\sum Z + b\bar{b}+\text{jets}$	$8.99 \cdot 10^5 \pm 948$	$1.00000^{+0.00000}_{-0.00001}$	$0.79704^{+0.00038}_{-0.00038}$	$0.79704^{+0.00038}_{-0.00038}$
$W_{\nu} \text{ np0}$	$1.38 \cdot 10^6 \pm 1.18 \cdot 10^3$	$1.00000^{+0.00000}_{-0.00000}$	$0.60429^{+0.00041}_{-0.00041}$	$0.60429^{+0.00041}_{-0.00041}$
$W_{\nu} \text{ np1}$	$2.58 \cdot 10^5 \pm 508$	$1.00000^{+0.00000}_{-0.00001}$	$0.66490^{+0.00092}_{-0.00093}$	$0.66490^{+0.00092}_{-0.00093}$
$W_{\nu} \text{ np2}$	$1.89 \cdot 10^5 \pm 435$	$1.00000^{+0.00000}_{-0.00001}$	$0.67908^{+0.00107}_{-0.00107}$	$0.67908^{+0.00107}_{-0.00107}$
$W_{\nu} \text{ np3}$	$5.05 \cdot 10^4 \pm 225$	$1.00000^{+0.00000}_{-0.00004}$	$0.69127^{+0.00205}_{-0.00206}$	$0.69127^{+0.00205}_{-0.00206}$
$W_{\nu} \text{ np4}$	$1.3 \cdot 10^4 \pm 114$	$1.00000^{+0.00000}_{-0.00014}$	$0.69856^{+0.00403}_{-0.00406}$	$0.69856^{+0.00403}_{-0.00406}$
$W_{\nu} \text{ np5}$	$3.45 \cdot 10^3 \pm 58.7$	$1.00000^{+0.00000}_{-0.00053}$	$0.70542^{+0.00780}_{-0.00792}$	$0.70542^{+0.00780}_{-0.00792}$
$W_{\mu\nu} \text{ np0}$	$1.39 \cdot 10^6 \pm 1.18 \cdot 10^3$	$1.00000^{+0.00000}_{-0.00000}$	$0.54285^{+0.00042}_{-0.00042}$	$0.54285^{+0.00042}_{-0.00042}$
$W_{\mu\nu} \text{ np1}$	$2.56 \cdot 10^5 \pm 506$	$1.00000^{+0.00000}_{-0.00001}$	$0.58005^{+0.00097}_{-0.00097}$	$0.58005^{+0.00097}_{-0.00097}$
$W_{\mu\nu} \text{ np2}$	$1.88 \cdot 10^5 \pm 433$	$1.00000^{+0.00000}_{-0.00001}$	$0.58172^{+0.00113}_{-0.00113}$	$0.58172^{+0.00113}_{-0.00113}$
$W_{\mu\nu} \text{ np3}$	$5.09 \cdot 10^4 \pm 226$	$1.00000^{+0.00000}_{-0.00004}$	$0.58343^{+0.00218}_{-0.00218}$	$0.58343^{+0.00218}_{-0.00218}$
$W_{\mu\nu} \text{ np4}$	$1.3 \cdot 10^4 \pm 114$	$1.00000^{+0.00000}_{-0.00014}$	$0.57809^{+0.00434}_{-0.00435}$	$0.57809^{+0.00434}_{-0.00435}$
$W_{\mu\nu} \text{ np5}$	$3.5 \cdot 10^3 \pm 59.1$	$1.00000^{+0.00000}_{-0.00052}$	$0.55517^{+0.00848}_{-0.00851}$	$0.55517^{+0.00848}_{-0.00851}$
$W_{\tau\nu} \text{ np0}$	$1.37 \cdot 10^6 \pm 1.17 \cdot 10^3$	$1.00000^{+0.00000}_{-0.00000}$	$0.09480^{+0.00025}_{-0.00025}$	$0.09480^{+0.00025}_{-0.00025}$
$W_{\tau\nu} \text{ np1}$	$2.55 \cdot 10^5 \pm 505$	$1.00000^{+0.00000}_{-0.00001}$	$0.12114^{+0.00065}_{-0.00064}$	$0.12114^{+0.00065}_{-0.00064}$
$W_{\tau\nu} \text{ np2}$	$1.88 \cdot 10^5 \pm 434$	$1.00000^{+0.00000}_{-0.00001}$	$0.13127^{+0.00078}_{-0.00077}$	$0.13127^{+0.00078}_{-0.00077}$
$W_{\tau\nu} \text{ np3}$	$5.05 \cdot 10^4 \pm 225$	$1.00000^{+0.00000}_{-0.00004}$	$0.14281^{+0.00157}_{-0.00155}$	$0.14281^{+0.00157}_{-0.00155}$
$W_{\tau\nu} \text{ np4}$	$1.3 \cdot 10^4 \pm 114$	$1.00000^{+0.00000}_{-0.00014}$	$0.14935^{+0.00317}_{-0.00312}$	$0.14935^{+0.00317}_{-0.00312}$
$W_{\tau\nu} \text{ np5}$	$4 \cdot 10^3 \pm 63.2$	$1.00000^{+0.00000}_{-0.00046}$	$0.14707^{+0.00578}_{-0.00561}$	$0.14707^{+0.00578}_{-0.00561}$
$\sum W + \text{jets}$	$5.67 \cdot 10^6 \pm 2.38 \cdot 10^3$	$1.00000^{+0.00000}_{-0.00000}$	$0.55230^{+0.00023}_{-0.00023}$	$0.55230^{+0.00023}_{-0.00023}$
$W + b\bar{b} \text{ np0}$	$6.5 \cdot 10^3 \pm 80.6$	$1.00000^{+0.00000}_{-0.00028}$	$0.51131^{+0.00624}_{-0.00624}$	$0.51131^{+0.00624}_{-0.00624}$
$W + b\bar{b} \text{ np1}$	$5.5 \cdot 10^3 \pm 74.2$	$1.00000^{+0.00000}_{-0.00033}$	$0.49182^{+0.00680}_{-0.00679}$	$0.49182^{+0.00680}_{-0.00679}$
$W + b\bar{b} \text{ np2}$	$3 \cdot 10^3 \pm 54.7$	$1.00000^{+0.00000}_{-0.00061}$	$0.48682^{+0.00925}_{-0.00924}$	$0.48682^{+0.00925}_{-0.00924}$
$W + b\bar{b} \text{ np3}$	$1.5 \cdot 10^3 \pm 38.7$	$1.00000^{+0.00000}_{-0.00122}$	$0.50333^{+0.01316}_{-0.01317}$	$0.50333^{+0.01316}_{-0.01317}$
$\sum W + b\bar{b}+\text{jets}$	$1.65 \cdot 10^4 \pm 128$	$1.00000^{+0.00000}_{-0.00022}$	$0.49985^{+0.00393}_{-0.00393}$	$0.49985^{+0.00393}_{-0.00393}$
tchannel $e\nu$	$5.94 \cdot 10^3 \pm 77.1$	$1.00000^{+0.00000}_{-0.00031}$	$0.78469^{+0.00534}_{-0.00543}$	$0.78469^{+0.00534}_{-0.00543}$
tchannel $\mu\nu$	$5.98 \cdot 10^3 \pm 77.3$	$1.00000^{+0.00000}_{-0.00031}$	$0.65519^{+0.00617}_{-0.00622}$	$0.65519^{+0.00617}_{-0.00622}$
tchannel $\tau\nu$	$5.93 \cdot 10^3 \pm 77$	$1.00000^{+0.00000}_{-0.00031}$	$0.15300^{+0.00479}_{-0.00467}$	$0.15300^{+0.00479}_{-0.00467}$
schannel $e\nu$	$8.42 \cdot 10^3 \pm 91.8$	$1.00000^{+0.00000}_{-0.00022}$	$0.77434^{+0.00456}_{-0.00462}$	$0.77434^{+0.00456}_{-0.00462}$
schannel $\mu\nu$	$8.43 \cdot 10^3 \pm 91.8$	$1.00000^{+0.00000}_{-0.00022}$	$0.64457^{+0.00523}_{-0.00526}$	$0.64457^{+0.00523}_{-0.00526}$
schannel $\tau\nu$	$8.48 \cdot 10^3 \pm 92.1$	$1.00000^{+0.00000}_{-0.00022}$	$0.16321^{+0.00409}_{-0.00401}$	$0.16321^{+0.00409}_{-0.00401}$
Wtchannel	$1.33 \cdot 10^4 \pm 115$	$1.00000^{+0.00000}_{-0.00014}$	$0.35302^{+0.00417}_{-0.00415}$	$0.35302^{+0.00417}_{-0.00415}$
$\sum \text{sgtop}$	$5.65 \cdot 10^4 \pm 238$	$1.00000^{+0.00000}_{-0.00009}$	$0.61053^{+0.00210}_{-0.00212}$	$0.61053^{+0.00210}_{-0.00212}$
WWlnln np0	$4.98 \cdot 10^4 \pm 223$	$1.00000^{+0.00000}_{-0.00004}$	$0.74104^{+0.00196}_{-0.00197}$	$0.74104^{+0.00196}_{-0.00197}$
WWlnln np1	$2.5 \cdot 10^4 \pm 158$	$1.00000^{+0.00000}_{-0.00007}$	$0.75551^{+0.00271}_{-0.00273}$	$0.75551^{+0.00271}_{-0.00273}$
WWlnln np2	$1.5 \cdot 10^4 \pm 122$	$1.00000^{+0.00000}_{-0.00012}$	$0.77101^{+0.00343}_{-0.00346}$	$0.77101^{+0.00343}_{-0.00346}$
WWlnln np3	$1 \cdot 10^4 \pm 100$	$1.00000^{+0.00000}_{-0.00018}$	$0.77373^{+0.00418}_{-0.00424}$	$0.77373^{+0.00418}_{-0.00424}$
WZincl np0	$1.5 \cdot 10^4 \pm 122$	$1.00000^{+0.00000}_{-0.00012}$	$0.73525^{+0.00360}_{-0.00363}$	$0.73525^{+0.00360}_{-0.00363}$
WZincl np1	$1 \cdot 10^4 \pm 100$	$1.00000^{+0.00000}_{-0.00018}$	$0.74390^{+0.00437}_{-0.00442}$	$0.74390^{+0.00437}_{-0.00442}$
WZincl np2	$5 \cdot 10^3 \pm 70.7$	$1.00000^{+0.00000}_{-0.00037}$	$0.74895^{+0.00615}_{-0.00625}$	$0.74895^{+0.00615}_{-0.00625}$
WZincl np3	$5 \cdot 10^3 \pm 70.7$	$1.00000^{+0.00000}_{-0.00037}$	$0.77166^{+0.00595}_{-0.00606}$	$0.77166^{+0.00595}_{-0.00606}$
ZZincl np0	$1 \cdot 10^4 \pm 100$	$1.00000^{+0.00000}_{-0.00018}$	$0.70751^{+0.00455}_{-0.00460}$	$0.70751^{+0.00455}_{-0.00460}$

B.2. Event selection cuts

ZZincl np1	$4.5 \cdot 10^3 \pm 67.1$	$1.00000^{+0.00000}_{-0.00041}$	$0.71556^{+0.00675}_{-0.00685}$	$0.71556^{+0.00675}_{-0.00685}$
ZZincl np2	$4.99 \cdot 10^3 \pm 70.7$	$1.00000^{+0.00000}_{-0.00037}$	$0.73202^{+0.00629}_{-0.00638}$	$0.73202^{+0.00629}_{-0.00638}$
ZZincl np3	$2.5 \cdot 10^3 \pm 50$	$1.00000^{+0.00000}_{-0.00073}$	$0.71898^{+0.00905}_{-0.00923}$	$0.71898^{+0.00905}_{-0.00923}$
$\sum Diboson$	$1.57 \cdot 10^5 \pm 396$	$1.00000^{+0.00000}_{-0.00004}$	$0.74605^{+0.00110}_{-0.00111}$	$0.74605^{+0.00110}_{-0.00111}$
DrellYan ee	$1 \cdot 10^6 \pm 1 \cdot 10^3$	$1.00000^{+0.00000}_{-0.00000}$	$0.23348^{+0.00042}_{-0.00042}$	$0.23348^{+0.00042}_{-0.00042}$
DrellYan $\mu\mu$	$1 \cdot 10^6 \pm 1 \cdot 10^3$	$1.00000^{+0.00000}_{-0.00000}$	$0.25610^{+0.00043}_{-0.00043}$	$0.25610^{+0.00043}_{-0.00043}$
$\sum DrellYan$	$2 \cdot 10^6 \pm 1.41 \cdot 10^3$	$1.00000^{+0.00000}_{-0.00000}$	$0.24531^{+0.00030}_{-0.00030}$	$0.24531^{+0.00030}_{-0.00030}$
$b\bar{b}$ jets np0 j1x	$1 \cdot 10^4 \pm 100$	$1.00000^{+0.00000}_{-0.00018}$	$0.00900^{+0.00104}_{-0.00094}$	$0.00900^{+0.00104}_{-0.00094}$
$b\bar{b}$ jets np0 j2	$1 \cdot 10^4 \pm 100$	$1.00000^{+0.00000}_{-0.00018}$	$0.03571^{+0.00194}_{-0.00185}$	$0.03571^{+0.00194}_{-0.00185}$
$b\bar{b}$ jets np0 j3	$9.94 \cdot 10^3 \pm 99.7$	$1.00000^{+0.00000}_{-0.00018}$	$0.02233^{+0.00157}_{-0.00147}$	$0.02233^{+0.00157}_{-0.00147}$
$b\bar{b}$ jets np0 j4	$9.99 \cdot 10^3 \pm 100$	$1.00000^{+0.00000}_{-0.00018}$	$0.01121^{+0.00115}_{-0.00105}$	$0.01121^{+0.00115}_{-0.00105}$
$b\bar{b}$ jets np0 j5p	$2 \cdot 10^3 \pm 44.7$	$1.00000^{+0.00000}_{-0.00092}$	$0.00601^{+0.00226}_{-0.00170}$	$0.00601^{+0.00226}_{-0.00170}$
$b\bar{b}$ jets np1 j1x	$9.9 \cdot 10^3 \pm 99.5$	$1.00000^{+0.00000}_{-0.00019}$	$0.01303^{+0.00124}_{-0.00113}$	$0.01303^{+0.00124}_{-0.00113}$
$b\bar{b}$ jets np1 j2	$9.9 \cdot 10^3 \pm 99.5$	$1.00000^{+0.00000}_{-0.00019}$	$0.02344^{+0.00161}_{-0.00151}$	$0.02344^{+0.00161}_{-0.00151}$
$b\bar{b}$ jets np1 j3	$1 \cdot 10^4 \pm 100$	$1.00000^{+0.00000}_{-0.00018}$	$0.02821^{+0.00175}_{-0.00165}$	$0.02821^{+0.00175}_{-0.00165}$
$b\bar{b}$ jets np1 j4	$9.99 \cdot 10^3 \pm 100$	$1.00000^{+0.00000}_{-0.00018}$	$0.02312^{+0.00159}_{-0.00150}$	$0.02312^{+0.00159}_{-0.00150}$
$b\bar{b}$ jets np1 j5p	$2 \cdot 10^3 \pm 44.7$	$1.00000^{+0.00000}_{-0.00092}$	$0.01351^{+0.00309}_{-0.00256}$	$0.01351^{+0.00309}_{-0.00256}$
$b\bar{b}$ jets np2 j1x	$1 \cdot 10^4 \pm 100$	$1.00000^{+0.00000}_{-0.00018}$	$0.01111^{+0.00114}_{-0.00104}$	$0.01111^{+0.00114}_{-0.00104}$
$b\bar{b}$ jets np2 j2	$1 \cdot 10^4 \pm 100$	$1.00000^{+0.00000}_{-0.00018}$	$0.02311^{+0.00159}_{-0.00150}$	$0.02311^{+0.00159}_{-0.00150}$
$b\bar{b}$ jets np2 j3	$1 \cdot 10^4 \pm 100$	$1.00000^{+0.00000}_{-0.00018}$	$0.02960^{+0.00178}_{-0.00169}$	$0.02960^{+0.00178}_{-0.00169}$
$b\bar{b}$ jets np2 j4	$9.99 \cdot 10^3 \pm 100$	$1.00000^{+0.00000}_{-0.00018}$	$0.02222^{+0.00157}_{-0.00147}$	$0.02222^{+0.00157}_{-0.00147}$
$b\bar{b}$ jets np2 j5p	$2 \cdot 10^3 \pm 44.7$	$1.00000^{+0.00000}_{-0.00092}$	$0.03003^{+0.00430}_{-0.00380}$	$0.03003^{+0.00430}_{-0.00380}$
$b\bar{b}$ jets np3 j1x	$1 \cdot 10^4 \pm 100$	$1.00000^{+0.00000}_{-0.00018}$	$0.01340^{+0.00124}_{-0.00114}$	$0.01340^{+0.00124}_{-0.00114}$
$b\bar{b}$ jets np3 j2	$1 \cdot 10^4 \pm 100$	$1.00000^{+0.00000}_{-0.00018}$	$0.02351^{+0.00161}_{-0.00151}$	$0.02351^{+0.00161}_{-0.00151}$
$b\bar{b}$ jets np3 j3	$9.99 \cdot 10^3 \pm 100$	$1.00000^{+0.00000}_{-0.00018}$	$0.03072^{+0.00181}_{-0.00172}$	$0.03072^{+0.00181}_{-0.00172}$
$b\bar{b}$ jets np3 j4	$1 \cdot 10^4 \pm 100$	$1.00000^{+0.00000}_{-0.00018}$	$0.02851^{+0.00175}_{-0.00166}$	$0.02851^{+0.00175}_{-0.00166}$
$b\bar{b}$ jets np3 j5p	$2 \cdot 10^3 \pm 44.7$	$1.00000^{+0.00000}_{-0.00092}$	$0.03252^{+0.00445}_{-0.00395}$	$0.03252^{+0.00445}_{-0.00395}$
$b\bar{b}$ jets np4 j1x	$1 \cdot 10^4 \pm 100$	$1.00000^{+0.00000}_{-0.00018}$	$0.01590^{+0.00134}_{-0.00124}$	$0.01590^{+0.00134}_{-0.00124}$
$b\bar{b}$ jets np4 j2	$1 \cdot 10^4 \pm 100$	$1.00000^{+0.00000}_{-0.00018}$	$0.02691^{+0.00171}_{-0.00161}$	$0.02691^{+0.00171}_{-0.00161}$
$b\bar{b}$ jets np4 j3	$1 \cdot 10^4 \pm 100$	$1.00000^{+0.00000}_{-0.00018}$	$0.03301^{+0.00188}_{-0.00178}$	$0.03301^{+0.00188}_{-0.00178}$
$b\bar{b}$ jets np4 j4	$9.99 \cdot 10^3 \pm 100$	$1.00000^{+0.00000}_{-0.00018}$	$0.03042^{+0.00181}_{-0.00171}$	$0.03042^{+0.00181}_{-0.00171}$
$b\bar{b}$ jets np4 j5p	$1 \cdot 10^3 \pm 31.6$	$1.00000^{+0.00000}_{-0.00183}$	$0.02900^{+0.00630}_{-0.00528}$	$0.02900^{+0.00630}_{-0.00528}$
$\sum b\bar{b}$ jets	$2.09 \cdot 10^5 \pm 457$	$1.00000^{+0.00000}_{-0.00004}$	$0.02546^{+0.00040}_{-0.00038}$	$0.02546^{+0.00040}_{-0.00038}$

Table B.2.: Efficiency after the filter, efficiency after the trigger and total trigger efficiency $\epsilon_{Trigger}$.

B.2. Event selection cuts

B.2.1. Event numbers

Sample	Total events	Trigger	$1+1+1/1-1-$	$\#_T > 20$ GeV	$E_{LeadJet} > 85$ GeV	$P_{LeadLep} > 85$ GeV	$ \eta_{LeadLep} < 1$
$b'(350\text{GeV}) \rightarrow t$	42.1 ± 0.109	29.4 ± 0.0909	1.88 ± 0.023	1.8 ± 0.0225	1.55 ± 0.0209	1.45 ± 0.0202	1.06 ± 0.0172
$t'(350) \rightarrow q$	1.82 ± 0.00469	1.31 ± 0.00389	0.000837 ± 0.000101	0.000825 ± 0.0001	$0.000813 \pm 9.93 \cdot 10^{-5}$	$0.000801 \pm 9.85 \cdot 10^{-5}$	$0.000473 \pm 9.7 \cdot 10^{-5}$
$t'(350) \rightarrow b$	54.1 ± 0.14	28.1 ± 0.101	0.096 ± 0.00591	0.0917 ± 0.00577	0.0877 ± 0.00565	0.0786 ± 0.00535	0.0524 ± 0.00437
$t'(440) \rightarrow b'$	5.74 ± 0.0574	4.29 ± 0.0496	0.401 ± 0.0152	0.39 ± 0.015	0.362 ± 0.0144	0.335 ± 0.0139	0.245 ± 0.0119
$t\bar{t}$	$3.96 \cdot 10^3 \pm 8.85$	$2.32 \cdot 10^3 \pm 6.77$	10 ± 0.445	9.1 ± 0.424	4.33 ± 0.293	3.36 ± 0.258	2.36 ± 0.207
$t\bar{t}$ FullHad	$3.33 \cdot 10^3 \pm 8.61$	156 ± 1.86	0.111 ± 0.0497	0.0445 ± 0.0315	0 ± 0.0253	0 ± 0.0253	0 ± 0.0253
$\sum t\bar{t}$	$7.29 \cdot 10^3 \pm 12.3$	$2.47 \cdot 10^3 \pm 7.03$	10.1 ± 0.448	9.15 ± 0.426	4.33 ± 0.294	3.36 ± 0.259	2.36 ± 0.208
Zee np0	$3.31 \cdot 10^4 \pm 60.5$	$2.64 \cdot 10^4 \pm 54.1$	70.3 ± 2.79	1.11 ± 0.35	0 ± 0.126	0 ± 0.126	0 ± 0.126
Zee np1	$6.67 \cdot 10^3 \pm 26.5$	$5.73 \cdot 10^3 \pm 24.5$	15.4 ± 1.27	1.26 ± 0.364	0.21 ± 0.149	0.21 ± 0.149	0 ± 0.12
Zee np2	$2.01 \cdot 10^3 \pm 14.4$	$1.76 \cdot 10^3 \pm 13.5$	4.65 ± 0.693	0.827 ± 0.292	0.207 ± 0.146	0.207 ± 0.146	0.133 ± 0.103
Zee np3	560 ± 7.55	497 ± 7.12	1.53 ± 0.394	0.407 ± 0.204	0.204 ± 0.144	0.204 ± 0.144	0.162 ± 0.102
Zee np4	135 ± 3.49	121 ± 3.3	0.63 ± 0.238	0.27 ± 0.156	0.0901 ± 0.0901	0.0901 ± 0.0901	0 ± 0.103
Zee np5	40 ± 1.79	35.3 ± 1.68	0.48 ± 0.196	0.24 ± 0.139	0.16 ± 0.113	0.16 ± 0.113	0.08 ± 0.08
$Z\mu\mu$ np0	$3.29 \cdot 10^4 \pm 59.6$	$2.5 \cdot 10^4 \pm 52$	0.757 ± 0.286	0.108 ± 0.108	0 ± 0.123	0 ± 0.123	0 ± 0.123
$Z\mu\mu$ np1	$6.64 \cdot 10^3 \pm 26.5$	$5.37 \cdot 10^3 \pm 23.8$	0.316 ± 0.183	0.105 ± 0.105	0 ± 0.12	0 ± 0.12	0 ± 0.12
$Z\mu\mu$ np2	$1.98 \cdot 10^3 \pm 14.4$	$1.61 \cdot 10^3 \pm 12.9$	0.104 ± 0.104	0 ± 0.119	0 ± 0.119	0 ± 0.119	0 ± 0.119
$Z\mu\mu$ np3	555 ± 7.49	460 ± 6.81	0.404 ± 0.202	0.202 ± 0.143	0.202 ± 0.143	0.202 ± 0.143	0 ± 0.115
$Z\mu\mu$ np4	140 ± 3.62	114 ± 3.26	0 ± 0.106	0 ± 0.106	0 ± 0.106	0 ± 0.106	0 ± 0.106
$Z\mu\mu$ np5	40 ± 1.79	30.7 ± 1.57	0 ± 0.0913	0 ± 0.0913	0 ± 0.0913	0 ± 0.0913	0 ± 0.0913
$Z\tau\tau$ np0	$3.29 \cdot 10^4 \pm 59.7$	$6.21 \cdot 10^3 \pm 25.9$	0.758 ± 0.287	0.325 ± 0.188	0.108 ± 0.108	0 ± 0.123	0 ± 0.123
$Z\tau\tau$ np1	$6.65 \cdot 10^3 \pm 26.4$	$1.56 \cdot 10^3 \pm 12.8$	0.105 ± 0.105	0 ± 0.119	0 ± 0.119	0 ± 0.119	0 ± 0.119
$Z\tau\tau$ np2	$2.02 \cdot 10^3 \pm 14.5$	518 ± 7.33	0.104 ± 0.104	0.104 ± 0.104	0.104 ± 0.104	0.104 ± 0.104	0 ± 0.118
$Z\tau\tau$ np3	550 ± 7.42	149 ± 3.86	0 ± 0.114	0 ± 0.114	0 ± 0.114	0 ± 0.114	0 ± 0.114
$Z\tau\tau$ np4	145 ± 3.75	41.8 ± 2.01	0 ± 0.11	0 ± 0.11	0 ± 0.11	0 ± 0.11	0 ± 0.11
$Z\tau\tau$ np5	35 ± 1.57	10.8 ± 0.87	0 ± 0.0799	0 ± 0.0799	0 ± 0.0799	0 ± 0.0799	0 ± 0.0799
$\sum Z+\text{jets}$	$1.27 \cdot 10^5 \pm 117$	$7.57 \cdot 10^4 \pm 90.5$	95.6 ± 3.23	4.96 ± 0.771	1.28 ± 0.503	1.18 ± 0.506	0.285 ± 0.469
$Zee+b\bar{b}$ np0	315 ± 0.814	285 ± 0.774	0.728 ± 0.0391	0.082 ± 0.0131	0.105 ± 0.0047	0.00841 ± 0.00421	0.0021 ± 0.0021
$Zee+b\bar{b}$ np1	122 ± 0.385	110 ± 0.367	0.334 ± 0.0202	0.0962 ± 0.0108	0.0171 ± 0.00456	0.0171 ± 0.00456	0.00731 ± 0.00298
$Zee+b\bar{b}$ np2	42.3 ± 0.211	38.3 ± 0.201	0.161 ± 0.013	0.0581 ± 0.00784	0.0264 ± 0.00529	0.0254 ± 0.00518	0.0074 ± 0.0028
$Zee+b\bar{b}$ np3	19.1 ± 0.191	17.3 ± 0.182	0.0633 ± 0.011	0.0268 ± 0.00717	0.0134 ± 0.00507	0.0134 ± 0.00507	0.00192 ± 0.00192
$Z\mu\mu+b\bar{b}$ np0	317 ± 0.819	270 ± 0.756	0.0867 ± 0.0135	0.0296 ± 0.00791	0 ± 0.00241	0 ± 0.00241	0 ± 0.00241
$Z\mu\mu+b\bar{b}$ np1	123 ± 0.387	103 ± 0.355	0.0698 ± 0.00925	0.0368 ± 0.00671	0.0049 ± 0.00245	0.00368 ± 0.00212	0.00368 ± 0.00212
$Z\mu\mu+b\bar{b}$ np2	42.3 ± 0.211	35.1 ± 0.193	0.0338 ± 0.00598	0.0137 ± 0.00381	0.00634 ± 0.00259	0.00529 ± 0.00236	0.00423 ± 0.00211
$Z\mu\mu+b\bar{b}$ np3	18.9 ± 0.189	15.6 ± 0.171	0.017 ± 0.00567	0.0113 ± 0.00463	0.00189 ± 0.00189	0.00189 ± 0.00189	0.00189 ± 0.00189
$Z\tau\tau+b\bar{b}$ np0	319 ± 0.823	270 ± 0.756	0.034 ± 0.0085	0.0191 ± 0.00638	0.00425 ± 0.00301	0.00213 ± 0.00213	0 ± 0.00242
$Z\tau\tau+b\bar{b}$ np1	121 ± 0.383	103 ± 0.355	0.0328 ± 0.0063	0.0158 ± 0.00437	0.00485 ± 0.00243	0.00121 ± 0.00121	0 ± 0.00138
$Z\tau\tau+b\bar{b}$ np2	43.3 ± 0.216	12.1 ± 0.114	0.00757 ± 0.00286	0.00541 ± 0.00242	0.00216 ± 0.00153	0.00108 ± 0.00108	0.00108 ± 0.00108
$Z\tau\tau+b\bar{b}$ np3	19.1 ± 0.191	5.58 ± 0.103	0.00191 ± 0.00191	0.00191 ± 0.00191	0 ± 0.00217	0 ± 0.00217	0 ± 0.00217
$\sum Z+b\bar{b}+\text{jets}$	$1.5 \cdot 10^3 \pm 1.64$	$1 \cdot 10^3 \pm 1.34$	1.57 ± 0.0519	0.397 ± 0.0248	0.0918 ± 0.0119	0.0795 ± 0.0111	0.0296 ± 0.00754
$W_{\nu\nu}$ np0	$3.46 \cdot 10^5 \pm 294$	$2.09 \cdot 10^5 \pm 229$	0 ± 0.285	0 ± 0.285	0 ± 0.285	0 ± 0.285	0 ± 0.285
$W_{\nu\nu}$ np1	$6.47 \cdot 10^4 \pm 127$	$4.3 \cdot 10^4 \pm 104$	0.5 ± 0.354	0.5 ± 0.354	0 ± 0.285	0 ± 0.285	0 ± 0.285
$W_{\nu\nu}$ np2	$1.89 \cdot 10^4 \pm 43.4$	$1.28 \cdot 10^4 \pm 35.8$	0.499 ± 0.223	0.299 ± 0.173	0 ± 0.114	0 ± 0.114	0 ± 0.114
$W_{\nu\nu}$ np3	$5.05 \cdot 10^3 \pm 22.5$	$3.49 \cdot 10^3 \pm 18.7$	0.0999 ± 0.0999	0.0999 ± 0.0999	0 ± 0.114	0 ± 0.114	0 ± 0.114

$W_{e\nu} np4$	$1.26 \cdot 10^3 \pm 11.1$	884 ± 9.28	0.195 ± 0.138	0.195 ± 0.138	0.195 ± 0.138	0.195 ± 0.138	0.0974 ± 0.0974	0 ± 0.111
$W_{e\nu} np5$	345 ± 5.87	243 ± 4.93	0.1 ± 0.1	0.1 ± 0.1	0.1 ± 0.1	0.1 ± 0.1	0 ± 0.114	0 ± 0.114
$W_{\mu\nu} np0$	$3.47 \cdot 10^5 \pm 295$	$1.88 \cdot 10^5 \pm 217$	1.25 ± 0.559	1.25 ± 0.559	1.25 ± 0.559	1.25 ± 0.559	0 ± 0.285	0 ± 0.285
$W_{\mu\nu} np1$	$6.41 \cdot 10^4 \pm 127$	$3.72 \cdot 10^4 \pm 96.4$	2.75 ± 0.83	2.75 ± 0.83	2 ± 0.708	0 ± 0.285	0 ± 0.285	0 ± 0.285
$W_{\mu\nu} np2$	$1.88 \cdot 10^4 \pm 43.3$	$1.09 \cdot 10^4 \pm 33$	1.5 ± 0.387	1.2 ± 0.346	1.2 ± 0.346	0.2 ± 0.141	0.2 ± 0.141	0 ± 0.114
$W_{\mu\nu} np3$	$5.05 \cdot 10^3 \pm 22.4$	$2.95 \cdot 10^3 \pm 17.1$	0.497 ± 0.222	0.497 ± 0.222	0.397 ± 0.199	0 ± 0.113	0 ± 0.113	0 ± 0.113
$W_{\mu\nu} np4$	$1.29 \cdot 10^3 \pm 11.3$	743 ± 8.57	0.297 ± 0.171	0.297 ± 0.171	0.198 ± 0.14	0.0989 ± 0.0989	0.0989 ± 0.0989	0 ± 0.113
$W_{\mu\nu} np5$	350 ± 5.92	194 ± 4.41	0 ± 0.114	0 ± 0.114	0 ± 0.114	0 ± 0.114	0 ± 0.114	0 ± 0.114
$W_{\tau\nu} np0$	$3.42 \cdot 10^5 \pm 292$	$3.24 \cdot 10^4 \pm 90.1$	0 ± 0.285	0 ± 0.285	0 ± 0.285	0 ± 0.285	0 ± 0.285	0 ± 0.285
$W_{\tau\nu} np1$	$6.38 \cdot 10^4 \pm 126$	$7.73 \cdot 10^3 \pm 44$	0.251 ± 0.251	0.251 ± 0.251	0.251 ± 0.251	0 ± 0.286	0 ± 0.286	0 ± 0.286
$W_{\tau\nu} np2$	$1.88 \cdot 10^4 \pm 43.4$	$2.47 \cdot 10^3 \pm 15.7$	0.2 ± 0.141	0.2 ± 0.141	0.2 ± 0.141	0 ± 0.114	0 ± 0.114	0 ± 0.114
$W_{\tau\nu} np3$	$5.04 \cdot 10^3 \pm 22.4$	720 ± 8.48	0.2 ± 0.141	0.2 ± 0.141	0.2 ± 0.141	0.0999 ± 0.0999	0.0999 ± 0.0999	0 ± 0.114
$W_{\tau\nu} np4$	$1.29 \cdot 10^3 \pm 11.3$	192 ± 4.36	0 ± 0.113	0 ± 0.113	0 ± 0.113	0 ± 0.113	0 ± 0.113	0 ± 0.113
$W_{\tau\nu} np5$	350 ± 5.54	51.5 ± 2.12	0 ± 0.0998	0 ± 0.0998	0 ± 0.0998	0 ± 0.0998	0 ± 0.0998	0 ± 0.0998
$\sum W + \text{jets}$	$1.3 \cdot 10^6 \pm 561$	$5.53 \cdot 10^5 \pm 365$	8.34 ± 1.32	8.34 ± 1.32	6.89 ± 1.22	0.593 ± 0.804	0.496 ± 0.798	0 ± 0.8
$W + b\bar{b} np0$	160 ± 1.98	81.8 ± 1.42	0.32 ± 0.0888	0.32 ± 0.0888	0.222 ± 0.0739	0.0246 ± 0.0246	0.0246 ± 0.0246	0 ± 0.0281
$W + b\bar{b} np1$	130 ± 1.75	63.9 ± 1.23	0.142 ± 0.0579	0.142 ± 0.0579	0.142 ± 0.0579	0.0236 ± 0.0236	0 ± 0.0269	0 ± 0.0269
$W + b\bar{b} np2$	70 ± 1.28	34.1 ± 0.892	0.0467 ± 0.033	0.0467 ± 0.033	0.0467 ± 0.033	0 ± 0.0266	0 ± 0.0266	0 ± 0.0266
$W + b\bar{b} np3$	30 ± 0.775	15.1 ± 0.55	0.02 ± 0.02	0.02 ± 0.02	0.02 ± 0.02	0.02 ± 0.02	0.02 ± 0.02	0 ± 0.02
$\sum W + b\bar{b} + \text{jets}$	390 ± 3.04	195 ± 2.15	0.529 ± 0.113	0.529 ± 0.113	0.43 ± 0.101	0.0683 ± 0.0477	0.0446 ± 0.0494	0.02 ± 0.0512
tchannel $e\nu$	358 ± 4.64	281 ± 4.11	0.421 ± 0.159	0.421 ± 0.159	0.421 ± 0.159	0.0602 ± 0.0602	0.0602 ± 0.0602	0 ± 0.0685
tchannel $\mu\nu$	359 ± 4.64	235 ± 3.75	0.78 ± 0.216	0.78 ± 0.216	0.66 ± 0.199	0.36 ± 0.147	0.12 ± 0.0848	0.06 ± 0.06
tchannel $\tau\nu$	356 ± 4.63	54.5 ± 1.81	0 ± 0.0685	0 ± 0.0685	0 ± 0.0685	0 ± 0.0685	0 ± 0.0685	0 ± 0.0685
schannel $e\nu$	23.4 ± 0.255	18.1 ± 0.225	0.0806 ± 0.015	0.0806 ± 0.015	0.0723 ± 0.0142	0.0139 ± 0.00622	0.00834 ± 0.00482	0.00556 ± 0.00393
schannel $\mu\nu$	23.4 ± 0.255	15.1 ± 0.205	0.0472 ± 0.0115	0.0472 ± 0.0115	0.0361 ± 0.01	0.00833 ± 0.00481	0.00833 ± 0.00481	0.00278 ± 0.00278
schannel $\tau\nu$	23.5 ± 0.255	3.84 ± 0.103	0.00277 ± 0.00277	0.00277 ± 0.00277	0.00277 ± 0.00277	0 ± 0.00316	0 ± 0.00316	0 ± 0.00316
Wchannel	729 ± 6.33	257 ± 3.76	0.439 ± 0.155	0.439 ± 0.155	0.384 ± 0.145	0.11 ± 0.0777	0.11 ± 0.0777	0.11 ± 0.0777
\sum sgtop	$1.87 \cdot 10^3 \pm 10.2$	865 ± 6.96	1.77 ± 0.318	1.77 ± 0.318	1.58 ± 0.302	0.552 ± 0.19	0.307 ± 0.147	0.178 ± 0.138
WWinln np0	102 ± 0.459	75.9 ± 0.395	0.0904 ± 0.0136	0.0904 ± 0.0136	0.074 ± 0.0123	0 ± 0.00234	0 ± 0.00234	0 ± 0.00234
WWinln np1	49.3 ± 0.312	37.3 ± 0.271	0.0434 ± 0.00926	0.0434 ± 0.00926	0.0375 ± 0.00861	0.00197 ± 0.00197	0.00197 ± 0.00197	0.00197 ± 0.00197
WWinln np2	22 ± 0.18	17 ± 0.158	0.11 ± 0.0127	0.11 ± 0.0127	0.106 ± 0.0125	0.0588 ± 0.0093	0.0559 ± 0.00906	0.0235 ± 0.00588
WWinln np3	8.9 ± 0.089	6.89 ± 0.0783	0.117 ± 0.0102	0.117 ± 0.0102	0.113 ± 0.01	0.0828 ± 0.00859	0.0748 ± 0.00816	0.0418 ± 0.0061
WZinln np0	33.2 ± 0.271	24.4 ± 0.232	0.73 ± 0.0402	0.73 ± 0.0402	0.64 ± 0.0376	0.00885 ± 0.00443	0.00443 ± 0.00313	0.00221 ± 0.00221
WZinln np1	19.9 ± 0.2	14.8 ± 0.172	0.503 ± 0.0317	0.503 ± 0.0317	0.449 ± 0.0299	0.0898 ± 0.0134	0.0838 ± 0.0129	0.0439 ± 0.00936
WZinln np2	11 ± 0.156	8.28 ± 0.135	0.265 ± 0.0242	0.265 ± 0.0242	0.228 ± 0.0225	0.0907 ± 0.0142	0.0907 ± 0.0142	0.0535 ± 0.0108
WZinln np3	4.65 ± 0.0658	3.59 ± 0.0578	0.119 ± 0.0105	0.119 ± 0.0105	0.106 ± 0.00994	0.0651 ± 0.00779	0.0605 ± 0.0075	0.0355 ± 0.00574
ZZinln np0	24.7 ± 0.247	17.5 ± 0.208	0.183 ± 0.0213	0.183 ± 0.0213	0.0964 ± 0.0154	0.00494 ± 0.00349	0.00494 ± 0.00349	0.00247 ± 0.00247
ZZinln np1	11.2 ± 0.168	8.05 ± 0.142	0.0775 ± 0.0139	0.0775 ± 0.0139	0.04 ± 0.01	0.0125 ± 0.00559	0.0125 ± 0.00559	0.0025 ± 0.0025
ZZinln np2	4.4 ± 0.0623	3.22 ± 0.0533	0.0238 ± 0.00458	0.0238 ± 0.00458	0.0141 ± 0.00352	0.00264 ± 0.00153	0.00264 ± 0.00153	0.000881 ± 0.000881
ZZinln np3	1.4 ± 0.028	1.01 ± 0.0238	0.0106 ± 0.00244	0.0106 ± 0.00244	0.00785 ± 0.0021	0.00392 ± 0.00148	0.00392 ± 0.00148	0.00224 ± 0.00112
\sum Diboson	293 ± 0.764	218 ± 0.658	2.27 ± 0.0673	2.27 ± 0.0673	1.91 ± 0.0613	0.422 ± 0.026	0.396 ± 0.0253	0.25 ± 0.0184
DrellYan ee	$6.14 \cdot 10^4 \pm 61.4$	$1.43 \cdot 10^4 \pm 29.7$	1.04 ± 0.253	1.04 ± 0.253	0.123 ± 0.0868	0.0614 ± 0.0614	0.0614 ± 0.0614	0 ± 0.0699
DrellYan $\mu\mu$	$6.37 \cdot 10^4 \pm 63.7$	$1.63 \cdot 10^4 \pm 32.2$	0.255 ± 0.127	0.255 ± 0.127	0 ± 0.0726	0 ± 0.0726	0 ± 0.0726	0 ± 0.0726
\sum DrellYan	$1.25 \cdot 10^5 \pm 88.5$	$3.06 \cdot 10^4 \pm 43.8$	1.3 ± 0.283	1.3 ± 0.283	0.123 ± 0.113	0.0614 ± 0.0951	0.0614 ± 0.0951	0 ± 0.101

B. Cut efficiencies and event yields

$b\bar{b}$ jets np0 j1x	$8.52 \cdot 10^7 \pm 8.52 \cdot 10^5$	$7.67 \cdot 10^5 \pm 8.08 \cdot 10^4$	$0 \pm 9.7 \cdot 10^3$	$0 \pm 9.7 \cdot 10^3$	$0 \pm 9.7 \cdot 10^3$	$0 \pm 9.7 \cdot 10^3$	$0 \pm 9.7 \cdot 10^3$	$0 \pm 9.7 \cdot 10^3$
$b\bar{b}$ jets np0 j2	$2.96 \cdot 10^6 \pm 2.96 \cdot 10^4$	$1.06 \cdot 10^5 \pm 5.59 \cdot 10^3$	0 ± 337	0 ± 337	0 ± 337	0 ± 337	0 ± 337	0 ± 337
$b\bar{b}$ jets np0 j3	$1.07 \cdot 10^5 \pm 1.07 \cdot 10^3$	$2.39 \cdot 10^3 \pm 160$	10.7 ± 10.7	0 ± 12.2	0 ± 12.2	0 ± 12.2	0 ± 12.2	0 ± 12.2
$b\bar{b}$ jets np0 j4	$2.42 \cdot 10^3 \pm 24.2$	27.1 ± 2.56	0 ± 0.276	0 ± 0.276	0 ± 0.276	0 ± 0.276	0 ± 0.276	0 ± 0.276
$b\bar{b}$ jets np0 j5p	48.8 ± 1.09	0.293 ± 0.0847	0 ± 0.0278	0 ± 0.0278	0 ± 0.0278	0 ± 0.0278	0 ± 0.0278	0 ± 0.0278
$b\bar{b}$ jets np1 j1x	$1.52 \cdot 10^7 \pm 1.53 \cdot 10^5$	$1.99 \cdot 10^5 \pm 1.75 \cdot 10^4$	$0 \pm 1.75 \cdot 10^3$	$0 \pm 1.75 \cdot 10^3$	$0 \pm 1.75 \cdot 10^3$	$0 \pm 1.75 \cdot 10^3$	$0 \pm 1.75 \cdot 10^3$	$0 \pm 1.75 \cdot 10^3$
$b\bar{b}$ jets np1 j2	$1.03 \cdot 10^7 \pm 1.03 \cdot 10^5$	$2.41 \cdot 10^5 \pm 1.58 \cdot 10^4$	$0 \pm 1.18 \cdot 10^3$	$0 \pm 1.18 \cdot 10^3$	$0 \pm 1.18 \cdot 10^3$	$0 \pm 1.18 \cdot 10^3$	$0 \pm 1.18 \cdot 10^3$	$0 \pm 1.18 \cdot 10^3$
$b\bar{b}$ jets np1 j3	$6.67 \cdot 10^5 \pm 6.67 \cdot 10^3$	$1.88 \cdot 10^4 \pm 1.12 \cdot 10^3$	0 ± 76.1	0 ± 76.1	0 ± 76.1	0 ± 76.1	0 ± 76.1	0 ± 76.1
$b\bar{b}$ jets np1 j4	$1.99 \cdot 10^4 \pm 199$	459 ± 30.2	0 ± 2.26	0 ± 2.26	0 ± 2.26	0 ± 2.26	0 ± 2.26	0 ± 2.26
$b\bar{b}$ jets np1 j5p	346 ± 7.74	4.67 ± 0.899	0 ± 0.197	0 ± 0.197	0 ± 0.197	0 ± 0.197	0 ± 0.197	0 ± 0.197
$b\bar{b}$ jets np2 j1x	$3.26 \cdot 10^6 \pm 3.27 \cdot 10^4$	$3.63 \cdot 10^4 \pm 3.44 \cdot 10^3$	0 ± 372	0 ± 372	0 ± 372	0 ± 372	0 ± 372	0 ± 372
$b\bar{b}$ jets np2 j2	$3.89 \cdot 10^6 \pm 3.89 \cdot 10^4$	$8.98 \cdot 10^4 \pm 5.91 \cdot 10^3$	0 ± 443	0 ± 443	0 ± 443	0 ± 443	0 ± 443	0 ± 443
$b\bar{b}$ jets np2 j3	$6.77 \cdot 10^5 \pm 6.77 \cdot 10^3$	$2 \cdot 10^4 \pm 1.16 \cdot 10^3$	0 ± 77.1	0 ± 77.1	0 ± 77.1	0 ± 77.1	0 ± 77.1	0 ± 77.1
$b\bar{b}$ jets np2 j4	$3.58 \cdot 10^4 \pm 358$	795 ± 53.3	0 ± 4.08	0 ± 4.08	0 ± 4.08	0 ± 4.08	0 ± 4.08	0 ± 4.08
$b\bar{b}$ jets np2 j5p	845 ± 18.9	25.4 ± 3.28	0 ± 0.482	0 ± 0.482	0 ± 0.482	0 ± 0.482	0 ± 0.482	0 ± 0.482
$b\bar{b}$ jets np3 j1x	$4.94 \cdot 10^5 \pm 4.94 \cdot 10^3$	$6.62 \cdot 10^3 \pm 572$	0 ± 56.3	0 ± 56.3	0 ± 56.3	0 ± 56.3	0 ± 56.3	0 ± 56.3
$b\bar{b}$ jets np3 j2	$1.17 \cdot 10^6 \pm 1.17 \cdot 10^4$	$2.75 \cdot 10^4 \pm 1.79 \cdot 10^3$	0 ± 133	0 ± 133	0 ± 133	0 ± 133	0 ± 133	0 ± 133
$b\bar{b}$ jets np3 j3	$3.75 \cdot 10^5 \pm 3.75 \cdot 10^3$	$1.15 \cdot 10^4 \pm 658$	0 ± 42.8	0 ± 42.8	0 ± 42.8	0 ± 42.8	0 ± 42.8	0 ± 42.8
$b\bar{b}$ jets np3 j4	$2.82 \cdot 10^4 \pm 282$	805 ± 47.7	0 ± 3.22	0 ± 3.22	0 ± 3.22	0 ± 3.22	0 ± 3.22	0 ± 3.22
$b\bar{b}$ jets np3 j5p	962 ± 21.5	31.3 ± 3.88	0 ± 0.548	0 ± 0.548	0 ± 0.548	0 ± 0.548	0 ± 0.548	0 ± 0.548
$b\bar{b}$ jets np4 j1x	$6.95 \cdot 10^4 \pm 695$	$1.11 \cdot 10^3 \pm 87.7$	0 ± 7.92	0 ± 7.92	0 ± 7.92	0 ± 7.92	0 ± 7.92	0 ± 7.92
$b\bar{b}$ jets np4 j2	$3.4 \cdot 10^5 \pm 3.4 \cdot 10^3$	$9.15 \cdot 10^3 \pm 558$	0 ± 38.7	0 ± 38.7	0 ± 38.7	0 ± 38.7	0 ± 38.7	0 ± 38.7
$b\bar{b}$ jets np4 j3	$2 \cdot 10^5 \pm 2 \cdot 10^3$	$6.61 \cdot 10^3 \pm 364$	0 ± 22.8	0 ± 22.8	0 ± 22.8	0 ± 22.8	0 ± 22.8	0 ± 22.8
$b\bar{b}$ jets np4 j4	$2.88 \cdot 10^4 \pm 288$	875 ± 50.2	0 ± 3.28	0 ± 3.28	0 ± 3.28	0 ± 3.28	0 ± 3.28	0 ± 3.28
$b\bar{b}$ jets np4 j5p	$1.34 \cdot 10^3 \pm 42.2$	38.7 ± 7.19	0 ± 1.52	0 ± 1.52	0 ± 1.52	0 ± 1.52	0 ± 1.52	0 ± 1.52
$\sum b\bar{b}$ jets	$1.25 \cdot 10^8 \pm 8.74 \cdot 10^5$	$1.54 \cdot 10^6 \pm 8.47 \cdot 10^4$	$10.7 \pm 9.96 \cdot 10^3$	$0 \pm 9.96 \cdot 10^3$	$0 \pm 9.96 \cdot 10^3$	$0 \pm 9.96 \cdot 10^3$	$0 \pm 9.96 \cdot 10^3$	$0 \pm 9.96 \cdot 10^3$
SBR $b'(350\text{GeV}) \rightarrow t$	0.00000 ± 0.29090	0.00001 ± 1.12590	0.01422 ± 141.55506	0.07080 ± 704.91698	0.20944 ± 2085.37572	0.24451 ± 2434.63255	0.24451 ± 2434.63255	0.36477 ± 3632.08508
SBR $t'(350) \rightarrow q$	0.00000 ± 0.01254	0.00000 ± 0.05034	0.00001 ± 0.06300	0.00003 ± 0.32290	0.00011 ± 1.09235	0.00014 ± 1.34537	0.00016 ± 1.63536	0.00019 ± 1.98925
SBR $t'(350) \rightarrow b$	0.00000 ± 0.37362	0.00001 ± 1.07694	0.00073 ± 7.22884	0.00360 ± 35.88772	0.01183 ± 117.83837	0.01326 ± 132.04841	0.01819 ± 181.08925	0.02543 ± 254.64814
SBR $t'(440) \rightarrow b'$	0.00000 ± 0.03960	0.00000 ± 0.16436	0.00303 ± 30.20620	0.01535 ± 152.82384	0.04889 ± 486.84001	0.05657 ± 563.27958	0.08543 ± 850.64814	0.11819 ± 1181.08925

Table B.3.: Number of events after each event selection cut for the same-sign dilepton category. The numbers are rescaled to an integrated luminosity of $\mathcal{L} = 50\text{pb}^{-1}$.

B.2.2. Efficiencies

B.2. Event selection cuts

$b\bar{b}$ jets np4 j1x	$6.95 \cdot 10^4 \pm 695$	$0.01590^{+0.00134}_{-0.00124}$	$0.00000^{+0.01146}_{-0.00090}$	$0.00000^{+0.00000}_{-0.00000}$	$0.00000^{+0.00000}_{-0.00000}$	$0.00000^{+0.00000}_{-0.00000}$	$0.00000^{+0.00000}_{-0.00000}$	$0.00000^{+0.00000}_{-0.00000}$	$0.00000^{+0.00018}_{-0.00000}$
$b\bar{b}$ jets np4 j2	$3.4 \cdot 10^5 \pm 3.4 \cdot 10^3$	$0.02691^{+0.00171}_{-0.00188}$	$0.00000^{+0.00679}_{-0.00554}$	$0.00000^{+0.00000}_{-0.00000}$	$0.00000^{+0.00000}_{-0.00000}$	$0.00000^{+0.00000}_{-0.00000}$	$0.00000^{+0.00000}_{-0.00000}$	$0.00000^{+0.00000}_{-0.00000}$	$0.00000^{+0.00018}_{-0.00000}$
$b\bar{b}$ jets np4 j3	$2 \cdot 10^5 \pm 2 \cdot 10^3$	$0.03301^{+0.00178}_{-0.00178}$	$0.00000^{+0.00000}_{-0.00000}$	$0.00000^{+0.00000}_{-0.00000}$	$0.00000^{+0.00000}_{-0.00000}$	$0.00000^{+0.00000}_{-0.00000}$	$0.00000^{+0.00000}_{-0.00000}$	$0.00000^{+0.00000}_{-0.00000}$	$0.00000^{+0.00018}_{-0.00000}$
$b\bar{b}$ jets np4 j4	$2.88 \cdot 10^4 \pm 288$	$0.03042^{+0.00181}_{-0.00171}$	$0.00000^{+0.00601}_{-0.00000}$	$0.00000^{+0.00000}_{-0.00000}$	$0.00000^{+0.00000}_{-0.00000}$	$0.00000^{+0.00000}_{-0.00000}$	$0.00000^{+0.00000}_{-0.00000}$	$0.00000^{+0.00000}_{-0.00000}$	$0.00000^{+0.00018}_{-0.00000}$
$b\bar{b}$ jets np4 j5p	$1.34 \cdot 10^3 \pm 42.2$	$0.02900^{+0.00630}_{-0.00528}$	$0.00000^{+0.06124}_{-0.00000}$	$0.00000^{+0.00000}_{-0.00000}$	$0.00000^{+0.00000}_{-0.00000}$	$0.00000^{+0.00000}_{-0.00000}$	$0.00000^{+0.00000}_{-0.00000}$	$0.00000^{+0.00000}_{-0.00000}$	$0.00000^{+0.00183}_{-0.00000}$
$\sum b\bar{b}$ jets	$1.25 \cdot 10^8 \pm 8.74 \cdot 10^5$	$0.01568^{+0.00062}_{-0.00057}$	$0.00450^{+0.01023}_{-0.00372}$	$0.00000^{+0.00000}_{-0.00000}$	$0.00000^{+0.00000}_{-0.00000}$	$0.00000^{+0.00000}_{-0.00000}$	$0.00000^{+0.00000}_{-0.00000}$	$0.00000^{+0.00000}_{-0.00000}$	$0.00000^{+0.00000}_{-0.00000}$

Table B.4.: Efficiencies for each cut in comparison to the previous one (see definition in Eq. (4.7)). A total efficiency is shown in the last column. The upper and lower limits are calculated from Eq. (4.9) and Eq. (4.8).

B.3. Cut efficiency plots

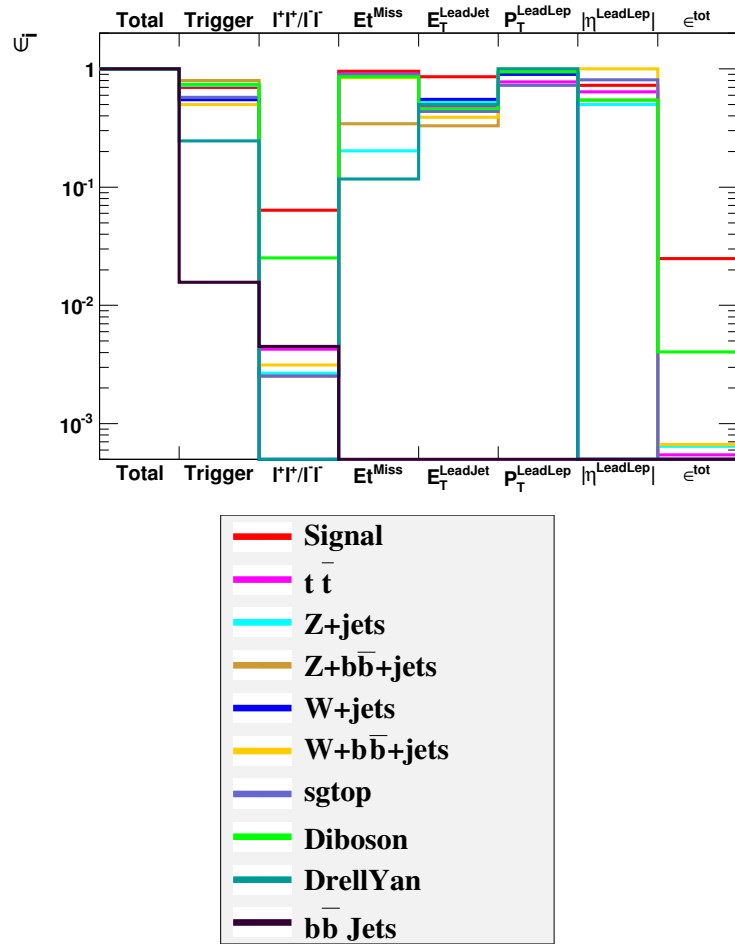


Figure B.1.: Cut efficiencies for the $b'(350 \text{ GeV}) \rightarrow t$ signal sample and all BG sample categories. The legend is also applicable to the following plots (figures B.2, B.3 and B.4).

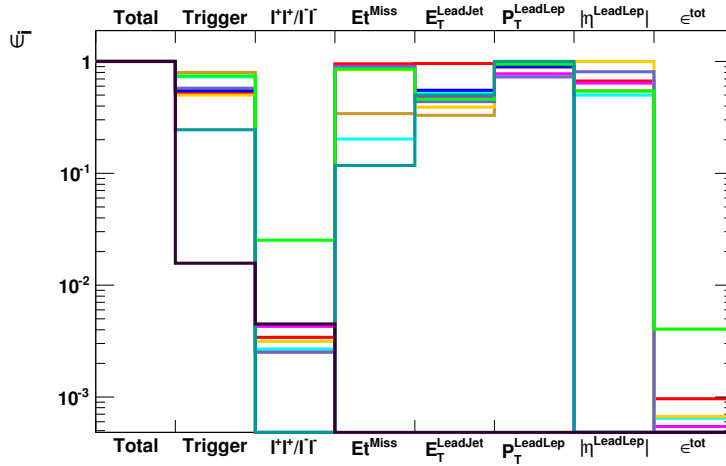


Figure B.2.: Cut efficiencies for the $t'(350 \text{ GeV}) \rightarrow b$ signal sample and all BG sample categories.

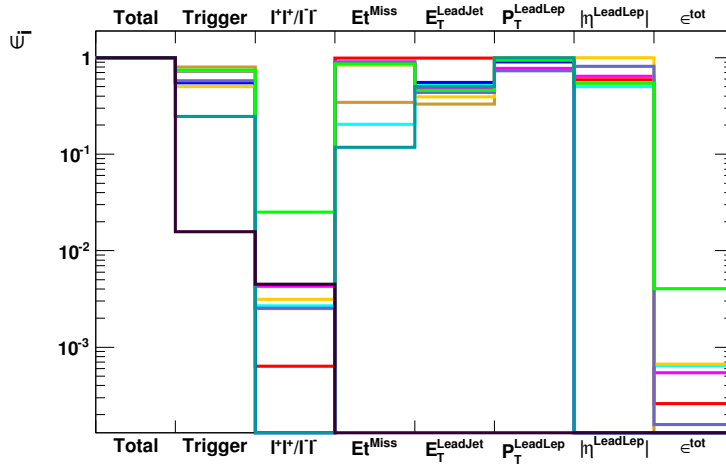


Figure B.3.: Cut efficiencies for the $t'(350 \text{ GeV}) \rightarrow q$ signal sample and all BG sample categories.

B. Cut efficiencies and event yields

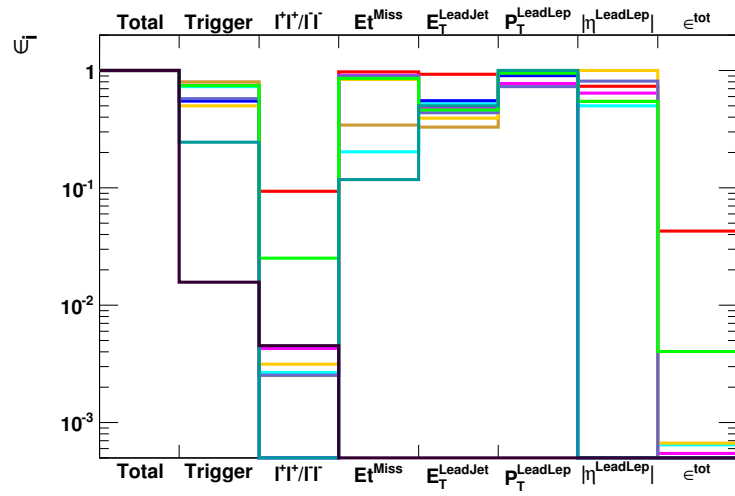


Figure B.4.: Cut efficiencies for the $t'(440 \text{ GeV}) \rightarrow b'$ signal sample and all BG sample categories.

B.4. Signal over background plots

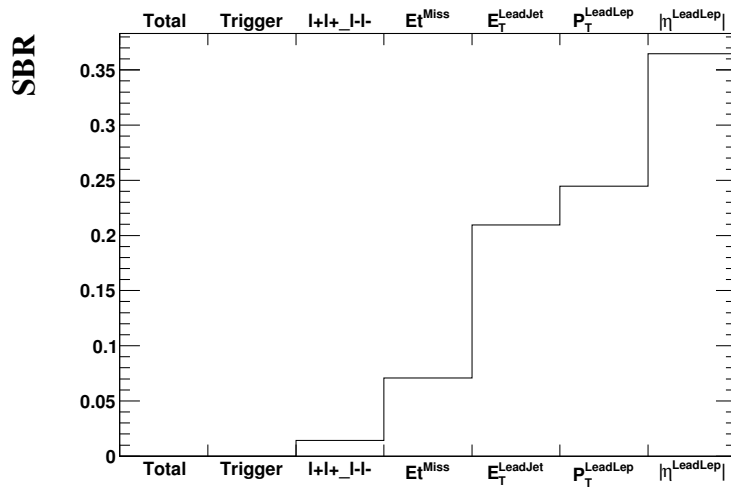


Figure B.5.: Signal over background ratios for the $b'(350 \text{ GeV}) \rightarrow t$ signal sample as a function of the event selection cuts.

B. Cut efficiencies and event yields

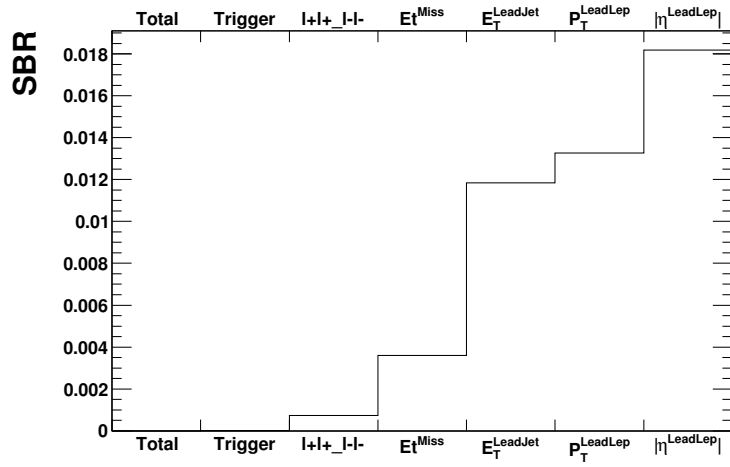


Figure B.6.: Signal over background ratios for the $t'(350 \text{ GeV}) \rightarrow b$ signal sample as a function of the event selection cuts.

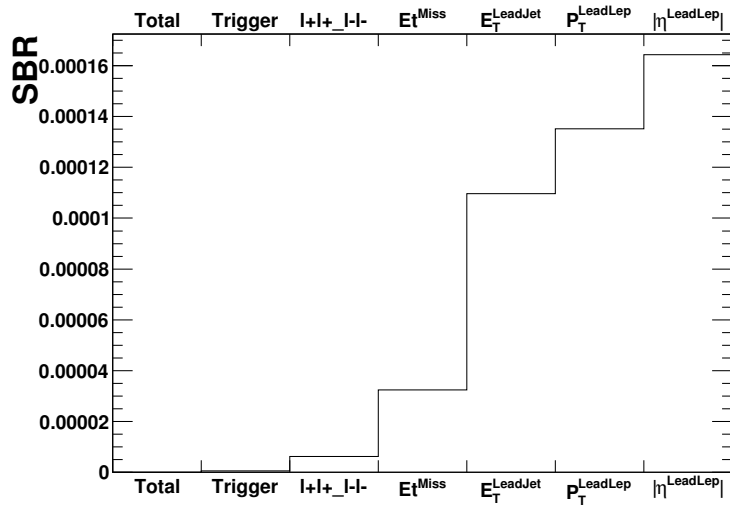


Figure B.7.: Signal over background ratios for the $t'(350 \text{ GeV}) \rightarrow q$ signal sample as a function of the event selection cuts.

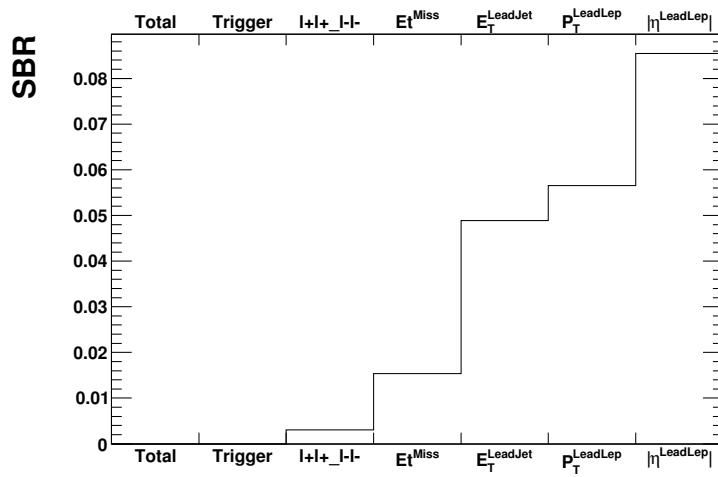


Figure B.8.: Signal over background ratios for the $t'(440 \text{ GeV}) \rightarrow b'$ signal sample as a function of the event selection cuts.

C. Counting analysis

C.1. Single toy sample with modified cross sections

Sample	Measured events in signal region	Measured ratio in control regions	Expected events in signal region	Expected ratio in control regions
pseudo-data	147			
$W e \nu$ +jets (MC)	0.00	0.61	0.0 ± 0.0	0.6
$W \mu \nu$ +jets (MC)	0.00	0.63	0.0 ± 0.0	0.6
$Z e e$ +jets (MC)	3.80	0.66	3.4 ± 2.0	0.6
$Z \mu \mu$ +jets (MC)	0.00	0.62	0.0 ± 0.0	0.6
$t \bar{t}$ (MC)	58.1	1.35	69.0 ± 6.6	1.6
other (MC)	8.80		8.8 ± 2.0	
Result	76.4		33.6 ± 0.5	

Table C.1.: Results for the measured events and control ratios after the counting analysis. The analysis is run on a toy pseudo-data sample with modified cross sections and with an integrated luminosity of $\mathcal{L} = 50 \text{ pb}^{-1}$. The errors on the measured quantities are obtained from a dedicated toy study, described in section 4.7.2 (table C.4).

C.2. Yield and ratio distributions after toy studies

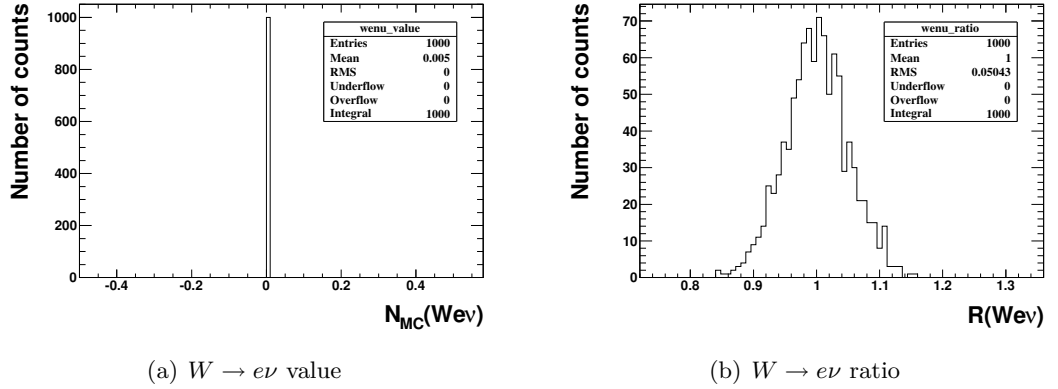


Figure C.1.: Distributions of the yields and ratios of $W \rightarrow e\nu$ after the counting analysis with 1000 different toy samples

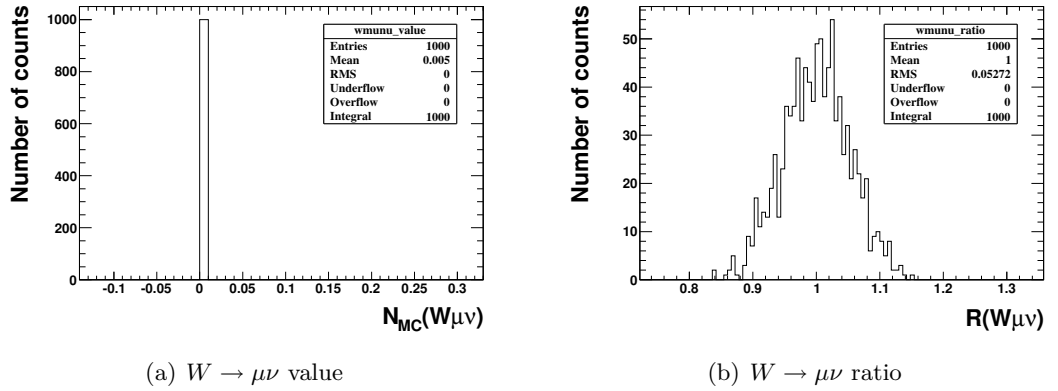


Figure C.2.: Distributions of the yields and ratios of $W \rightarrow \mu\nu$ after the counting analysis with 1000 different toy samples

C.2. Yield and ratio distributions after toy studies

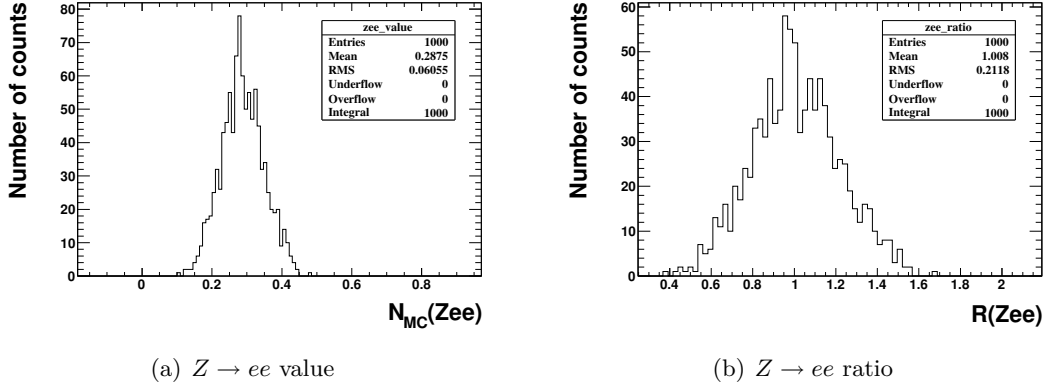


Figure C.3.: Distributions of the yields and ratios of $Z \rightarrow ee$ after the counting analysis with 1000 different toy samples

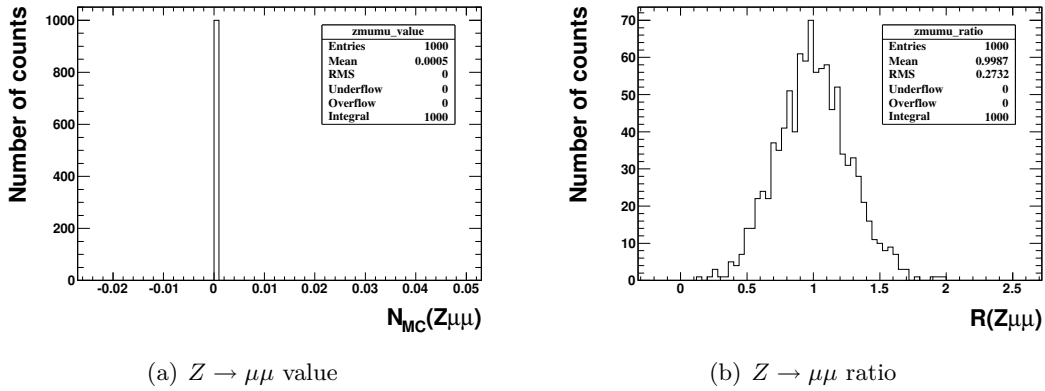


Figure C.4.: Distributions of the yields and ratios of $Z \rightarrow \mu\mu$ after the counting analysis with 1000 different toy samples

C. Counting analysis

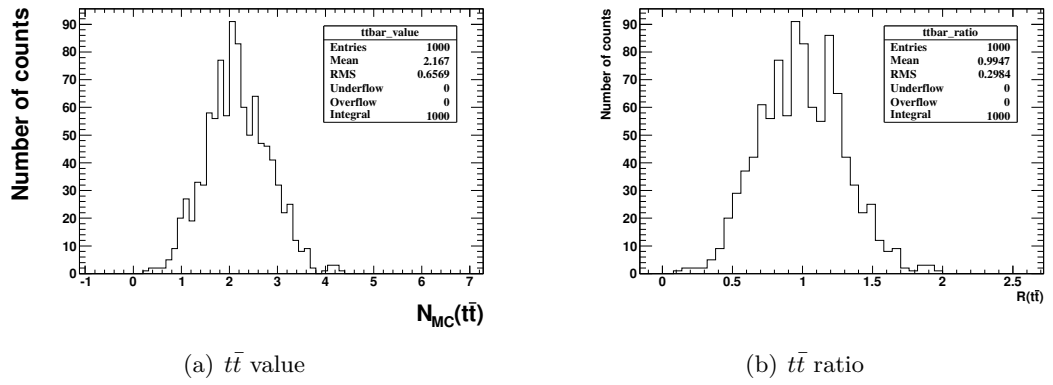


Figure C.5.: Distributions of the yields and ratios of $t\bar{t}$ after the counting analysis with 1000 different toy samples

C.3. Mean and RMS values after toy studies

Sample	Yield μ	Yield σ	Yield $\frac{\sigma}{\sqrt{1000}}$	Ratio μ	Ratio σ	Ratio $\frac{\sigma}{\sqrt{1000}}$
$W_{e\nu}+\text{jets}$	0	0	0	0.588	0.057	0.002
$W_{\mu\nu}+\text{jets}$	0	0	0	0.586	0.056	0.002
$Z_{ee}+\text{jets}$	0.163	0.055	0.002	0.573	0.193	0.006
$Z_{\mu\mu}+\text{jets}$	0	0	0	0.562	0.276	0.009
$t\bar{t}$	3.517	0.807	0.026	1.615	0.371	0.012
Signal yield	1.732	2.891	0.091			

Table C.2.: Mean values μ and standard deviations σ of yields and ratios after the counting analysis with 1000 different toy samples. The analysis was performed with $\mathcal{L} = 50 \text{ pb}^{-1}$ and modified cross sections.

Sample	Yield μ	Yield σ	Yield $\frac{\sigma}{\sqrt{1000}}$	Ratio μ	Ratio σ	Ratio $\frac{\sigma}{\sqrt{1000}}$
$W_{e\nu}+\text{jets}$	0	0	0	1.0000	0.0113	0.0004
$W_{\mu\nu}+\text{jets}$	0	0	0	1.0000	0.0113	0.004
$Z_{ee}+\text{jets}$	5.703	0.264	0.008	1.000	0.046	0.002
$Z_{\mu\mu}+\text{jets}$	0	0	0	1.000	0.061	0.002
$t\bar{t}$	43.45	2.809	0.089	0.998	0.065	0.002
Signal yield	20.99	10.63	0.34			

Table C.3.: Mean values μ and standard deviations σ of yields and ratios after the counting analysis with 1000 different toy samples. The analysis was performed with $\mathcal{L} = 1 \text{ fb}^{-1}$ and default cross sections.

Sample	Yield μ	Yield σ	Yield $\frac{\sigma}{\sqrt{1000}}$	Ratio μ	Ratio σ	Ratio $\frac{\sigma}{\sqrt{1000}}$
$W_{e\nu}+\text{jets}$	0	0	0	0.5868	0.0123	0.0004
$W_{\mu\nu}+\text{jets}$	0	0	0	0.5841	0.0123	0.0004
$Z_{ee}+\text{jets}$	3.246	0.256	0.008	0.569	0.045	0.001
$Z_{\mu\mu}+\text{jets}$	0	0	0	0.557	0.061	0.002
$t\bar{t}$	70.83	3.57	0.11	1.627	0.082	0.003
Signal yield	32.19	13.09	0.41			

Table C.4.: Mean values μ and standard deviations σ of yields and ratios after the counting analysis with 1000 different toy samples. The analysis was performed with $\mathcal{L} = 1 \text{ fb}^{-1}$ and modified cross sections.

C.4. Yields and ratios as a function of the true signal contribution after toy studies

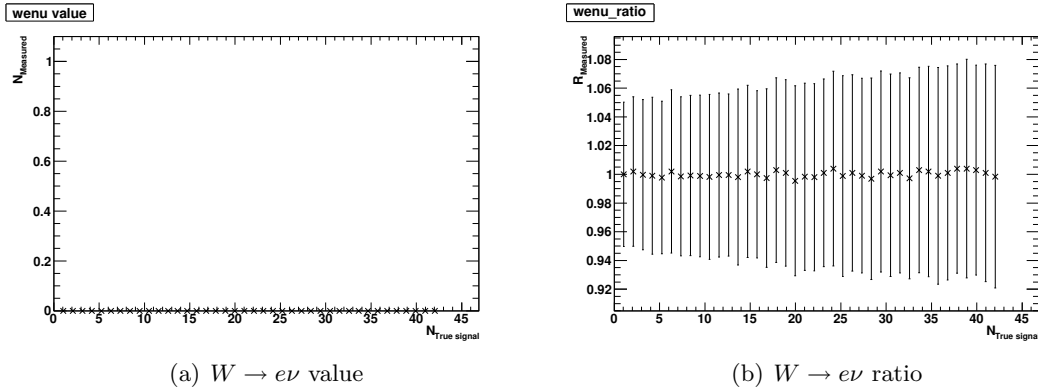


Figure C.6.: The computed yields and ratios of $W \rightarrow e\nu$ as a function of the true signal contribution. Each point consists of 1000 different toy samples. Plotted are the mean values and the standard deviations are denoted by the error bars.

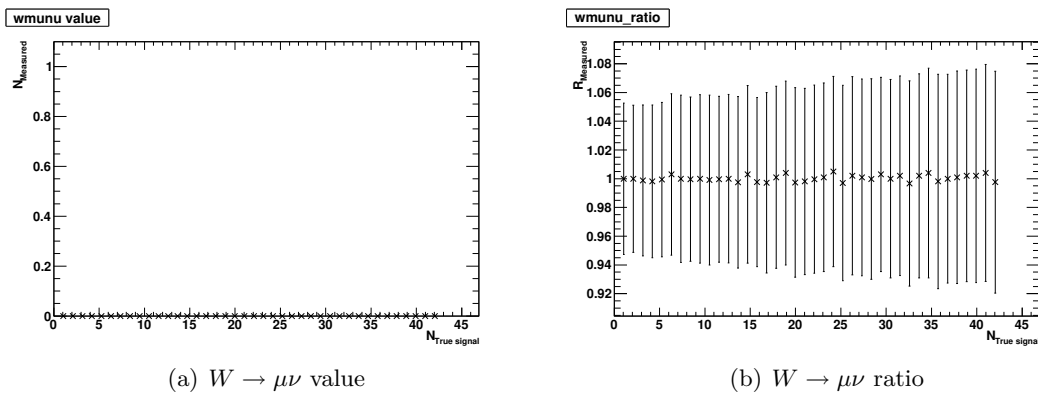


Figure C.7.: The computed yields and ratios of $W \rightarrow \mu\nu$ as a function of the true signal contribution. Each point consists of 1000 different toy samples. Plotted are the mean values and the standard deviations are denoted by the error bars.

C. Counting analysis

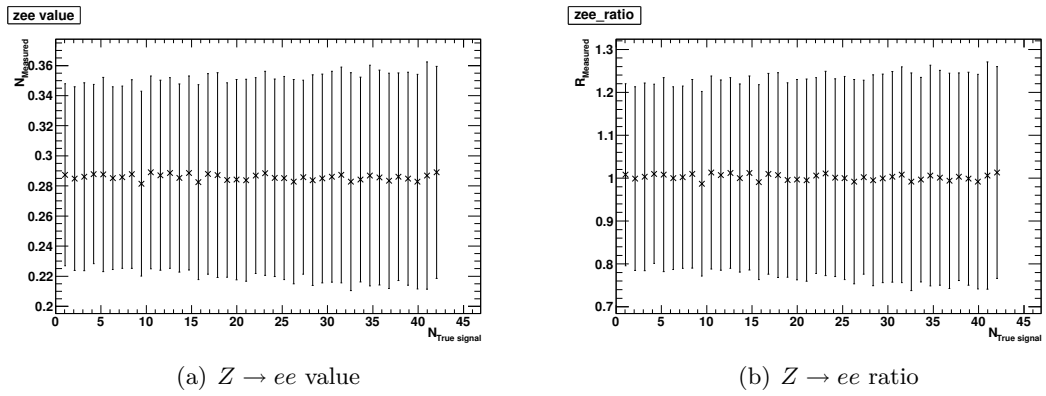


Figure C.8.: The computed yields and ratios of $Z \rightarrow ee$ as a function of the true signal contribution. Each point consists of 1000 different toy samples. Plotted are the mean values and the standard deviations are denoted by the error bars.

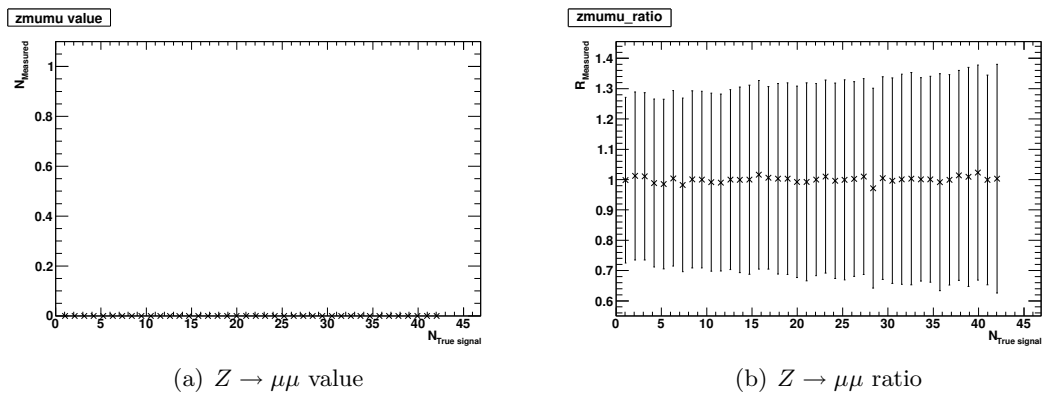


Figure C.9.: The computed yields and ratios of $Z \rightarrow \mu\mu$ as a function of the true signal contribution. Each point consists of 1000 different toy samples. Plotted are the mean values and the standard deviations are denoted by the error bars.

C.4. Yields and ratios as a function of the true signal contribution after toy studies

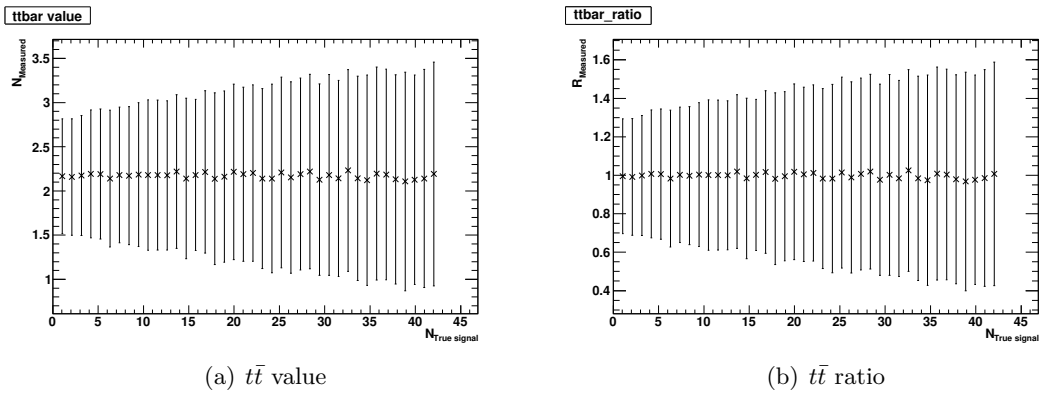


Figure C.10.: The computed yields and ratios of $t\bar{t}$ as a function of the true signal contribution. Each point consists of 1000 different toy samples. Plotted are the mean values and the standard deviations are denoted by the error bars.

D. Cut optimisation

D.1. Optimisation with additional variable N_{Jets}

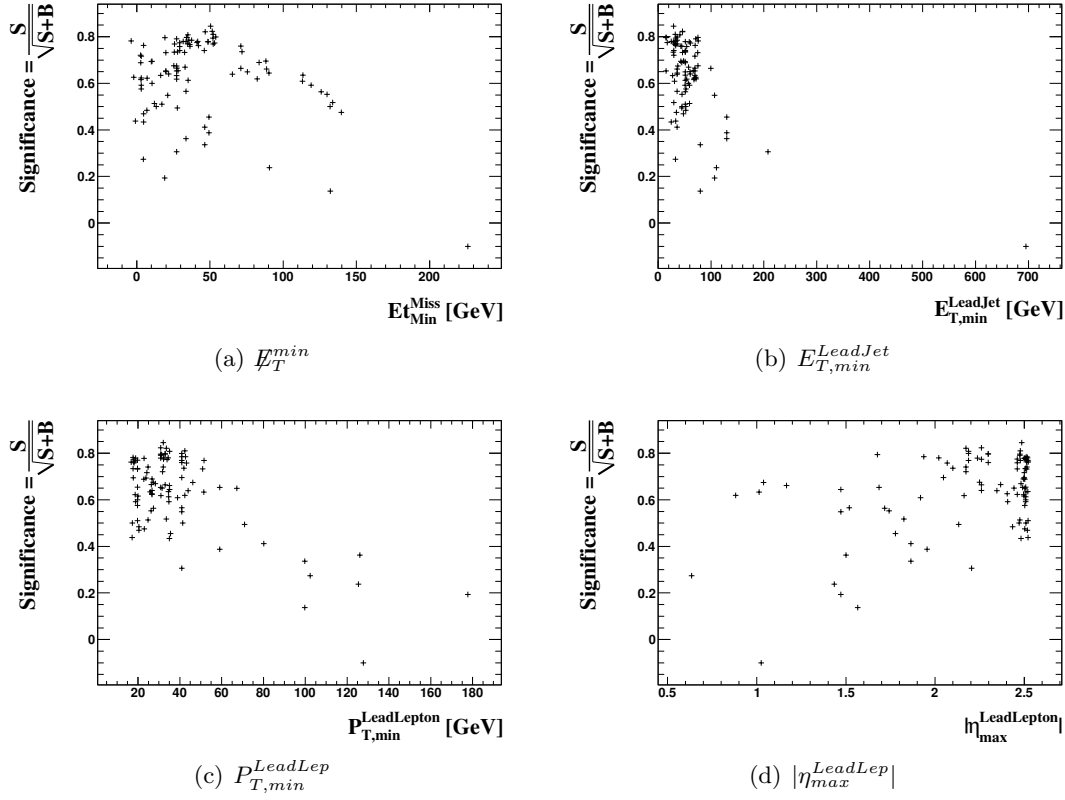


Figure D.1.: Significance $S/\sqrt{S+B}$ as a function of the cut values after optimisation with *TMVA* and with additional optimised variable N_{Jets} .

D. Cut optimisation

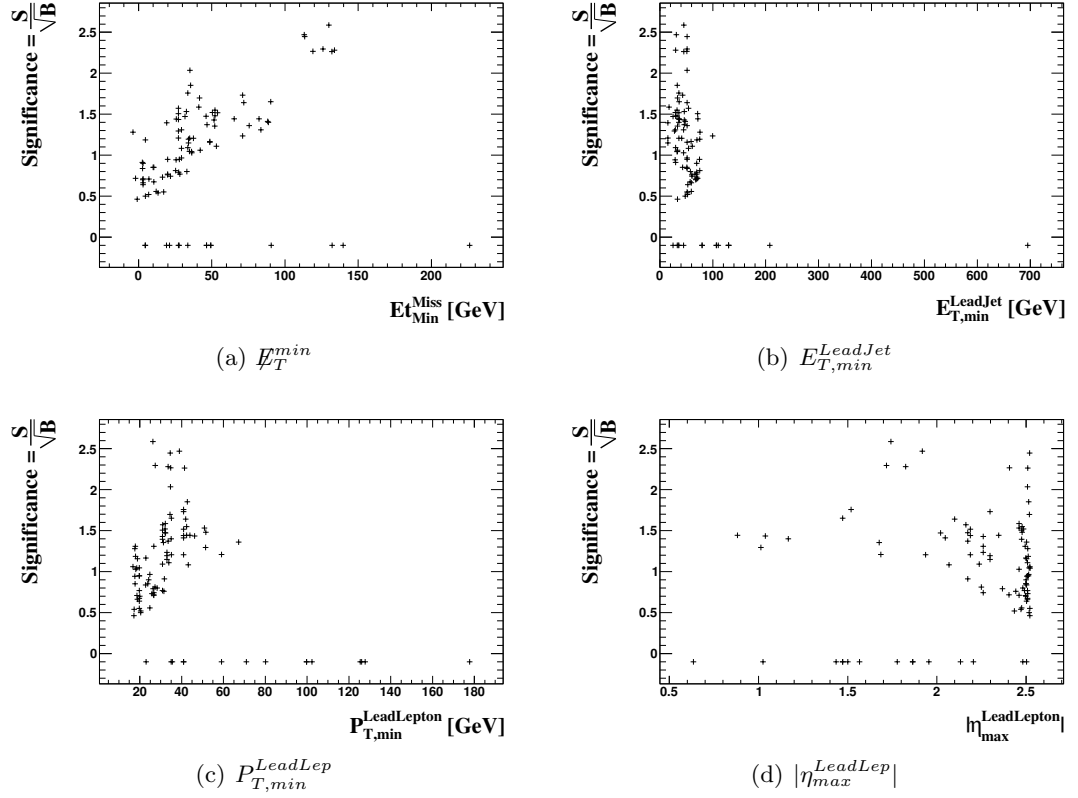


Figure D.2.: Significance S/\sqrt{B} as a function of the cut values after optimisation with *TMVA* and with additional optimised variable N_{Jets} .

Bibliography

- [1] W Hou. Source of CP Violation for Baryon Asymmetry of the Universe. Technical report, 2008. URL <http://arxiv.org/abs/0803.1234v3>.
- [2] Lyndon Evans and Philip Bryant. LHC machine. *Journal of Instrumentation*, 3(08):S08001, 2008. URL <http://stacks.iop.org/1748-0221/3/i=08/a=S08001>.
- [3] The ATLAS Collaboration and G. Aad et al. The ATLAS Experiment at the CERN Large Hadron Collider. *JINST*, 3(S08003), 2008. URL <http://iopscience.iop.org/1748-0221/3/08/S08003>.
- [4] C. Amsler et al. (Particle Data Group). *The Review of Particle Physics*. Physics Letters B667, 1 (2008) and 2009 partial update for the 2010 edition.
- [5] Jim Holt. Beyond the standard model. *Scientific American*, 2006.
- [6] Francis Halzen and Alan D. Martin. *Quarks and Leptons*. Wiley, 1985.
- [7] Martin Luscher. Lattice QCD: From quark confinement to asymptotic freedom. *Annales Henri Poincare*, 4:S197–S210, 2003.
- [8] Stefan Stohl. PANDA (antiProton ANnihilation at DArmstadt): die starke kraft - oder wie halten die quarks zusammen? *Welt der Physik*, 2005. URL <http://www.weltderphysik.de/de/377.php>.
- [9] O. Bär. Lecture: Theoretische Einführung in das Standardmodell der Elementarteilchenphysik. WS 2008/2009.
- [10] M Kobayashi and T Maskawa. CP violation in the Renormalizable Theory of Weak Interaction. *Progr. Theor. Phys.*, 49(2):6, Feb 1973.
- [11] The ALEPH Collaboration, the DELPHI Collaboration, the L3 Collaboration, the OPAL Collaboration, the SLD Collaboration, the LEP Electroweak Working Group, and the SLD electroweak, heavy flavour groups. Precision electroweak measurements on the Z resonance. *Phys.Rept.*, 427(257), 2006. URL <http://arxiv.org/abs/hepex/0509008>.
- [12] A.D. Sakharov. Violation of CP Symmetry, C-Asymmetry and Baryon Asymmetry of the Universe. *JETP Lett.*, 5:24–27, 1967.
- [13] Bob Holdom. The discovery of the fourth family at the LHC: what if? *Journal of High Energy Physics*, 2006(08):076, 2006. URL <http://stacks.iop.org/1126-6708/2006/i=08/a=076>.

Bibliography

- [14] Bob Holdom, WS Hou, Tobias Hurth, Michelangelo Mangano, Saleh Sultansoy, and Gokhan Unel. Four statements about the fourth generation. *PMC Physics A*, 3(1):4, 2009. ISSN 1754-0410. doi: 10.1186/1754-0410-3-4. URL <http://www.physmathcentral.com/1754-0410/3/4>.
- [15] Michael E. Peskin and Tatsu Takeuchi. New constraint on a strongly interacting Higgs sector. *Phys. Rev. Lett.*, 65(8):964–967, Aug 1990. doi: 10.1103/PhysRevLett.65.964.
- [16] The ALEPH Collaboration, the DELPHI Collaboration, the L3 Collaboration, the OPAL Collaboration, and the LEP Electroweak Working Group. A Combination of Preliminary Electroweak Measurements and Constraints on the Standard Model. Technical Report CERN-PH-EP/2006-042, CERN, Geneva, 2006. URL <http://arxiv.org/abs/hep-ex/0612034>.
- [17] LEP EWWG. Fit to S,T, Summer 2006. URL http://lepewwg.web.cern.ch/LEPEWWG/plots/summer2006/s06_stu_contours.eps.
- [18] Graham D. Kribs, Tilman Plehn, Michael Spannowsky, and Tim M. P. Tait. Four generations and Higgs physics. *Phys. Rev. D*, 76(7):075016, Oct 2007. doi: 10.1103/PhysRevD.76.075016. URL <http://arxiv.org/abs/0706.3718>.
- [19] Hong-Jian He, Nir Polonsky, and Shufang Su. Extra families, Higgs spectrum and oblique corrections. *Phys. Rev. D*, 64(5):053004, Jul 2001. doi: 10.1103/PhysRevD.64.053004. URL <http://arxiv.org/abs/hep-ph/0102144>.
- [20] CDF Collaboration (F. Abe et al.). The CDF Detector: An overview. Technical Report FERMILAB-PUB-88-25-E, Tevatron, 1988. URL http://www-cdf.fnal.gov/physics/tech_ps/PUB-88-25-E.ps.
- [21] S. Abachi et al. The D \emptyset Detector. *Nucl. Instrum. Meth.*, A338:185–253, 1994. doi: 10.1016/0168-9002(94)91312-9.
- [22] The CDF collaboration. Search for Heavy Top $t' \rightarrow Wq$ in Lepton Plus Jets Events in $\int \mathcal{L} dt = 4.6 \text{ fb}^{-1}$. *Conf. Note 10110*, 2010. URL http://www-cdf.fnal.gov/physics/new/top/confNotes/tprime_CDFnotePub.pdf.
- [23] T. Aaltonen et al. . Search for New Bottomlike Quark Pair Decays $Q\bar{Q} \rightarrow (tW^\mp)(\bar{t}W^\pm)$ in Same-Charge Dilepton Events. *Phys. Rev. Lett.*, 104(9):091801, Mar 2010. doi: 10.1103/PhysRevLett.104.091801.
- [24] B. Adeva et al. The construction of the L3 experiment. *Nuclear Instruments and Methods in Physics Research Section A: Accelerators, Spectrometers, Detectors and Associated Equipment*, 289(1-2):35 – 102, 1990. ISSN 0168-9002. doi: DOI:10.1016/0168-9002(90)90250-A. URL <http://www.sciencedirect.com/science/article/B6TJM-470F3FY-4B/2/6a007b800a0bfaf46838e6b33386fc3e>.

- [25] L3 Collaboration. Search for Heavy Neutral and Charged Leptons in e^+e^- Anihilation at LEP. *Phys. Lett. B.*, 517(CERN-EP-2001-046):75–85, 2001. URL <http://arxiv.org/abs/hep-ex/0107015v1>.
- [26] H. Lacker and A. Menzel. Constraints on CKM matrix elements within a fourth generation. January 14-16 2010, Taipei, Second Workshop on Beyond 3 Generation Standard Model.
- [27] H. Lacker and A. Menzel. Simultaneous Extraction of the Fermi constant and PMNS matrix elements in the presence of a fourth generation. *HU-EP-10/10*, 2010. URL <http://arxiv.org/abs/1003.4532>.
- [28] A. Menzel. Diploma thesis: Constraints on Matrix Elements of the Quark and Neutrino Mixing Matrix within a Four Generation Standard Model with CKMfitter, 2010.
- [29] J. Charles, A. Höcker, H. Lacker, S. Laplace, F. R. Le Diberder, J. Malcles, J. Ocariz, M. Pivk, and L. Roos. CP violation and the CKM matrix: assessing the impact of the asymmetric B factories. *The European Physical Journal C - Particles and Fields*, 41:1–131, 2005. ISSN 1434-6044. URL <http://dx.doi.org/10.1140/epjc/s2005-02169-1>. 10.1140/epjc/s2005-02169-1.
- [30] CERN. Accelerators Optics. URL <http://cern-accelerators-optics.web.cern.ch/cern-accelerators-optics/>.
- [31] Lucio Rossi. Superconductivity: its role, its success and its setbacks in the Large Hadron Collider of CERN. *Superconductor Science and Technology*, 23(3):034001, 2010. URL <http://stacks.iop.org/0953-2048/23/i=3/a=034001>.
- [32] A.D. Martin, W.J. Stirling, R.S. Thorne, and G. Watt. Parton distributions for the LHC. *Eur.Phys.J.*, C63(189-285):157, 2009. URL <http://arxiv.org/abs/0901.0002v3>.
- [33] The CMS Collaboration and S. Chatrchyan et al. The CMS Experiment at the CERN LHC. *JINST*, 3(S08004), 2008. URL <http://iopscience.iop.org/1748-0221/3/08/S08004>.
- [34] The LHCb Collaboration and A. Augusto Alves Jr. et al. The LHCb Detector at the LHC. *JINST*, 3(S08005), 2008. URL <http://iopscience.iop.org/1748-0221/3/08/S08005>.
- [35] The ALICE Collaboration and K. Aamodt et al. The ALICE Experiment at the CERN LHC. *JINST*, 3(S08002), 2008. URL <http://iopscience.iop.org/1748-0221/3/08/S08002>.
- [36] AC Team. CERN-AC-9906026. URL <http://www.cern.ch>.
- [37] Wikimedia Commons. Pseudorapidity2.png. URL <http://commons.wikimedia.org/wiki/File:Pseudorapidity2.png>.

Bibliography

- [38] .G Aad et al. Atlas pixel detector electronics and sensors. *Journal of Instrumentation*, 3(07):P07007, 2008. URL <http://stacks.iop.org/1748-0221/3/i=07/a=P07007>.
- [39] The ATLAS Collaboration. ATLAS: Detector and physics performance technical design report. Volume 1. Technical Report CERN-LHCC-99-14, CERN, 1999.
- [40] The ATLAS collaboration. ATLAS liquid argon calorimeter: Technical design report. *TDR*, 1996. CERN-LHCC-96-41.
- [41] The ATLAS collaboration. ATLAS tile calorimeter: Technical design report. *TDR*, 1996. CERN-LHCC-96-42.
- [42] The ATLAS collaboration. CMS, the Compact Muon Solenoid. Muon technical design report. *TDR*, 1997. CERN-LHCC-97-32.
- [43] J Haller, A Dos Anjos, Nick Ellis, M Landon, R Spiwoks, T Wengler, W Wiedenmann, and H Zoernig. Configuration of the ATLAS trigger. oai:cds.cern.ch:849080. Technical Report ATL-DAQ-CONF-2005-024. ATL-COM-DAQ-2005-030. CERN-ATL-COM-DAQ-2005-030, CERN, Geneva, 2005.
- [44] The ATLAS collaboration. Observation of inclusive electrons in the ATLAS experiment at $\sqrt{s} = 7$ TeV. Technical Report ATLAS-CONF-2010-073, CERN, Geneva, 2010.
- [45] R Nicolaidou, L Chevalier, S Hassani, J F Laporte, E Le Menedeu, and A Ouraou. Muon identification procedure for the ATLAS detector at the LHC using Muonboy reconstruction package and tests of its performance using cosmic rays and single beam data. *Journal of Physics: Conference Series*, 219(3):032052, 2010. URL <http://stacks.iop.org/1742-6596/219/i=3/a=032052>.
- [46] L. Asquith et al. Performance of Jet Algorithms in the ATLAS Detector. 2010. URL <https://svnweb.cern.ch/trac/atlasgrp/browser/CombPerf/JetETMiss/jetalgonote/trunk/JetAlgo.pdf>.
- [47] G. Aad et al. (The ATLAS collaboration). *Expected performance of the ATLAS experiment: detector, trigger and physics*. CERN, Geneva, 2009.
- [48] G.Z. Blazey et al. Run II Jet Physics: Proceedings of the Run II QCD and Weak Boson Physics Workshop. URL <http://arxiv.org/abs/hep-ex/0005012>.
- [49] M. Aliev, H. Lacker, U. Langenfeld, S. Moch, P. Uwer, and M. Wiedermann. – HATHOR – HAdronic Top and Heavy quarks crOss section calculator. Technical Report DESY 10-091, HU-EP-10-33, SFB/CPP-10-60, DESY, 2010. URL <http://arxiv.org/abs/1007.1327v1>.
- [50] The ATLAS Collaboration. The ATLAS Simulation Infrastructure. *Eur. Phys. J. C*, 2010. URL <http://arxiv.org/abs/1005.4568>.

- [51] V. Jain et al. The ATLAS Physics Analysis Workbook - Release 15. Technical report, CERN, 2010. URL <https://twiki.cern.ch/twiki/bin/view/AtlasProtected/PhysicsAnalysisWorkBookRel15>.
- [52] Torbjörn Sjöstrand and Stephen Mrenna and Peter Skands. PYTHIA 6.4 physics and manual. *Journal of High Energy Physics*, 2006(05):026, 2006. URL <http://arxiv.org/abs/hep-ph/0603175>.
- [53] Michelangelo L. Mangano, Fulvio Piccinini, Antonio D. Polosa, Mauro Moretti, and Roberto Pittau. ALPGEN, a generator for hard multiparton processes in hadronic collisions. *Journal of High Energy Physics*, 2003(07):001, 2003. URL <http://arxiv.org/abs/hep-ph/0206293>.
- [54] Stefano Frixione and Bryan R. Webber. Matching NLO QCD computations and parton shower simulations. *Journal of High Energy Physics*, 2002(06):029, 2002. URL <http://arxiv.org/abs/hep-ph/0204244>.
- [55] S. Agostinelli and others. Geant4 — a simulation toolkit. *Nuclear Instruments and Methods in Physics Research*, A(506):250–303, 2003. doi: NA.
- [56] R. Brun et al. ROOT. URL <http://root.cern.ch/>.
- [57] O. M. Kind. A++ - An object oriented analysis framework for ATLAS. URL http://www-eep.physik.hu-berlin.de/ATLAS/a_plusplus.
- [58] The CMS Collaboration. Search for A Fourth Generation b' Quark in tW Final State at CMS in pp Collisions at $\sqrt{s} = 10$ TeV. Jul 2009. URL <http://cdsweb.cern.ch/record/1195747/>.
- [59] I. Abt et al. The Tracking, calorimeter and muon detectors of the H1 experiment at HERA. *Nucl. Instrum. Meth.*, A386:348–396, 1997. doi: 10.1016/S0168-9002(96)00894-7.
- [60] P Speckmayer, A Höcker, J Stelzer, and H Voss. The toolkit for multivariate data analysis, TMVA 4, <http://tmva.sourceforge.net/>. *Journal of Physics: Conference Series*, 219(3):032057, 2010. URL <http://stacks.iop.org/1742-6596/219/i=3/a=032057>.
- [61] The ATLAS Collaboration. ATLAS: Detector and physics performance technical design report. Volume 2. Technical Report CERN-LHCC-99-15, CERN, 1999.

List of Figures

1.1. Fermion pair production	2
1.2. Particle masses	4
1.3. Electron-Photon coupling	5
1.4. Strong coupling constant	7
1.5. Quark confinement	8
1.6. Hadronic production cross section at Z resonance	14
1.7. Triangle anomaly	15
1.8. LEP EW group S,T fit	18
1.9. CERN accelerator complex	23
1.10. Parton distribution functions	24
1.11. LHC experiments	25
2.1. ATLAS detector overview	27
2.2. Pseudorapidity	29
2.3. ATLAS inner detector	30
2.4. ATLAS pixel detector	30
2.5. ATLAS calorimeters	32
2.6. ATLAS muon spectrometer	33
2.7. ATLAS event rates and processing times	35
2.8. ATLAS trigger system	36
4.1. b' same-sign dilepton decay channel	43
4.2. Heavy quark production cross sections	44
4.3. Z -decay with photon conversion	46
4.4. Z production with additional parton	47
4.5. Single top production channels	49
4.6. Z production with additional parton	49
4.7. E_T of jets in $W e \nu$ Np0 sample	52
4.8. Distribution of N_{Jets} for same-sign charged dileptons	54
4.9. Distribution of \cancel{E}_T	55
4.10. Distributions of $E_T^{LeadJet}$ and $P_T^{LeadLep}$	56
4.11. Distributions of $ \eta^{LeadLep} $ for specific samples	57
4.12. Distribution of $ \eta^{LeadLep} $	57
4.13. Distribution of $ \eta^{LeadLep} $ for different Z decay channels	58
4.14. Number of jets with all event selection cuts	59
4.15. Cut efficiencies	63
4.16. Signal over background ratios	64

List of Figures

4.17. Approximately needed integrated luminosity for a 5σ discovery	65
4.18. \cancel{E}_T in e^+e^- and $\mu^+\mu^-$ final states	68
4.19. Control regions for the counting analysis	69
4.20. Control ratios as a function of the iteration step	73
4.21. Signal and control regions for counting analysis with mixing sample	74
4.22. Control ratios as a function of the iteration step	76
4.23. Signal and W +jets control regions for counting analysis with mixing sam- ple containing varied cross sections	77
4.24. $t\bar{t}$ and Z +jets control regions for counting analysis with mixing sample, containing varied cross sections	78
4.25. Signal yield after toy studies	81
4.26. Signal yield after toy studies as a function of the true signal contribution	83
4.27. Input variables for tmv analysis	84
4.28. Signal efficiency as function of background rejection	85
4.29. Signal/Background efficiencies as a function of the optimised cut values	86
4.30. Significance S/\sqrt{B} as a function of ϵ_S and of the optimised cut values	87
4.31. Significance $S/\sqrt{S+B}$ as a function of ϵ_S and of the optimised cut values	88
4.32. Significances for optimisation with additional variable N_{Jets}	90
4.33. N_{Jets} in signal region with optimised cuts	91
4.34. Needed integrated luminosity for a 5σ discovery	92
B.1. Cut efficiencies plot ($b'(350 \text{ GeV}) \rightarrow t$)	114
B.2. Cut efficiencies plot ($t'(350 \text{ GeV}) \rightarrow b$)	115
B.3. Cut efficiencies plot ($t'(350 \text{ GeV}) \rightarrow q$)	115
B.4. Cut efficiencies plot ($t'(440 \text{ GeV}) \rightarrow b'$)	116
B.5. Signal over background ratio ($b'(350 \text{ GeV}) \rightarrow t$)	117
B.6. Signal over background ratio ($t'(350 \text{ GeV}) \rightarrow b$)	118
B.7. Signal over background ratio ($t'(350 \text{ GeV}) \rightarrow q$)	118
B.8. Signal over background ratio ($t'(440 \text{ GeV}) \rightarrow b'$)	119
C.1. Yields and ratios of $W \rightarrow e\nu$ after toy studies	122
C.2. Yields and ratios of $W \rightarrow \mu\nu$ after toy studies	122
C.3. Yields and ratios of $Z \rightarrow ee$ after toy studies	123
C.4. Yields and ratios of $Z \rightarrow \mu\mu$ after toy studies	123
C.5. Yields and ratios of $t\bar{t}$ after toy studies	124
C.6. Yields and ratios of $W \rightarrow e\nu$ after toy studies as a function of the true signal contribution	127
C.7. Yields and ratios of $W \rightarrow \mu\nu$ after toy studies as a function of the true signal contribution	127
C.8. Yields and ratios of $Z \rightarrow ee$ after toy studies as a function of the true signal contribution	128
C.9. Yields and ratios of $Z \rightarrow \mu\mu$ after toy studies as a function of the true signal contribution	128

C.10. Yields and ratios of $t\bar{t}$ after toy studies as a function of the true signal contribution 129

D.1. Significance $S/\sqrt{S+B}$ as a function of the optimised cut values 131

D.2. Significance S/\sqrt{B} as a function of the optimised cut values 132

List of Tables

1.1. Fermions of the Standard Model	2
1.2. Elementary forces of the Standard Model	3
1.3. Fermions of the SM including a 4th family	16
1.4. Parameter sets for (S, T) shifts	18
1.5. Current mass limits on 4th generation fermions	20
1.6. Precisely measured CKM matrix elements	20
2.1. η coverage of the muon detection chambers	34
4.1. Final states of b' decays	42
4.2. MC Signal samples	45
4.3. Electron selection cuts	51
4.4. Muon selection cuts	51
4.5. Jet selection cuts	53
4.6. Event selection cuts	59
4.7. Number of generated events, events after the filter and events after the trigger used in the simulation.	62
4.8. Efficiency after the filter, efficiency after the trigger and total trigger efficiency $\epsilon_{Trigger}$	63
4.9. Lepton categories to define control regions	68
4.10. Results of counting analysis with default mixing sample	72
4.11. Results of counting analysis with mixing sample containing varied cross sections	75
4.12. Results of counting analysis with toy sample	80
4.13. Mean values and standard deviations of yields and ratios after the toy studies	81
4.14. Final optimised cut values	89
4.15. Yields and significances before and after cut optimisation	91
A.1. MC samples	97
B.1. Number of generated events	102
B.2. Generator efficiencies	105
B.3. Cut numbers	108
B.4. Cut efficiencies	113
C.1. Results of counting analysis with toy sample containing varied cross sections	121

List of Tables

C.2. Mean values and standard deviations of yields and ratios after the toy studies ($\mathcal{L} = 50 \text{ pb}^{-1}$, modified cross sections)	125
C.3. Mean values and standard deviations of yields and ratios after the toy studies ($\mathcal{L} = 1 \text{ fb}^{-1}$, default cross sections)	125
C.4. Mean values and standard deviations of yields and ratios after the toy studies ($\mathcal{L} = 1 \text{ fb}^{-1}$, modified cross sections)	125

Danksagung

An dieser Stelle möchte ich mich bei allen bedanken, die mir beim Anfertigen dieser Arbeit geholfen haben.

Mein Dank gilt zunächst Herrn Prof. Dr. Heiko Lacker. Seit meiner Bachelorarbeit hat er es mir ermöglicht in der Arbeitsgruppe "Experimentelle Elementarteilchenphysik" mitzuwirken und bereits parallel zu meinem Studium Erfahrungen zu sammeln. Zudem hat er es mir ermöglicht, dass ich in dem vergangenen Jahr meine Masterarbeit in einem sehr interessanten Themengebiet anfertigen konnte und er hatte stets Zeit, wenn Fragen und Probleme aufgetreten sind.

Ebenso möchte ich mich bei Rocco Mandrysch bedanken, der mir bei vielen Aufgaben und Problemen geholfen hat und auch außerhalb des Arbeitsumfeldes für interessante Diskussionen und Gespräche zur Verfügung stand. Außerdem hat er mich beim Anfertigen einiger Teile dieser Arbeit sehr unterstützt.

Außerdem danke ich Dr. Malik Aliev und Dr. Sergio Grancagnolo für eine produktive Zusammenarbeit.

Ich danke Oliver Maria Kind, der das in dieser Arbeit verwendete Analyseframework *A++* entwickelt hat und mir insbesondere bei programmiertechnischen Problemen stets mit Rat und Tat zur Seite stand.

Ich möchte außerdem Florian Bernlochner, Thomas Lück, Andreas Menzel und Dr. Malik Aliev für das Durchlesen und die Hilfe bei vielen Teilen dieser Arbeit danken. Ebenso möchte ich allen Mitarbeitern der Arbeitsgruppe "Experimentelle Elementarteilchenphysik" dafür danken, dass sie zu jeder Zeit eine sehr nette Arbeitsatmosphäre schaffen.

Ich möchte mich außerdem auch bei meinen Eltern dafür bedanken, dass sie mir dieses Studium ermöglicht und mich vielfältig unterstützt haben. Schließlich danke ich ganz besonders meiner Freundin Kim für ihre Geduld und ihre Unterstützung.

Selbständigkeitserklärung

Ich erkläre, dass ich die vorliegende Arbeit selbständig und nur unter Verwendung der angegebenen Literatur und Hilfsmittel angefertigt habe.

Berlin, den 5. Oktober 2010

Dennis Wendland